**Department of Physics and Astronomy**
**Curtin Institute for Radio Astronomy**

# The Australian Mid-latitude Continental Ionosphere with Respect to Low-frequency Radio Astronomy

**David Edwin Herne**

**This thesis is presented for the Degree of**
**Doctor of Philosophy**
**of**
**Curtin University**

**June 2016**

# Author's Declaration

To the best of my knowledge and belief this thesis contains no material previously published by any other person except where due acknowledgement has been made. This thesis contains no material which has been accepted for the award of any other degree or diploma in any university.

# Abstract

This thesis will show that the Murchison Radio Observatory (MRO) site is an excellent location from which to conduct radio astronomy at VHF frequencies. This result is supported by the findings of a Square Kilometre Array (SKA) site selection committee mandated investigation into the RFI environment and ionospheric variability of the Murchison region of Western Australia. In this work, the ionosphere is characterised and its response to impinging VHF radio waves clearly established. This activity will contribute to an operational requirement (calibration) of the Murchison Widefield Array radio telescope (MWA) and delivery of the project's scientific goals (high fidelity imaging). Characterisation involved the acquisition and mapping of ionospheric absolute total electron content (aTEC) measured as total electron content units, $10^{16}$ electron $m^{-2}$ (TECU) and scintillation (as $S_4$) data over a period of the first half of solar cycle 24. Readings were performed at first (epoch 1 - E1) on the MRO (2008-2009) and later (epoch 2 - E2) at (1) Boolardy homestead, adjacent to the MRO and (2) on a site 519 km south of the MRO on the Australian Space Academy campus at Meckering (2012-2014). Observations revealed annual, inter-annual and diurnal variability on timescales of minutes and greater. Rapid, anomalous, event-related changes over short (minute to hourly) timescales were detected. These included the response of the ionosphere to a significant CME event (March 17$^{th}$ 2013) and a transient event (October 15$^{th}$ 2013). Clear evidence for large amplitude (several TECU) travelling ionospheric disturbances (TIDs), was produced and described in detail. The directions of 2 TIDs were calculated with ±12% and ±9% uncertainty and their speeds to ±19% and ±8% accuracy respectively. During E1, TEC levels rarely exceeded 20 TECU (99.0% < 20 TECU). During E2, TEC at Boolardy rarely exceeded 60 TECU (99.5% < 60 TECU). At the same time, TEC at Meckering rarely exceeded 50 TECU (98.1% < 50 TECU). The significance of these TEC levels is discussed with respect to imaging requirements for the MWA including

implications for Faraday rotation (FR), which is the tendency for the plane of polarisation of linearly polarised radio signals to be rotated by free electrons in the presence of a magnetic field (the Earth's) and refraction effects. At both sites over both E1 and E2, $S_4$ was reliably undetectable. Returned values fell typically within the range 0.0 to <<0.1. Occasional excursions in $S_4$ are discussed and are shown to be the result of signal interferences through multi-path effects. Differences between the disposition of the ionosphere at Boolardy and at Meckering, 519 km to the south, are discussed. Whereas TEC levels at Meckering were typically very close in value to those at Boolardy, background levels at the latter over E2 were often ranged a little higher (by a few TECU). Modelling of the response of the ionosphere to VHF (50-300 MHz) radio waves was undertaken. In the radio astronomy community, these frequencies are regarded and discussed as being of *low-frequency*. This expression is employed occasionally throughout this work. The consequences for the selection of parameters used in the calibration of the MWA, including thin-shell ionosphere height, were studied. Many radio astronomy calibration models confine the ionospheric TEC contribution to a thin-shell located at some altitude above the Earth's surface. The effective altitude however, was demonstrated to vary over not greater than hourly timescales and should be recalculated accordingly. Dual frequency GPS systems provided accurate line-of-sight (slant) aTEC readings that were converted to vertical TEC values. These data, incorporated into an appropriate modelling process, demonstrated that a single thin-shell ionosphere height returns such inaccurate FR values that all polarisation information in an image can quickly be lost. For a change of 1 TECU, FR ranges from ~4π radians at an observation frequency of 50 MHz and elevation of 30° to 0.03π radians at 300 MHz and 90° elevation (zenith). Improving model thin-shell height selection with the aid of the International Reference Ionosphere model (IRI-2012) was investigated. The difference in output of this model with measured TEC values over E1 and E2 was studied and reported. E1 incorporated a period of time

at the very beginning of solar cycle 24 (2008-2009) and E2, the peak of the cycle (2012-2014). The mean RMS difference between the model output over E1 was low (1.3 TECU) and over E2 was less accurate (4.3 TECU). Over the peak of the cycle in 2014, the mean RMS difference was considerably higher (7.5 TECU). The climatological IRI-2012 model did not predict observed TEC values well during periods of high sunspot number (SSN). The system architecture and benefits to the MWA and other low-frequency radio telescopes obtained by orbiting a triple, low-frequency beacon equipped satellite (in a cubesat form factor) are outlined and discussed. The proposed mission was regarded very highly at a conference on the subject held at Mount Stromlo Observatory in Canberra in 2014. Inaccurate claims published in a leading astronomical journal by over 80 authors regarding the nature of the Australian, mid-latitude, continental, ionosphere were refuted with a peer-reviewed letter. An SKA RFI study, conducted in 2005/2006 by a CSIRO ATNF team that included this author demonstrated that a low RFI noise environment is encountered in the region occupied by the MRO.

# Acknowledgements

I take this opportunity to first thank my Thesis advisors Professor Mervyn Lynch and Doctor John Kennewell, without whose guidance, inspiration, patience and perseverance this work would not have been possible. Their intellect, knowledge and experience were essential in guiding this work to completion. I thank Dr Kennewell too, for the use of his Australian Space Academy campus at Meckering in Western Australia for the locating some of my experimental apparatus, which enabled observations that would otherwise have been impossible. A chance meeting with Professor Lynch at Curtin University in late 2004, during which he outlined a new project opportunity that would lead to the establishment of the MWA, presented opportunities that I hope I have grasped to the best of my abilities. Radio astronomy in Western Australia owes an enormous debt to Professor Lynch, which as difficult as it is today to conceive, would not have existed here without his tireless and largely unrecognised efforts. I further take the opportunity to thank engineering staff of the Curtin Institute for Radio Astronomy for their support in monitoring experimental apparatus and collecting readings. I express my gratitude especially to Curtin engineer David Emrich, who managed the maintenance of equipment and collection of data at Boolardy homestead. I extend a sincere thanks to the United States Airforce Office of Scientific Research (USAFOSR) for their provision of the three, high quality, dual-frequency GPS receivers that were an essential instrumental component of this work. Thank you too, to CSIRO ATNF with whom I served as a staff member during 2005/2006 in the role of field support for the collection of RFI data during the SKA site verification and selection process. In particular, I thank Ron Beresford, lead engineer on the project that led eventually to a successful bid for a significant component of the SKA, the SKA-Low radio telescope. The CSIRO also also provided me access to their solar powered instrument van that had been used during the RFI studies, to later house some of my equipment. This solar powered facility proved

to be the most reliable that I used over the course of the study, providing 100% uptime. Next, my thanks and gratitude extend to Professor Don Backer (dec.) who gave me the opportunity to take part in his initial radio astronomy experiment in Western Australia, The Precision Array for Probing the Epoch of Reionisation. Professor Backer and senior investigator, Doctor Richard Bradley, extended to me the opportunity, completely untested, to construct vital components that were to host experimental apparatuses and to join them and others as co-author on the collaboration's first paper. Thanks also to Professor Judd Bowman, to whom I acted in field support for his epoch of reionisation experiment, Edges and to Judd and Cassie Bowman for their support and encouragement. I acknowledge and thank the staff of Haystack Observatory, with whom the earliest site selection visits and field experiments were conducted under often very trying conditions. I thank in particular, Professor Colin Lonsdale, Doctor Diya Oberoi and Doctor Brian Corey, each of whom provided a great deal of encouragement. Directly in the field of GPS TEC measurement, I thank Doctor Anthea Coster of Haystack Observatory for her contribution to my understanding of GPS systems and to Doctor Charles Carrano, who wrote the GPS analysis program SCINDA that our systems employed. I offer thanks also to Western Australian based Horizon Energy for the donation of components from which we constructed 3 solar-power supply trailers, which continue in use. Finally, I extend my thanks and gratitude to those families in whose homes in the Murchison region, on Mileura and Boolardy Stations, we were accommodated and who made us so much at home while we were visiting and who also provided practical support. These included Patrick and Lian Walsh and Mark and Carolyn Halleen and their families.

# Dedication

I lovingly dedicate this thesis to my wife Leanne, for her unfailing support and encouragement over an often quite stressful period. I thank too, my children Kate, Claire, John and Emmett for freeing up your father for this undertaking. I think too of my parents, now departed, Dermot (Don) and Jenny, who provided my brothers and me a loving and secure home. Thanks to my brother Doctor Matthew C. Herne for his endless encouragement. I remember also two men who were instrumental in building my confidence, Doctor Phillip J. Kesley and Mr Robert (Bill) Coles Reitze, each of whom saw potential in me when I couldn't. I remember too, the men of the early astronaut corps and the later Apollo astronauts who were inspirational and especially Neil Armstrong's encouragement in personal correspondence. Finally, to my grandchildren, currently Imogen, Ruby and Zoe and hopefully future blessings, Papa loves you.

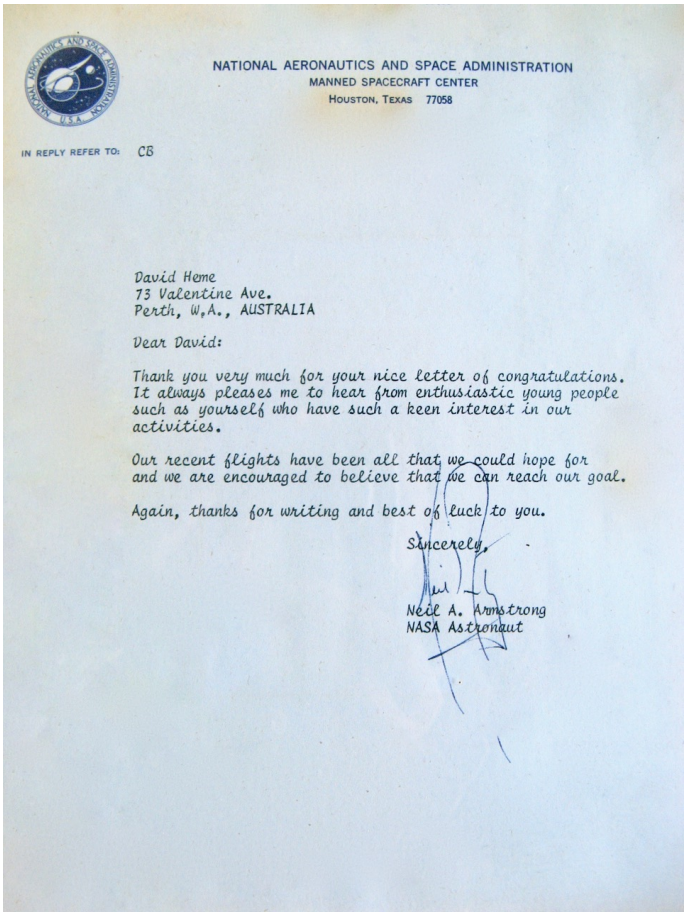

NATIONAL AERONAUTICS AND SPACE ADMINISTRATION
MANNED SPACECRAFT CENTER
HOUSTON, TEXAS 77058

IN REPLY REFER TO: CB

David Heme
73 Valentine Ave.
Perth, W.A., AUSTRALIA

Dear David:

Thank you very much for your nice letter of congratulations. It always pleases me to hear from enthusiastic young people such as yourself who have such a keen interest in our activities.

Our recent flights have been all that we could hope for and we are encouraged to believe that we can reach our goal.

Again, thanks for writing and best of luck to you.

Sincerely,

Neil A. Armstrong
NASA Astronaut

# Table of Contents

# List of Figures

# List of Tables

# Glossary of Acronyms and Abbreviations

| | |
|---|---|
| **1T** | 1 Tile Expedition (March 2007) |
| **32T** | 32 Tile MWA instrument |
| **128T** | 128 Tile MWA instrument |
| **A&A** | Astronomy & Astrophysics (journal) |
| **ADC** | Analogue to Digital Convertor |
| **AE** | Auroral Electrojet |
| **AGU** | American Geophysical Union |
| **AGW** | Atmospheric Gravity Wave (as distinct to gravitational waves) |
| **ATA** | Allen Telescope Array |
| **aTEC** | absolute Total Electron Content |
| **ASA** | Australian Space Academy (Meckering) |
| **ASKAP** | Australian Square Kilometre Array Pathfinder |
| **ASSC** | Australian Space Sciences Conference |
| **ATNF** | Australia Telescope National Facility |
| **BIMA** | Berkeley Illinois Maryland Association millimetre wave interferometer |
| **B-V** | Brunt-Väisälä (pulsation/frequency) |
| **CIRA** | Curtin Institute for Radio Astronomy |
| **CME** | Coronal Mass Ejection |
| **CML** | Calibration Measurement Loop |
| **CODE** | Centre for Orbit Determination Europe |
| **CSIRO** | Commonwealth Scientific and Industrial Research Organisation |
| **DCC** | Distance Correlation Coefficient |
| **DMSP** | Defence Meteorological Satellite Programme |
| **ED** | ExpeDition series expeditions to the Murchison Radio Observatory |
| **EDGES** | Experiment to Detect the Global EoR Signature |
| **E1** | Epoch number 1 (2008-2009) |
| **E2** | Epoch number 2 (2012-2015) |
| **EE** | Equatorial Electojet |
| **EIA** | Equatorial Ionisation Anomaly |

| | |
|---|---|
| **EMC** | ElectroMagnetic Compatibility |
| **EOR** | Epoch Of Reionisation |
| **Es** | sporadic E |
| **EUV** | Extreme Ultraviolet |
| **FAI** | Field Aligned Irregularity |
| **foE** | Highest frequency ordinary ray reflected vertically in the E region |
| **foF2/1** | Highest frequency ordinary ray reflected vertically in the F2/F1 region |
| **FPGA** | Floating Point Gate Array |
| **FR** | Faraday Rotation |
| **FWHM** | Full Width Half Maximum |
| **GBO** | Green Bank Observatory |
| **GIM** | Global Ionospheric Map |
| **GPGPU** | General Purpose Graphics Processing Unit |
| **GPS** | Global Positioning System |
| **GMRT** | Giant Metrewave Radio Telescope |
| **HF** | High Frequency (3 - 30 MHz) |
| **hmF2** | Height of the peak value of the F2 region |
| **HTI** | Height-Time-Intensity (analysis) |
| **ICRAR** | International Centre for Radio Astronomical Research |
| **IGRF** | International Geomagnetic Reference Field |
| **IONEX** | IONosphere Map EXchange |
| **IPP** | Ionospheric Pierce Point |
| **IPS** | InterPlanetary Scintillation/Ionospheric Prediction Service |
| **IQI** | Ionosphere Quality Index |
| **ISM** | InterStellar Medium |
| **IRI** | International Reference Ionosphere |
| **LNA** | Low Noise Amplifier |
| **LOFAR** | Low Frequency Array for Radio astronomy |
| **LOS** | Line Of Sight |
| **LSTID** | Large-Scale Travelling Ionospheric Disturbance |
| **LWA** | Long Wavelength Array |

| | |
|---|---|
| **LT** | Local Time |
| **MDE** | Magnetic Dip Equator |
| **MIT** | Massachusetts Institute of Technology |
| **MLT** | Magnetic Local Time |
| **MWA** | Murchison Widefield Array (previously Mileura Widefield Array) |
| **MRO** | Murchison Radio Observatory |
| **NASA** | National Aeronautics and Space Administration |
| **NGDC** | National Geophysical Data Centre |
| **NOAA** | National Oceanographic and Atmospheric Administration |
| **NRAO** | National RAdio Observatory |
| **NSD** | Normalised Standard Deviation |
| **NSF** | National Science Foundation |
| **OSTM** | Ocean Surface Topography Mission |
| **PAPER** | Precision Array for the Epoch of Reionisation |
| **PED** | Peak Electron Density |
| **PFB** | Polyphase Filter Bank |
| **POSSUM** | Polarisation Sky Survey of the Universe's Magnetism |
| **RFI** | Radio Frequency Interference |
| **RINEX** | Receiver Independent Exchange Format |
| **RM** | Rotation Measure |
| **RRI** | Rahman Research Institute |
| **RTS** | Real Time System |
| **$S_4$** | Scintillation index |
| **SAGS** | Solar And Geophysical Summary reports |
| **SCINDA** | SCIntillation Network Detection Aid |
| **SED** | Storm Enhanced Density |
| **SEP** | Solar Energetic Particle |
| **SFU** | Solar Flux Unit ($10^{-22}$ $Wm^{-2}$ $Hz^{-1}$) |
| **SKA** | Square Kilometre Array |
| **STEC** | Slant Total Electron Content |
| **SSN** | Smoothed Sunspot Number |
| **TEC** | Total Electron Content |

| | |
|---|---|
| **TECU** | Total Electron Content Unit ($10^{16}$ $m^{-2}$) |
| **TFBC** | Triple low-Frequency Beacon equipped Cubesat |
| **TID** | Travelling Ionospheric Disturbance |
| **UPS** | Uninterruptible Power Supply |
| **URSI** | International Union of Radio Science |
| **USAFOSR** | United States Airforce Office Of Scientific Research |
| **USNO** | United States Naval Observatory |
| **UTC** | Universal Time Coordinates |
| **VHF** | Very High Frequency (30 - 300 MHz) |
| **VLBI** | Very Long Baseline Interferometry |
| **VTEC** | Vertical Total Ionospheric Content |
| **WA** | Western Australia |
| **WBMOD** | WideBand MODel ionospheric scintillation model |
| **X** | X series expeditions to the Murchison Radio Observatory |

# 1. Introduction

The world's premier VHF (low-frequency) radio observatory, the Square Kilometre Array's low-frequency component (SKA-Low), is being constructed in the Murchison region of Western Australia. A precursor to this instrument, the Murchison Widefield Array (MWA), has been operating since 2009 on the Murchison Radio Observatory (MRO) site, the planned home of the SKA-Low. This PhD thesis addresses several key questions relevant to low-frequency radio astronomy in Western Australia while investigating the disposition and dynamics of the local (km scale) and regional (thousands of km scale) ionosphere.

## 1.1. Radio Waves in the Ionosphere.

Wilhelm Sellmeier, in 1872 (Sellmeier 1872) proposed that 'ether oscillations' interact with 'material corpuscles' in Earth's atmosphere, resulting in dispersion of incoming oscillations. By this he formulated a theory of optical refraction. Although his thinking was predicated on the existence of a material 'ether', by which disturbances might be propagated, Sellmeier's theory anticipated Hendrik A. Lorentz's electron theory and survived J. Clerk Maxwell's revolutionary mathematical treatment of electromagnetism (Rawer 1993). Such was his insight, Sellmeier's dispersion equation, reformulated as a modern description of the interaction of electromagnetic field energy with a conductive medium, enjoys modern acceptance and has even been further refined with relativistic corrections (Morris 2010). Hence, it has long been known that electromagnetic radiation is subject to dispersion in passing through the ionosphere with lower frequencies more highly susceptible. It is therefore an imperative in the radio study of celestial phenomena, at low radio frequencies in particular, that the behaviour of radio waves in the ionosphere be well understood.

Radio astronomy had its genesis at what is today considered a low radio frequency, 20.5 MHz, with the serendipitous discovery of extraterrestrial radio waves by Karl G. Jansky (Jansky 1933). The first dedicated radio-astronomical instrument was built by Grote Reber soon after Jansky's paper was published. After attempts at detecting extraterrestrial radio signals at two frequencies, 3300 MHz and 900 MHz, he was successful at 160 MHz using a parabolic receiving dish of 9 m diameter and an electrical system of his own design (Reber was a qualified electrical engineer) (Reber 1942). Later instruments migrated largely to higher frequencies. However, low-frequency radio astronomy has enjoyed a resurgence recently with the advent of instruments such as the MWA in Western Australia (Lonsdale, Cappallo et al. 2009) and the Low-Frequency Array for radio astronomy (LOFAR) in the Netherlands (van Haarlem, Wise et al. 2013).

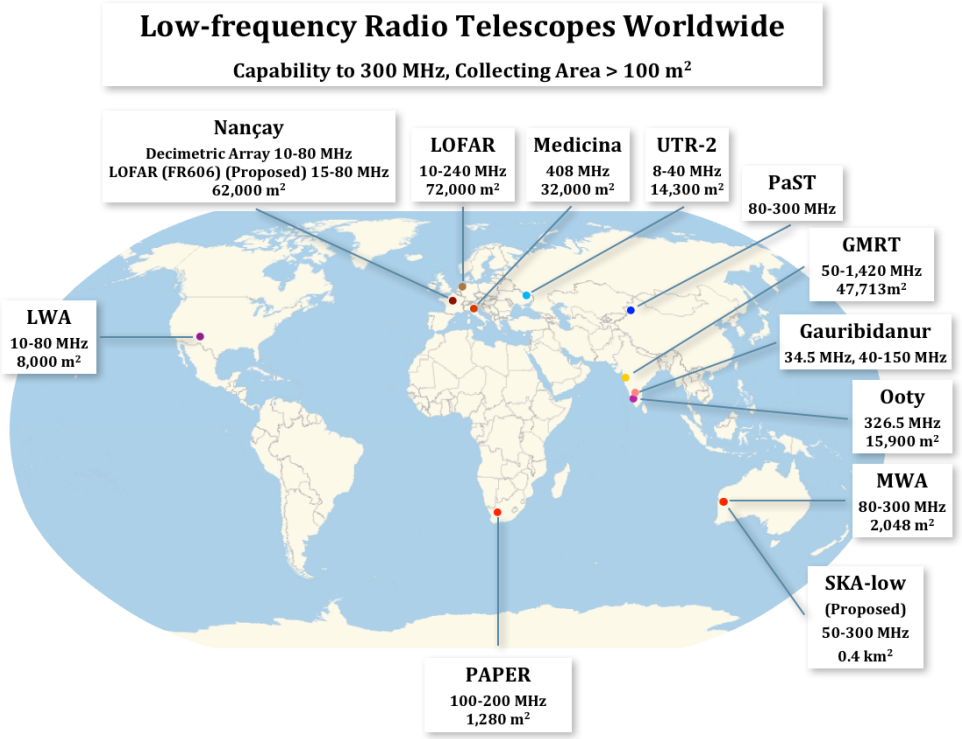


*Figure 1.1: The locations of major current or planned low-frequency radio telescopes worldwide. Several of these, including LOFAR, the MWA and PAPER are pre-cursors to the low-frequency component of the SKA (SKA-low), planned for construction in the Murchison, Western Australia.*

Figure 1.1 shows the locations and some parameters of current and planned large collecting area (>100 $m^2$) low-frequency$^+$ (below 300 MHz) instruments. $^+$In the field of radio astronomy, HF and VHF radio waves are universally discussed as 'low-frequency' radio waves.

## 1.2. Thesis Objectives and Outcomes.

Low-frequency radio astronomy, in particular, is subject to degrading effects of the ionosphere. The weakly ionised plasma of the ionosphere, permeated by the Earth's magnetic field, disperses radio waves to an amount that is proportional to the wavelength squared ($\lambda^2$) of impinging signals (Oberoi, Sharma et al. 2014). For frequencies in the VHF band, 50-300 MHz in the case of the MWA, the degrading effects of the ionosphere on science products therefore are much greater than at higher frequencies (GHz and greater) and must be understood and mitigated (Mitchell, Greenhill et al. 2008). The purpose of this thesis is to:

(1) characterise the ionosphere and its spatial and temporal variability over the Murchison region of Western Australia for an extended period of observation,

(2) provide a physical model of radio waves propagating through the ionosphere to aid decisions made in correcting for ionospheric degradation of images produced by the MWA,

(3) compare ionospheric model outputs to experimentally acquired TEC values, leading to a better understanding of the calibration of the MWA, particularly for the purpose of Faraday rotation (FR) correction and

(4) investigate opportunities to advance the goals of ionospheric science relevant to the needs of the MWA.

These objectives were met through:

(a) an extensive field campaign of (temporal and spatial) TEC measurement, including the deployment of experimental instrumentation at two locations separated on a Nth/Sth transect by 519 km,

(b) analysis of the ionosphere's inherent and dynamic character, including the impact of coronal mass ejections (CMEs) that impact the Earth's magnetosphere, plasmasphere and ionosphere and travelling ionospheric disturbances (TIDs),

(c) modelling of the response of the ionosphere to low-frequency radio waves, including perturbation induced refraction effects and the implications of assumptions made in how the ionosphere is treated in modelling,

(d) comparing ionospheric model outputs with TEC values acquired over a period of greater than one-half of one solar cycle (cycle 24) and (e) investigating activities that could be undertaken to improve our understanding of the ionosphere in direct relation to the MWA.

Thesis goal (3) is particularly relevant to the further development of radio astronomy on the MRO. The "Polarisation Sky Survey of the Universe's Magnetism" (POSSUM) is one of the eight major surveys to be undertaken on the CSIRO's Australian Square Kilometre Array Pathfinder (ASKAP) telescope (Gaensler, Landecker et al. 2010) (http://www.physics.usyd.edu.au/sifa/possum/). POSSUM, being a survey of galactic magnetism, is highly susceptible to FR in the ionosphere. This question is addressed in Chapter 6 (Section 6.5).

This thesis concludes with a discussion of possible future work including the feasibility of an Earth orbiting, triple VHF beacon equipped cubesat satellite for the purpose of better quantifying the ionosphere's effect on the Faraday rotation and scintillation of VHF radio signals from space and to assist in characterising radio telescope antenna beam patterns.

## 1.3. Thesis Activities.

I have studied the ionosphere above the MRO using dual-frequency GPS receivers over a period of eight years, at first in a campaign mode that allowed only occasional deployment of equipment and later with facilities that returned months of contiguous data. The MWA radio telescope was constructed over this interval on a wholly unimproved site permitting only seasonal access, with occasional power availability and a lack of facilities and communications being typical privations.

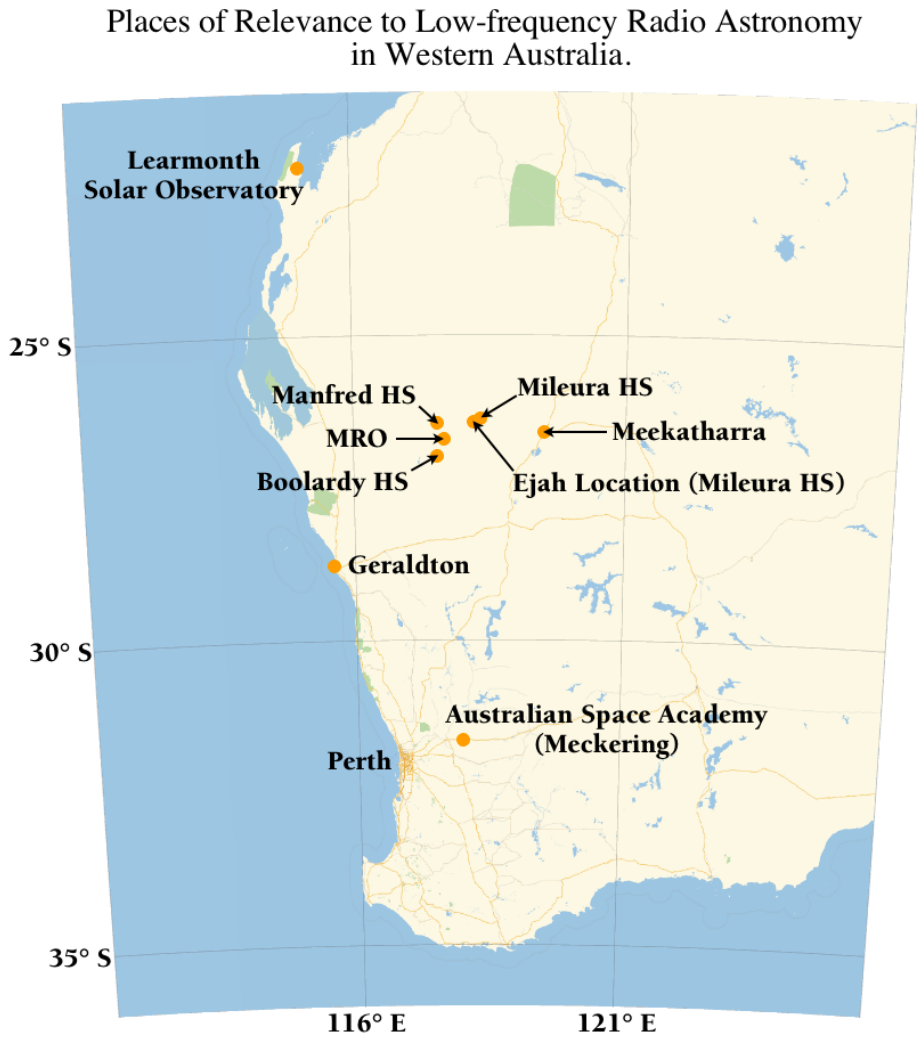


*Figure 1.2: Places of interest to low-frequency (VHF) radio astronomy in Western Australia and locations mentioned in this thesis. Mileura HS was the original site for the MWA, which is now located at the MRO on Boolardy Station.*

Figure 1.2 displays places of interest to VHF radio astronomy in Western Australia. Some (Mileura and Ejah) were the locations originally intended to house the MRO. GPS TEC monitoring equipment was located at Manfred homestead, the MRO, Boolardy homestead and at the Australian Space Academy campus at Meckering.

Data captured over an interval corresponding to a little more than half of one solar-activity cycle reveal a dynamic though well behaved ionosphere. The MWA, together with other instruments in its class, is designed to observe phenomena produced by events that occurred very early in the history of the Universe (Bowman et al. 2010).

The author is a founding member of the MWA, has participated in construction of the precursor instrument, the Thirty-two Tile Array (32T) and also led the first expedition to the site during which the first tile (1T) was installed in March 2007, thus enabling the earliest radio observations to be performed on the MRO. The author was also a part-time member of the CSIRO ATNF over the interval December 2004 - March 2006, responsible for RFI field support in Western Australia. My personal account of the early history and development of the MWA is included in this thesis (Chapter 2), as this work primarily is dedicated to the support of this instrument. I have been involved in development of the telescope since prior to the first field expeditions and assisted also in other projects that were fielded on the original and current sites of the MRO (Bowman, Barnes et al. 2007, Mitchell, Greenhill et al. 2010, Parsons, Backer et al. 2010).

# 2. The Murchison Widefield Array Radio Telescope (MWA).

The purpose of this chapter is principally to introduce the instrument in support of which this work has been conducted. In their design overview of the MWA, Lonsdale et al. identified 'spatially and temporally variable ionospheric propagation effects, including refraction, refractive scintillation, ionospheric opacity, and Faraday rotation' as principal design challenges for the instrument (Lonsdale, Cappallo et al. 2009). The authors also identified 'wide-field calibration and imaging', a separate though related issue, as another design challenge. Also, the 128 tile MWA, which is the current configuration (Tingay, Goeke et al. 2012), has a field of view at 150 MHz (at primary beam FWHM) of 610 $deg^2$. (The full moon subtends an area of ~0.2 $deg^2$) and therefore sees a large volume of the ionosphere during observations. Hence, a decision was made at the outset of the project and included in planning at the inaugural MWA Project Meeting (La Jolla, California, July 2006), to include studies of the ionosphere as a project priority. Three GPS systems were provided by the USAFSOR expressly for the study of the ionosphere in respect of the MWA and returned the data reported in this thesis. The description provided here of the MWA also highlights the motivation for this work.

The author has been an integral member of the team that constructed the telescope since the earliest expeditions to the Murchison region of Western Australia (Figure 2.1), during which both the instrument's original site, Mileura Cattle Station and its current location, Boolardy Cattle Station, were decided (Figure 1.2) and during which first light was achieved in March 2005 (Figure 2.4).


*Figure 2.1: Location of the Murchison Radio Observatory, in the sparsely populated Murchison Shire of Western Australia. One of Western Australia's longest running observatories, the Learmonth Solar Observatory is noted for geographic comparison.*

An understanding of the design of the MWA and hence, the telescope's observational parameters, guides this discussion and is developed in this chapter.

## 2.1. The Climate and Environment of the Murchison Region of Western Australia.

The climate of the Murchison region is considered semi-arid/arid, exhibiting an annual average rainfall of ~250 mm (http://bom.gov.au) (Figure 2.2). Of particular interest to the MWA project however, is the frequency of lightning ground strikes, which at the location of the MRO is between 0.5-1.0 per $km^2$ per annum. This rate places the MRO at close to the lowest end of the scale for Australia. A direct strike on infrastructure is not required however, to destroy sensitive, high-gain electronics such as mast-head or antenna pre-amplifiers. As a member of the CSIRO, Australia Telescope National Facility (ATNF) radio-

frequency interference (RFI) study team (Section 2.4), I witnessed the loss of such amplifiers remote to lightning strikes. The MWA operations team have planned for antenna losses due to lightning strikes.

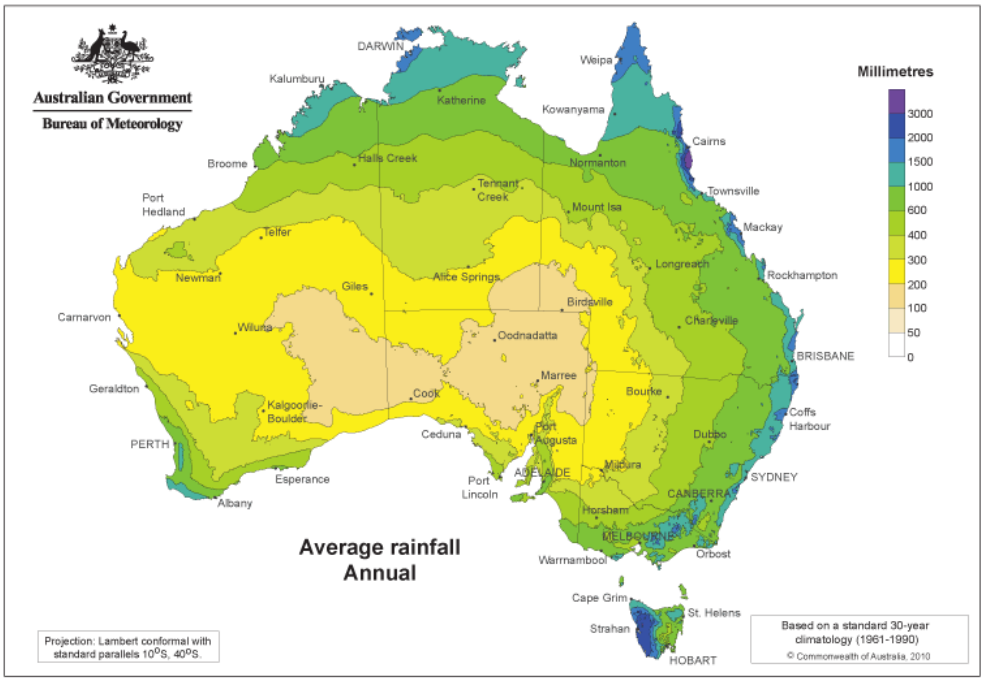


*Figure 2.2: Average annual rainfall over Australia. The Murchison is located in the yellow coloured region, which experiences between 200-300 mm annually.*

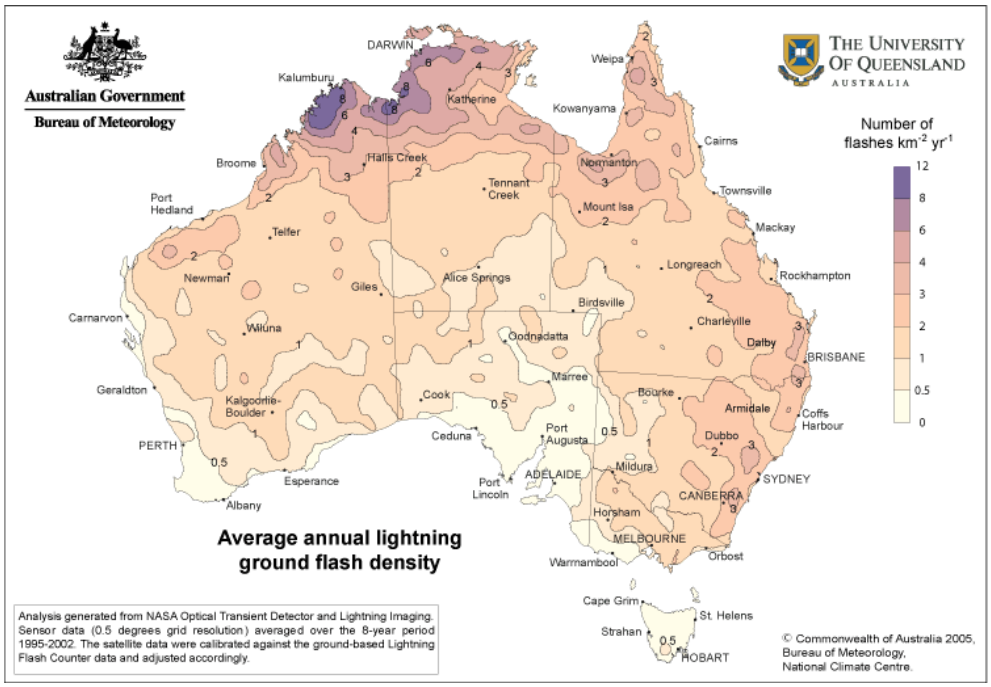


*Figure 2.3: Average annual lightning strike density (km$^{-2}$ per annum) over Australia. The Murchison experiences between 1-2 strikes per km$^2$ annually.*

## 2.2. MWA First Light.

The MWA achieved first light with an array of three tiles at a location known as Ejah, on Mileura Cattle Station on March 11th, 2005 (Bowman, Barnes et al. 2007), (Bhat, Wayth et al. 2007) (Figures 2.4).

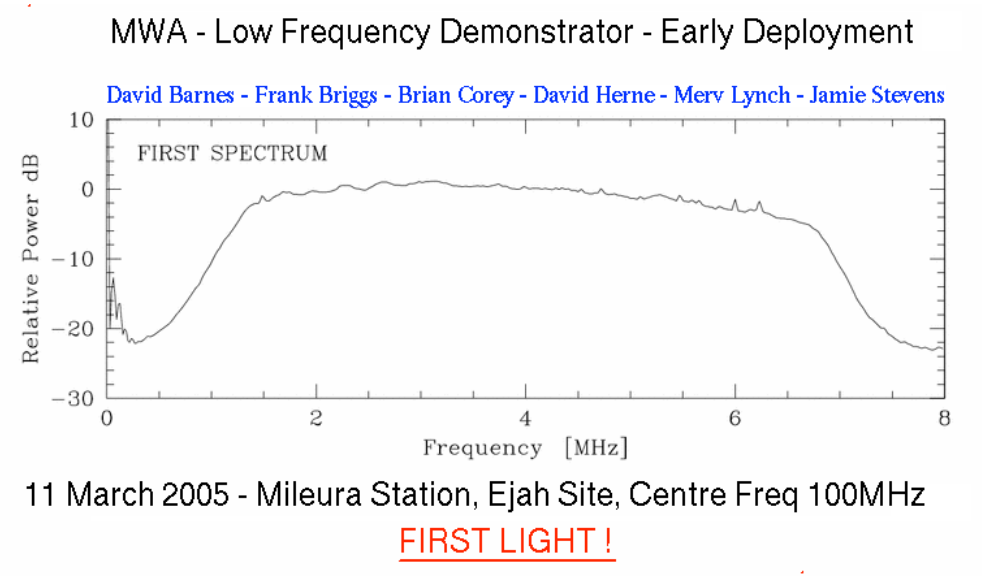


*Figure 2.4: The first spectrum achieved by the MWA at Mileura, March 2005. The bandpass is here centred at 100 MHz (at 4 MHz in the image). Image - Professor Frank Briggs.*

A document released in March 2015 celebrating the 10th anniversary of this event is presented in Appendix 9.1.

## 2.3. Early History of the MWA

The acronym MWA originally stood for *Mileura Widefield Array*, named for the cattle station which had been the instrument's intended home. Mileura homestead is situated 103 km to the north-east of Boolardy homestead, now the site of the Murchison Radio Observatory (MRO) (Figure 1.2, 2.5). Modelling studies conducted over the previous decade, including one by a team of ionosphere specialists (Kennewell, Caruana et al. 2005) had concluded that the Murchison region of Western Australia was an excellent candidate for hosting the proposed SKA.

Amongst those qualities, very low levels of scintillation were expected, an important consideration at low radio frequencies. The Geological Survey of Western Australia, a division of the Department of Mines and Petroleum concluded that the local region exhibited '*low mineral and petroleum prospectivity*'. Subsequently however, the international price returned for iron ore appreciated to levels such that nearby low-grade deposits became attractive for exploitation. The MRO is located in one of the most sparsely inhabited, accessible regions of Australia, with a population of up to 160 people occupying an area of approximately 50,000 square kilometres, a population density of 0.0032 $km^{-2}$ (Figure 2.1).

**The Murchison Widefield Array in the Murchison, 2005 - 2015**

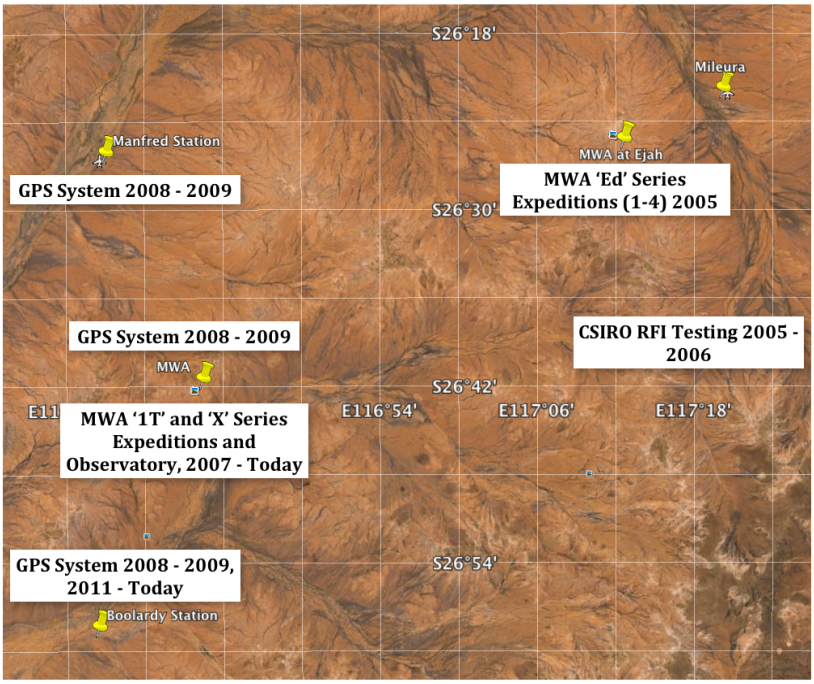


*Figure 2.5: Locations in the Murchison region of Western Australia of relevance to the MWA. The first radio astronomy experiments were conducted at Ejah, a location on Mileura Cattle Station in 2005. CSIRO radio frequency interference (RFI) testing, required as part of Australia's application to host the SKA, was conducted over the period 2005-2006 on Mileura., ~40 km south of the homestead. In March 2007, the MWA was relocated to Boolardy Cattle Station and operations have been conducted there since. GPS TEC measurements were conducted at Manfred Cattle Station, Boolardy homestead and on the site of the MWA, the Murchison Radio Observatory (MRO).*

### 2.3.1. The ED Series Expeditions.

Four ED series expeditions were mounted to Ejah in 2005. ED 1, from the 7th-16th of March 2005, witnessed the installation of the first tile, which had been prefabricated at Melbourne University by a team led by David Barnes, the ED series leader and Jamie Stevens, a PhD student under Professor Rachel Webster. Expedition members included David and Jamie, Professor Frank Briggs of the Australian National University, Brian Corey of MIT Haystack Observatory, Professor Mervyn Lynch and the author, representing Curtin University. An electrical fault destroyed many components on every circuit board of the beam former used on the expedition. However, the author, under guidance from Brian Corey, repaired the damage enough for the tile to be operated at zenith, bypassing badly damaged delay board circuits. During this expedition, apart from first light, radio reflections from a meteor were observed as was a possible event on the Sun.

The second expedition, ED 2, from the 16th-30th of April 2005, included Curtin PhD student Bruce Stansby who with Merv Lynch, David Barnes, Frank Briggs, Jamie Stevens, Brian Corey, Randall Wayth and Judd Bowman assembled a second tile that had been prefabricated by the author at Curtin University (Figure 2.6). I was unavailable to assist as my duties with the ATNF required me to attend the RFI testing system elsewhere on Mileura station (Section 2.4).

*Figure 2.6: An early, prototype tile designed and fabricated by the author, housing 16 first generation antennas. (ED2 - Tile 2). Image - David Herne.*

The third tile was constructed on-site by Bruce Stansby during ED 3 from the 15th-24th of June 2005. Electronics and cabling capacity permitted inputs from only 4 channels and so, one tile provided two inputs with the dual dipole outputs from 16 antennas and two tiles, numbers 2 and 3, drove a single channel each from a single set of 16 dipoles. ED 3 was attended also by Randal Wayth and Judd Bowman.

Expedition ED 4, which was an observing campaign, took place from the 11th-22nd of September 2005. Hardware comprising the three, fully populated ED series tiles remained in place at the close of ED 4 as expeditioners fully expected to resume operations in 2006. However, the development in 2006 and onwards of an iron ore mine at the Jack Hills, 43 km almost due north of the Mileura Ejah location and the subsequent substantial increase in traffic, principally ore bearing road trains equipped with high-power radio equipment, compromised the RFI integrity of Mileura Station. This rendered the property unsuitable for continued radio astronomy observations. Initial consensus was that

the ~190 km of unsealed, insubstantial road linking to Cue, located on the Great Northern Highway, to the mine site would prove impassable to heavy traffic for periods each year due to inundation and associated major road damage. Mining interests however, arranged for the road to be sealed without further improvement and commenced ore carting operations. Initial plans for construction of an electrified rail system to the site from a shipping port proposed for Oakajee, near Geraldton, on the mid-west coast are currently on hold. If built, depending on the route chosen, this railway line could compromise the entire region to radio astronomy, including the mandated MRO radio quiet zone.

In December 2005, I attended the inaugural Grote Reber radio astronomy conference and award presentation at the University of Tasmania in Hobart, hosted by Professor John Dickey and during which early progress was discussed. The inaugural Grote Reber Award recipient was the late Professor William C. Erickson (dec. 2015).

I attended several meetings dedicated to local radio astronomy projects in 2006, the first being the inaugural MWA project meeting at the Scripps Institution of Oceanography, UCSD, La Jolla, California in July 2006. MWA work packages were defined and assigned. The author accepted responsibility for local support of all operations. In August/ September, I attended PAPER project meetings at UC Berkeley and the NRAO Virginia (including Green Bank Observatory, West Virginia) (Parsons, Backer et al. 2009). I also attended an MWA project meeting in Melbourne in December, 2006.

### 2.3.2. The Move to Boolardy Cattle Station and 32T.

In December 2006, a party of four consortium members, including the author, visited Boolardy Station for the first time to locate and secure a new site for the MWA. Boolardy, like Mileura, had been deemed suitable for development as a radio astronomy host site. Members of the party

were Colin Lonsdale and Roger Capello (MIT Haystack Observatory) and Mervyn Lynch and myself representing Curtin University.

*Figure 2.7: Professors Mervyn Lynch (Curtin University) and Colin Lonsdale (MIT - Haystack Observatory) survey one location on Boolardy Station in December 2007.*

The choice of a new site was constrained by the requirement for Boolardy to continue operating as a cattle station, due to the terms of the lease over the property which, if violated, left the station vulnerable to native title claims. Consequently, one site in particular, east of the current site of the MRO, which exhibited excellent properties for the purpose was eliminated from further consideration due to its particular suitability to the grazing of cattle. The site selected for the MRO contains extensive weathered granite outcrops at the surface and a substrate of highly compacted, abrasive, bound quartz grains. The site of the MWA seldom floods (less than 100 year occurrence) as it is located in a saddle near to the highest local elevation of ~310 mAHD (metres above the Australian Height Datum). Water flows across the surface during rainfall episodes but only forms minor pools in local depressions.

In March of 2007, the author, together with Professor Mervyn Lynch, Professor Lister Stavely-Smith of the University of Western Australia (UWA), Dr Jamie Stevens installed the first, next-generation tile on the MRO (Figure 2.8). This enabled the first ever radio science observations to be conducted on the site. In November of that year, a team comprising the author, Mervyn Lynch, Brian Corey, Mark Derome (Haystack Observatory), Chris Williams (MIT), Anish Roshi (Rahman Research Institute, India) and antenna contractors Robert and Steven Burns (Burns Industries, Boston Massachusetts) installed the 32 tiles of the prototype 32 Tile Array (known as 32T) (Expeditions X1/X2). Initial images were produced by this 32 tile, 512 dipole antenna array (32T**)** (Lonsdale, Cappallo et al. 2009), (Oberoi, Matthews et al. 2011), (Williams, Hewitt et al. 2012).

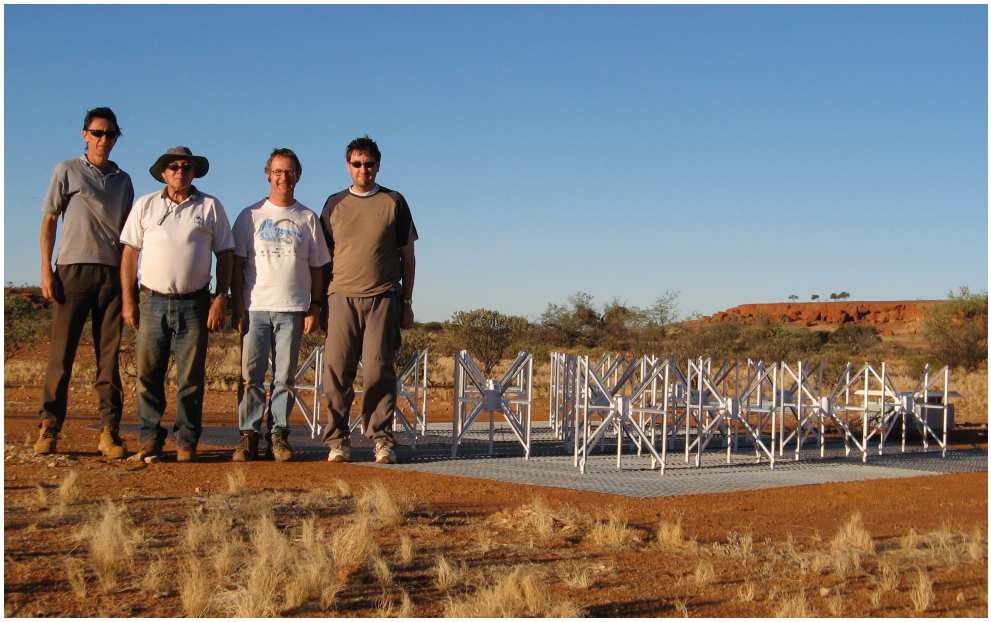

*Figure 2.8: Expedition 1T, March 2007, the first radio science experiment ever conducted on the site of the MRO. Team members - the author, Professor Mervyn Lynch, Professor Lister Stavely-Smith, Dr Jamie Stevens. Image - David Herne.*

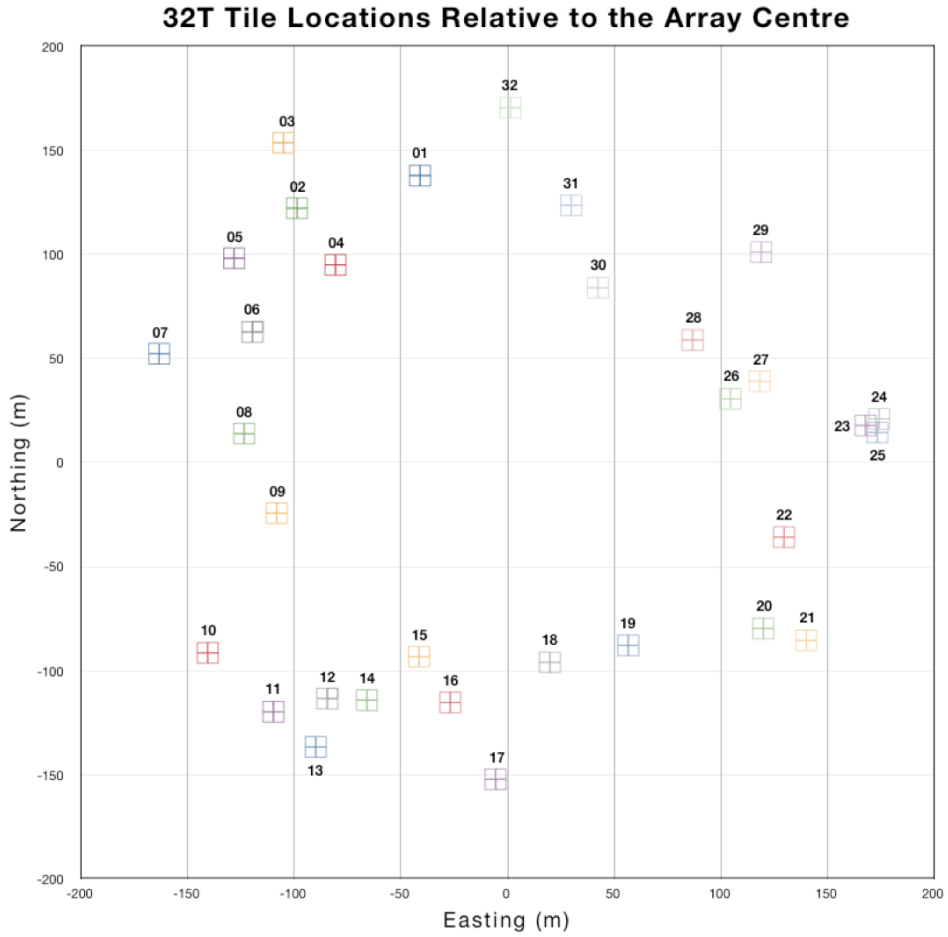


*Figure 2.9: Configuration of the initial, 32 tile MWA prototype array (32T). Mapping and surveying for the tile layout were performed by Professor Mervyn Lynch, David Herne and Divya Oberoi who was an Indian Consortium member. Image - David Herne.*

In July 2007, I was a member of the PAPER consortium (Precision Array to Probe the Epoch of Reionisation) who with the principal investigator, the late Professor Don Backer (UC Berkeley) and Erin Mastrantonio (NRAO, Charlottesville) conducted the first experiments on-site with a four tile, single antenna per tile array. PAPER is an EOR experiment. This expedition resulted in a paper published in the Journal of the American Astronomical Society (Parsons, Backer et al. 2010). Ron Beresford and Tony Sweetnam (CSIRO ATNF) attended.

In January 2008, I produced a system design for a possible MWA instrument and data facility (X4 Data Centre) and sourced a suitable RFI compliant structure that would accommodate the design through CSIRO

ATNF. This design and facility was not implemented. In March (X2.5), upgraded generation 1 antennas with short stubs on each dipole to reduce self-induced interference were trialled. This antenna was not adopted. In September 2008, Curtin University established the site office at the MRO.

In January 2009, I supported the radio experiment EDGES (Judd Bowman, Alan Rogers, MIT Haystack Observatory) on an expedition to the MRO. Attendees were Judd, Cassie Bowman and the author. On this and subsequent expeditions, I deployed GPS systems for the duration where opportunity permitted.

Currently, three projects are under active development on the MRO, the CSIRO's Australian Square Kilometre Array Prototype (ASKAP), the MWA and a single station prototype of the low-frequency (VHF) SKA observatory. The ASKAP, a Square Kilometre Array (SKA) prototype, is a dish-based antenna array (Johnston, Taylor et al. 2008). Another significant radio experiment that has been deployed to the facility is the Experiment to Detect the Global EoR Signature (EDGES), led by Dr Alan Rogers of Haystack Observatory and Professor Judd Bowman of Arizona State University (Bowman and Rogers 2010).

The current MWA radio telescope is a 128 tile, 2,048 crossed-dipole, aperture-synthesis, tile-based array in a dithered Reuleaux formation (Tingay, Goeke et al. 2012, Oberoi, Sharma et al. 2014). Results of observations completed with the initial 32 tile instrument have been published extensively (Bell, Murphy et al. 2014), (Bowman, Cairns et al. 2013), (Williams, Hewitt et al. 2012).

## 2.4. CSIRO ATNF RFI Studies.

The author was also a member of the CSIRO, Australia Telescope National Facility (ATNF) team that conducted mandated RFI testing of candidate and other sites in Western Australia, beginning in January

2005 and concluding in March 2006. This work resulted in an extensive, confidential, report to the SKA site selection committee on the RFI environment of the Murchison region that demonstrated its suitability to host the SKA.

*Figure 2.10: Radio Frequency Interference (RFI) testing on Mileura Station, original site of the MWA, Radio Telescope, January 2005 - March 2006, CSIRO ATNF. Author was a member of this team over the duration of the testing period.*

While conducting operations locally for the ATNF, I participated in the earliest expeditions during which construction of the first tiles of the MWA were undertaken. Over the period March 2005 to August 2009, I was a member of all but a single expedition to the telescope's respective locations on both Mileura Station and the current site on Boolardy Station. A remarkable coincidence is that the word 'mileura' means 'far seeing' in the local indigenous dialect. The author also installed a weather station (~117.5° E, ~26.62° S) in January 2005 that was later transferred to the 'breakaway' at Boolardy, a small mesa central to the MRO.

## 2.5. Telescope Design and Operational Parameters

The MWA is a tile based, aperture synthesis, phased-array radio telescope operating over the frequency range 80-300 MHz. The instrument is currently comprised of 128 tiles, each hosting 16 dual polarisation dipole antennas, for a total of 2048 antennas (Beardsley, Hazelton et al. 2012). This is a 'large-N' architecture, which is intended to sample the Fourier plane with high-fidelity. Design parameters and performance measures for the MWA are given in Table 2.1 below.

| Parameter | Value |
|---|---|
| Frequency range (MHz) | 80 - 300 |
| Number of tiles (N) | 128 |
| Number of antennas | 2048 dual polarisation |
| Total collecting area ($m^2$) | 2752 @ 150 MHz / 2534 @ 200 MHz |
| Field of view ($deg^2$) | 610 @ 150 MHz / 375 @ 200 MHz |
| Receiver Temperature (K) | 50 @ 150 MHz / 25 @ 200 MHz |
| Instantaneous Bandwidth (MHz) | 30.72 MHz |
| Spectral channels | 1024 (30 kHz spectral resolution) |
| Temporal resolution (cadence) | 0.5 s uncalibrated / 8.0 s calibrated |
| Polarisation | Full Stokes |
| Array voltage beams | 32 |
| Angular resolution 1.5 km array | 3' @ 150 MHz / 2' @ 200 MHz |
| Angular resolution 3 km array | 2' @ 150 MHz / 1' @ 200 MHz |
| Broadband survey speed | 1.5 x $10^5$ $deg^2$/hr (31 MHz, 10 mJy) |
| Narrowband survey speed | 190 $deg^2$/hr (0.04 MHz, 10 mJy) |

*Table 2.1: Design parameters and performance measures for the MWA (Tingay, Goeke et al. 2012).*

The MWA now maintains an active observing regime, with frequent visits by staff of the Curtin Institute of Radio Astronomy (CIRA) who perform maintenance tasks and the inspection of contractor works.

### 2.5.1. Antennas

Each antenna is a dual-polarisation, full-Stokes, active bowtie dipole in vertical configuration (Figure 2.9). Output signals are fed by two Agilent low noise amplifiers (LNA) and a balun. A single LNA is connected to two complementary bow-tie arms. A bias-T supplies 5 V dc to the antennas (LNAs) on an analogue coaxial cable.

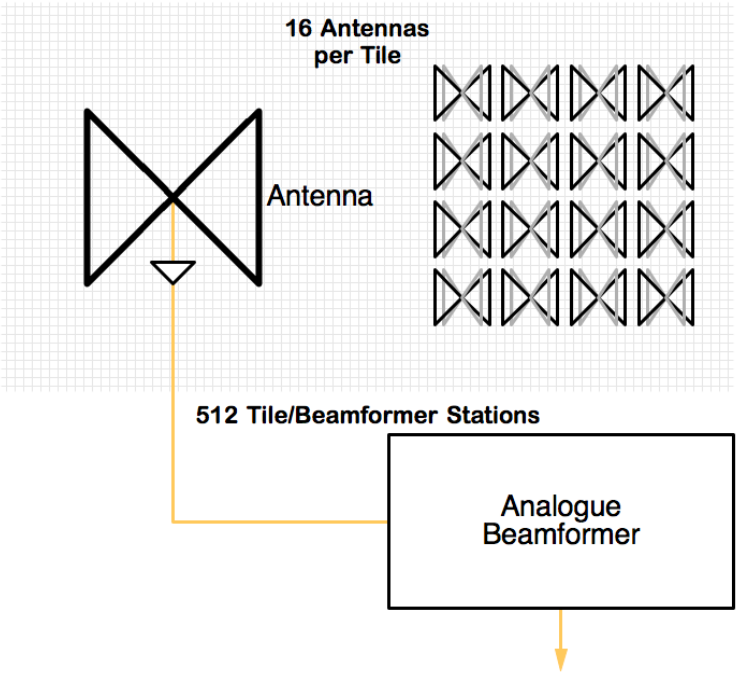


*Figure 2.11: Antenna/beamformer assembly. Each of the antennas is connected to the beamformer independently through a preamplifier (a single example of which is shown).*

A noteworthy difference between the early implementation of antenna groundscreens, on the ED series expeditions and today is the positioning of groundscreens on the ground rather than on mounting structures. The location of the MWA is such that water might flow across groundscreens during rainfall events but not pool as the MRO is on higher terrain than much of the local region.

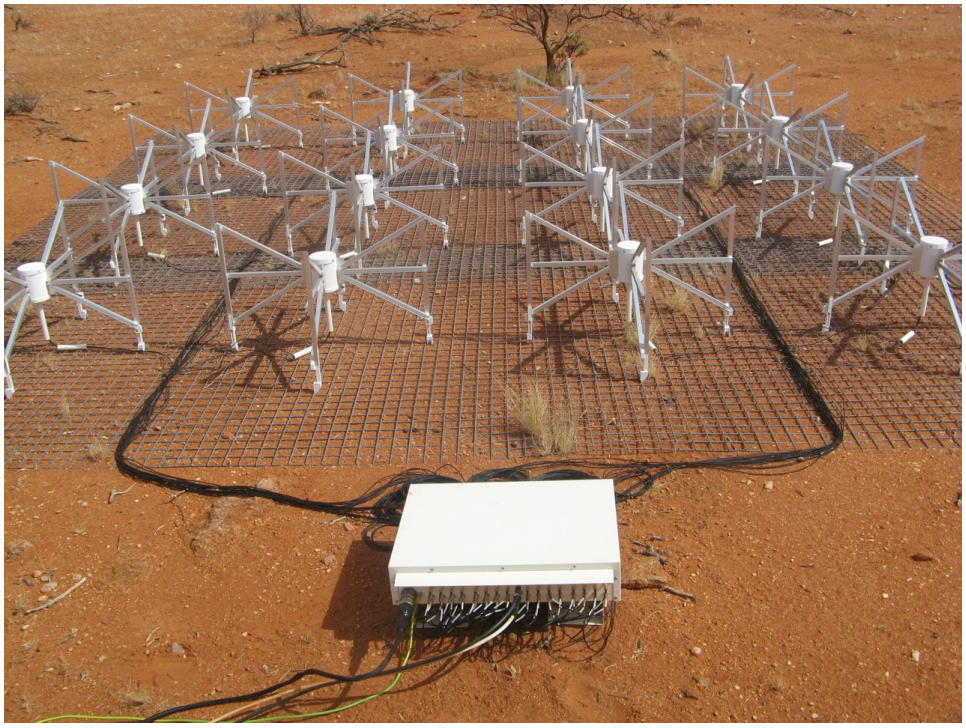

*Figure 2.12: A single tile of 16 antennas and a beamformer. The open bow-tie design suffers less wind loading than an equivalent closed panel design. The LNA for each complimentary pair of arms is housed in the white, central hub. Image - David Herne.*

Sixteen antennas are mounted on a single 'tile', which comprises a 5 m x 5 m ground screen of welded steel mesh laid directly onto the ground (Figure 2.10). A crossed bowtie design provides a broader antenna pattern than a single dipole with impedances better matched to the LNA across the whole frequency band. The antenna amplifier design is such that despite imperfect impedance matching, sky noise will dominate system temperature. Antenna centre spacing is 1100 mm, which is $\lambda/2$ at 136 MHz, near the design centre frequency of the array.

### 2.5.2. Beamformers

Beamformers are of analogue design. Each has inputs for 32 pre-amplifiers (channels), corresponding to the dual outputs of the 16 dipole antennas of a single tile. A single beamformer controls the antennas on a single tile. Up to eight beams are steered electronically by switching in physical delay lines comprised of 32 steps using five

binary-weighted delay steps. System gain is maintained through the switching process by gain-matching circuitry. This system architecture provides the advantage of very consistent behaviour over time, which is important in an instrument that might be expected to provide integration periods of months for any particular observation. Beamformers are commanded over a digital link from a receiver.

Signals from each of the 16 antennas on a single tile are combined to form two orthogonal X and Y polarised tile beams. These analogue outputs are transmitted over a coaxial cable to a corresponding receiver. Each receiver manages 8 beamformers and tiles.

Delay lines are switched in and out to point beams away from zenith. Beam shape changes as a function of pointing direction and observation frequency. These considerations need to be managed during calibration of the instrument.

### 2.5.3. Receivers

The MWA currently employs sixteen analogue receivers, each of which accepts inputs from eight tiles, providing inputs for 128 dipoles or 256 channels. Each antenna houses two pre-amplifiers, one for each polarisation. Sampling is conducted at 327 MHz by a field Programmable gate array (FPGA) based hardware design. Each receiver performs several functions, including:

- Analogue signal conditioning. This is required to equalise the total power received from each tile and to filter a bandpass between 80 and 300 MHz.
- Control of course pointing of each beamformer.
- Sampling of the incoming signal from each beamformer with an ADC on each channel.

- Channellisation of each incoming analogue stream using a coarse, polyphase filter bank (PFB) and
- Provide clock signals with which to generate a synchronised sampling clock at 655.36 MHz, a processing clock at 163.84 MHz and a timing pulse at second intervals.

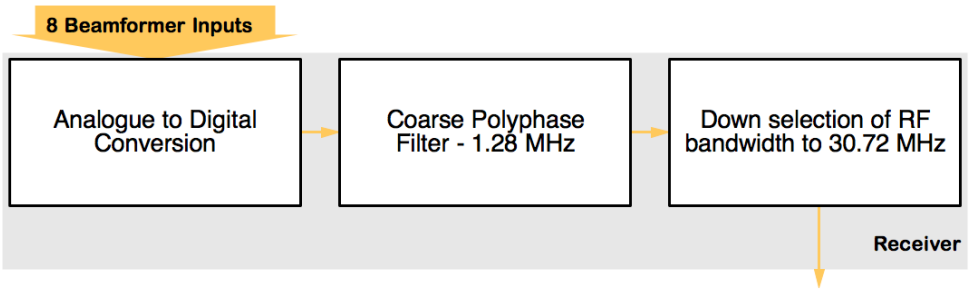


*Figure 2.13: Receiver. These are deployed close to those antenna tiles that they service; eight tiles each.*

### 2.5.4. Correlator

Real-time cross-correlation is performed using two technologies that perform tasks to which each is computationally and economically best suited (Tingay, Goeke et al. 2012). Polyphase filtering is performed by FPGA-based hardware. This results in finer spectral resolution than the coarse filtering performed by the receivers. This channelisation results in 3,072 x 10 kHz channels. The output of each PFB is 3,072 Nyqvist sampled, 10 kHz channels from 32 tiles, each of 2 polarisations. The subsequent cross-multiply and accumulate function is performed on general purpose graphics processing units (GPGPUs).

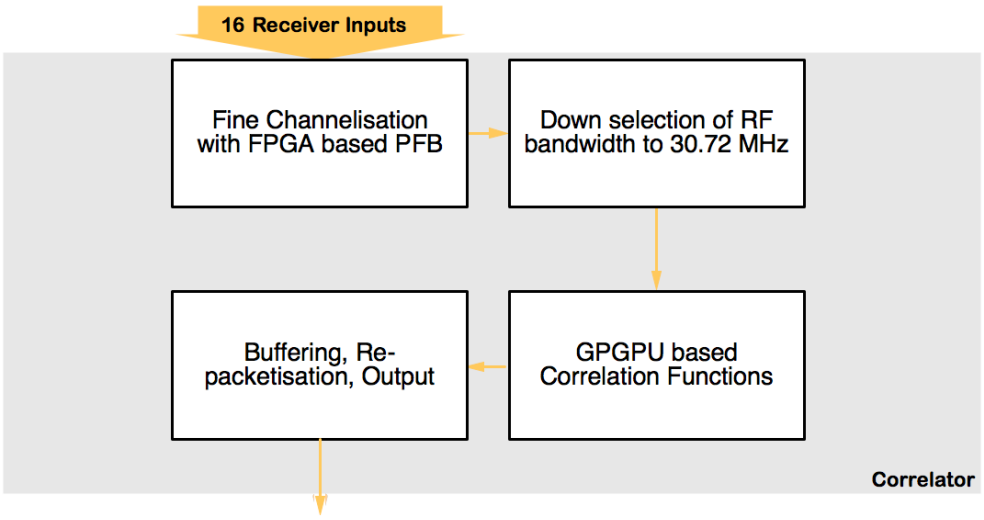


*Figure 2.14: Correlator. An FPGA and GPGPU based correlator accepts inputs from the 16 field-deployed receivers.*

The MWA correlator, taking full advantage of the hybrid, FPGA/GPGPU technology approach, implements an FX correlator (Fourier transform followed by a lag, cross-correlation) rather than the more common XF correlator. The cross power spectrum, $S(v)$ is found as:

$$S_{12}(v) = \int_{-\infty}^{\infty} V_1(t) e^{-i2\pi vt}\, dt \times \int_{-\infty}^{\infty} V_2(t) e^{2\pi vt}\, dt, \qquad (2.1)$$

which is the product of the Fourier transform of each antenna pair $V_1$ and $V_2$. This approach is computationally more efficient but has previously suffered from a rapid increase in the amount of data being produced. The MWA correlator's hybrid design alleviates this problem, as the software based approach to the second part of the correlation procedure, executed in GPGPUs, permits averaging and other procedures that reduce the data overhead without loss of precision. Correlation is followed by calibration and imaging and other operations under control of the real-time system.

### 2.5.5. Real-Time System

Apart from observations, several tasks must be completed within the telescope's observational cadence of eight seconds. Whereas these tasks are performed by systems mentioned previously and others, control is provided by the real-time system (RTS) that calls upon resources that are required at each step.

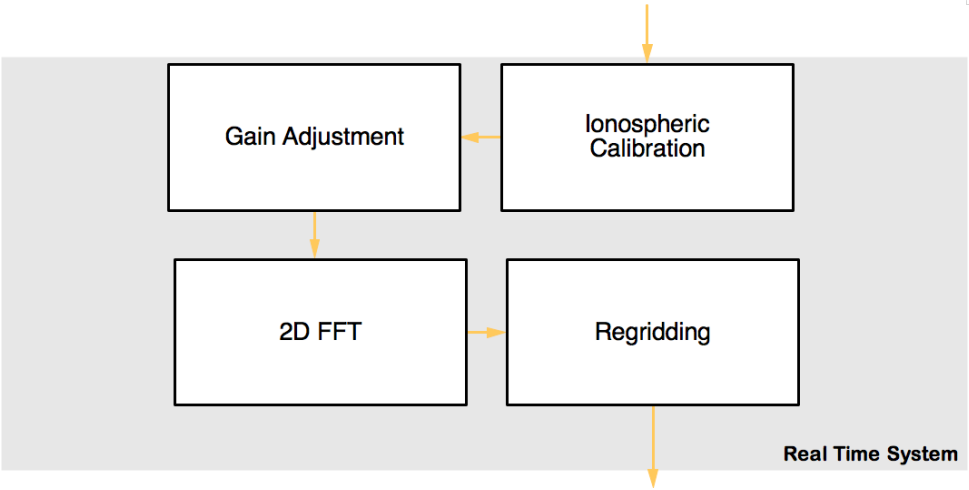


*Figure 2.15: Additional components of the Real Time System. Resources are called upon as required.*

Three tasks managed by the real-time system that impose constraints on system performance are correlation, previously discussed, imaging and telescope calibration. In the context of radio interferometers, imaging is a well understood process. Calibration however, is less well understood. The requirements of calibration for various classes of observations are well thought out (Mitchell, Greenhill et al. 2008), the accuracies and required precision, however and the means by which these are achieved are not so well understood. Quoting our paper (Ord, Mitchell et al. 2010), '*the refractive effects of the ionosphere toward each source are measured and assumed to be direction-dependent angular displacements that are constant across the field of view.*' The process to remove offsets is an accepted practice, is to stretch the ionosphere as a thin *phase screen* to counter displacements. This is performed by application of a commonly applied *rubber sheet* model. However, I will

demonstrate in later chapters that, taking into consideration the curved nature and depth of the ionosphere, a thin screen is insufficient in accounting for actual refraction. Further, well known disturbances in the ionosphere that can affect imaging dramatically, such as travelling ionospheric disturbances (TIDs) cannot be incorporated into thin screen models. Attempting to do so would be futile. I will draw on observed behaviours to demonstrate this assertion. Further, telescope self-calibration is insufficient for observations requiring knowledge of the ionospheric aTEC, such as those sensitive to Faraday rotation as the instrument is fundamentally incapable of producing these measures. External means of measuring aTEC must be provided. We have attempted this through use of GPS systems.

The final word in applying three-dimensional processes to modelling ionospheric behaviour will be provided by the application of three-dimensional tomography, which is not attempted here, however, an ionosphere exhibiting properties involving depth is approached in the following chapters.

The real-time system might call on further resources than currently implemented in performing a more rigorous program of instrument calibration but will easily cope with additional performance overheads.

## 2.6. Radio Astronomy with the MWA

The MWA is a survey instrument that will initially address three initiatives in radio interferometry, being the detection and characterisation of the Epoch of Reionisation (EOR), solar imaging and heliospherics and study of the variable (and transient) radio sky at these low frequencies. Each area of study will take advantage of different aspects of the telescope's capabilities. Study of the EOR will take particular advantage of the ability of this instrument to integrate a signal over very long intervals (Bowman and Rogers 2010, Bowman,

Cairns et al. 2013), up to months for each imaging cycle, at very low signal levels. Solar imaging (Oberoi and Benkevitch 2010) will take advantage of the instrument's ability to resolve features on the face of the sun, providing the ability to pinpoint the location of events that generate particular radio signals, which in turn are tied to particular processes occurring on the sun. Study of the variable radio sky will take advantage of the MWA to resolve short lived signals. Each capability provides the opportunity to produce novel results and very useful science.

### 2.6.1. Epoch of Reionisation

The EoR is that age in the early universe when neutral hydrogen, the predominant form of matter, underwent ionisation induced by the earliest luminous sources. It is believed that this epoch existed between redshifts of 6 and 10 (Lonsdale, Cappallo et al. 2009). Recent findings by Judd Bowman and Alan Rogers (Bowman and Rogers 2010) employing Edges on the MRO, have placed a lower limit on $\Delta z$, the redshift width (duration) of the era of the EOR, of less than 0.06. The MWA will measure the EOR power spectrum via the 21 cm signal over a large range of redshifts (Beardsley, Hazelton et al. 2012).

Beardsley et. al. estimated MWA sensitivity employing parameters given in Table 2.2. The number of tiles shown is less than the full 128 deployed as sixteen are not integrated in EoR measurements.

| Parameter | Value |
|---|---|
| Number of antennas | 1792 (of 2048 total) |
| Central Frequency | 158 MHz (z~8) |
| Field of view | 31° |
| Effective area per antenna | 14.5 $m^2$ |
| Total bandwidth | 8 MHz |
| $T_{sys}$ | 440 K |
| Channel width | 40 kHz |
| Latitude | -26.701° |
| Primary field RA | $6^h$ |
| Secondary field RA | $0^h$ |

*Table 2.2: MWA observational parameters for EoR sensitivity estimation.*

EOR fields will be observed between zenith angles of 0 and 45 degree and the MWA is expected, after a full season of observation, to detect the power spectrum amplitude with a SNR ~ 14.

The magnitude of the EOR is such that integration times of 1000 hour are expected at very high dynamic range and high resolution (Oberoi and Lonsdale 2012). Such measurements will place high expectation on calibration of the instrument, to Faraday rotation in particular, which will require highly resolved TEC values. This issue is discussed at length in Chapter 7.

### 2.6.2. Solar Heliospheric Studies

Radio astronomy at MWA frequencies has the potential to provide a powerful probe of processes occurring on the Sun, as these processes often radiate at low frequency (Oberoi, Matthews et al. 2011). However, coronal emission features for example are often complex and can evolve

over short intervals in each domain of interest, spatial, temporal and spectral. (Oberoi, Sharma et al. 2014). However, the high temporal, spectral and spatial fidelity of the MWA have addressed these issues from the inception of the instrument (Oberoi and Benkevitch 2010). Thanks to high-speed, digital signal processing, high observational cadence and high spectral resolution, rapidly evolving features on the Sun will be observed. (Currently, whereas the bandwidth of the MWA brackets 80 - 300 MHz, there is a design study presently under way to determine whether the lower limit might be pushed down to 50 MHz, which will further benefit solar imaging.)

Several studies in solar heliospherics are accessible to the MWA, including:

#### 2.6.2.1. Solar radio bursts.

Imaging polarisation and spectral properties of all classes of emission, including flares, coronal mass ejections (CMEs), X-ray flares, solar energetic particle events (SEPs) and currently unknown mechanisms. Coronal mass ejections are considered principal drivers of interplanetary disturbances (Liu, Manchester et al. 2007). Ejected matter often entrains solar magnetic field lines that reconnect with the Earth's magnetic field, with the consequence of matter generated by a CME streaming into the terrestrial environment.

#### 2.6.2.2. Solar Flux Calibration of the MWA.

Due to the Sun's intrinsic temporal and spectral variability, solar events are difficult to measure. However, accurate, absolute flux calibration is necessary to interpret processes occurring on the Sun. Future studies of extra-solar planetary systems might well benefit from these studies as the fidelity with which a host star's variability is accounted needs to meet the increasing requirements for sensitivity of measurements.

#### 2.6.2.3. Quiet Sun Science.

The opportunity exists to better characterise the relatively steady, background solar emission at low frequencies, which is believed to originate in the corona at $10^6$ K and vary slowly with time. 32T has the capability of imaging and tracking the temporal and spatial evolution of coronal emission with a high dynamic range over a broad spectral band. Figure 2.14 displays both a radio image of the quite Sun with much of the image being produced by the corona (left hand panel) beyond the disk of the photosphere (red circle) and an image at 310 Å, which is in the extreme ultraviolet.

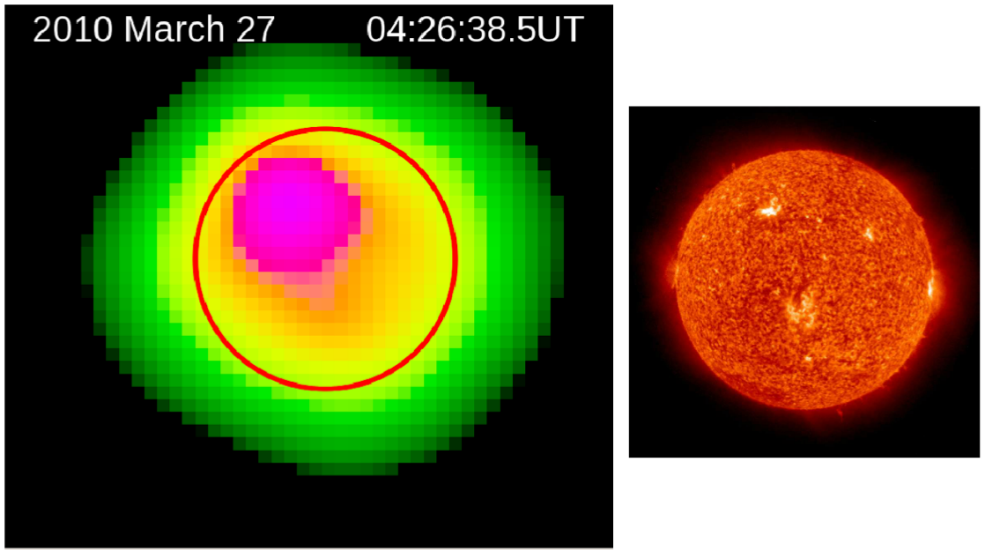


*Figure 2.16: A 32T radio image of the quiescent Sun (left - 193.3 MHz - XX polarization) and a 304 Å image from SOHO/EIT (right), taken a few hours earlier (01:19 UT) (Oberoi, Matthews et al. 2011). The red circle on the 32T image represents the size of the optical solar disc and a bright region is observed in the northeastern quadrant. Celestial north is toward the top of the images.*

### 2.6.3. Solar, Galactic and Cosmic Magnetism Studies

Magnetic fields acting on a plasma induce a rotation in the polarisation of impinging electromagnetic waves. This is true of both the interstellar, ionised medium (ISM) and the environment local to the Earth, comprising the heliosphere, magnetosphere, plasmasphere and the

ionosphere. However, the ISM imposes orders of magnitude greater Faraday rotation (FR) on galactic signals but varies slowly and is essentially stationary over observational intervals. (Oberoi and Lonsdale 2012). These authors observed that rotation measure (RM) due to the interstellar medium is interesting as the subject of study in its own right leading to a better understanding of cosmic magnetic fields. Others have studied this aspect of cosmology in detail and that of solar heliospheric magnetic fields (Liu, Manchester et al. 2007, Mao, Gaensler et al. 2008, Rust, Haggerty et al. 2008).

### 2.6.4. Transient Studies

Transient and variable source studies have been a target of study since the earliest days of the MWA 32 tile array (32T) (Bell, Murphy et al. 2014). Whereas the study by Bell et al. observed short timescale (26 minute) variable sources with 32T, their variability could not be ascribed to a particular phenomena and might have resulted from the calibration strategy employed or ionospheric effects. In the study by Bell et. al, no transient events were discerned. However, as the size of the array has grown (now at 128 tiles with 256 funded), sensitivity has increased. High-time resolution (100 μs) and high frequency resolution (10 kHz) voltage data are now captured (Tremblay, Ord et al. 2014). The MWA now has demonstrated the ability to capture short duration single pulses, with observations of the Crab pulsar (J0534+2200) and Crab Giant Pulses, which are thought to comprise intrinsically, approximately nanosecond duration, bright pulses. Transients range over timescales of milliseconds to months (Croft, Bower et al. 2010). Some radio transients have no counterparts at other wavelengths, increasing the value of these observations.

Another proposed, related activity is the tracking of space debris (Tingay, Kaplan et al. 2013). The MWA would operate as a component of a bistatic radar in the commercial FM broadcast band of 87.5-108 MHz.

As an imaging system, the MWA would detect multiple targets reflecting broadcast signals. The target performance is the detection of debris >0.5 m in radius to ~1000 km altitude.

## 2.7. Calibration of the MWA

The MWA operates in the frequency regime 80-300 MHz with extension to 50 MHz currently under discussion. At these frequencies, the ionosphere is both refractive and birefringent, leading to pronounced scintillation and FR of radio signals (Rawer, 1993). Therefore, images produced by telescopes operating at VHF frequencies must be calibrated against ionospheric effects in order to produce images of the highest fidelity. As the ionosphere varies over differing time scales, instruments require regular calibration to maintain their image fidelity. Therefore, understanding characteristic timescales in the ionosphere is will benefit instrument calibration.

Although both positively charged species (positive ions) and negatively charged species (electrons) exist in the ionosphere and magnetosphere, it is the electrons in the ionosphere that are principally responsible for interferences. The relevant metric therefore, is the electron content of the ionosphere. A measure of the total numbers of electrons along line-of-sight paths between the observing instrument and object under investigation is the total electron content (TEC). One TEC unit (TECU) is equivalent to $1 \times 10^{16}$ electrons $m^{-2}$.

Being a real-time instrument, the MWA requires calibration in real-time (Lonsdale, Cappallo et al. 2009). In this context, real-time refers to the eight second cadence of the telescope. Calibration is a critical step. The MWA has the potential to produce tens of gigabytes of data per second. Hence, off-line storage of raw data is impractical and the observatory will only store processed images.

Two distinct calibration regimes are relevant to the requirements of the MWA. One, self-calibration, is capable of removing mainly refraction induced, positional errors in the locations of sources. The second, absolute calibration, enables the *unwinding* of FR but requires knowledge of the total electron content of the ionosphere, rather than differences in electron content across the sky, which is an output of the self-calibration process. Each is discussed in turn, following discussion of the response of the ionosphere to VHF radio waves.

The MWA is a full Stokes, static array (Bernardi, Greenhill et al. 2013) that presents particular challenges to calibration (Mitchell, Greenhill et al. 2008). These include *direction-dependent gain*, *signal polarisation response* and *source confusion*. Rather than presenting a consistent antenna geometry towards astronomical targets, as in the case of a moveable dish, static arrays present a slowly varying geometry as the sky drifts overhead.

### 2.7.1. Dependence of Calibration on the Response of the Ionosphere to VHF Radio Waves

The study of extraterrestrial magnetic fields requires accurate calibration of the Earth's contribution to measured FR, which is a function of the electron content of the ionosphere, plasmasphere and magnetosphere. Free electrons induce a rotation of the plane of polarisation of incident waves, which results in an observed RM. Resulting FR is a function of RM and $\lambda$ such that:

$$FR = RM \times \lambda^2 . \tag{2.2}$$

Here, FR increases dramatically at lower frequencies, at tens to hundreds of megaHertz due to the squared contribution of wavelength. Therefore, accurate removal of the terrestrial component of the measured FR is essential in order to measure accurately solar, galactic and cosmic magnetic field strengths and orientations. To accomplish

this task, the aTEC of (principally) the ionosphere must be measured accurately.

### 2.7.2. Self-Calibration

A technique for calibration of interferometers known a *peeling* has been applied to the calibration of the MWA (Mitchell, Greenhill et al. 2008). Peeling removes refraction dependent-errors. At low frequencies, the sky is heavily populated with bright sources and is confusion limited, meaning that many sources might contribute both to a single instrument element and also cause contamination of a pixel's sidelobes by unresolved distant sources. This calibration scheme is executed in the real-time system (RTS) which also includes the calibration measurement loop (CML) that is at the heart of the calibration scheme and which measures apparent angular offsets induced by the ionosphere and the system gain toward known compact astronomical sources across the sky.

### 2.7.3. Externally Generated Calibration Methods

Currently, no external calibration methods or data are employed in the imaging process or pipeline. An appropriately implemented facility could be incorporated into the ionospheric calibration pipeline (Figure 2.13).

## 2.8. Related Long-Wavelength Astronomy Projects

Other radio astronomy experiments are or have been performed on the MRO. Significant experiments amongst these are two discussed briefly here.

### 2.8.1. PAPER

PAPER is an experiment being conducted jointly by researchers at The University of California, Berkeley (Aaron Parsons principal investigator) and the National Radio Astronomy Observatory (NRAO), Charlottesville, Virginia (Richard Bradley principal investigator). Researchers at Curtin University (Professor Mervyn Lynch and I) were members while the experiment was being conducted in Western Australia. PAPER is designed to detect the EOR. The first run of this experiment took place at the MRO (latitude −26° 44, longitude 116° 40′ ) in July 2007. I was a member of this expedition and an author on the resulting paper (Parsons, Backer et al. 2009).

*Figure 2.17: PAPER, field deployment in July 2007. Professor Don Backer (dec.) stands in the foreground, team member Erin Mastrantonio near the doorway and the author in the shadows. EMC enclosure (behind notebook computers), housed instruments as a sealed unit once setup was complete.*

*Figure 2.18: Economic, large volume EMC enclosure (Faraday cage) designed and constructed by the author following a design by Richard Bradley of the National Radio Observatory, Charlottesville, Virginia. Enclosure employed by PAPER during the field campaign (PWA-4) in July 2009 at the MRO (Figure 2.17).*

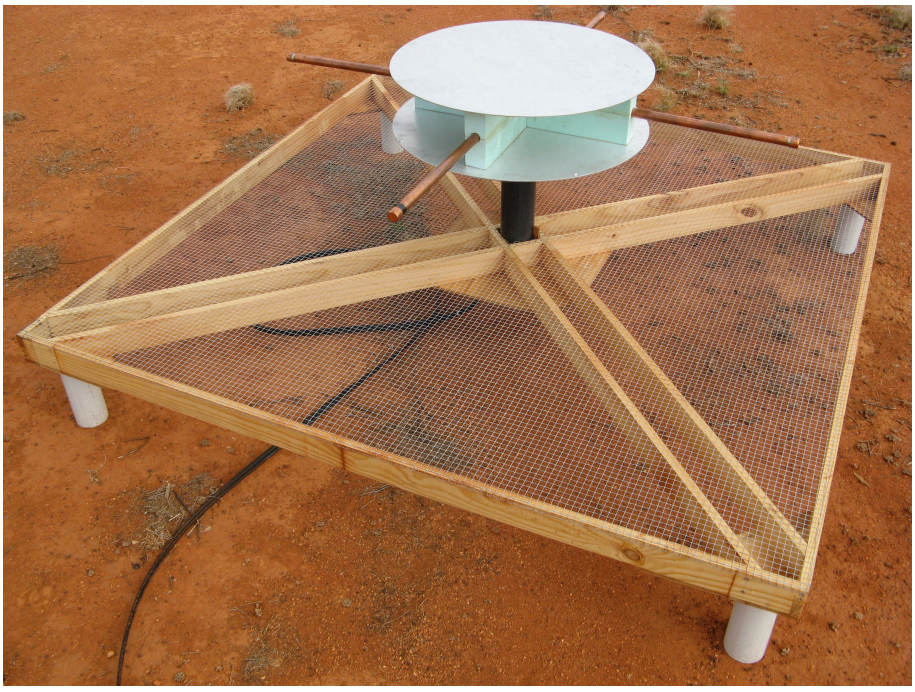

*Figure 2.19: One of four PAPER ground screens designed and constructed by the author. Each mounts a single sleeved-dipole antenna.*

I designed and constructed the EMC enclosure and 4 ground screens used in this experiment, each of which performed satisfactorily.

This deployment (PWA-4), together with another at NRAO Green Bank (PGB-8), Galford Meadow site, demonstrated initial calibration sufficient for modelling strong sources that allowed ionospheric refraction and temperature-dependent gains to be taken into account. Calibration relied heavily on producing a static model of the primary beam.

Data from the initial PWA-4 and PGB-8 deployments were used to generate an all-sky map that achieves a thermal noise level of 10 mJy beam$^{-1}$ (corresponding to 620 mK, for a 2.15 x $10^{-5}$ sr synthesised beam size at 156.4 MHz) integrated across a band from 138.8 MHz to 174.0 MHz. This represents a first iteration in a cycle of improvement wherein sky models are used to improve array calibration, which in turn allows increasingly accurate sky models to be generated. Results achieved demonstrate the need for a next level of calibration, modelling, and foreground suppression that will be pursued in future PAPER deployments.

### 2.8.2. Edges

EDGES (the Experiment to Detect the Global EoR Signature) is an experiment designed to further constrain parameters that define the epoch of the EOR and which, after deployment to the MRO, resulted in a paper published in the journal Nature (Bowman and Rogers 2010). I accompanied visitors to the MRO and provided local support until August 2009.

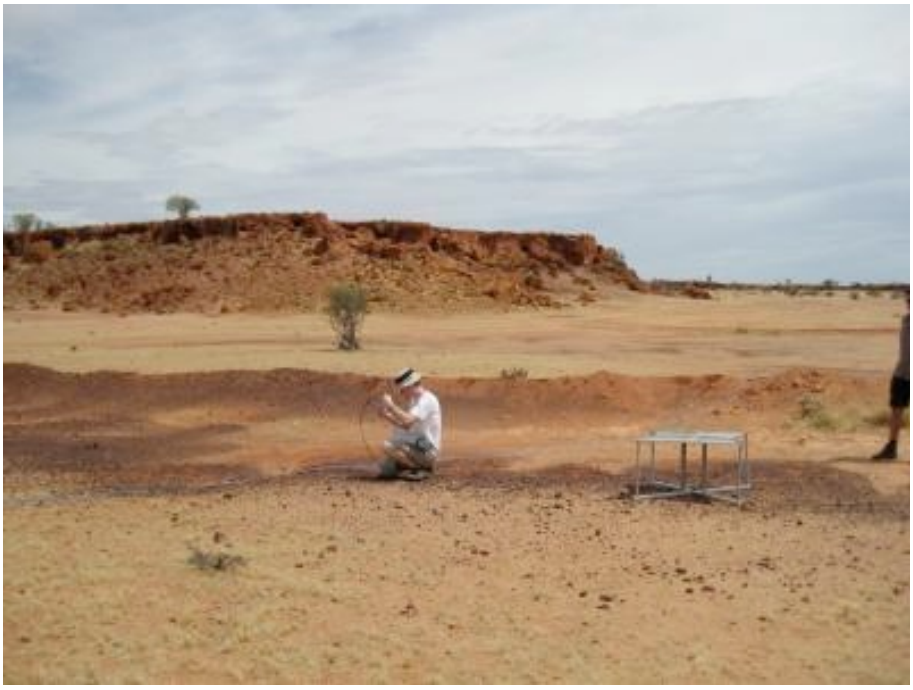

*Figure 2.20: Professor Judd Bowman, Arizona State University, EDGES principal investigator assembling the single Edges antenna on the MRO in 2009.*

## 2.9. Conclusion

Construction of the MWA began on a wholly unimproved site in March 2005, beginning as both prototype hardware and software and culminating in a national facility. The MWA was established initially as three tiles on Mileura Station. Four expeditions (ED series expeditions) were conducted until the advent of iron ore mining in nearby Jack Hills compromised the radio integrity of the site. Beginning again in March 2007 with an expedition (1T) to Boolardy Station, which I led, new hardware and software were trialled. Later, the MWA was constructed during a series of expeditions (X series expeditions), beginning with the laying of several tiles in November 2007 (X1/X2). During these expeditions, I deployed GPS systems in the study of ionospheric TEC and scintillation as opportunity permitted. I took part in all but a few expeditions of the prototype series (to July/August 2009).

Over this period, I participated in most of the MWA project related conferences, workshops and project meetings, including:

- The inaugural Grote Reber Conference (Hobart, December 2005).
- The inaugural MWA Project Meeting (La Jolla, California, July 2006).
- Visit to Haystack Observatory (Massachusetts, September 2006).
- MWA Project Meeting (Melbourne, December 2006).
- SKA Pathfinder Conference (CSIRO ATNF, Marsfield, Sydney, March 2007).
- MWA Project Meeting (Hawaii, December, 2007).
- SKA Pathfinder Conference (UWA, Perth, March 2008).
- MWA Project Meeting (Perth, March 2008).
- MWA Project Meeting (Haystack Observatory, Massachusetts, June /July 2008).
- MWA Project Meeting (Geraldton, October/November 2008).
- ICRAR opening ceremony (Perth, September 2009).
- MWA Project Meeting (Sydney, June, 2010).

My final visit to the MRO was conducted in July/August 2009 (X8.0). In October 2009 I suffered a significant injury unrelated to this work that required several months of convalescence. I have continued to support the MWA through the provision of data and advice on a regular basis. Over the period of this project, I have authored 8 papers and conference posters and co-authored a further 28 peer reviewed papers and conference presentations.

In November 2007, Curtin University established the MWA Operations Support Office and in this capacity I acted in support of all projects hosted at the MRO, including PAPER (as a team member) and EDGES (assisting), both of which are EOR experiments.

The first overseas trial of PAPER took place on the MRO in July 2007. Other team members present were Professor Don Backer (UC Berkeley) and Erin Mastrantonio (NRAO, Charlottesville, Virginia). The successful conclusion to this expedition resulted in the first peer reviewed paper (Parsons, Backer et al. 2009) of the operational instrument, of which I was a co-author. In support of this program, I concluded several activities, including:

- Attendance at PAPER project meetings at UC Berkeley, NRAO Virginia and Green Bank Observatory, West Virginia (August/ September 2006).

- Construction of project hardware and facilities, including 3 groundscreens and a refrigerator-sized Faraday enclosure, the design for which was based on a design by a principal investigator, Professor Richard Bradley (NRAO Charlottesville). Construction was completed in June 2007.

- Participation on the inaugural PAPER expedition as a team member (July 2007).

EDGES principal investigator Judd Bowman (ASU Tempe Az.) has conducted several visits to the MRO. The experiment is ongoing. I travelled with Professor Bowman and his wife, Dr Cassie Bowman, to the MRO in January 2009 to support this experiment.

Summary

(1) The author was a member of the first expedition to the Murchison Radio Observatory (Mileura) in March 2005 and the Murchison Radio Observatory (Boolardy) in March 2007. Assisted in the selection of both sites.

(2) First light from an MWA tile was achieved on Mileura Station on the 11$^{th}$ March 2005. The author was a member of the expedition (ED1) during which this was accomplished (Appendix 9.1).

(3) The author was a member of the CSIRO ATNF (now CASS) team that conducted RFI studies required by the site selection committee of the SKA organisation (January 2005 - March 2006).

(4) The author led the first expedition (1T), to install a radio science capable array of 16 antennas on the site of the MRO in March 2007.

(5) Preliminary images have been returned by the 32 tile, precursor instrument including the ones reproduced in Figure 2.19.

(6) The 32 tile precursor instrument has been employed in the study of space weather, in particular relating to impacts on Earth's ionosphere. The author is co-author on several papers relating to this work.

(7) The full, 128 tile MWA instrument has recently been commissioned on the Murchison Radio Observatory in Western Australia. The author continues as a a member of the MWA consortium and has been actively involved in construction of this instrument.

(8) For proper operation, the MWA requires that the ionospheric contribution to image degradation be mitigated through accurate calibration. Self-calibration is sufficient for certain classes of observation. Absolute calibration, which requires an accurate knowledge of the ionospheric TEC content, is required for other, important classes of observation and is a subject of this thesis.

(9) The MWA, designed to cover the frequency range 80-350 MHz, will be unique in performing observations in the 'FM' radio frequency band at 90 - 110 MHz. The LOFAR array in Europe excludes this frequency range due to very high levels of interference.

(10) The observational cadence of the MWA is 8 seconds, which allows ample time for newly determined TEC readings to be acquired from the GPS system by the calibration computer.

(11) The author was a party to a further two radio astronomy experiments that have been conducted on the MRO, namely PAPER in July 2007 (team member) (Parsons, Backer et al. 2009) and EDGES in 2009 (acknowledged contribution).

(12) Results achieved with PAPER demonstrate the need for higher fidelity calibration, modelling and foreground suppression that will be pursued in future PAPER deployments.

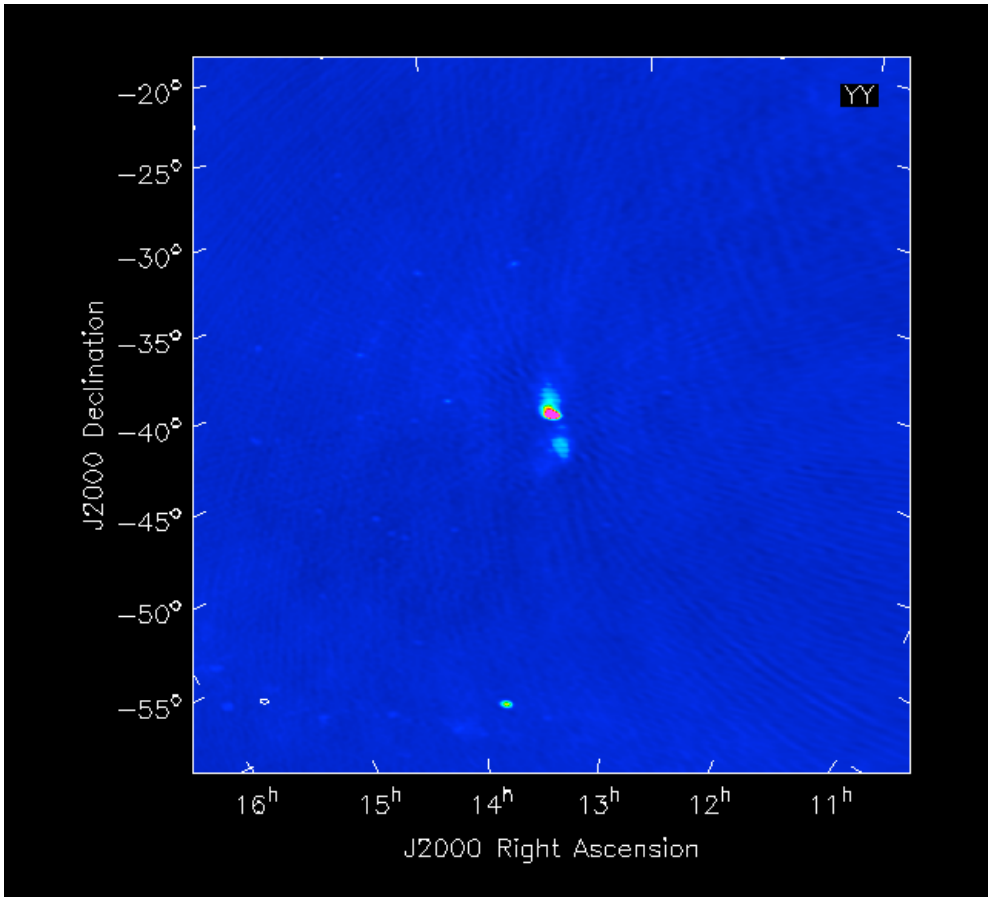


*Figure 2.21: Centaurus A imaged by the MWA thirty-two tile array (32T). Chris Williams, MIT, September 2011.*

# 3. The Ionosphere

The purpose of this chapter is to provide an introduction to the ionosphere, that region of the Earth's atmosphere and near-space environment that contains non-negligible numbers of ions and free electrons and through which the propagation of radio waves may be significantly affected (Rawer 1993). In respect to low-frequency (VHF) radio astronomy, it is necessary to understand ionospheric structure so that the ionosphere's degrading effects on acquired imagery can be mitigated through accurate calibration of the telescope (although some observations do not require *a priori* knowledge of the state of the ionosphere and rely instead on self-calibration techniques (Mitchell et al. 2008)). This chapter provides a description of the ionosphere in general and highlights aspects of particular relevance to radio astronomy, which are noted.

Ionising solar radiation produces charged species from gases present in the atmosphere, creating an ionosphere that is highly structured and dynamic, differentiated horizontally, vertically and temporally (Roble 1996). However, modelling the structure and dynamics of the ionosphere is a highly complex task involving a wide range of spatial and temporal scales.

The ionosphere consists at all times of at least one layer of peak ionisation (F-region) (Figure 3.1). This is due to the structure of the ionosphere, which is determined by several factors including downward increasing atmospheric gas density, which leads to a greater probability of ionisation, recombination processes and increasing downward attenuation of ionising solar radiation. Due to these and other factors including the particular chemistry of the Earth's atmosphere, several distinct layers or regions might at times be present at differing altitudes (Figure 3.1).

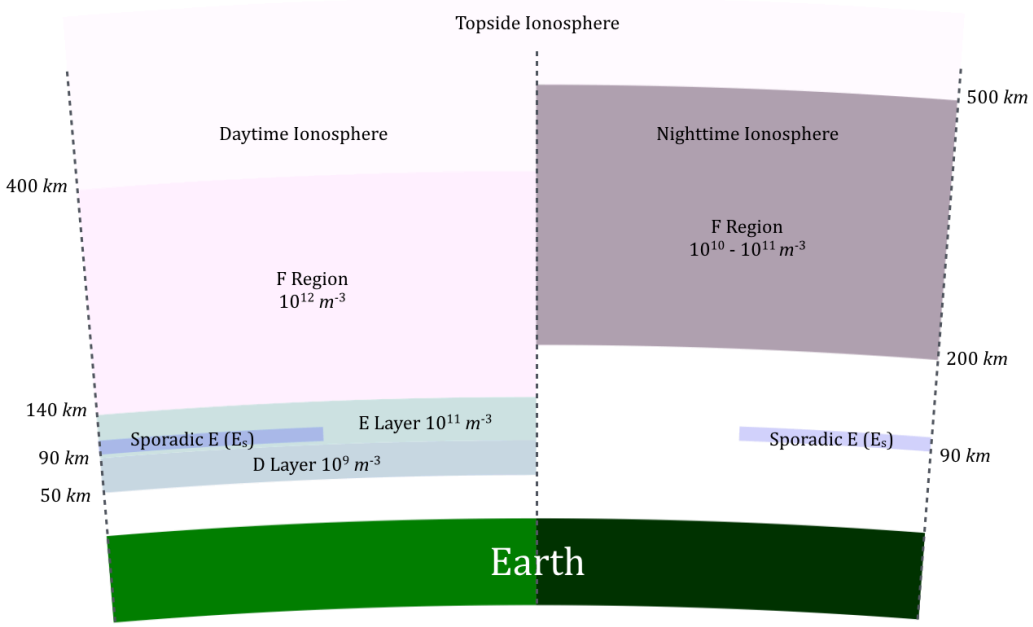


*Figure 3.1: Structure of Earth's ionosphere displaying features most relevant to low-frequency radio astronomy. The upper extent of the ionosphere (topside) extends well beyond the 400 km shown and exhibits falling TEC through the plasmasphere and magnetosphere beyond. Sporadic E ($E_s$) displays complex structure, as discussed in Section 3.4.4 Other layers, such as separate F1, F2 and a D Layer are discussed.*

Further, the atmosphere and ionosphere are permeated by the Earth's magnetic field. Above 1000 km altitude, behaviour of the plasma, largely free of collisional recombination, is dominated by the magnetic field and is referred to as the plasmasphere. This region, which marks the inner boundary to the magnetosphere, is permeated by cool plasma composed principally of $H^+$ ions and electrons and smaller concentrations of $O^+$ and $He^+$ ions. The plasmasphere contributes a non-insignificant influence on incoming radio waves (Carrano, Anghel et al. 2009) and is accounted for in the processing of data relevant to this thesis.

The ionosphere consists of both positively charged ions and negatively charged electrons. However, as the mass of an ion vastly exceeds that of the electron, each responds to radio waves of different frequency. To any practical extent, it is the excitation of free electrons that contributes

almost entirely to those effects of interest to radio astronomy (Budden 1985).

Together with the solar wind, which imparts energy and momentum, the atmosphere, ionosphere, magnetosphere and plasmasphere comprise a system that exhibits a complex morphology, driven by as much as $10^{11}$ W of electrical energy generated by the impinging solar radiation (Lyon 2000). However, prior to looking more closely at the structure and dynamic behaviour of the ionosphere, it is appropriate to consider the relationship between the ionosphere and the underlying atmosphere.

## 3.1. Dependance on the Composition and Structure of Earth's Atmosphere

The Earth's atmosphere is a system of gases blanketing the planet with properties determined by gravity, insolation and the Earth's magnetic field. Up to approximately 120 km altitude, the atmosphere is dominated chemically by the gases nitrogen (78%) and oxygen (~21%), the principle species. In this region, argon (0.93%) presence is significant. Carbon dioxide (~0.038% with seasonal and hemispherical variation) is an important greenhouse gas and therefore relevant to consideration of the atmosphere's heat budget. Minor components such as water vapour ($H_2O$), which is a greenhouse gas and along with $CO_2$ is spectrally ubiquitous, nitric oxide ($NO^+$), hydroxyl ($OH^-$) and sodium ($Na^+$) are important photochemical species up to about 100 km (Egeland 1996). Figure 3.2 gives the numbers of principal neutral atmospheric species against altitude in the atmosphere at the location of the MRO after the atmospheric model *MSIS-E-90* (Section 5.1) (Hedin 1991).

Atmospheric pressures range from approximately 1013 hPa at sea level to the vacuum of space, toward which the atmosphere is comprised

increasingly of charged particles that behave as a plasma and are subject to the influence also of the Earth's magnetic field (magnetosphere) and that of the Sun (heliosphere).

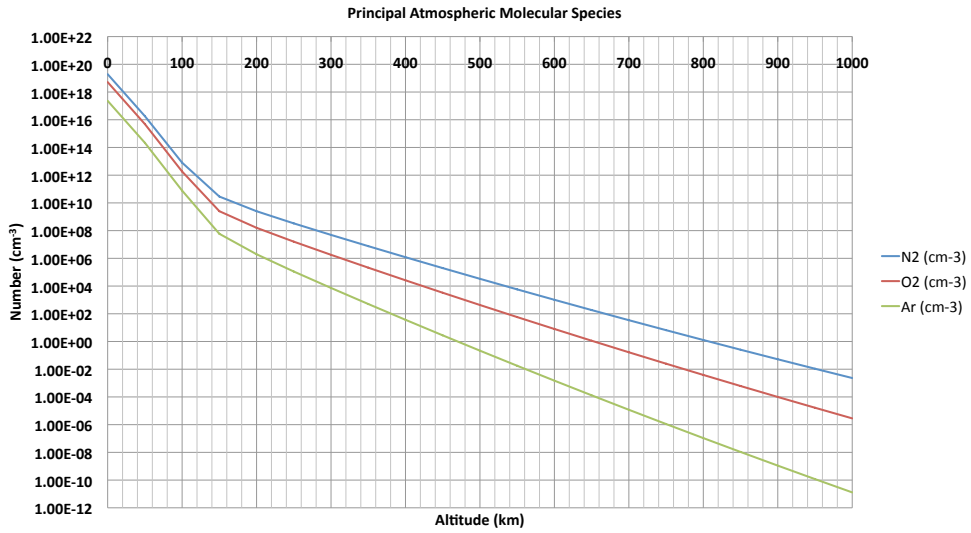


*Figure 3.2: Number densities of the principal atmospheric species against altitude over the MRO (-26.7° latitude, 116.7° longitude) in January 2009, produced by the model MSIS-E-90.*

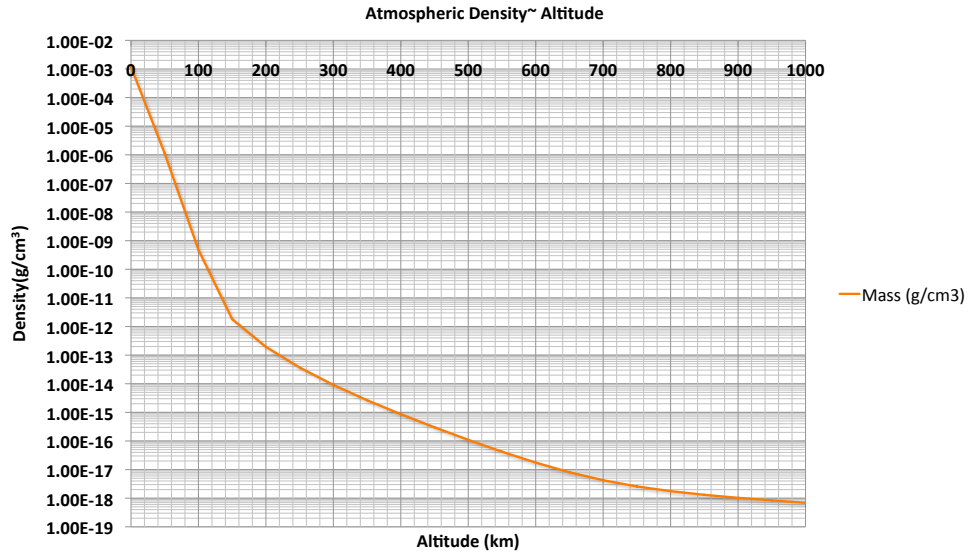


*Figures 3.3 (a) Atmospheric gas density over the MRO (-26.7° latitude, 116.7° longitude) to 1000 km altitude in January 2009, produced by the model MSIS-E-90. Figure 3.3 (b) expands the lower atmosphere's profile.*

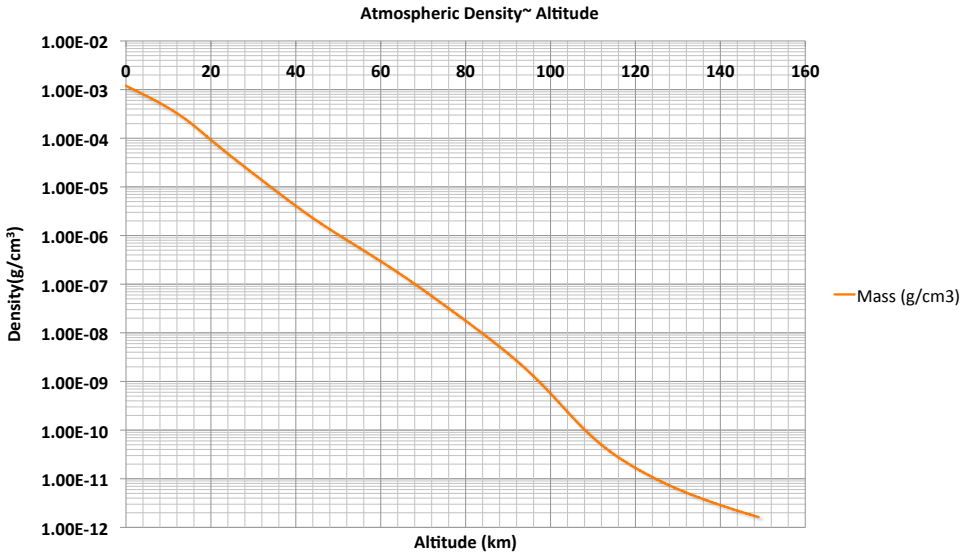


*Figures 3.3(b): Atmospheric gas density over the MRO (-26.7° latitude, 116.7° longitude) to 150 km altitude in January 2009, produced by the model MSIS-E-90. Figure 3.3 (b) expands the lower atmosphere's profile.*

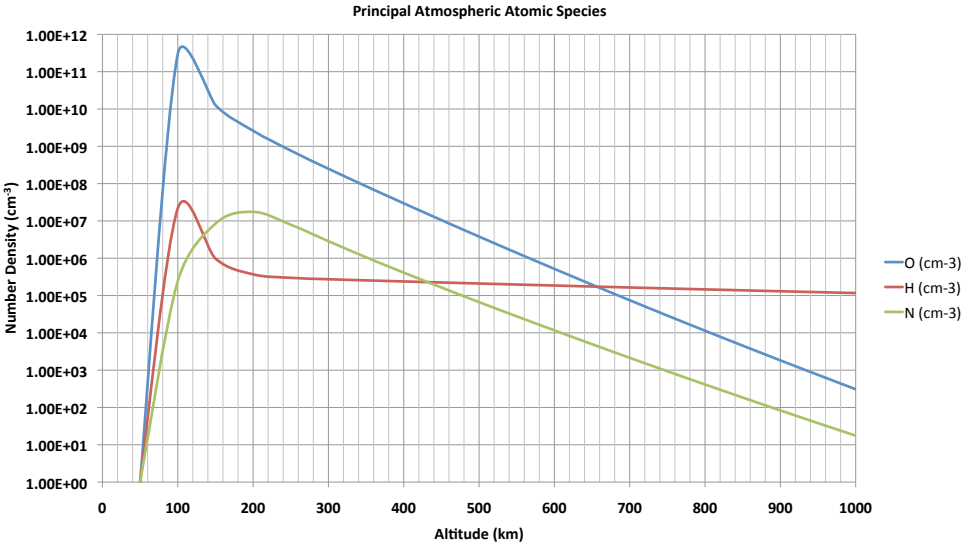


*Figure 3.4: Number density of the principal atmospheric charged atomic species over the MRO (-26.7° latitude, 116.7° longitude) in January 2009, produced by the model MSIS-E-90.*

Gases are differentiated in the atmosphere principally under the influence of gravity. Heavier molecules dominate at lower altitudes, lighter molecules and radicals higher in altitude. Figures 3.3 (a) and (b) describe the mean density of the atmosphere at the location of the MRO

after the model MSIS-E-90. Figure 3.4 describes the number density of principal charged (atomic) atmospheric species against altitude in the atmosphere at the location of the MRO.

As the ionosphere is dependent on the physical structure of the atmosphere, the extent of which is subject to an energy budget (Egeland 1996), local atmospheric temperatures should be considered. Figure 3.5 shows modelled temperatures in the atmosphere over the MRO for January and June 2009 after the model MSIS-E-90.

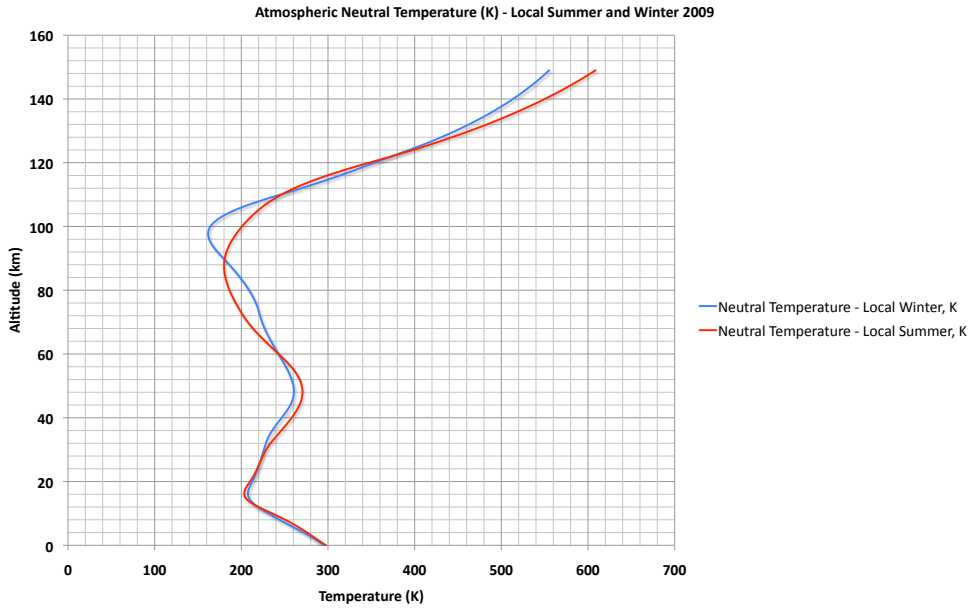


*Figure 3.5: Temperature profile of the neutral atmosphere over the MRO (-26.7° latitude, 116.7° longitude) in January (red trace) and June 2009 (blue trace), produced by the model MSIS-E-90.*

Processes occur in the atmosphere that determine the extent and temporal variability of the ionosphere. The preeminence of these processes is governed by the particular composition of the atmosphere at altitude, atmospheric pressure and the nature of ionisation sources which either promote ionisation or recombination of ionic species. At a given altitude, one or other of these will dominate. Typically, lower in the atmosphere, recombination is rapid and therefore atmospheric gases are weakly ionised. In these regions too, gravity influences strongly both the behaviour and the composition of species. Beyond the

bulk of the atmosphere, recombination rates are very much lower. Here, diffusion and at higher altitudes, transport along magnetic field lines are more important in the transport of charged species. A process that leads to the availability of species for ionisation is the photodissociation of molecules in the atmosphere.

$$X_2 + h\nu = X + X \tag{3.1}$$

where $X_2$ is a molecule, $h\nu$ is a photon in the extreme ultraviolet (EUV) band and $X$ is a corresponding atomic species. Following this, EUV band photons ionise atoms through the process of photoionisation

$$X + h\nu = X^+ + e_n, \tag{3.2}$$

where $e_n$ is an unbound, low-energy electron and $X^+$ is the ionised state of atom $X$.

The distribution of electrons and ions is governed by the rates of ionisation and recombination that over a given interval might exist more or less in equilibrium or fluctuate rapidly in response to external forcing, as in the diurnal cycle for example. Recombination takes the form of two possible processes

$$X^+ + e_n \rightarrow X \tag{3.3}$$

and

$$YX^+ + e_n \rightarrow X + Y. \tag{3.4}$$

At higher latitudes, other processes are also important, such as those involving electrons and ions precipitating out of the magnetosphere. Such precipitation includes that induced by VLF signals, known as whistlers and others that propagate along magnetic field lines and cause electrons to precipitate where these signals impinge the radiation belt electrons upon reentry.

Physical processes are also important in governing the extent and distribution of charged species. These are discussed in section 3.5.

## 3.2. Physical Extent

The ionosphere is an extension of the atmosphere, of which 99.99997% exists below the 100 km altitude considered the boundary of the atmosphere to space (the Kàrmàn line) (Lutgens 1995). This altitude is also that at which the transport of atmospheric gases by molecular diffusion becomes dominant (the turbopause) with turbulent mixing having ceased. Here species are distributed vertically according to mass. The majority of the ionosphere in respect of the numbers of charged species, exists between 100 and 500 km (Carrano, Anghel et al. 2009).

The atmosphere's chemistry and energy budget, solar flux, cosmic ray exposure and the Earth's gravitational and magnetic field are the principal determinants of the ionosphere's constitution and behaviour. Whereas one may comment on the nature of the ionosphere in quite general terms, the requirements of radio astronomy are quite specific. A detailed knowledge over epochs determined by the cadence and sensitivity of a particular instrument and the physical extent of the instrument in the case of telescope arrays is required. In particular, disturbances in the ionosphere result in distortions to images received by radio telescopes on the ground. Travelling ionospheric disturbances (TIDs), momentary changes to the ionosphere's fine grained structure, are capable of affecting the fidelity of a radio telescope's imagery. These occur during periods of rapid changes in the concentration of charged species. Perturbations occur regularly.

Therefore, it is opportune now to consider the ionosphere's structure specifically.

## 3.3. Structure

As discussed previously, the ionosphere, although quite tenuous, is nevertheless highly structured. To a zeroth order approximation, the

ionosphere consists of regions of electrons of varying density in layered concentric spherical shells above the Earth. However, the ionosphere's structure is driven by phenomena that are diurnal in nature, particularly solar radiation in the EUV and soft X-ray (xuv) bands. Therefore, the composition of the actual ionosphere reflects the influence of these daily drivers, which produces large variations in composition at varying scales. Large scale gradients, superimposed with smaller irregularities impose the need to study the ionosphere at scales relevant to activities of interest. This constraint is particularly important to radio astronomy because signals might be integrated over periods (up to months) that are much greater than timescales over which the ionosphere remains more or less stable at the spatial scales of interest. Longitudinal gradients exist due to the diurnal forcing of the ionosphere, particularly close to sunrise and after sunset.

As TEC is dependent on solar flux, the zenith angle of the Sun is also a factor in ionisation levels and hence TEC also exhibits latitudinal variation.

Therefore, the shell of ionisation that defines the ionosphere is variable spatially, in latitude, longitude and altitude and temporally. However, as atmospheric density falls with altitude, the ionosphere's response changes significantly. Density gradients in the atmosphere drive flows that produce instabilities which in turn draw energy from these flows (as witnessed in Kolmogorov turbulence). The instabilities are turbulent in the lower atmosphere (troposphere) and result in phenomena that influence the ionosphere through a variety of processes.

Above the turbopause the atmospheric species are distributed vertically by mass, causing variations with altitude. Below the turbopause the species are well mixed due to turbulent behaviour.

Several layers or regions are recognised. These exhibit varying behaviours and play very different roles in determining the structure of the ionosphere. These are discussed next.

### 3.3.1. The F Region

The F region, which exists from about 140 km altitude, tailing off toward the maximum extent of the ionosphere, exhibits the most persistent and distinct region of enhanced electron density. The region above F layer peak density is known as the topside ionosphere, so named because the characteristics of this region could not be readily discerned from ground based radio soundings but were eventually studied using satellite radio and rocket sounding measurements. Attempts have been made to construct accurate topside electron profiles from ground based ionograms. Studies have investigated correlations between parameters, such as scale height (*H* - Figure 4.3), the highest frequency ordinary ray reflected vertically in the F2/F1 region (foF2) and the height of the peak value of the F region (hmF2) (Zhang, Reinisch et al. 2006). The ordinary ray (o ray) is one of two orthogonal components of an unpolarised ray along with the extraordinary ray (e ray) that experience different refractive indices when passing into a birefringement medium. The two rays therefore undergo differing amounts of refraction. These parameters are discussed in Section 5.2.

During daytime, the F region often comprises two layers of electron density maxima, known as the F1 (lower) and F2 (upper) layers. These exhibit typically, peak electron densities of $3 \times 10^{11}$ $m^{-3}$ at an altitude of order 180 km and $10^{12}$ $m^{-3}$ at altitudes of up to 350 km. The neutral, molecular density is of the order $10^{15}$ $m^{-3}$ (Egeland 1996). Lower in the

F region, solar flux produces ionisation products at a rate that produces a peak, the F1 layer, that is quickly lost to recombination overnight.

The F region therefore, exhibits the greatest electron density through the ionospheric profile and is often the only one that persists through a complete diurnal cycle. The principle ions in this region are $O^+$, $NO^+$, $O_2^+$ and $N_2^+$. Important reactions are:

$$N_2^+ + O \rightarrow NO^+ + N \qquad (3.5)$$

and in the lower, F1 region:

$$O^+ + O_2 \rightarrow O_2^+ + O \ . \qquad (3.6)$$

In the lower F region, below about 200 km, the species $NO^+$, $O_2^+$ and $O^+$ dominate while in the F2 region, $O^+$ and lighter species dominate. Ionisation is driven by XUV photons of wavelengths between 10 and 90 nm. At altitudes above ~600 km, lighter atomic ions such as $H^+$ and $He^+$ are significant abundance and likely to dominate, with all species becoming fully ionised in the upper reaches of the topside ionosphere.

The continuity equation for the F layer is:

$$\frac{dn_e}{dt} = q - \beta n_e + v \bullet \nabla n_e \qquad (3.7)$$

where $q$ is the electron production rate, $n_e$ is the electron density and $\beta$ is the recombination rate coefficient. The final term in equation 3.7 recognises the significance of ion drift, $v$ , in this plasma at altitude along magnetic field lines which, when coupled at midlatitudes to the magnetic conjugate ionosphere in the opposite hemisphere, contributes ions and electrons to that ionosphere (Egeland 1996). Further, large scale ion and electron density structures extend out from the F layer into the plasmasphere and may become detached as plasmaspheric plumes (Darrouzet and De Keyser 2013).

As with the ionosphere overall, the F layer exhibits temporal and spatial variability. Rodger et. al (1992) discuss the formation of ionisation troughs in the mid-latitude ionosphere, defined as a temporary depletion of electron density of the order one magnitude over ambient. These authors concluded that:

(1) A mid-latitude trough is principally a nighttime phenomenon, although it might be observed at anytime.

(2) Mid-latitude troughs occur only rarely in summer over which season they are confined to midnight hours. Troughs are regularly observed in winter and during equinoxes.

(3) There is generally an inverse relationship between electron temperature $T_e$ and electron concentration $N_e$ in mid-latitude troughs but not in high-latitude troughs.

(4) The poleward edge of the trough is usually field-aligned.

(5) The trough latitude decreases during the night.

(6) During periods of increased geomagnetic activity, the trough is observed at lower latitudes for a given magnetic local time (MLT), $t_{mlt}$, defined as:

$$t_{mlt} = \frac{(180° + \phi_{d,0} - \phi_{d,s})}{15}, \qquad (3.8)$$

where $ø_{d,0}$ is the dipole longitude of the observer and $ø_{d,s}$ is the sub-solar point. MLT takes the units hours where ø is in degrees (Sabaka, Olsen et al. 2002).

(7) Those features of a mid-latitude trough listed here occur independently of the level of solar activity.

A range of structures are observed in the F region, including TIDs (Yokoyama , Waldock and Jones 1984, Waldock and Jones 1987, MacDougall, Abdu et al. 2009, England, Immel et al. 2010, Shiokawa, Mori et al. 2013) and spread-F (Bowman 1981, Taylor, Jahn et al. 1998, Chen, Lee et al. 2011, Oberoi and Lonsdale 2012). Spread F can take the

form of frequency-spread F, range-spread F and total (mixed mode) spread F.

These phenomena are discussed further in Section 3.4, Structures and Disturbed Modes in the Ionosphere.

### 3.3.2. The E Layer

The E layer exists between approximately 90 and 140 km altitude and is weakly ionised. Electron density is $10^{11}$ $m^{-3}$ during the day, up to 6 orders of magnitude less than the neutral density at 120 km altitude (Egeland 1996). Electron density falls to about $10^{10}$ during the night when solar flux is absent and recombination processes dominate but is maintained by cosmic radiation and possible meteoroid influx. The principal ions in this region are $O_2^+$ and $NO^+$:

$$N_2^+ + O_2 \rightarrow N_2 + O_2^+ . \qquad (3.9)$$

Lyman-α radiation of 121.5 nm is capable of ionising $NO$, which has an ionisation potential of 9.264 eV and is the main ionising source at this height. Dissociative recombination, in this case a two step process, is the dominant loss term and takes the form:

$$O_2^+ + e_n \rightarrow O_2 \rightarrow O + O . \qquad (3.10)$$

The continuity equation for the E layer is:

$$\frac{dn_e}{dt} = q - \alpha n_e^2 , \qquad (3.11)$$

where $q$ is the electron production rate and $\alpha$ is the recombination rate coefficient.

The E layer originates below the atmosphere's notional 100 km altitude cutoff (Kármán Line) and is subject, in addition to the principal ionising

flux (EUV), to physical disturbance from sudden ionospheric disturbances (SIDs), traveling ionospheric disturbances (TIDs) and storm enhanced density variations (SEDs) and chemical alteration (species enhancement). This is true also of the F region. Further, less significant drivers, such as magnetised Rossby waves (Kaladze, Aburjania et al. 2004) may be involved. These are discussed in section 3.4.

A phenomenon strongly associated with the E layer is variation in the strength of the Earth's magnetic field at the Earth's surface due to electrical currents flowing principally in this layer (Davies 1965). Constantly changing, these fluxes induce variations in the magnetic field over daily and seasonal time scales. However, these currents are also driven by solar activity. Therefore, under conditions of low, or quiet, solar activity, denoted $S_q$, variations in the magnetic field occur slowly. $S_q$, electric currents are typically stronger during the day and stronger during periods of high sunspot number by about 50%.

Under conditions of high solar activity, during which geomagnetic storms might occur, large variations in the ambient magnetic field can occur over periods of minutes (Herne, Kennewell et al. 2013). Solar plasma ejected from the Sun are captured by the Earth's magnetic field and reduce the ionospheric currents and therefore the associated magnetic field. Examples of these processes are discussed in Chapter 4.

Other significant phenomena are enhanced currents in a narrow region centred on the magnetic equator, which are known as the equatorial electrojet (EE) and currents centred in auroral regions, known as the auroral electrojet (AE). These phenomena lead to short-term fluctuations of over tens of TECU over short timescales of minutes to hours.

A tenuous phenomena, sporadic E ($E_s$) is characterised by highly ionised, thin regions in the E layer. (Oberoi and Lonsdale 2012). Although these layers are thin, they display a large electron density

contrast against the surrounding ionosphere (2:1) and may therefore produce large refraction effects. These structures, along with others such as spread F, have been studied for over half a century (Little, Rayton et al. 1956). $E_s$ has been probed by methods including ionosondes (Wakai, Ohyama et al. 1987), incoherent scatter radar at Arecibo (430 MHz) (Hysell, Nossa et al. 2013), galactic radio source scintillations (Little, Rayton et al. 1956), Doppler-sorted interferometry, using digital ionosondes (Parkinson and Dyson 1998), VHF propagation effects (Rasmussen, Kossey et al. 1980) and more recently, ionosonde height-time-intensity (HTI) has been employed in measuring descent rates and tidal periodicities of $E_s$ (Haldoupis, Meek et al. 2006).

### 3.3.3. The D Layer

The D layer is the lowest layer of the ionosphere, existing between 50 and 90 km altitude. It is also the least distinct, represented by a subtle step in electron density at mid-latitudes (Egeland 1996). Electron density in the D layer is typically $10^9$ $m^{-3}$ during the day, possibly reaching $10^{10}$ $m^{-3}$ and falling to $10^8$ $m^{-3}$ at night. Daytime values are up to two orders of magnitude less than the next region in altitude, the E layer. The most important property of the D layer is its absorption VHF radio waves rather than refraction, due to high collision frequency of electrons with neutral molecules.

Important ionisation sources are Lyman alpha, soft X-rays and cosmic rays. X rays of wavelength 0.1 to 1.0 nm are important below 90 km. Solar protons also reach this layer. These are produced by solar flares. Therefore, during quiet periods, density changes on a diurnal scale are consistent.

In addition to the primary ions are $NO^+$ and $O_2^+$, negative molecular ions are present, such as those produced in equation (3.12). Due to the

relatively high gas pressure in this layer, recombination is rapid and therefore the layer is weakly ionised.

$$2O_2 + e_n \rightarrow O_2^- + O_2 . \qquad (3.12)$$

A further layer can form towards the Earth's magnetic poles, distant to the mid-latitude layer of interest, during major flare events and is contained within or adjacent to the lowest D layer. This is known as the enhanced D ($D_e$) layer.

## 3.4. Structures and Disturbed Modes in the Ionosphere

The ionosphere can be viewed as being comprised of permanent structures situated mostly above Earth's atmosphere (E and F layers) superimposed with diurnal structures (F1 layer, D region) and transient events over shorter timescales (spread F, $E_s$, TIDs, SEDs etc.). Changes in TEC occur over varied timescales. When changes occur quickly and dramatically, as demonstrated on hourly timescales (Uma, Brahmanandam et al. 2012), transient events might be responsible. This section provides a review of ephemeral structures and irregularities that develop in the ionosphere and is summarised in Table 3.1 that follows.

Large-scale horizontal gradients, particularly around sunrise and sunset, give rise to structures such as equatorial plumes and spread-F. Persistent, anomalously large electron content, the equatorial ionisation anomaly (EIA), is created in the vicinity of the magnetic (dip) equator by E cross B drift (ExB). ExB drift is the result of electron movement under the electric and magnetic fields present at a particular location. Mid-latitude troughs form on the equatorward boundary of the nighttime auroral oval (England, Immel et al. 2010). A trough is a region of depleted electron density. The auroral oval extends from approximately magnetic latitude 60° S to 80° S (and the same in the northern hemisphere). The MRO is not directly affected by either

phenomenon, however, disturbed modes at smaller scales in the wider ionosphere are driven by these. In many respects, understanding the dynamic ionosphere involves understanding the coupling of the atmosphere and ionosphere via wave action, example types being acoustic and atmospheric gravity waves, Kelvin waves, Rossby waves and collisional drift waves. Energy transfer through wave action in the atmosphere and ionosphere produces phenomena that can be observed experimentally and deserves further consideration.

### 3.4.1. Acoustic Waves

Acoustic and atmospheric gravity waves are longitudinal systems distinguished by characteristic scales. Over shorter intervals, local pressure differences produce waves at audible frequencies (sound waves). The motions of these acoustic waves obey Euler's equations (Rawer 1993) and dissipate quickly, although waves of infrasound wavelengths might propagate into the ionosphere with increasing amplitude, which is characteristic of wave motion in a gas that exhibits an exponentially decreasing density. However, refraction and in the upper atmosphere, absorption in the low-density gases present, limit propagation to higher altitudes.

### 3.4.2. Atmospheric Gravity Waves

For wavelengths of greater than about 1 km, buoyancy and therefore, gravitation are further considerations. An atmospheric gravity wave (AGW) is created when a quiescent fluid, in this case the atmosphere, is disturbed. An example is a rising plume of gas that reaches into the upper levels of the atmosphere. As the GW propagates upwards, its amplitude grows exponentially with altitude (Vadas, Liu et al. 2014). Vedas et. al found that the dissipation of AGWs from deep convective plumes excites upward and downward propagating secondary AGWs

with horizontal wavelengths of $\lambda_H$ ~100 – 4000 km and phase speeds of $c_H$ ~100–500 m/s. These waves transfer significant amounts of momentum from the lower atmosphere to the thermosphere and ionosphere.

Energy transport by gravity waves is non-negligible in the upper atmosphere and as long as attenuation is small, wave speed increases at increasing altitudes. At some point, as wave speed increases. non-linear processes occur and energy is transferred to an increasing number (spectral range) of waves at smaller scales (as occurs in Kolmogorov turbulence), thus limiting the distance over which the original GW can exert an influence. In concert, refractive and reflective processes continue to apply, further complicating consequent observed phenomena. Large, secondary AGWs propagate globally and reach altitudes of > 400 km (Borries, Jakowski et al. 2009).

### 3.4.3. Traveling Ionospheric Disturbances

AGWs create perturbations of the ionospheric plasma known as travelling ionospheric disturbances (TIDs) with a range of size scale, classified as large-scales TIDs , medium-scale TIDs and small-scale TIDs. MacDougall et. al (2009) found that large scale TIDs are excited by high latitude processes in auroral regions usually associated with geomagnetic storms and they are observed at mid-latitudes only when the Kp index >~4 (MacDougall, Abdu et al. 2009, MacDougall and Jayachandran 2011). In Figures 4.1 and 4.2, I display TEC data for two locations separated by ~500 km on a ~Nth/Sth transect that were captured during a geomagnetic storm when the Kp index >6. The event is discussed in Chapter 6.

### 3.4.4. Sporadic E

These transient structures that are apparent during daylight and nighttime hours within the E region (Otsuka, Tani et al. 2008), exhibit a semidiurnal periodicity in layer descent as revealed by ionogram height-time-intensity (HTI) observations (Hajkowicz 1994, Haldoupis, Meek et al. 2006, Harris, Cervera et al. 2012). $E_s$ is often thin, as little as 1 km deep and highly stratified (Parkinson and Dyson 1998, Oberoi and Lonsdale 2012). When applied to ionogram recordings made during a summer period from solstice to equinox on the island of Milos (36.71N; 24.51E), analysis revealed that the daytime layer started at ~120 km altitude at ~06:00 hr local time and descended at a rate of ~0.8 - 1.5 km/hr to altitudes below 100 km by 18:00 hr local. The nighttime layer would then appear above ~120 km altitude descending at the higher rate of 1.6 - 2.2 km/hr. Kagan (Kagan 2002) asserts that the study of inhomogeneities in the near-Earth region to be one of the key requirements of understanding ionospheric physics.

Of relevance to the MWA, midlatitude sporadic E has been observed with a wavelike structure with horizontal wavelengths of up to 2-3 km (Hysell, Nossa et al. 2013).

### 3.4.5. Spread F

Spread F (King 1970) is predominantly a nighttime feature of the ionosphere, observed less at mid-latitudes than equatorial regions. The consensus is that the phenomenon is produced by the passage of medium-scale travelling ionospheric disturbances (MSTIDs) with further diffuse reflections produced by small-scale structures, perhaps Kolmogorov turbulence. The MSTIDs are produced by acoustic or gravity waves lower in the atmosphere.

### 3.4.6. Kolmogorov Turbulence

The turbulent dissipation of energy of waves at one scale by waves generated at smaller scales (George 2009). As waves in vertical motion in the atmosphere increase in velocity into lessening pressure, a shock wave may cause the wavefront to breakup into a turbulent systems of waves at successively smaller scales in which the energy of the original wave is dissipated. As the Reynolds number increases vertically, small excursions in the flow are no longer damped by the flow and grow in magnitude. Energy in the flow is dissipated by work done by small-scale turbulent flow. This is characterised by the Kolmogorov *microscale*, defined as:

$$\eta_K \equiv \left( \frac{\nu^3}{\varepsilon} \right)^{\frac{1}{4}}, \tag{3.13}$$

where $\nu$ is the kinematic viscosity and $\varepsilon$ is the rate of dissipation of turbulence kinetic energy per unit mass due to viscous stresses.

The overall dissipation rate is determined by the rate of energy transfer from the large scale flow.

### 3.4.7. Scintillation

Scintillation of radio signals passing through the ionosphere were first observed by Hey et. al (1946), for the radio star Cygnus at 64 MHz. Signals acquired by receivers 210 km apart lacked correlation whereas signals acquired by stations separated by approximately 4 km demonstrated 'fairly good' correlation, suggesting a local cause for this scintillation induced effect (Kung Chie and Chao-Han 1982). Observations by Thompson in 1958 of fading in radio transmissions from spacecraft such as Sputnik (Smith 1959), firmly established the Earth's own near-space environment as the source of the interference observed in these signals.

Scintillation is observed in both the amplitude and frequency of signals. The discovery in the early 1970s of scintillation in radio signals at giga-hertz frequencies (Kung Chie and Chao-Han 1982) provided the opportunity to study the phenomenon through the use of satellite beacons. Coherent multiple frequency studies were conducted , leading to an understanding at finer scales of the structure of the ionosphere.

**Ionosphere Disturbed Modes and Associated Spatial Scales and Epochs**

| Mode of Disturbance | Driver/Vector | Index/ Unit | Spatial Scale | Temporal Scale | Region(s)/ Layers Affected | Reference/s |
|---|---|---|---|---|---|---|
| Expansion/ contraction (diurnal) | Daily cycle (diurnal) | | Global | hr | All | |
| Expansion/ contraction (annual) | Seasonal cycle (annual) | | Global | Yearly | All | |
| Scintillation | Small-scale electron density variations | $S_4$ | Regional | sec - min | Principally equatorial and polar | (Kung Chie and Chao-Han 1982) |
| Equatorial ionisation anomaly | Daily cycle | TECU | Global | min | ±15° latitude over the Australian region | |
| Mid-latitude Trough | Rapid terrestrial magnetic field dip angle change with latitude | $m^{-3}$ | Regional - 60° N/S | daily | E/F | (Rawer 1993) |
| Acoustic waves | Classical pressure gradients | m $s^{-1}$ | << 1 km | daily | Lowest ionosphere | (Rawer 1993) |
| Atmospheric gravity waves | Several including deep convective plumes | m $s^{-1}$ | > 1 km | daily | D/E/F | (Vadas, Liu et al. 2014) |

| Ionosphere Disturbed Modes and Associated Spatial Scales and Epochs | | | | | | |
|---|---|---|---|---|---|---|
| **Mode of Disturbance** | **Driver/Vector** | **Index/ Unit** | **Spatial Scale** | **Temporal Scale** | **Region(s)/ Layers Affected** | **Reference/s** |
| Large-scale traveling ionospheric disturbance (LSTID) | Several including terminator movement or atmospheric gravity waves | $TECUs^{-1}$ | $\lambda >$ 1000 km | 300 - 1000 m/s | Polar, equatorial, midlatitudes when the Kp index > ~4, E/F layer | (MacDougall, Abdu et al. 2009), (Idrus, Abdullah et al. 2013) |
| Medium-scale traveling ionospheric disturbance (MSTID) | Suggested - electro-dynamical coupling between the $E_S$ layer and F region through polarization electric fields. | $TECUs^{-1}$ | 100s km | m/s | Regional, E/F layer | (Otsuka, Tani et al. 2008, Helmboldt, Lazio et al. 2012) |
| Short-scale traveling ionospheric disturbance (SSTID) | Acoustic gravity waves | $TECUs^{-1}$ | 10s km | m/s | Regional, E/F layer | (Otsuka, Tani et al. 2008, Helmboldt, Lazio et al. 2012) |
| Sudden ionospheric disturbance (SID) | Solar flare activity, increased solar radiation between 0.1 - 1 nm. | $TECUs^{-1}$ | Local | Sec (duration usually < 1 hr) | D region | (Egeland 1996) |
| Storm enhanced density (SED) | Geomagnetic storms (plasmaspheric drainage plume) Coronal mass ejection (CME) | $TECUs^{-1}$ | Regional | hr | E/F layer | (Yuan, Xiong et al. 2013) |
| Sporadic E | Drift wave instability - collisional regime | $TECUs^{-1}$ | Regional | daily | E layer | (Haldoupis, Meek et al. 2006) |
| Sporadic-E TID | Collisional Drift Waves | $TECUs^{-1}$ | up to km | min | Sporadic E layer | (Otsuka, Tani et al. 2008, Hysell, Nossa et al. 2013) |

| Ionosphere Disturbed Modes and Associated Spatial Scales and Epochs | | | | | | |
|---|---|---|---|---|---|---|
| **Mode of Disturbance** | **Driver/Vector** | **Index/ Unit** | **Spatial Scale** | **Temporal Scale** | **Region(s)/ Layers Affected** | **Reference/s** |
| Farley-Buneman Instability | Atmospheric turbulence (gravity waves) | | Regional, 105-115 km altitude | | E layer, principally polar, equatorial | (Gurevich and Zybin 1995) |
| Spread F | Specular reflections from large scale TIDs / equatorial bubbles with cascaded disturbances / Kolmogorov | TECU | Regional | hr | F layer | (Bowman 1981, T. Harris) |
| Turbulence - Kolmogorov | Turbulence at larger scales dissipating at smaller scales | m/s, km/hr | Regional, local | 10's sec - mins | D/E/F layers | |
| Turbulence - Alfvénic | | | | | | |
| Kelvin wave | Coriolis Force | | Regional | | | (Chen and Miyahara 2012) |
| Lightning (conventional ?) | Electromagnetic (whistler) inducement of particle precipitation. | J | Local | sec | D layer - effects propagating into the E layer | |
| Lightning (sprite?) | | J | Local | | | |
| Wind-Driven Kelvin-Helmholtz Turbulence | Sheared wind profile | | Regional | | Sporadic E layer | (Bernhardt 2002) |
| Atmospheric species enhancement | Species production, winds | x $m^{-3}$ | Regional | | All | (England, Immel et al. 2010) |
| Magnetized Rossby waves | Reynolds stresses/Coriolis force | | Regional | | E/F layer | (Kaladze, Wu et al. 2007), (Kaladze, Aburjania et al. 2004) |

| Ionosphere Disturbed Modes and Associated Spatial Scales and Epochs | | | | | | |
|---|---|---|---|---|---|---|
| **Mode of Disturbance** | **Driver/Vector** | **Index/ Unit** | **Spatial Scale** | **Temporal Scale** | **Region(s)/ Layers Affected** | **Reference/s** |
| Large scale zonal flows | Small scale magnetized Rossby waves | $m^{-3}$ $s^{-1}$ | Regional | | E layer | (Kaladze, Wu et al. 2007) |
| Heavy ion trough | $O^+$ depletion | $m^{-3}$ | Regional | | F layer | (Quegan, Bailey et al. 1982), (Rodger, Moffett et al. 1992) |
| Light ion trough | $H^+$ depletion | $m^{-3}$ | Regional | | F layer | (Quegan, Bailey et al. 1982), (Rodger, Moffett et al. 1992) |

*Table 3.1: A summary of disturbed modes in the ionosphere. Relevant literature is cited in the References column.*

## 3.5. Aspects of Ionosphere Dynamics and Structure of Particular Relevance

For the purposes of this study, ionospheric structure and dynamics, are of particular interest for the following reasons:

(1) The modelling of refraction and Faraday rotation at low radio frequencies requires knowledge of bulk properties of the ionosphere. In Chapter 4, I demonstrate the importance of understanding the ionosphere as a physical system. Many models, even those employed for purposes of astronomical instrument calibration, treat the ionosphere as merely a thin-shell (thin-

screen) that instantaneously acts on incoming radio waves, producing distortions to wave fronts. I will demonstrate that whereas the use of a thin shell representing the ionosphere can provide accurate determinations of, for example, Faraday rotation, the height at which the screen is placed is an important consideration. The value and local angle of the Earth's magnetic field varies with height but some models assume a height, which might lead to large errors in determinations of FR and therefore in this aspect of calibration of the MWA telescope.

(2) In Chapter 6, I describe the ionosphere over the MRO based on *in situ* measurements conducted over many years. Whereas the ionosphere in the mid-west, mid-latitude location of the MRO is well behaved, the requirement for understanding its dynamics over large intervals, due to imaging periods (up to months), requires an understanding of the ionosphere's dynamic properties.

(3) In Chapter 4 (Section 4.2), I propose a mechanism built on the International Reference Ionosphere model (IRI) by which the appropriate thin-shell height might be selected for accurate FR modelling under ambient conditions at a particular location and date/time.

The discussion in this chapter of the ionosphere is predicated on these interests.

## 3.6. Summary

(1) Though weakly ionised, the ionosphere contributes significantly to distortions of radio signals over a wide range of frequencies but particularly of interest to MWA radio astronomy in the 80 - 300 MHz frequency range.

(2) Table 3.2 summarises the electronic characteristics of the ionosphere by region (Egeland 1996):

| | | Electron Density | | |
|---|---|---|---|---|
| Region | Height (km) | Daytime ($m^{-3}$) | Nighttime ($m^{-3}$) | Ion/ Ionisation Sources |
| F2 | 200-400 | $10^{12}$ | $10^{11}$ | EUV, transport from below |
| F1 | 140-200 | $3x10^{11}$ | $10^{10}$ | EUV, auroral particles |
| E | 90 - 140 | $10^{13}$ | $10^{11}$ | EUV, auroral particles |
| D | 50 - 90 | $10^{9}$ | $10^{8}$ | EUV, cosmic rays |

*Table 3.2: Summary of the electron densities of recognised major ionospheric layers (Egeland 1996).*

(3) Behaviours of the ionosphere vary over a range of time scales (epochs) due to the many processes that govern the production and annihilation of charged species and are summarised in Table 3.1.

# 4. Modelling Ionospheric Effects on VHF Radio Waves.

The purpose of this chapter is to provide understanding of the ionosphere's influence on VHF radio waves, which requires knowledge of its extent and dynamics at any particular moment (Rawer 1993). Modelling the ionosphere in respect of low-frequency (VHF) radio astronomy however, provides insights into bulk properties that might lead to better characterisation with accuracy appropriate to instrument calibration (Mitchell, Greenhill et al. 2010). The principal objective of this chapter is to explore the implications of adding the depth dimension to a model ionosphere that is typically represented as a thin, phase screen (thin shell) (Mitchell, Greenhill et al. 2008, Helmboldt, Lazio et al. 2012, McFadden, Ekers et al. 2012, Sieradzki, Cherniak et al. 2013, Sotomayor-Beltran, Sobey et al. 2013). In respect of MWA calibration, the difference in the location of calibration sources, derived from catalogues of known positions and the observed locations of sources, are reconciled by applying appropriate offsets to the positions of latter. Models such as ionFR (Sotomayor-Beltran, Sobey et al. 2013), employ a thin shell in calculating the amount of FR imposed on radio signals. Such models are not only incapable of accounting for refraction, as demonstrated in this chapter but assume peak electron density heights that might not be appropriate at a given moment, also demonstrated here. Further, IonFR uses data provided by the *Centre for Orbit Determination in Europe* (CODE) and maps the global ionosphere incorrectly (discussed in Chapters 6 and 7).

This chapter will:

(1) develop an understanding of the contribution of a more realistic ionosphere to refraction and Faraday rotation,

(2) discuss the importance of accurate determinations of ionospheric electron content to realistic quantification of FR and

(3) compare the implications for FR of modelling the ionosphere as a thin-shell against an ionosphere that exhibits depth, permeated by a height-dependent magnetic field and electron density distribution.

Modelling is investigated using several cases. The first five present studies of the effects of ionospheric refraction. The simplest case, that of a homogeneous, slab (flat Earth) ionosphere, is studied first, stepping through a slab ionosphere exhibiting a free electron gradient. Next, cases of curved ionospheres exhibiting, in the first instance, a homogeneous electron profile and later, a curved ionosphere that exhibits an electron gradient are studied, followed by a comparative study of cases three and four. Whereas the first five cases involve refraction in declination (elevation), the sixth case involves refraction in right ascension, essentially a distinct process (Komesaroff 1960). Such a progression provides both the opportunity to explore fundamental questions regarding behaviour of radio waves transiting the ionosphere and reveals insights into the sophistication required of a model. The implications for FR is then studied and the issue of scintillation is discussed.

## 4.1. The Model Ionosphere.

Cases [1] and [2] consider a slab (flat) ionosphere. The first invokes a slab of uniform electron density and therefore, uniform refractive index $\mu_i$. The second employs a free electron profile derived from GPS TEC data and a modelled Chapman profile. For each of these cases, it will be seen that refraction is absent and each case is pursued no further. Cases [3] and [4], involve a curved ionosphere and refraction in elevation, equivalent to refraction in declination (Komesaroff 1960). Case [5] continues the comparison of cases [3] and [4] with a particular

geometry and case [6], involves refraction in right ascension. These are modelled in Mathematica in parallel to their development in this chapter. Mathematica routines developed are presented in Appendix 9.1.

However, prior to modelling the ionosphere, assumptions and approximations to a fully realised physical interpretation must be noted. These are dealt with first.

Calibration of the MWA is an operational requirement in real-time (Ord, Mitchell et al. 2010, Tingay, Goeke et al. 2012). Within the MWA's eight second cadence, the positional offsets of calibrators in the image field due to refraction are calculated against model positions and corrections applied across the entire field of view. For this purpose, the ionospheric contribution to position errors can be modelled as a thin shell in which the shell is stretched like a 2 dimensional membrane to correctly align calibrators with catalogue positions (Mitchell, Greenhill et al. 2008). I will demonstrate in this chapter however, that calibration performed employing this method, although adequate for self-calibration, is inadequate for calibration with respect to FR, which requires knowledge of both the absolute ionospheric TEC and the ionosphere's geometry.

### 4.1.1. The Lorentzian Plasma.

In calculating the ionosphere's refractive index, $\mu$, relevant properties of the ionospheric plasma must be settled upon. Most significant amongst these are the separate susceptibilities of ions and electrons to stimulation by electromagnetic radiation. Texts typically consider the ionosphere a homogeneous, positive space charge in which loosely bound electrons are freely excited by incoming electromagnetic radiation (Rawer 1993). Here, the vibrational frequency of electrons is of the order we are interested in for VHF radio astronomy. The

positively charged ions however, being three orders of magnitude more massive exhibit vibrational frequencies vastly below those of interest to radio astronomy. The characteristic plasma frequency, dependent on electrons only, is found as

$$f_{plasma} = \frac{e}{2\pi}\sqrt{\frac{Ne}{m_e\ \varepsilon_0}}, \tag{4.1}$$

where $e$ is the charge on the electron, $Ne$ the number of free electrons, $m_e$ the mass of the electron and $\varepsilon_0$ is the ionospheric dielectric constant. Clearly, the corresponding plasma frequency dependent on positively charged ions, is much lower (Budden 1985).

The ionosphere's phase refractive index is dependent on both the plasma frequency $f_{plasma}$ and the propagating frequency $f_{obs}$. Taking (4.1), the ionospheric phase refractive index $\mu_i$ is derived as

$$\mu_i = \sqrt{1-\left(\frac{f_{plasma}}{f_{obs}}\right)^2}. \tag{4.2}$$

The U.S. Department of Commerce publication *Ionospheric Radio Propagation*, (Davies 1990), lists ten properties ascribed to the ionosphere, including that of the respective contributions of electrons and ions. Others include an electrically neutral medium, statistically uniform charges such that no resulting space charge exists. Further, thermal motions of electrons are considered unimportant. In *The Propagation of Radio Waves*, K. G. Budden (Budden 1985) discusses the importance of thermal properties in respect of transient ionospheric disturbances. Consequently, as thermal effects are not considered, treatments of ray propagation in the ionosphere assume a slowly varying medium (that is, free of thermally induced, short time scale variations). Transient phenomena were observed however and are discussed in Chapter 6.

With the electron gas treated as a cold plasma, thermally induced electron oscillations are not considered. Further, Earth's magnetic field is not implicit in treatment of the ionosphere although assumes a significant role in the plasmasphere and magnetosphere. Ray tracing is confined to a vertical plane, which is unrealistic where the Earth's magnetic field is applied, as the direction of such field is only occasionally aligned such as not to cause rays to deviate from the plane. (However, in the analysis and discussion of Faraday rotation in this chapter, the Earth's magnetic field is necessarily accounted for.)

### 4.1.2. Group Velocity and Group Refractive Index.

It has been shown (Eqn. 4.2) that the plasma phase refractive index is a function of wave frequency and that the ionosphere is dispersive. As the ionosphere is a dispersive medium, even spectrally pure radio waves are broadened such that expressions employing a term for wave velocity in the medium must refer to the group (or envelope) velocity. This is applicable where the medium is not highly dispersive, which would result in the severe distortion of the group's modulation envelope. The relationship for the group refractive index $\mu'$ becomes

$$\mu' = \left(1 - \left(\frac{f_{plasma}}{f_{obs}}\right)^2\right)^{-\frac{1}{2}} \qquad [4.3]$$

Refractive index of the medium therefore, refers to the group refractive index.

### 4.1.3. The Troposphere

Many authors have studied the physical interaction of the atmosphere and the ionosphere to investigate energy budgets and coupling (Roble and Ridley 1994, Roble 1996, Taylor, Jahn et al. 1998, England, Immel et

al. 2010) including the use of a satellite based GPS receiver (as opposed to a satellite borne transmitter) (Liou, Pavelyev et al. 2006). However, one group investigated the contribution of the troposphere to refraction of radio waves (Daniell, Carrano et al. 2007). These researchers studied tropospheric refraction under quiet and disturbed conditions in the atmosphere, including the presence on two occasions of hurricanes and quiet and disturbed conditions in the ionosphere (storm enhanced density - SED). They concluded that above 10° elevation, the troposphere contributes very little to refraction effects. I have limited my research to elevations above 30° to limit multipath effects and therefore, neglect any effects of tropospheric refraction in modelling.

### 4.1.4. Chapman Theory and the Chapman Profile.

An electron profile is derived, in this instance, from the simplest that might be deduced from theory, a Chapman profile (Davies 1965). Ionospheric electron content is derived from measured GPS data. Peak TEC values are assigned, which then determine electron content at various altitudes through application of the Chapman profile. This profile in useful for illustrative purposes.

Chapman in 1931, developed a relationship with which to determine electron concentration, $N$(z), as a function of height above the ground. Chapman theory describes the simplest type of ionised layer that can be deduced from theoretical considerations (Davies 1965). This expression acknowledges the varying electron distribution within the ionosphere and became known as the Chapman Law (Feltens 2001), where

$$N_e(z) = N_m e^{\frac{1}{2}[1-z-e^{-z}]} \tag{4.4}$$

and

$$z = \frac{h - h_m}{H}. \tag{4.5}$$

$N_e$(z) is the electron density at any point along the Chapman Profile, $h$ is height above Earth's surface at which $N_e$ is to be quantified, $N_m$ is the maximum electron density of the Chapman Profile, $h_m$ is the height of maximum electron density $N_m$ above Earth's surface and $H$ is the scale height. Atmospheric temperature and mass density respectively are derived after the model NRLMSISE-00 for March 17th, 2013 and shown in Figures 4.1 and 4.2. The date used in modelling, March 17th, 2013, is significant, being the day a CME impacted the Earth. This event is described in Chapter 6.

Scale height (*H*) is that distance in the ionosphere over which electron density (in this case) falls by a factor of $\frac{1}{e}$. The fundamental formula for *H* is:

$$H = \frac{mg}{kT}, \tag{4.6}$$

where, in the case of an isotropic atmosphere of uniform composition, *m* is the mean molecular mass of the atmosphere, *g* is gravitational acceleration, *k* is Boltzmann's constant (1.38 x $10^{-23}$ J·K$^{-1}$) and *T* is the mean temperature of the atmosphere. At the surface of the Earth, *H* takes on values of the order 8.5 km.

At altitude, *H* takes on the approximation:

$$H \approx 0.848\left(1+\frac{h}{R_{Earth}}\right)^2 \frac{T}{m}, \tag{4.7}$$

where *h* is the height above the surface of the Earth, *T* is the atmospheric temperature and *m* is the local mean molecular mass of the atmosphere, as displayed in Figures 4.1 and 4.2.

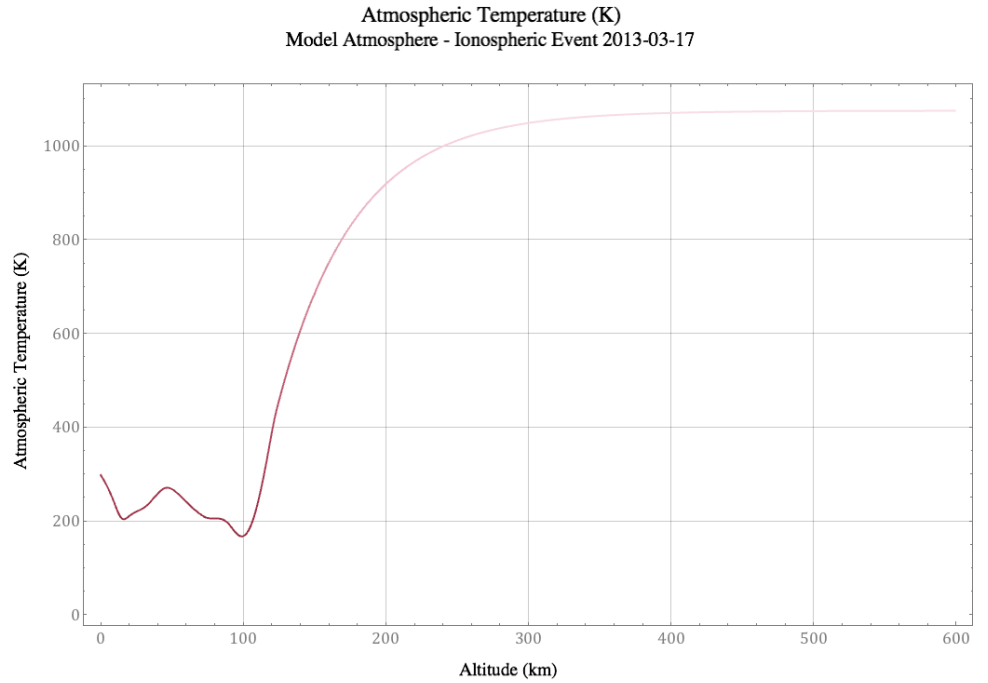


*Figure 4.1: Atmospheric temperature, $T_{Atmosphere}$, for March 17th, 2013, calculated using NASA's NRLMSISE-00 Atmosphere Model.*

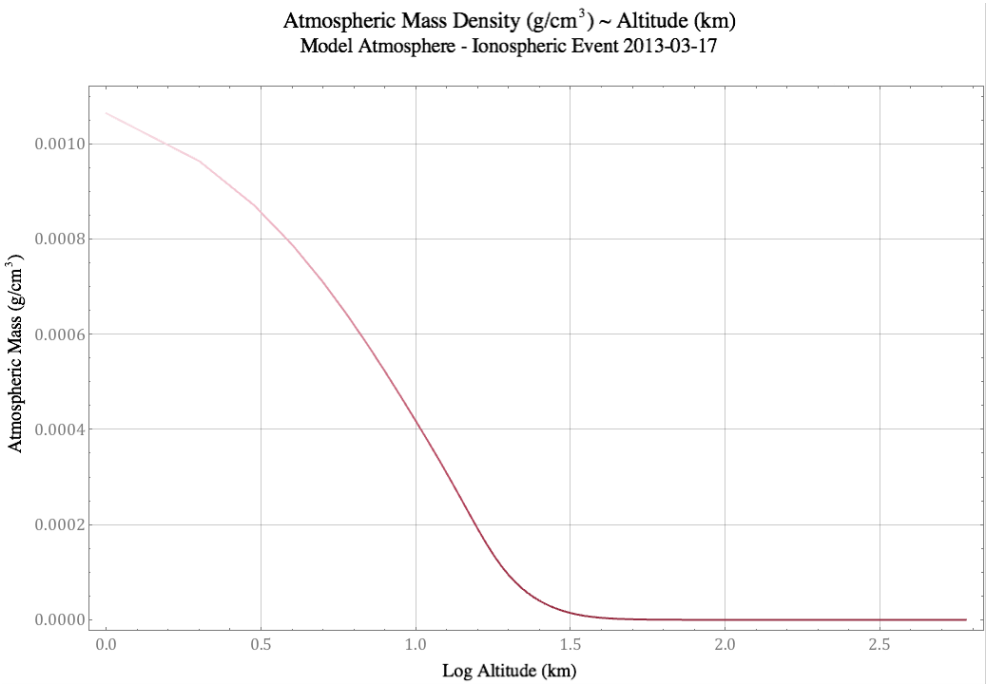


*Figure 4.2: Atmospheric mass density, $M_{Atmosphere}$, for March 17th, 2013, calculated using NASA's NRLMSISE-00 Atmosphere Model.*

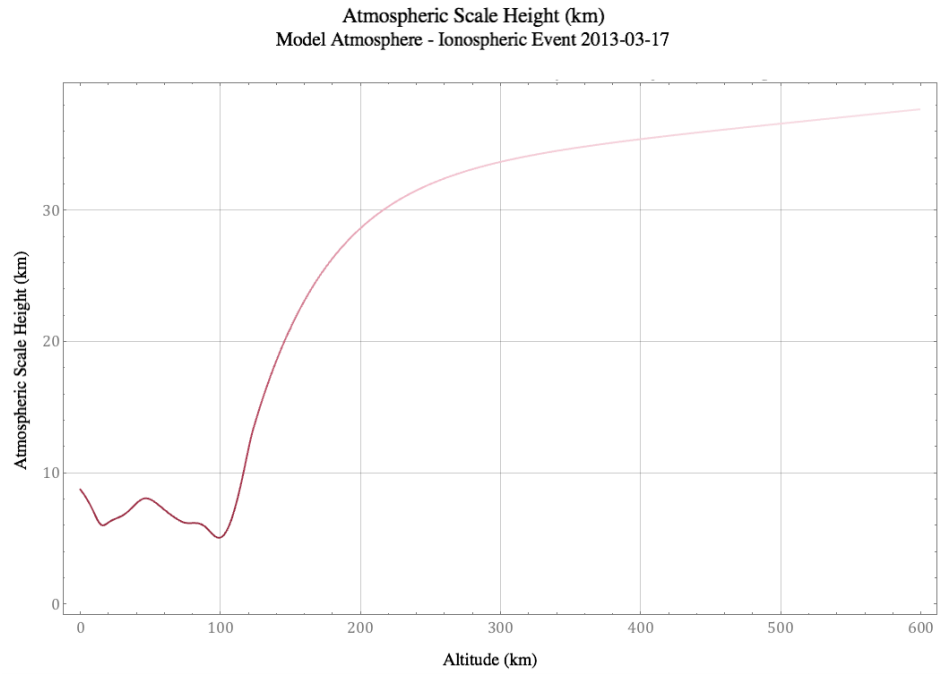


*Figure 4.3: Atmospheric scale height (H), that distance over which atmospheric density as returned by the model NRLMSISE-00, falls by 1/e.*

The relationships given in equations (4.1), (4.2) and (4.3) are used to create the Chapman profile for electron content in the ionosphere (Figure 4.4). This is a single layer profile that ignores the much smaller E layer contribution.

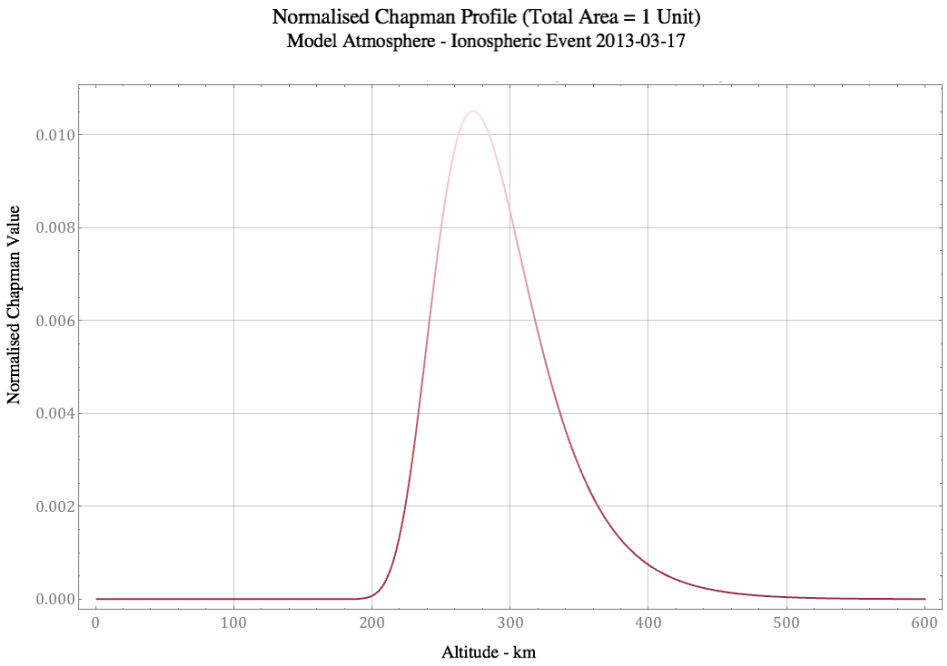


*Figure 4.4: A normalised Chapman profile which is employed in creating ionospheric electron profiles.*

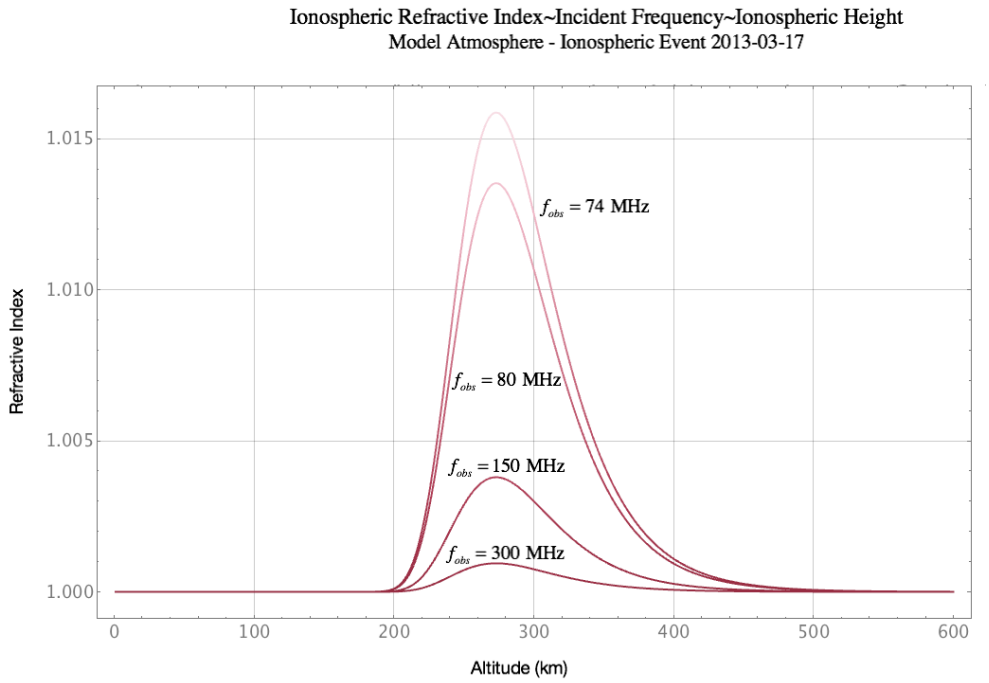


*Figure 4.5: Ionospheric refractive index at four radio frequencies over the MRO on 17th March 2013, employing a Chapman profile (Figure 4.6) applied to GPS derived TEC data.*

Figure 4.5 displays typical refractive index values derived from captured data and the derived Chapman profile (Figure 4.4), in this case over the MRO on March17$^{th}$, 2013.

The dates and location of data used in this chapter are noted where applicable.

### 4.1.5. Case [1] - Homogeneous, Slab Ionosphere.

The homogeneous, slab ionosphere is a familiar case. Radio astronomers often incorporate ionospheric effects as an even simpler case, that of a thin shell which is stretched in the plane of the ionosphere to accommodate differences in the apparent locations of calibration celestial objects (calibrators) with those provided by model positions (Williams, Hewitt et al. 2012). The case of a three-dimensional ionosphere however, has been discussed and evaluated, including in discussion central to the design of the MWA (Tingay, Goeke et al. 2012).

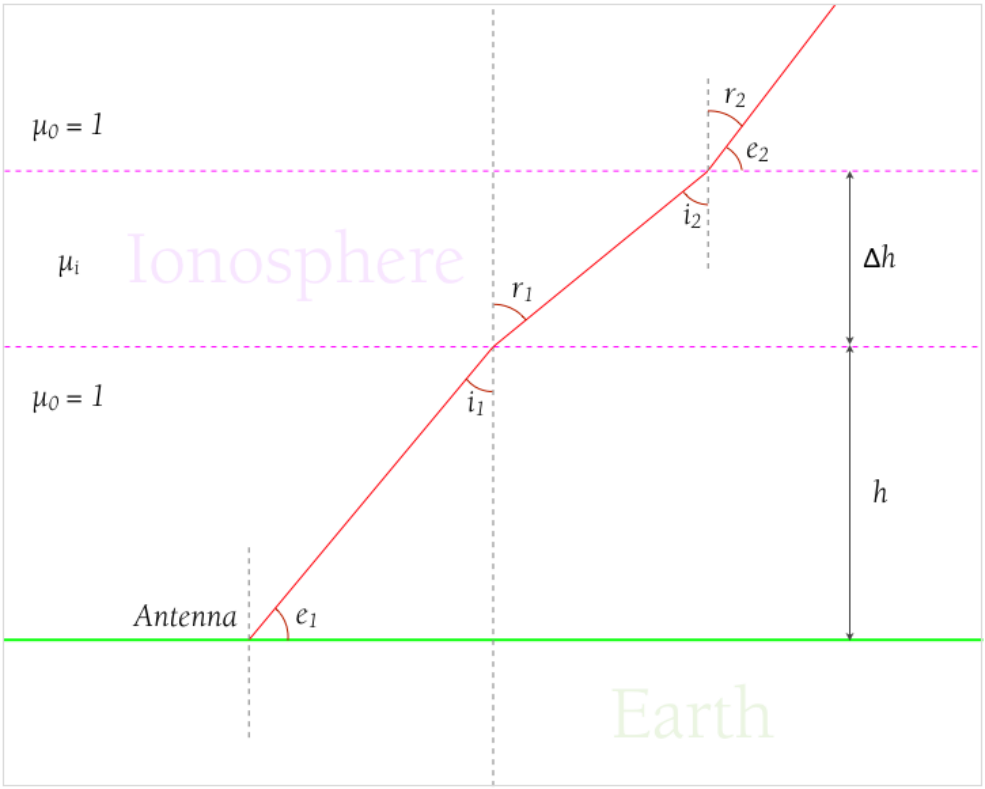


*Figure 4.6: Ray path through a homogeneous, plane ionosphere of thickness Δh at height h. Where horizontal gradients are ignored, there is no refraction observed in the transit of a radio wave through this ionosphere.*

In terms of ray tracing through the ionosphere however, Figure 4.6 illustrates the approach taken in this chapter. The ray path is regarded as commutable, with no distinction given to a ray received (or emitted) by the antenna, which is observing the ionosphere with an elevation $e_1$. The non-ionospheric refractive index $\mu_0$, both above and below the

ionosphere, is taken to have a value of 1.0. The refractive index of the ionosphere is arbitrary, taken here as $\mu_i$.

In each case, angle $e_1$ is the antenna elevation angle, $e_2$ is the ionosphere entry/exit elevation angle, $i_n$ is the incidence angle (taking the case looking outwards through the ionosphere) and $r_1$ and $r_2$ are the refracted angles. The distance $h$ is the height to the ionosphere above the Earth's surface and $\Delta h$ is the depth of the ionosphere or the depth of a layer within the ionosphere.

Here

$$i_1 = \frac{\pi}{2} - e_1, \tag{4.8}$$

$$\sin r_1 = \frac{\mu_i}{\mu_0} \sin i_1, \tag{4.9}$$

$$i_2 = r_1, \tag{4.10}$$

$$\sin r_2 = \frac{\mu_0}{\mu_1} \sin i_2 = \frac{\mu_0}{\mu_1} \sin r_1 = \frac{\mu_0}{\mu_1} \frac{\mu_1}{\mu_0} \sin i_1. \tag{4.11}$$

Therefore

$$r_2 = i_1 \text{ and } e_2 = e_1. \tag{4.12}$$

Refraction is not witnessed under this model of a ray transiting this particular model ionosphere.

### 4.1.6. Case [2] - Slab Ionosphere Featuring an Electron Profile.

Again, $\mu_0$ both above and below the ionosphere is taken to be 1.0. The electron density profile within the ionosphere is arbitrary. This case does not encompass horizontal gradients and so the ionosphere is

considered to change electron content slowly horizontally, rather than experiencing rapid changes associated with TIDs and SIDs for example.

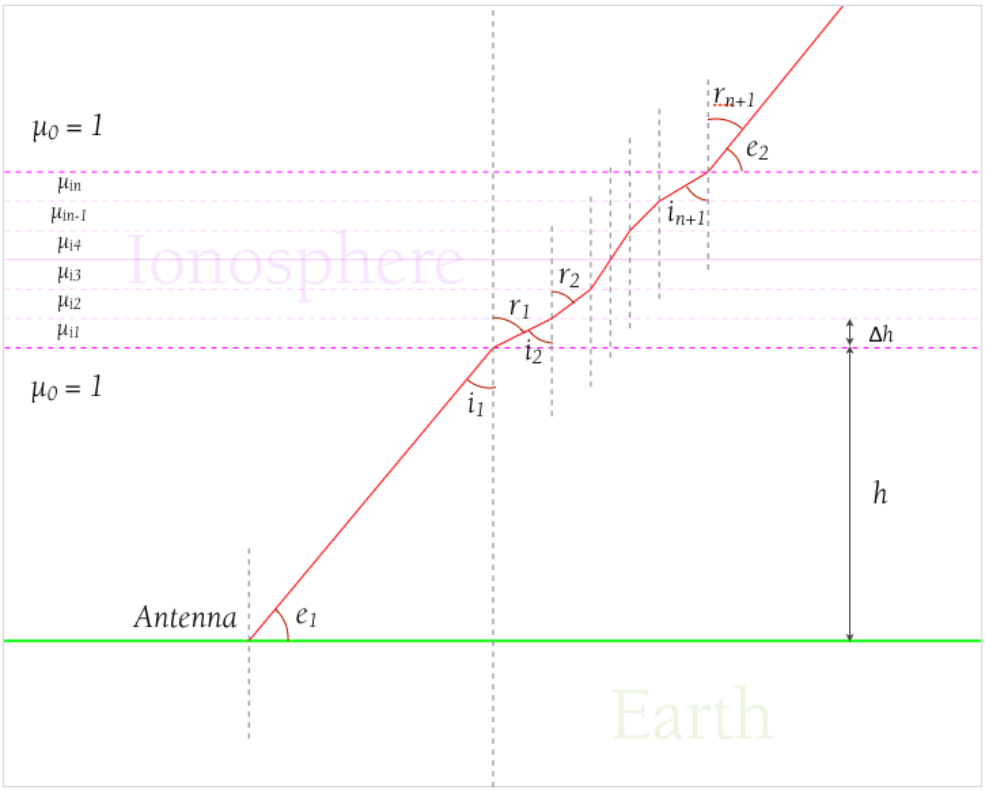


*Figure 4.7: Ray path through an inhomogeneous, plane ionosphere. With horizontal gradients ignored, there is no refraction observed in the transit of a radio wave through this ionosphere.*

Here

$$i_1 = \frac{\pi}{2} - e_1, \tag{4.13}$$

$$\sin r_1 = \frac{\mu_{i1}}{\mu_0} \sin i_1, \tag{4.14}$$

$$i_2 = r_1, \tag{4.15}$$

$$\sin r_2 = \frac{\mu_{i2}}{\mu_{i1}} \sin i_2 = \frac{\mu_{i2}}{\mu_{i1}} \frac{\mu_{i1}}{\mu_0} \sin i_1, \tag{4.16}$$

$$i_3 = r_2, \tag{4.17}$$

$$\sin r_3 = \frac{\mu_{i3}}{\mu_{i2}} \sin i_3 = \frac{\mu_{i3}}{\mu_{i2}} \frac{\mu_{i2}}{\mu_{i1}} \frac{\mu_{i1}}{\mu_0} \sin i_1, \tag{4.18}$$

$$i_4 = r_3, \tag{4.19}$$

$$\sin r_i = \frac{\mu_{ii}}{\mu_{ii-1}} \frac{\mu_{ii-1}}{\mu_{ii-2}} \ldots \frac{\mu_{i3}}{\mu_{i2}} \frac{\mu_{i2}}{\mu_{i1}} \frac{\mu_{i1}}{\mu_0} \sin i_1, \tag{4.20}$$

$$\sin r_i = \frac{\mu_{ii}}{\mu_0} \sin i_1, \tag{4.21}$$

$$\sin r_{n+1} = \frac{\mu_{in+1}}{\mu_0} \sin i_1. \tag{4.22}$$

However

$$\mu_{in+1} = \mu_0, \tag{4.23}$$

therefore

$$\sin r_{n+1} = \sin i_1, \tag{4.24}$$

$$r_{n+1} = i_1 \text{ and } e_2 = e_1. \tag{4.25}$$

Refraction is also not witnessed under this model of a ray transiting the ionosphere.

### 4.1.7. Case [3] - Curved, Homogeneous Ionosphere.

In the case of a curved Earth and ionosphere, polar coordinates are employed in determining ray paths to the antenna *O* from a source at infinity. Figure 4.8 shows the resulting model with *O* located at a distance *a* from the centre of the Earth *C*. Subsequently, *a* is taken as the radius in all calculations. A ray's lower ionosphere penetration point $P_1$ ,shown in Figure 4.9, forms an angle $i_1$ with a normal at that point to the surface of the earth. This ray is refracted at an angle $r_1$ to the same

normal. The point at which a ray penetrates the upper ionosphere $P_2$ forms an angle $i_2$ to a normal at the earth's surface. The associated refracted ray forms an angle $r_2$ to the same normal. The ionosphere's refractive index $\mu_i$ is an arbitrary value.

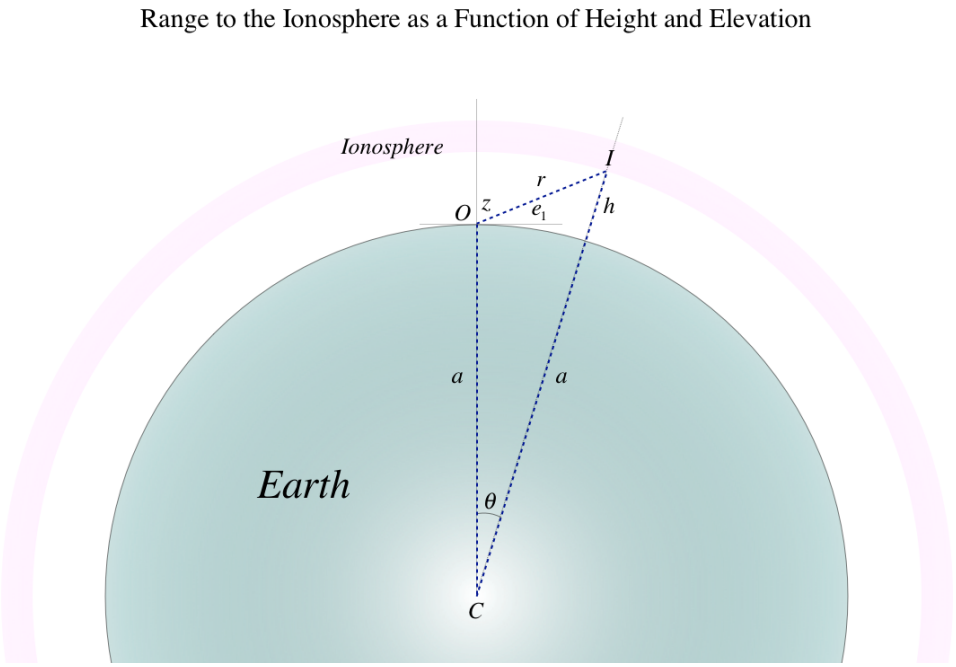


*Figure 4.8: Range to the ionosphere from the centre of the Earth as a function of height and observation elevation.*

Point Q (Figure 4.9) is the apparent (imaginary) location of the observer (antenna) to a vector coincident with the upper, extra-ionospheric ray when extrapolated to the ground and which produces an angle e2 to the normal at the surface of the earth at that point.

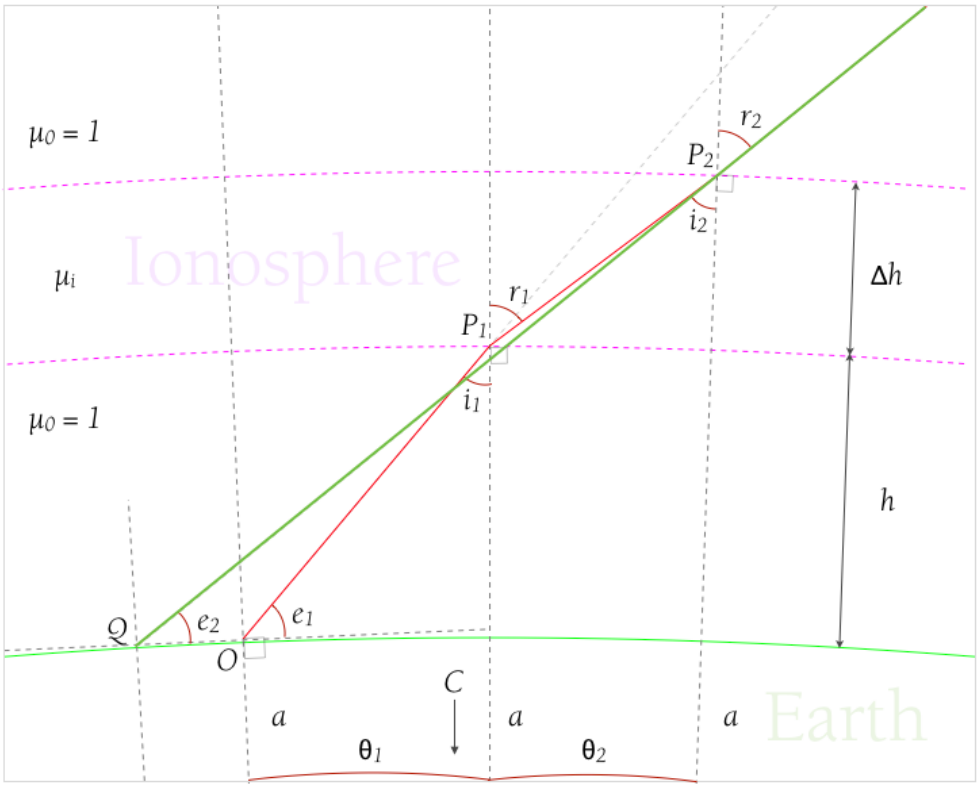


*Figure 4.9: Ray path through a homogeneous, curved ionosphere.*

The law of sines is used with Figure 4.9 to find $i_1$. For the triangle formed by $P_1OC$:

$$\frac{\sin i_1}{a} = \frac{\sin(e_1 + \frac{\pi}{2})}{a+h}, \tag{4.26}$$

therefore

$$i_1 = \sin^{-1}(\frac{a}{a+h}\cos e_1). \tag{4.27}$$

The law of sines is used also to find $i_2$. For the triangle formed by $P_2P_1C$:

$$\frac{\sin i_2}{a+h} = \frac{\sin(\pi - r_1)}{a+h+\Delta h}, \tag{4.28}$$

$$i_2 = \sin^{-1}(\frac{a}{a+h+\Delta h}\cos e_1). \tag{4.29}$$

Further, $r_1$ and $r_2$ can be given in terms of $i_1$ and $i_2$ respectively:

$$\sin r_1 = \frac{\mu_i}{\mu_0}\sin i_1, \tag{4.30}$$

giving

$$r_1 = \sin^{-1}(\frac{\mu_i}{\mu_0}\sin i_1) \text{ and} \tag{4.31}$$

$$\sin r_2 = \frac{\mu_0}{\mu_i}\sin i_2, \tag{4.32}$$

giving

$$r_2 = \sin^{-1}(\frac{\mu_0}{\mu_i}\sin i_2). \tag{4.33}$$

Refraction therefore, at $P_1$ is a function of $\mu_i$ and $i_1$ and at $P_2$, a function of $\mu_i$ and $i_2$ such that:

$$\delta r_{P_1} = r_1(\mu_i, i_1) - i_1 \text{ and} \tag{4.34}$$

$$\delta r_{P_2} = r_2(\mu_i, i_2) - i_2. \tag{4.35}$$

The total refraction, $\delta r$ , of the ray is found as:

$$\delta r = \delta r_{P_1} + \delta r_{P_2} = (r_1 - i_1) + (r_2 - i_2), \tag{4.36}$$

leading to a relationship for $\delta r$ :

$$\delta r = -\sin^{-1}(\frac{a\cos(e_1)}{a+h}) + \sin^{-1}(\frac{a\cos(e_1)\mu_1}{(a+h)\mu_0})$$

$$+\sin^{-1}(\frac{a\cos(e_1)}{a+h+\Delta h}\cos(e_1)) - \sin^{-1}(\frac{a\cos(e_1)\mu_1}{(a+h+\Delta h)\mu_0}), \tag{4.37}$$

where $\delta r$ is a function of known parameters, $a$, $h$, $\Delta h$, $e_1$, $\mu_0$ and $\mu_1$, each of which may be varied to assess their respective impacts on the resulting $\delta r$, as shown in Figures 4.10 to 4.12.

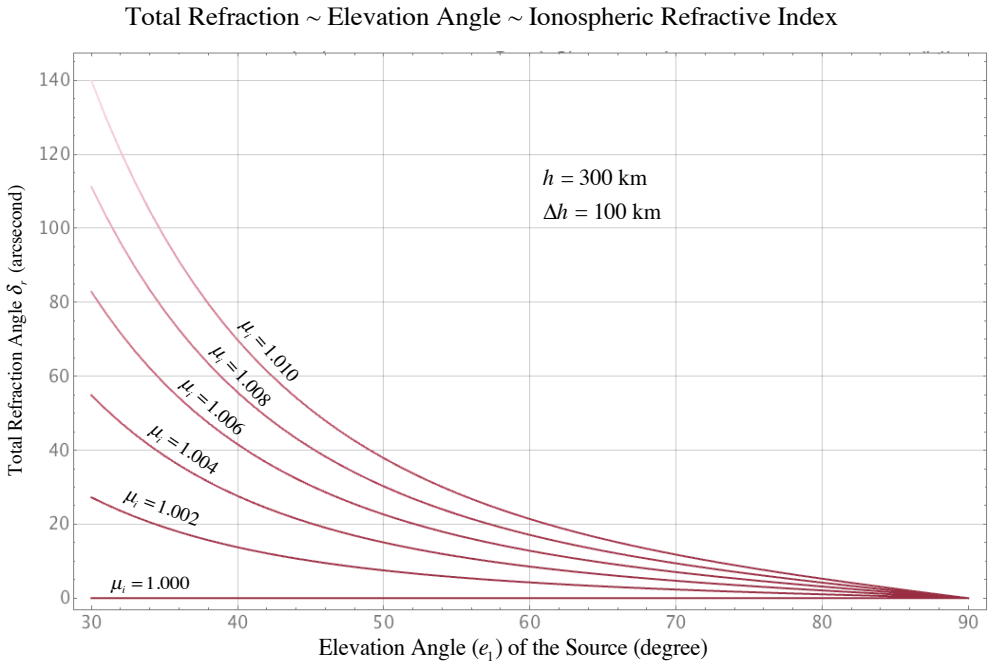


*Figure 4.10: Refraction occurring for a ray passing through a homogeneous, curved ionosphere as a function of refractive index, elevation angle ($e_1$) ionosphere height (h) and depth ($\Delta h$).*

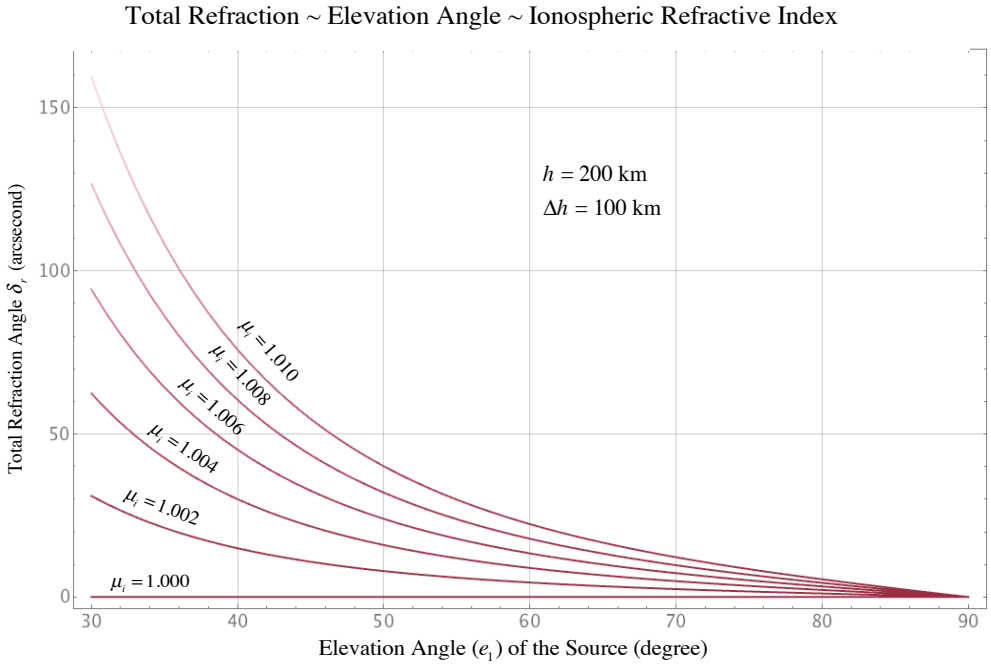


*Figure 4.11: Refraction occurring for a ray passing through a homogeneous, curved ionosphere as a function of refractive index, elevation angle ($e_1$) ionosphere height (h) and depth ($\Delta h$).*

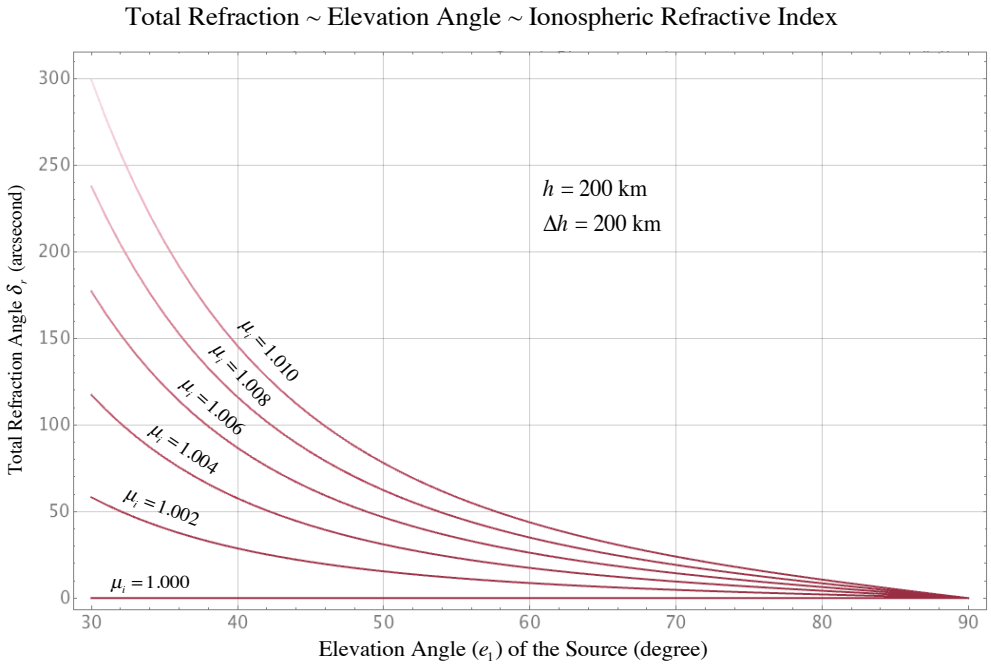


*Figure 4.12: Refraction occurring for a ray passing through a homogeneous, curved ionosphere as a function of refractive index, elevation angle ($e_1$) ionosphere height (h) and depth (Δh).*

Figures 4.10, 4.11 and 4.12 demonstrate that aspects of the geometry of even a homogeneous ionosphere, such as the height and depth, lead to significant differences in the effective refractive index and the associated refraction.

A major issue in employing a homogeneous, curved ionosphere, even where the TEC is known, is the assigned ionospheric depth. Volumetric electron number densities depend on the ionosphere's depth. Figure 4.13 features an ionosphere, the depth of which was determined by the Chapman profile produced previously (Figure 4.4).

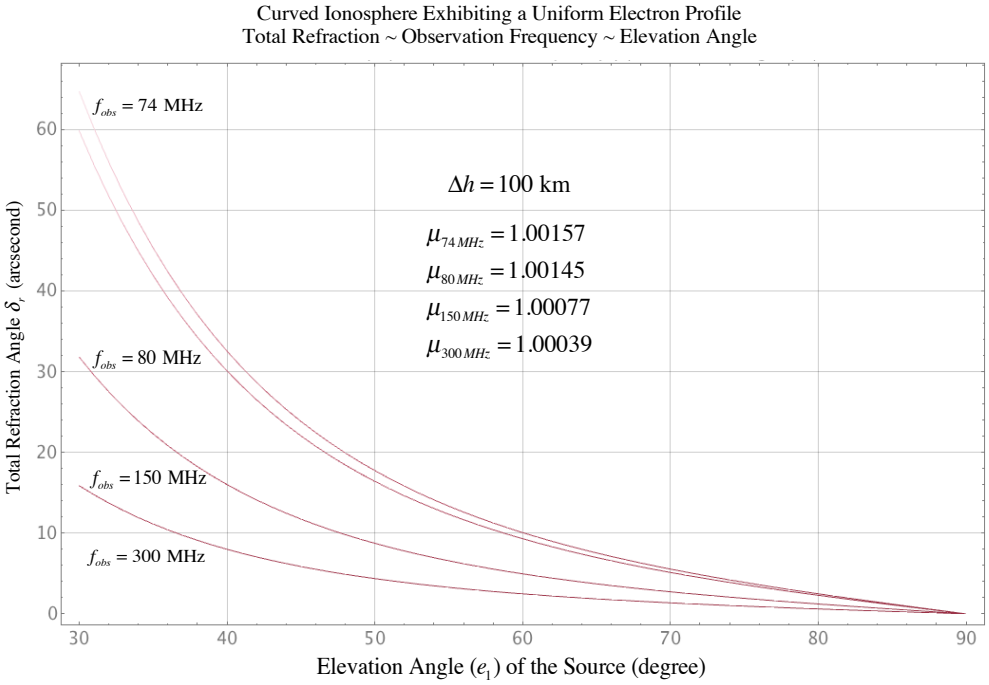


*Figure 4.13: Refraction as a function of wave frequency for a depth calculated for a given electron content and depth determined from the previously calculated Chapman profile (see Figure 4.6) and associated refractive indices.*

The effective, uniform electron number density is four orders of magnitude less than the peak value returned by Chapman theory for an inhomogeneous ionosphere, $10^8$ $m^{-3}$ as opposed to $10^{12}$ $m^{-3}$. The findings of this case and the following case (Case 4) are compared and consequences for the MWA studied in Section 4.1.9.

The next case investigates the outcome of providing the ionosphere an electron gradient, based on Chapman theory.

### 4.1.8. Case [4] - Curved Inhomogeneous Ionosphere Featuring an Electron Density Profile.

In the case of a curved ionosphere that features a varying refractive index profile due to a varying electron density, the ionospheric profile might be treated as a series of ($n$) layers, as shown in figure 4.14. Each discrete ionospheric layer would exhibit a separate refractive index $\mu_j$ ,where $1 \leq j \leq n$.

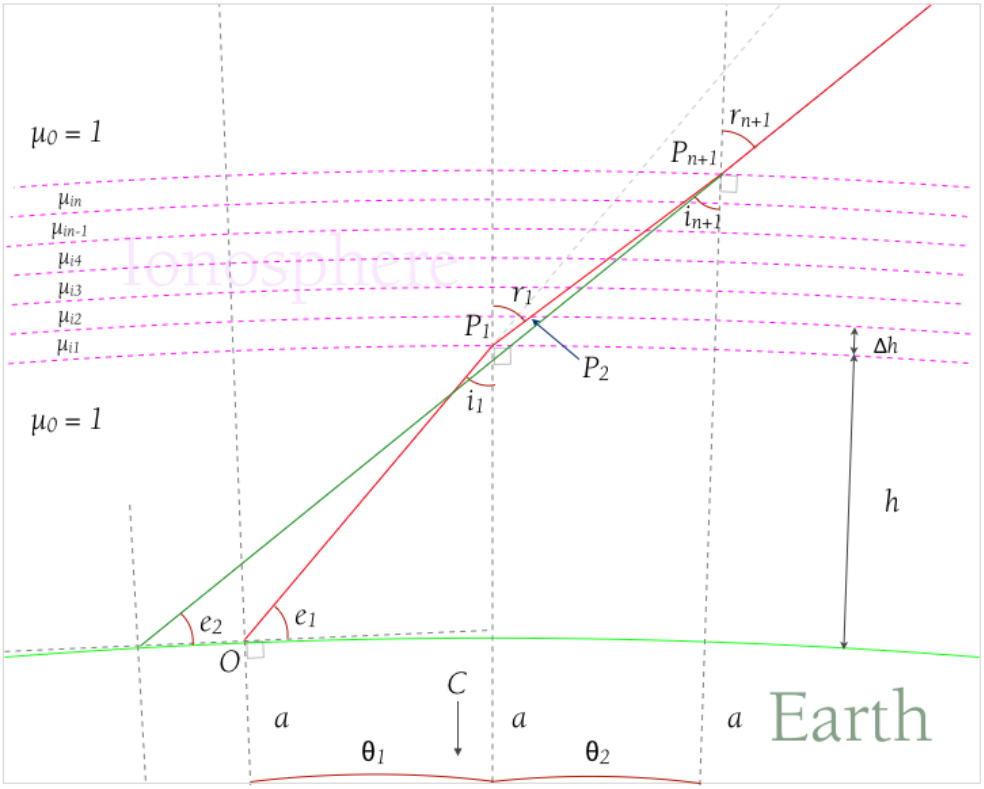


*Figure 4.14: Ray path through a curved ionosphere that exhibits structure in TEC.*

As in the previous case of a curved, homogeneous ionosphere, the law of sines is used in determination of the value of the angle $i_1$, that angle which a ray propagating from the observer (O) produces with a normal to the Earth's surface below. For the triangle formed by $P_1OC$:

$$\frac{\sin i_1}{a} = \frac{\sin(e_1 + \frac{\pi}{2})}{a+h}, \tag{4.38}$$

therefore

$$i_1 = \sin^{-1}(\frac{a}{a+h}\cos e_1). \tag{4.39}$$

From this relationship, $r_i$ can be found as:

$$\sin r_1 = \frac{\mu_i}{\mu_0}\sin i_1, \tag{4.40}$$

giving:

$$r_1 = \sin^{-1}(\frac{\mu_i}{\mu_0}\sin i_1). \tag{4.41}$$

Again, the law of sines is also used in determination of the value of the angle $i_2$. However, the triangle formed by $P_2P_1C$ is that which is separated from $P_1OC$ by a change in height of incremental $\Delta h$, being equivalent to the depth of the ionosphere divided by $n$, the number of ionospheric layers. For the next layer:

$$\frac{\sin i_2}{a+h} = \frac{\sin(\pi - r_1)}{a+h+\Delta h}, \tag{4.42}$$

$$i_2 = \sin^{-1}(\frac{a}{a+h+\Delta h}\cos e_1). \tag{4.43}$$

Further, $r_2$ can be given in terms $i_2$:

$$\sin r_2 = \frac{\mu_0}{\mu_i}\sin i_2, \tag{4.44}$$

giving:

$$r_2 = \sin^{-1}(\frac{\mu_0}{\mu_i}\sin i_2). \tag{4.45}$$

Refraction therefore, at $P_1$ is a function of $r_1(\mu_i, i_1)$ and $i_1$ and at $P_2$, a function of $r_2(\mu_i, i_2)$ and $i_2$ such that:

$$\delta r_{P_1} = r_1 - i_1 \text{ and} \tag{4.46}$$

$$\delta r_{P_2} = r_2 - i_2. \tag{4.47}$$

An iterative process is then followed to determine subsequent values of $\delta r$, such that:

$$\delta r = \delta r_{P_1} + \delta r_{P_2} + \delta r_{P_3} + ... + \delta r_{P_n} + \delta r_{P_{n+1}}, \tag{4.48}$$

or expressed as a sum as:

$$\delta r = \sum_{n=1}^{k} \delta r_{P_n}, \tag{4.49}$$

where *n+2* is equal to the number of layers into which the ionosphere is divided. The refractive index of the layers is as shown in Figure 4.15.

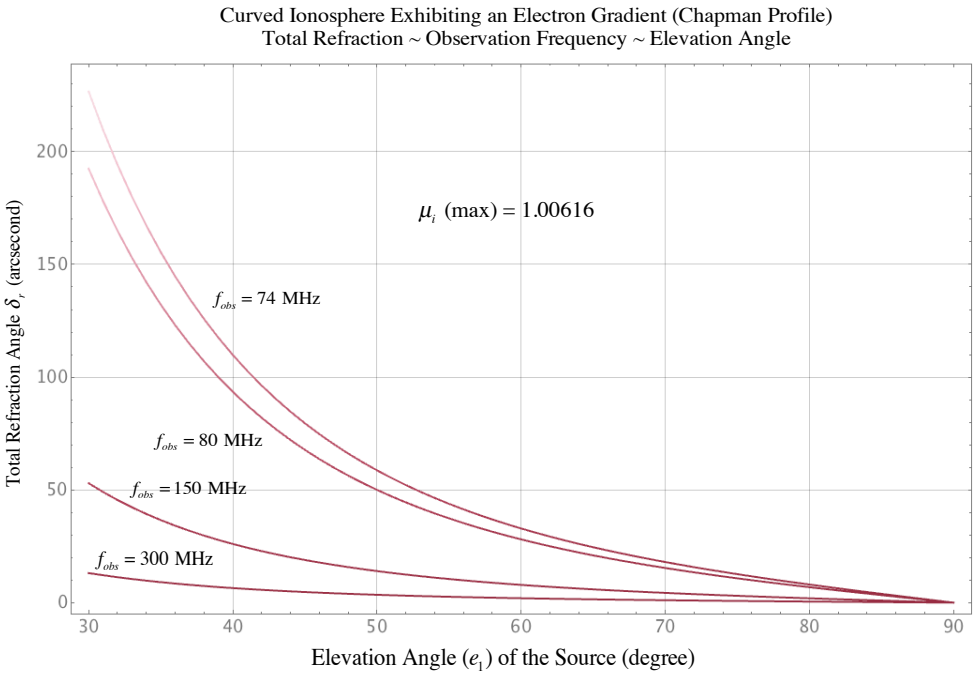


*Figure 4.15: Ionospheric refractive index at four radio frequencies over the MRO on 17th March 2013, employing a Chapman profile (see Figure 4.6) applied to GPS-derived TEC data.*

### 4.1.9. Cases [3] and [4] Compared and Implications for the MWA.

Cases [3] and [4], those involving a curved ionosphere of homogeneous electron profile and structured profile respectively, have been studied in detail. I have demonstrated that refraction even through a slab ionosphere exhibiting an electron gradient does not take place.

One issue when comparing curved, homogeneous and inhomogeneous ionospheres is choosing appropriate depths ($\Delta h$) and electron content (TEC) for each. The TEC in each case must be equivalent. However, the chosen ionospheric thickness, in the case of the homogeneous ionosphere, determines electron number density at any particular point, whereas the model chosen to describe the ionosphere in the inhomogeneous case pre-determines the profile and therefore, the effective depth of the ionosphere. Here, values of aTEC that were consistent with those on a particular day were used (March 17$^{th}$, 2013). This day will be used in further studies. As a consequence, markedly differing amounts of refraction are imparted on transiting radio waves (Figures 4.13 and 4.15). Refractive indices necessarily differ, however, corresponding values can be found in each plot. To further illustrate the differing regimes, a special case is studied.

Ionospheric refraction in the case of a curved ionosphere featuring a Chapman profile is compared with angular resolution of the MWA in Table 4.1.

| MWA | | Ionosphere Featuring a Chapman Profile | |
|---|---|---|---|
| Angular resolution 3 km array at 150 MHz | Angular resolution 3 km array at 200 MHz | Refraction at 150 MHz and 50° Elevation | Refraction at 300 MHz and 50° Elevation |
| 2’ | 1’ | 15’ | 3’ |

*Table 4.1: A comparison of the angular resolution of the MWA when construction is complete, at a maximum separation between elements (tiles) of 3 km and refraction in a modelled ionosphere (Chapman profile) at similar frequencies and observations at 50° elevation.*

At the highest frequency studied (300 MHz) and at 50° elevation, ionospheric refraction is three times larger than the angular resolution of the MWA, rising to an order of magnitude at 150 MHz.

### 4.1.10. Case [5] - Curved Homogeneous Slab and Curved Inhomogeneous Symmetrical Ionospheres Exhibiting Equivalent aTEC.

A curved single slab with a TEC of 50 TECU, a midpoint height of 300 km and a $\Delta h$ of 100km, extends from 250 to 350 km. It is homogeneous and will have an electron density $N_e$ of

$$N_e = \frac{TEC}{\Delta h} = 5 * 10^{12} m^{-3}. \quad (4.50)$$

This is compared with a 5 layer curved inhomogeneous ionosphere, symmetrical about the midpoint height and of 50 TECU with the following parameters:

250 to 270 km - TEC of 5 TECU.
270 to 290 km - TEC of 10 TECU.
290 to 310 km - TEC of 20 TECU [$N_e = TEC / \Delta h = 10.0 * 10^{12} m^{-3}$].
310 to 330 km - TEC of 10 TECU.
330 to 350 km - TEC of 5 TECU.

The study frequency of 182 MHz corresponds to the frequency at which events were observed in the ionosphere using the MWA and which are discussed here and in Chapter 6.

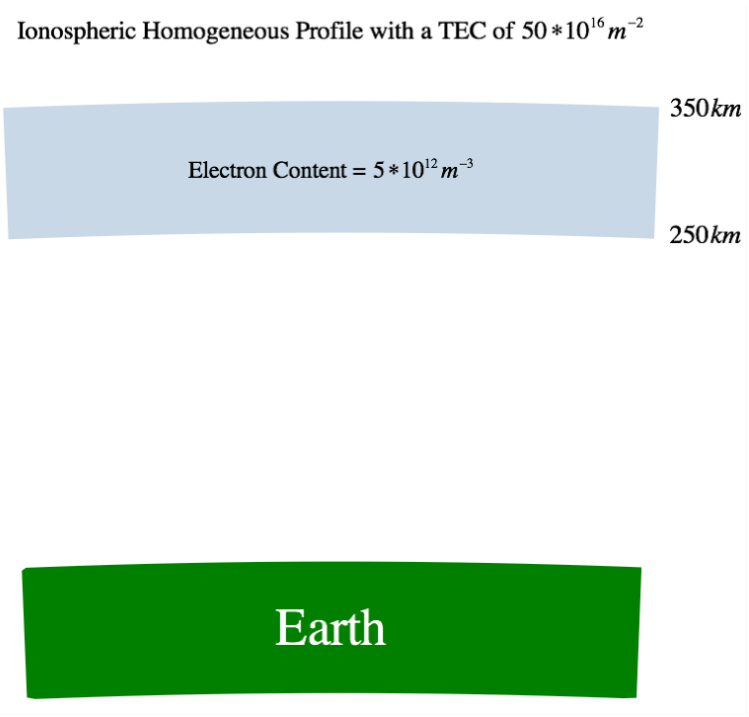


*Figure 4.16: Form of a curved, homogeneous ionosphere of aTEC of 50 TECU.*

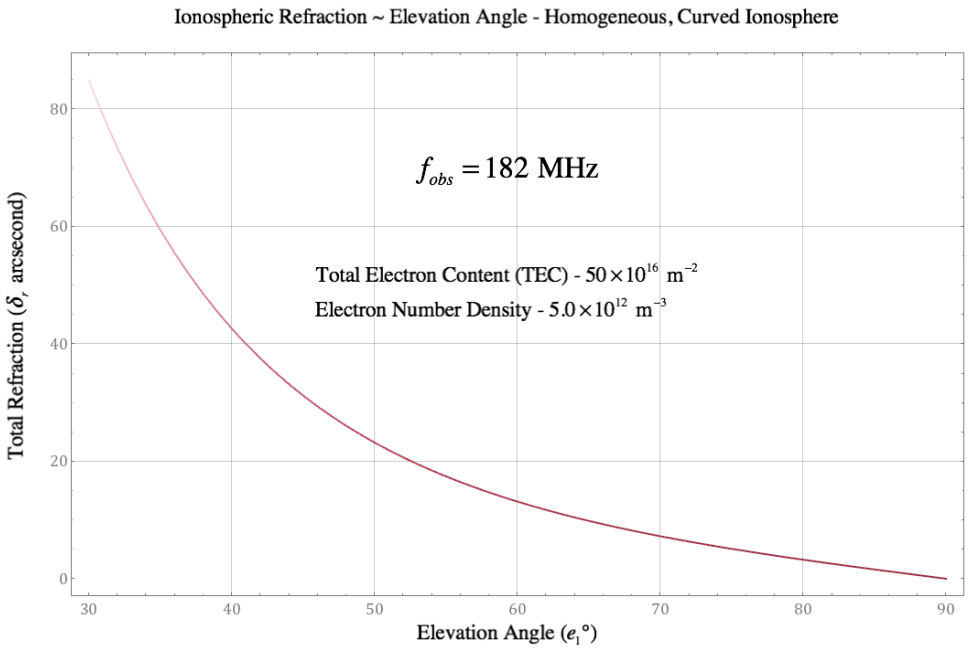


*Figure 4.17: Refraction in a curved, homogeneous ionosphere of aTEC of 50 TECU.*

The curved, homogeneous ionosphere in this example, takes on the form given in Figure 4.16 and the associated refraction is given in Figure 4.17. The curved, inhomogeneous ionosphere, takes on the form given in Figure 4.18. and the associated refraction is given in Figure 4.19.

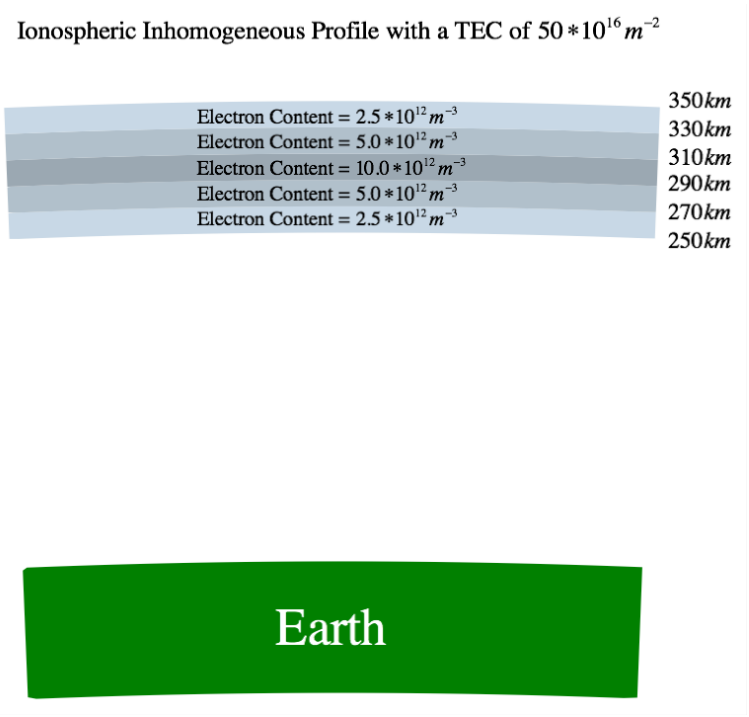


*Figure 4.18: Form of a curved, inhomogeneous ionosphere of aTEC of 50 TECU*

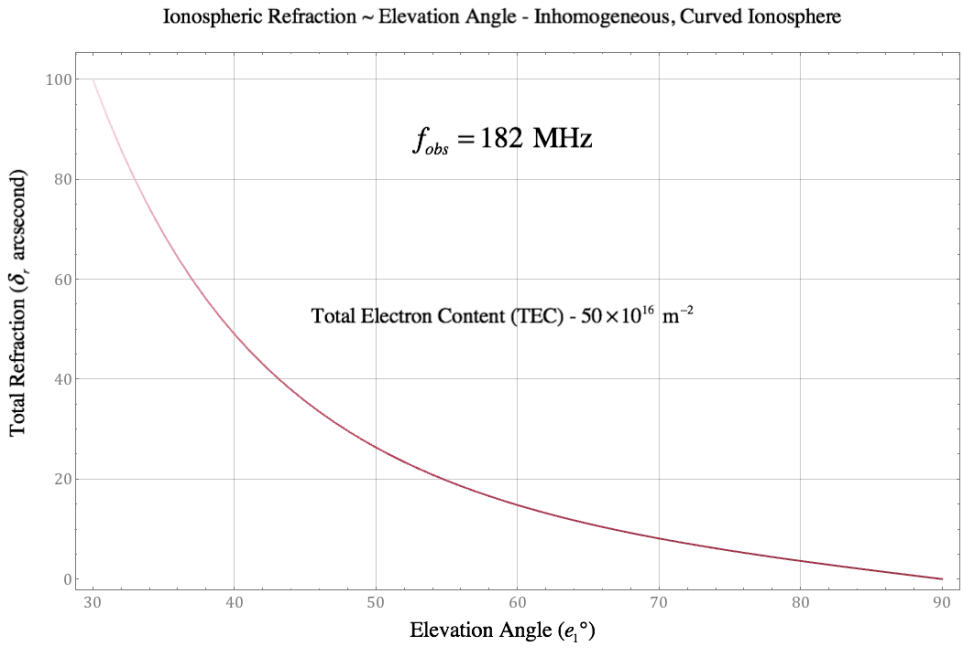


*Figure 4.19: Refraction in a curved, inhomogeneous ionosphere of aTEC of 50 TECU.*

As shown in Figure 4.20, over the elevation range 50° to 85°, refraction in a curved, inhomogeneous ionosphere is greater than that in a curved, homogeneous ionosphere of identical extent by approximately 12% to 13.5% for an aTEC value of 50 TECU and an observation frequency of

182 MHz. The case for use of an inhomogeneous profile is seen clearly in this result.

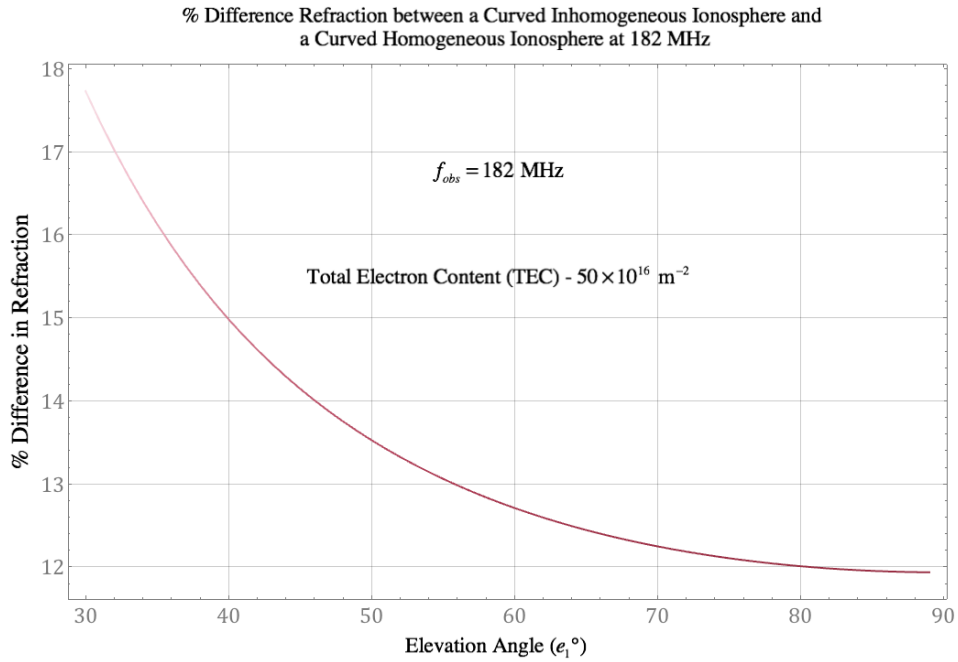


*Figure 4.20: % Difference in the Refraction in a curved, inhomogeneous ionosphere of aTEC of 50 TECU ~ a curved, homogeneous ionosphere of aTEC of 50 TECU.*

### 4.1.11. Case [6] - Refraction in Right Ascension.

In his paper *Ionospheric Refraction in Radio Astronomy*, M. Komesaroff commented that to a first order, refraction in right ascension depends only on changes in total electron content of the ionosphere in an east-west direction (Komesaroff 1960). Excursions in TEC in this direction are principally associated with tTIDs.

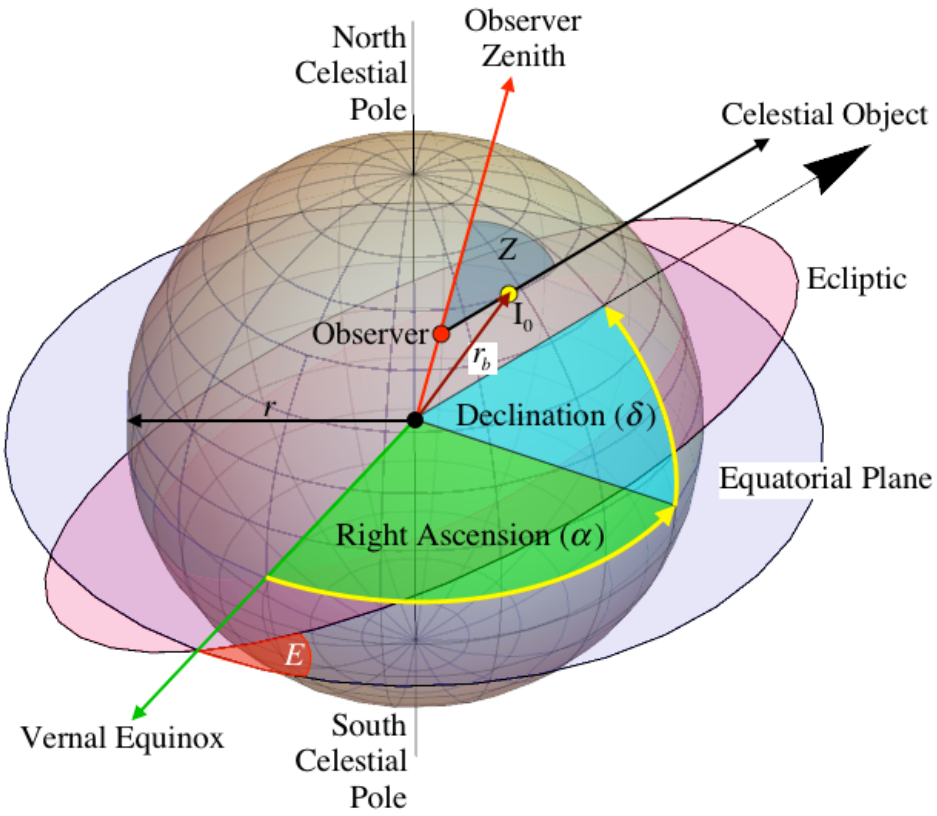


*Figure 4.21: Parameters employed in discussing refraction in right ascension (RA) due to horizontal, time varying gradients in the electron content of the ionosphere. One proposed cause for such gradients is the effect of travelling ionospheric disturbances (TIDs). The ecliptic (E) is inclined at 23.4° to the equatorial plane.*

Here, changes in right ascension may be found as

$$\Delta(\alpha) = \frac{d \bullet \varpi(\sigma) \sec\delta \bullet \sec\varphi_a \sec k_{0m}}{2(r_b + \frac{3d}{2}) f^2} \bullet \frac{\partial(f_c^2)}{\partial L}, \qquad (4.51)$$

where $\alpha$ is right ascension, $\delta$ is declination, $\varphi_a$ is the latitude of the upper ionospheric penetration point $k_{0m}$ is the angle between the ray tangent and radius vector (which is the point in the ionosphere where $k_{0m}$ is being measured). $r_b$ is the radius of the lower ionospheric bounding surface (at $I_0$), $d$ is the ionosphere's total effective thickness, $f$ is the observation frequency, $c_f$ is the F layer critical frequency and $L$ is the longitude to the east of the observer. The function $\varpi(\sigma)$ is found as

$$\varpi(\sigma) = \frac{3}{4\sigma}\{[\frac{1+\sigma}{2\sigma^{\frac{1}{2}}}]\ln[\frac{1+\sigma^{\frac{1}{2}}}{1-\sigma^{\frac{1}{2}}}]-1\}, \tag{4.52}$$

and $\sigma$ is found as

$$\sigma = \frac{f_c^2}{f^2}\sec^2 k_{0m}. \tag{4.53}$$

I will show in chapter 6 that TIDs are important drivers of ionosphere variability at levels that cause significant FR and therefore, loss of polarisation knowledge of an electromagnetic wave over a variety of timescales ranging from minutes to hours and longer.

### 4.1.12. Case [7] - The Perturbed Ionosphere.

On 15th October 2013, transient events in the ionosphere produced aberrations in a sequence of observations produced by the MWA (discussed in Section 6.3). At an observation frequency of 182 MHz, a consistent 160 arcsec bifurcation of radio sources was observed at an R.A. ≈ 23 hr 19 m 48 s, Dec. ≈ -27° 30' and an elevation of 74° between the times of 21:44 and 23:18 local time (UTC +8 hours).

Figure 4.22 displays the image of a source captured during the observations. This event provided the motivation to perturb the model ionosphere using a numerical model developed in this chapter in an attempt to reproduce conditions that would replicate this event. Figure 4.23 displays the refraction in an unperturbed, inhomogeneous ionosphere for a range of TEC values for a propagating 182 MHz signal. The numerical modelling shows that the refraction observed in the MWA images isn't apparent in this ionosphere at elevations above ~36.4° and a TEC of 150 TECU. Therefore, an unperturbed ionosphere of this geometry is not capable of producing the observed refraction at the observation elevation and the maximum TEC values encountered during the course of this work.

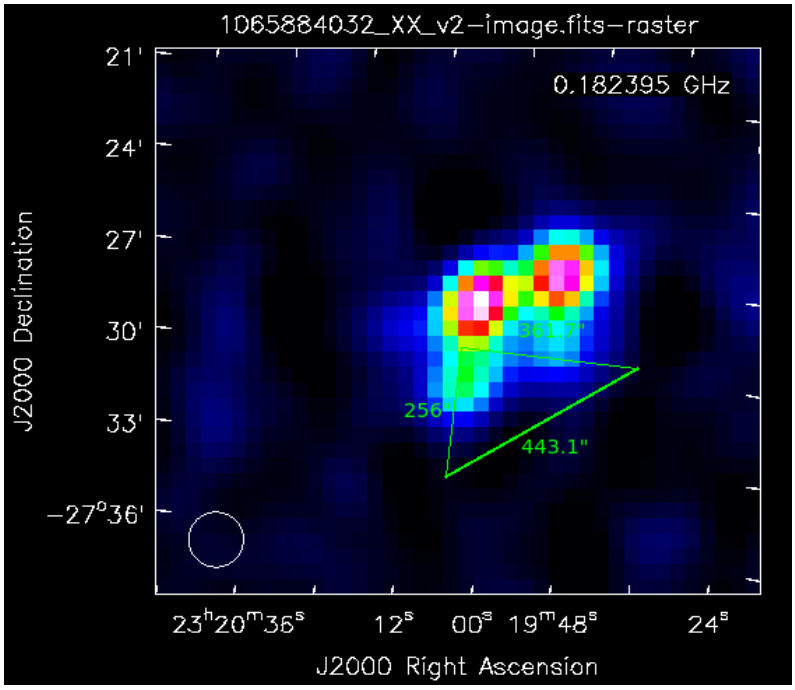


*Figure 4.22: Observed bifurcated celestial source on the evening of 15th October 2013. (Image captured by N. Hurley-Walker, CIRA)*

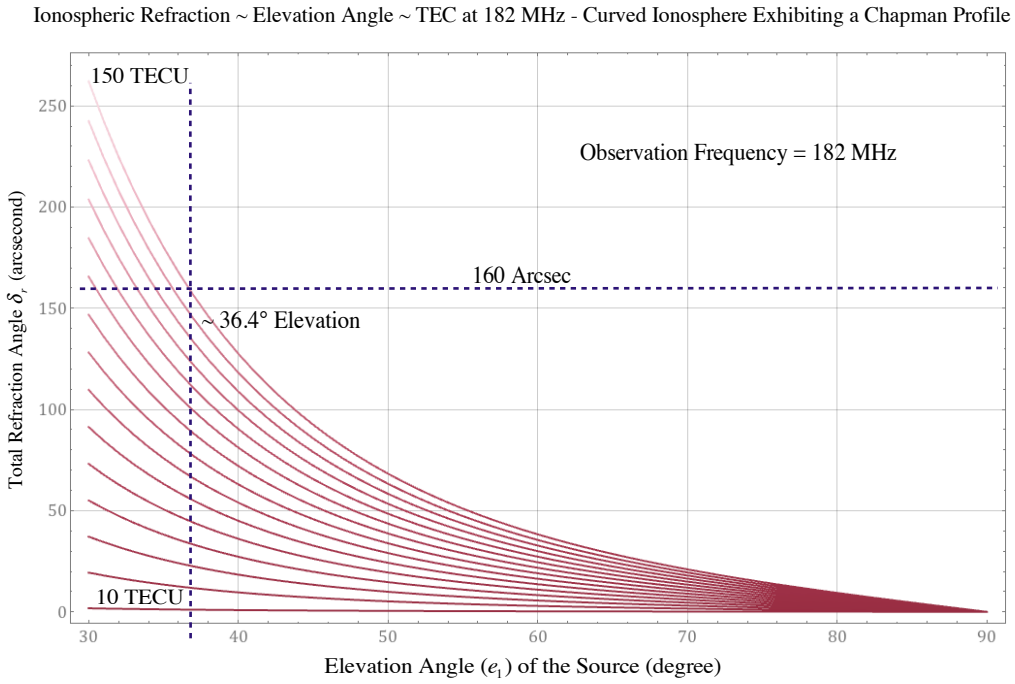


*Figure 4.23: Ionospheric refractive index at an observation frequency of 182 MHz in a curved, inhomogeneous ionosphere displaying a Chapman profile with TEC values ranging from 10 TECU to 150 TECU. Refraction observed on the evening of 15th October 2013 was equivalent to that which would have been encountered at elevations below ~36.4° at TEC levels of 150 TECU, an unrealistic TEC value.*

In attempting to further explore, via modelling, other forms of perturbation to the ionospheric electron density, I chose the simplest form of perturbation, that of a spherical region of enhanced TEC so that ray tracing could be readily performed (Figure 4.24, eqn. 4.54). Another geometry, that of a thick convex lens, was investigated also.

One would expect that a TID might realistically be characterised by a local gradient in electron density (e.g. Figure 4.42) rather than a uniform region as modelled here. However, Figure 4.23 demonstrates that a realistic increase in TEC alone could not account for the observed refraction. Other, more sophisticated geometries could be employed with further effort. However, these would be unlikely to better illustrate the issue (He, Li et al. 2012, He, Xia et al. 2013).

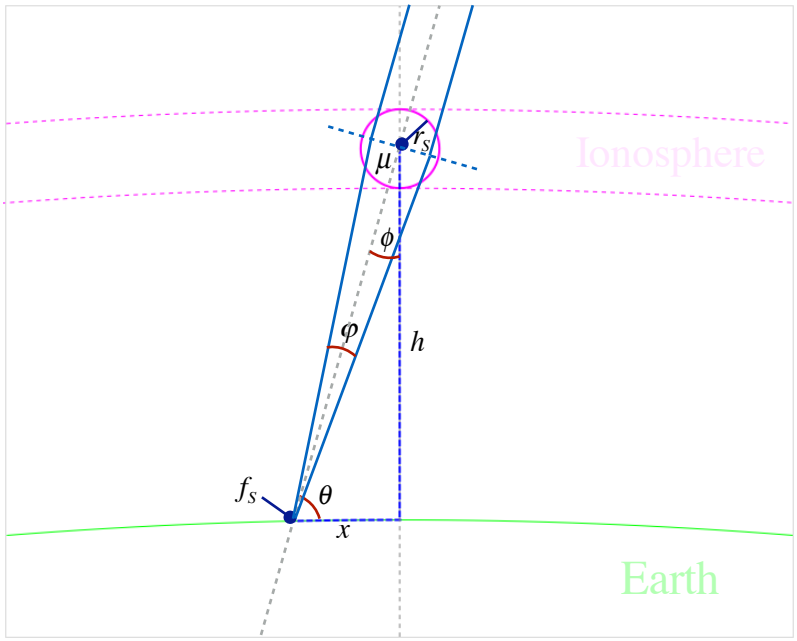


*Figure 4.24: Geometry for paraxial ray tracing through a spherical TEC enhanced region of the ionosphere. The circle shows the localised region of the ionosphere that may be modelled with a progressively enhanced electron density.*

In Figure 4.24, a paraxial ray bundle (solid blue lines) of a width determined by the angle $\varphi$ that is equivalent to the observed bifurcation of the image (160 arcsec) and the height $h$ of the spherical region above the Earth's surface is brought to a focus $f_S$. The elevation of the observation $\theta$ was 74°. Here, $\mu$ is the uniform refractive index of the

spherical region and the radius of the region is $r_s$. There would doubtless be a region preceding and trailing that in Figure 4.24, of increasing electron density and decreasing electron density respectively, however, a region of altered geometry in the electron profile is necessary to produce the observed refraction. During observations, $f_s$ did not necessarily coincide with the observer (MWA tiles), a distance *x* from the zenith point of the irregularity, however, this geometry was chosen to demonstrate the capability of an irregularity to produce the observed bifurcation of the celestial object. The formula for finding the focal point of a spherical lens, as found in optics texts such as that by Hecht and Zajac, is given in equation 4.54:

$$f_S = \frac{\mu r_S}{2(\mu - 1)}. \tag{4.54}$$

Here, $f_s$ is the focal length of a spherical lens, $\mu$ is the lens' refractive index (group refractive index for VHF radio waves in a dispersive medium) and $r_s$ is the radius of the spherical lens. Equation 4.55 describes the case of a similar, convex lens, where two convex surfaces are separated by a distance *d*, the thickness of the lens:

$$f_{TL} = \frac{1}{\left((\mu - 1)\left(\frac{1}{r_1} - \frac{1}{r_2} + \frac{(\mu - 1)d}{\mu * r_1 * r_2}\right)\right)}. \tag{4.55}$$

Here, $f_{TL}$ is the focal length of a thick convex lens, $\mu$ is the lens' refractive index and $r_1$ is the radius of the spherical lens toward observer (telescope) and $r_2$ is the radius of the lens toward the stellar object and is a negative value for a convex lens.

With the goal therefore, of producing the necessary refraction (160 arcsec) required to create the observed bifurcated image (Figure 4.22), the group refractive indices required of the disturbed regions are found by solving Equation 4.3 (page 74) for $f_{plasma}$, where $\mu$' is found from Equations 4.5 and 4.6 (page 102) for the 2 cases and by solving

Equation 4.1 (page 73) for *Ne*. Inserting into these equations arbitrary, though realistic values for $h$ and $r_s$, produces the group refractive indices of the perturbing regions.

Taking $h$ = 320 km, being a typical height to the peak of the ionospheric electron density (Figures 4.27 and 4.28), $f_s$ = 409 km for an observational elevation $\Theta$ of 74°. Taking $r_s = 50$ km results in $\mu'$ = 1.049. Applying the same parameters where appropriate to the case of a thick lens (eqn. 4.55), with radii $r_1$ = 50 km and $r_2$ = -50 km (by convention for a biconvex lens) and $d$ = 50 km, $\mu'$ = 1.063. On 13th October 2013, between 21:00 and 23:00 local (UTC + 8 hr), local TEC ≈ 10 TECU (Figure 6.44 (iv)). This corresponds to;

$$Ne_{ambient} = 1.00 \times 10^{12} \text{ electrons/m}^3.$$

The solution to Equations 4.1 and 4.3 with respect to *Ne* gives:

$$Ne = \frac{4\left(-\varepsilon_R {f_{OBS}}^2 m_e \pi^2 + \varepsilon_R {f_{OBS}}^2 m_e \pi^2 {\mu_{REGION}}^2\right)}{e^2} \qquad [4.56]$$

Therefore, for the spherical perturbation (Figure 4.24, eqn. 4.54),

$$Ne_{spherical} = 4.59 \times 10^{13} \text{ electrons/m}^3.$$

For the lenticular perturbation (eqn. 4.55),

$$Ne_{lenticular} = 5.64 \times 10^{13} \text{ electrons/m}^3.$$

Therefore, the higher electron density perturbing regions needed to exhibit 46 times higher *Ne* than the ambient level in the case of the spherical perturbation and 56 times higher *Ne* than the ambient level in the case of the lenticular perturbation. While these values are perhaps unrealistic in the unperturbed ionosphere, SEDs have been shown to produce comparable excursions in electron density (Oberoi and Lonsdale 2012). Therefore, the case is strongly supported by evidence, that perturbations of specific geometries were capable of perturbing the ionosphere (Figure 4.22) the amount required to observe the distortions in the images that were evident.

## 4.2. Faraday Rotation.

Faraday rotation (FR) is a phenomena whereby the plane of polarisation of linearly polarised waves rotate as they propagate in a dispersive medium. FR is an angular quantity and takes the units of radian. In this thesis, the amount of FR experienced by a signal is often expressed in quantities of π radian, where 1 π radian corresponds to a rotation of 180° and is easily visualised. Many, many revolutions are often experienced by a signal, which also is more easily pictured in quantities of π radian. The two characteristic waves comprising an electromagnetic wave, the ordinary and extraordinary waves, exhibit differing phase velocities when propagating in a magnetised, conductive medium. These separate delays cause the associated linear plane of polarisation to rotate. The amount of rotation experienced depends on the wavelength of the propagating wave. However, the component experienced in common by all electromagnetic waves is known as the rotation measure (*RM*), which is found (Oberoi and Lonsdale 2012) as

$$RM = \frac{e^3}{8\pi^2 \varepsilon_0 m^2 c^3} \int Ne \, \boldsymbol{B} \bullet \boldsymbol{ds} \text{ (radians/m}^2\text{)}. \tag{4.57}$$

In the case of trans-ionospheric propagation, the term *Ne* refers to the electron content of the medium encountered by the transiting wave and ***B*** the magnetic field experienced. Therefore, where functions describing *Ne* and the ***B*** for a given increment in altitude along the line-of-sight (LOS) are known, the RM can be determined. Numerically, this may be found as

$$RM = \frac{e^3}{8\pi^2 \varepsilon_0 m^2 c^3} \sum_{h=1}^{n} Ne_h \, \mathrm{B}_h \cos(\theta) \sec(z_h') \Delta s, \tag{4.58}$$

where $Ne_h$ is the electron content of the ionosphere at height *h,* $\mathrm{B}_h$ is the magnetic field amplitude at *h*, $z_h'$ is the local zenith angle of the LOS path at altitude and $\theta$ is the difference between the LOS and the Earth's

local magnetic dip angle, which at the location of the MWA is ~60.1°. Therefore, $\theta$ at zenith is ~30° or π/6 radians. The value of $\theta$ changes very slowly with altitude (<0.5°) over the altitude range of interest here, being 1000 km (Table 4.1).

At a given altitude, $z$' is found as

$$\sin(z'_h) = \frac{a}{a+h}\sin(z_h), \qquad [4.59]$$

where $z$ is the initial zenith angle at each step, $a$ is the radius of the Earth and $h$ is the altitude at each increment (Figures 4.7, 4.25).

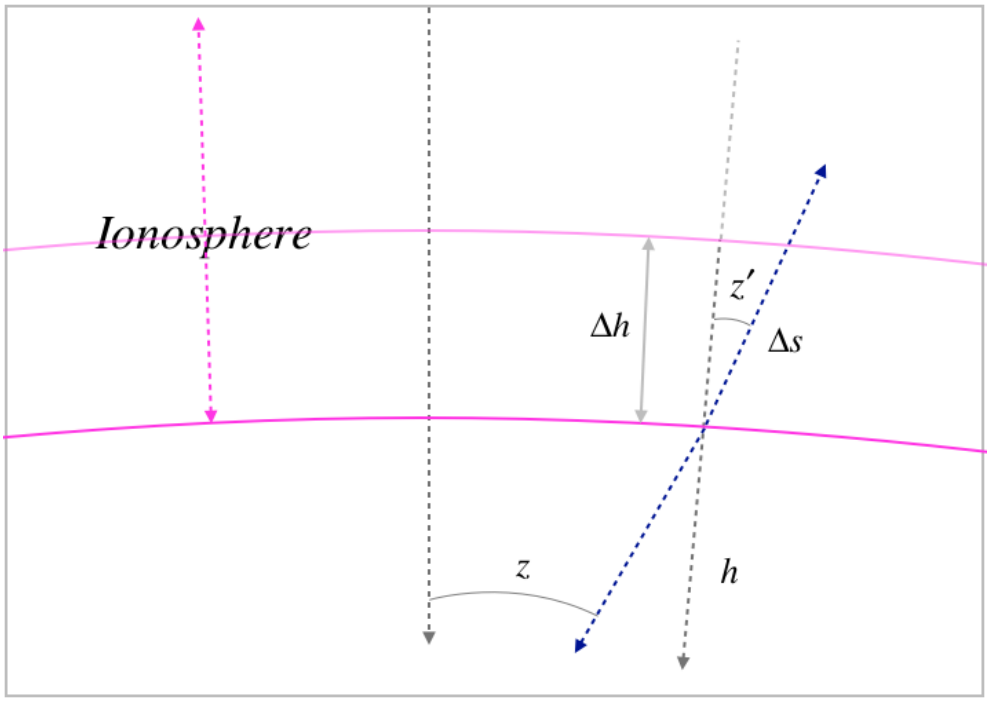


*Figure 4.25: Zenith angle (z) to the LOS (•••) is dependent on location in the ionosphere and must be re-calculated at every step in determining FR.*

FR is the product of the RM and the square of the observation wavelength, found as

$$FR = RM * \lambda^2 . \qquad (4.60)$$

The $\lambda^2$ dependence of FR on incoming signals means that VHF radio astronomy is particularly susceptible to the degrading effects of the

ionosphere on image quality. Close attention therefore is given here to the issue of FR in constraining image quality. In this section, a comparison is made between the FR at MWA frequencies calculated using an ionosphere featuring depth and an ionosphere treated as a thin-shell. In modelling FR under regimes appropriate to VHF radio astronomy, an ionosphere treated as a thin-shell, which is a two-dimensional screen conforming to and above the surface of the Earth and onto which the entire electron content of the ionosphere, plasmasphere and magnetosphere is assigned, is employed almost universally, (McFadden, Ekers et al. 2012, Oberoi and Lonsdale 2012, Sieradzki, Cherniak et al. 2013, Sotomayor-Beltran, Sobey et al. 2013). Others dismiss the ionospheric contribution to FR in studies, claiming small contributions, which in the case of much higher frequencies (Mao, Gaensler et al. 2008) is justified. In his PhD dissertation, Opperman (Opperman 2007) questioned the use of a fixed height, thin-shell model as used by CODE (450 km fixed) and investigated varying shell heights.

The problem is studied in this section as a comparison of outcomes from modelling the ionosphere as (i) a thin-shell, (ii) as a profile generated by the IRI-2012 ionosphere model (http://iri.gsfc.nasa.gov) and (iii) as a Chapman profile that I generated previously from first principles. It will be demonstrated here that the thin-shell model finds close agreement with the other two approaches but only when the screen height is varied in altitude, according to changes in the structure of the ionosphere.

### 4.2.1. FR in an Ionosphere Featuring an Electron Density Profile.

Two electron density profiles are developed. One conforms to a Chapman profile that I developed from first principles, discussed in Section 4.1.4 (Figure 4.4). The second was produced by running the online version of IRI-2012 (http://omniweb.gsfc.nasa.gov/vitmo/iri2012_vitmo.html) with appropriate parameters (see Table 4.2).

*Table 4.2: Parameters and associated values used in producing an ionospheric profile under the IRI-2012 model.*

| Parameter | Value |
|---|---|
| Date | 17th March 2013 |
| Coordinates Type | Geographic |
| Latitude | -26.984 |
| Longitude | 116.535 |
| Height | 1000 km |
| Start | 80 km |
| Stop | 1000 km |
| Step size | 1 km |

The Chapman profile used to model the ionospheric electron content was studied earlier in this chapter in refraction studies (Figures 4.4 and 4.5). Figure 4.26 shows the profile in ionisation.

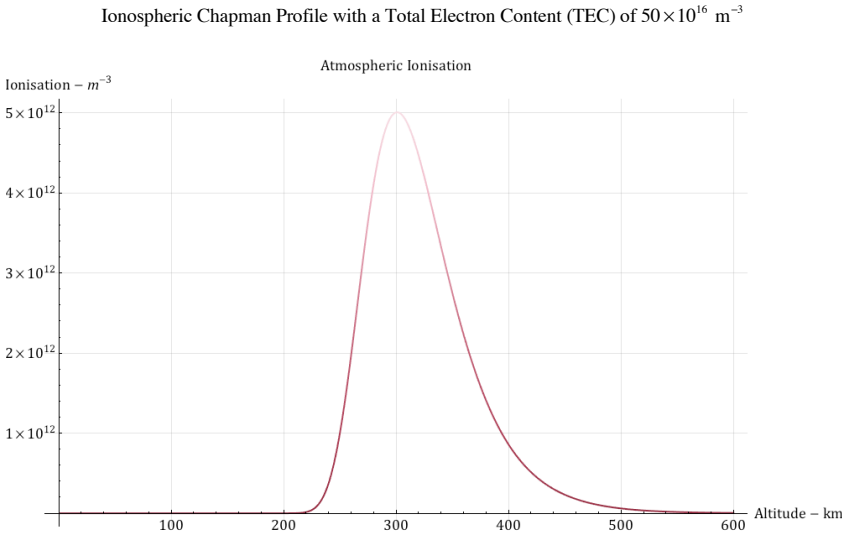


*Figure 4.26: A Chapman profile produced for ionospheric TEC used in comparison to profiles produced using IRI-2012 and a thin-shell approximation.*

The International Reference Ionosphere is a long established and respected (Bilitza, Altadill et al. 2014) ionospheric model. Most papers,

many referenced here previously, refer to the model in discussing FR and ionospheric TEC. Figures 4.27 and 4.28 display outputs of the model over each hour of the day 17th March 2013 at the MRO.

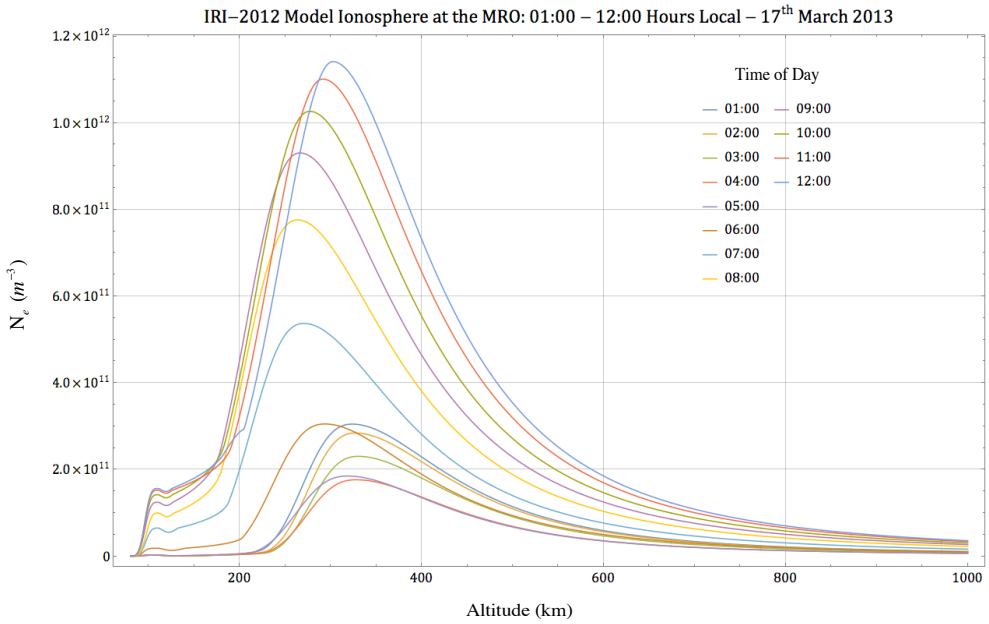


*Figure 4.27: Ionospheric TEC profiles for the first 12 hours of 17th March, 2013, produced for the site of the MRO under the IRI-2012 model.*

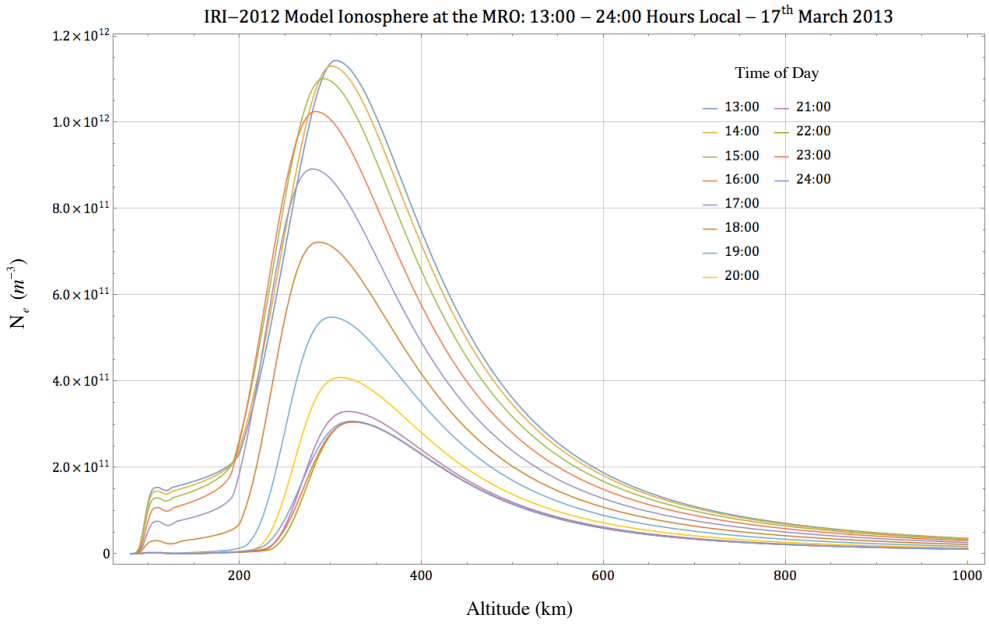


*Figure 4.28: Ionospheric TEC profiles for the second 12 hours of 17th March, 2013, produced for the site of the MRO under the IRI-2012 model.*

Differences between the profiles observed in Figures 4.26 (Chapman profile), 4.27 and 4.29 (IRI-2012 profile) include:

(1) A broader TEC envelope for the IRI-2012 ionosphere, resulting in a lower peak TEC under this model. The IRI-2012 model assigns a higher proportion of the TEC to both the topside ionosphere, 68.4% at 12:00 hours local (min), ranging to 78.1% at 21:00 hours local (max) and structure lower in the ionosphere. This resulted in a higher centroid (median) altitude than for the Chapman model, which assigned 63.9% of the ionosphere to the topside.

(2) The IRI-2012 model returns TEC values and envelopes that are dependent on time of day. A single envelope was developed for the Chapman profile.

The IRI-2012 climactic model, the outcome of considerable intellectual pursuit over many decades, must be considered the more accurate in this discussion. However, it will be seen (Section 6.5) that the model fails to produce realistic TEC profiles under event-driven conditions, as one must reasonably expect. The Chapman profile however, is useful for giving ready access to a useful (for modelling purposes) ionosphere.

In computing FR, one must assign values to the Earth's magnetic field strength and direction. Magnetic field components were modelled under the *International Geomagnetic Reference Field* (*IGRF-12* - http://www.ngdc.noaa.gov/geomag-web/) at 100 km intervals and then interpolated (linear) to 1 km (Table 4.3).

| Alt | Dec | Inc | H | T | E | N | Vertical |
|---|---|---|---|---|---|---|---|
| **0** | 0.227 | -60.604 | 27298.2 | 55614.6 | 27298.0 | 107.9 | -48454.1 |
| **100** | 0.120 | -60.556 | 25982.2 | 52855.0 | 25982.1 | 54.3 | -46028.1 |
| **200** | 0.020 | -60.507 | 24749.8 | 50272.8 | 24749.8 | 8.6 | -43758.4 |
| **300** | -0.073 | -60.459 | 23594.6 | 47854.2 | 23594.6 | -30.2 | -41633.1 |
| **400** | -0.160 | -60.410 | 22510.5 | 45586.7 | 22510.4 | -62.9 | -39641.2 |
| **500** | -0.241 | -60.361 | 21492.2 | 43458.9 | 21492.0 | -90.4 | -37772.5 |
| **600** | -0.316 | -60.311 | 20534.6 | 41460.3 | 20534.3 | -113.3 | -36017.8 |
| **700** | -0.386 | -60.263 | 19633.4 | 39581.5 | 19633.0 | -132.4 | -34368.9 |
| **800** | -0.452 | -60.214 | 18784.4 | 37813.7 | 18783.8 | -148.0 | -32818.0 |
| **900** | -0.512 | -60.166 | 17983.9 | 36148.9 | 17983.2 | -160.7 | -31358.0 |
| **1000** | -0.568 | -60.118 | 17228.4 | 34579.9 | 17227.6 | -170.9 | -29982.5 |

*Table 4.3: Magnetic field components (nT) produced by the International Geomagnetic Reference Field (IGRF-12) model for use in this chapter.*

Here, **Alt** is the altitude at which a magnetic field determination is made, **Dec** is the angle subtending the vector pointing to true north (**N**) and the vector toward magnetic north (**H**) from the location of the observer. The value for **N** is negative if the vector points south. **Vertical** is the vertical magnetic field component. **E** is the component of the magnetic field pointing east. **Inc** is the angle that subtends **H** and the vector (**T**) resulting from the addition of each component vector. **T** therefore is the total effective magnetic field strength in the direction given by angles **Dec** and **Inc**. These three components were employed in further modelling.

### 4.2.3. The Thin-shell Ionosphere.

For a thin shell approximation to the ionosphere and where VTEC is known over a particular interval, here 0-1000 km, RM approximates to

$$RM \approx \frac{e^3}{8\pi^2 \varepsilon_0 m^2 c^3} B_h \cos(\theta) \sec(i') VTEC_0^{1000}, \qquad (4.61)$$

where the magnetic field component $B_h$ is the value of the magnetic field at altitude $h$.

### 4.2.4. Ionosphere with a Chapman Profile and Thin-shell Ionosphere Compared.

The form of the equation for RM given in equation (4.55) was used together with five MWA observational frequencies in determining expected FR measures (Table 4.4). Further investigation beyond the scope of this thesis; in particular, ionospheric tomography, will improve modelling of ionospheric profiles.

Table 4.4 displays FR measures at MWA observational frequencies (80-300 MHz) and the proposed extended observational regime down to 50 MHz. This result is of significance to the use of GPS satellite information in the calibrations of VHF radio telescopes. At the lowest frequency proposed for an extended capability, the MWA will lose FR information (FR ≥ π radians) for a 1 TECU change in aTEC at zenith. At the maximum frequency of 300 MHz, this information is lost for an ~25 TECU change at zenith. The significance of this outcome is investigated further in chapter 6.

| **FR for 1 TECU** | Observation Frequency (MHz) | | | | |
|---|---|---|---|---|---|
| Observation Elevation (°) | 50 | 80 | 160 | 240 | 300 |
| 30 | 3.9917 π | 1.5593 π | 0.3898 π | 0.1732 π | 0.1109 π |
| 45 | 2.5758 π | 1.0062 π | 0.2515 π | 0.1118 π | 0.0716 π |
| 60 | 1.8763 π | 0.7329 π | 0.1832 π | 0.0814 π | 0.0521 π |
| 75 | 1.4893 π | 0.5818 π | 0.1454 π | 0.0646 π | 0.0414 π |
| 90 | 1.2535 π | 0.4896 π | 0.1224 π | 0.0544 π | 0.0348 π |

*Table 4.4: Values of FR in units of π radians calculated for an ionosphere modelled with a Chapman profile permeated by a magnetic field modelled at corresponding intervals, for MWA observational frequencies (including the proposed frequency extension to 50 MHz).*

The differences between FR values calculated for an ionosphere that exhibits a Chapman profile and those based on a thin shell approximation for several shell heights (altitudes) are provided over MWA frequencies, down to the proposed lower limit and range of elevations (30°, 60° and 90°). Differences are also plotted and points of coincidence between the two models displayed. Tables 4.5, 4.6 and 4.7 give $FR_{\text{Chapman Model}}$ as a percentage of $FR_{\text{Thin-shell}}$. Negative values correspond to higher FR predicted by the thin-shell model. Figures 4.29, 4.30 and 4.31 plot the values in corresponding tables and demonstrate that at particular altitudes, $FR_{\text{Chapman-Model}}$ and $FR_{\text{Thin-shell}}$ agree closely, to within 0.2% in the worst case. However, selection of the appropriate thin-shell height is necessary to achieve close agreement.

| **Elevation of 30°** | % Difference in FR at Observation Frequency (MHz) | | | | |
|---|---|---|---|---|---|
| Thin Shell Height (km) | 50 | 80 | 160 | 240 | 300 |
| 210 | -9.17 | -3.58 | -0.89 | -0.4 | -0.25 |
| 230 | -6.95 | -2.71 | -0.68 | -0.3 | -0.19 |
| 250 | -4.71 | -1.84 | -0.46 | -0.2 | -0.13 |
| 270 | -2.45 | -0.96 | -0.24 | -0.11 | -0.07 |
| 290 | -0.17 | -0.07 | -0.02 | -0.01 | 0 |
| 310 | 2.12 | 0.83 | 0.21 | 0.09 | 0.06 |
| 330 | 4.44 | 1.74 | 0.43 | 0.19 | 0.12 |
| 350 | 6.79 | 2.65 | 0.66 | 0.29 | 0.19 |
| 370 | 9.15 | 3.56 | 0.89 | 0.4 | 0.25 |
| 390 | 11.53 | 4.5 | 1.13 | 0.5 | 0.32 |
| 410 | 13.03 | 5.44 | 1.36 | 0.6 | 0.39 |
| 430 | 16.36 | 6.39 | 1.6 | 0.71 | 0.45 |

*Table 4.5: Percentage difference between the $FR_{Chapman\ Model}$ and the $FR_{Thin\ Shell}$ at an elevation of 30°. Negative values correspond to higher values of $FR_{Thin\ Shell}$.*

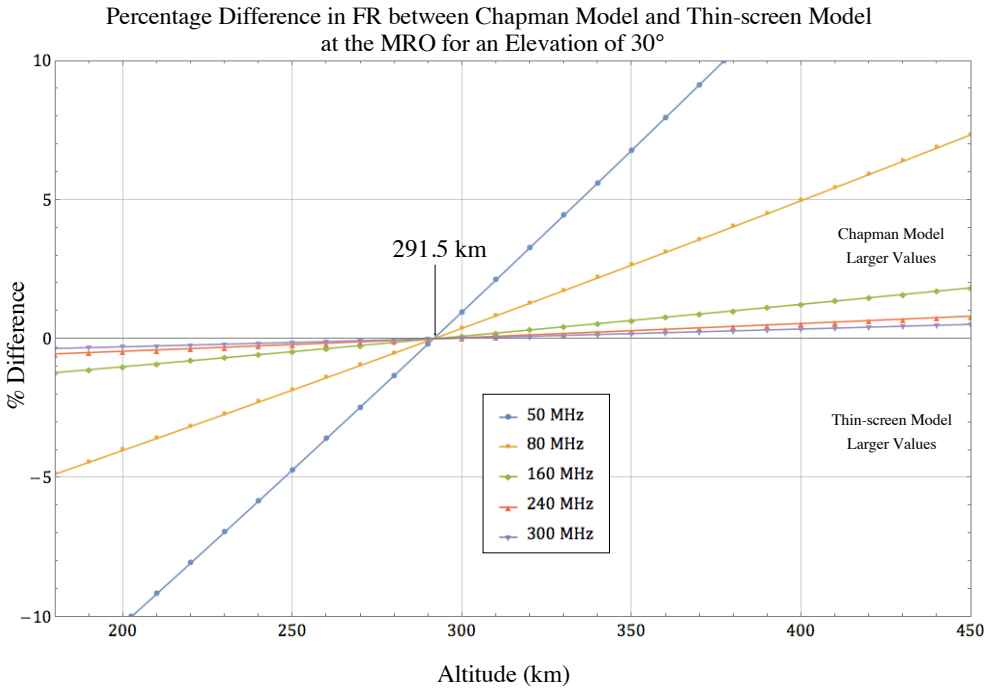


*Figure 4.29: Plot of values presented in Table 4.5. The difference between models falls to less than a value of 0.2% at a thin-shell altitude of 291.5 km.*

| **Elevation of 60°** | % Difference in FR at Observation Frequency (MHz) | | | | |
|---|---|---|---|---|---|
| Thin Shell Height (km) | 50 | 80 | 160 | 240 | 300 |
| 210 | -4.71 | -1.84 | -0.46 | -0.2 | -0.13 |
| 230 | -3.58 | -1.4 | -0.35 | -0.15 | -0.1 |
| 250 | -2.44 | -0.95 | -0.24 | -0.11 | -0.07 |
| 270 | -1.3 | -0.51 | -0.13 | -0.06 | -0.04 |
| 290 | -0.15 | -0.06 | -0.01 | -0.01 | 0 |
| 310 | 1.02 | 0.4 | 0.1 | 0.04 | 0.03 |
| 330 | 2.19 | 0.85 | 0.21 | 0.09 | 0.06 |
| 350 | 3.36 | 1.31 | 0.33 | 0.15 | 0.09 |
| 370 | 4.55 | 1.78 | 0.44 | 0.2 | 0.13 |
| 390 | 5.75 | 2.24 | 0.56 | 0.25 | 0.16 |
| 410 | 6.95 | 2.71 | 0.68 | 0.3 | 0.19 |
| 430 | 8.16 | 3.12 | 0.8 | 0.35 | 0.23 |

*Table 4.6: Percentage difference between the $FR_{Chapman\ Model}$ and the $FR_{Thin\ Shell}$ at an elevation of 60°. Negative values correspond to higher values of $FR_{Thin\ Shell}$.*

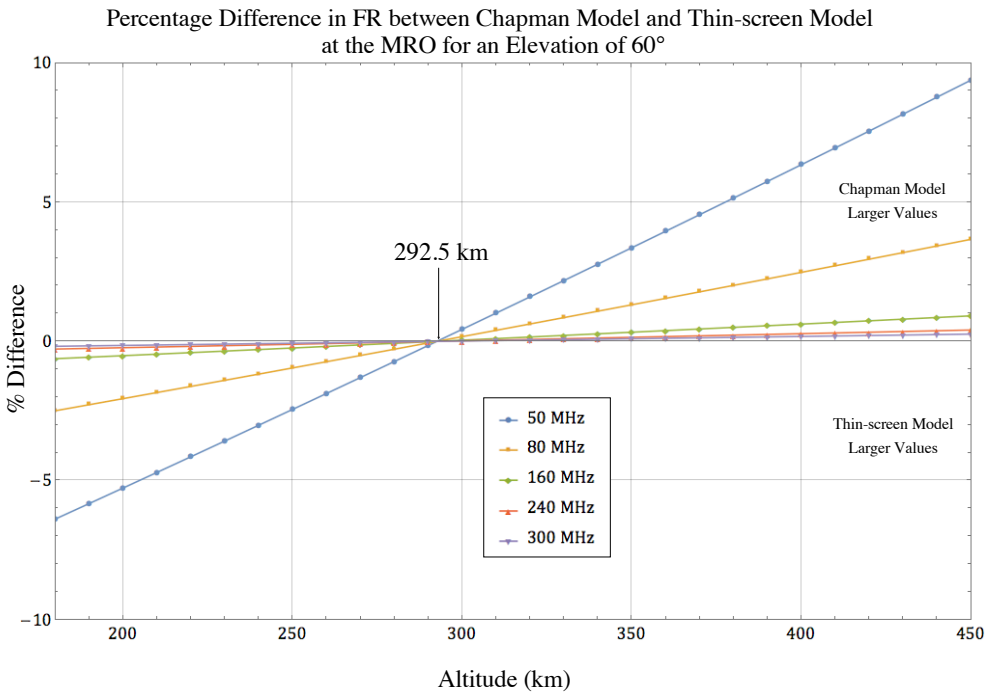


*Figure 4.30: Plot of values presented in Table 4.6. The difference between models falls to less than a value of 0.2% at a thin-shell altitude of 292.5 km.*

| **Elevation of 90°** | % Difference in FR at Observation Frequency (MHz) | | | | |
|---|---|---|---|---|---|
| Thin Shell Height (km) | 50 | 80 | 160 | 240 | 300 |
| 210 | -4 | -1.56 | -0.39 | -0.17 | -0.11 |
| 230 | -3.04 | -1.19 | -0.3 | -0.13 | -0.08 |
| 250 | -2.08 | -0.81 | -0.2 | -0.09 | -0.06 |
| 270 | -1.11 | -0.43 | -0.11 | -0.05 | -0.03 |
| 290 | -0.13 | -0.05 | -0.01 | -0.01 | 0 |
| 310 | 0.85 | 0.33 | 0.08 | 0.04 | 0.02 |
| 330 | 1.84 | 0.72 | 0.18 | 0.08 | 0.05 |
| 350 | 2.84 | 1.11 | 0.28 | 0.12 | 0.08 |
| 370 | 3.84 | 1.5 | 0.38 | 0.17 | 0.11 |
| 390 | 4.85 | 1.89 | 0.47 | 0.21 | 0.13 |
| 410 | 5.87 | 2.29 | 0.57 | 0.25 | 0.16 |
| 430 | 6.89 | 2.69 | 0.67 | 0.3 | 0.19 |

*Table 4.7: Percentage difference between the $FR_{Chapman\ Model}$ and the $FR_{Thin\ Shell}$ at an elevation of 90° (zenith). Negative values correspond to higher values of $FR_{Thin\ Shell}$.*

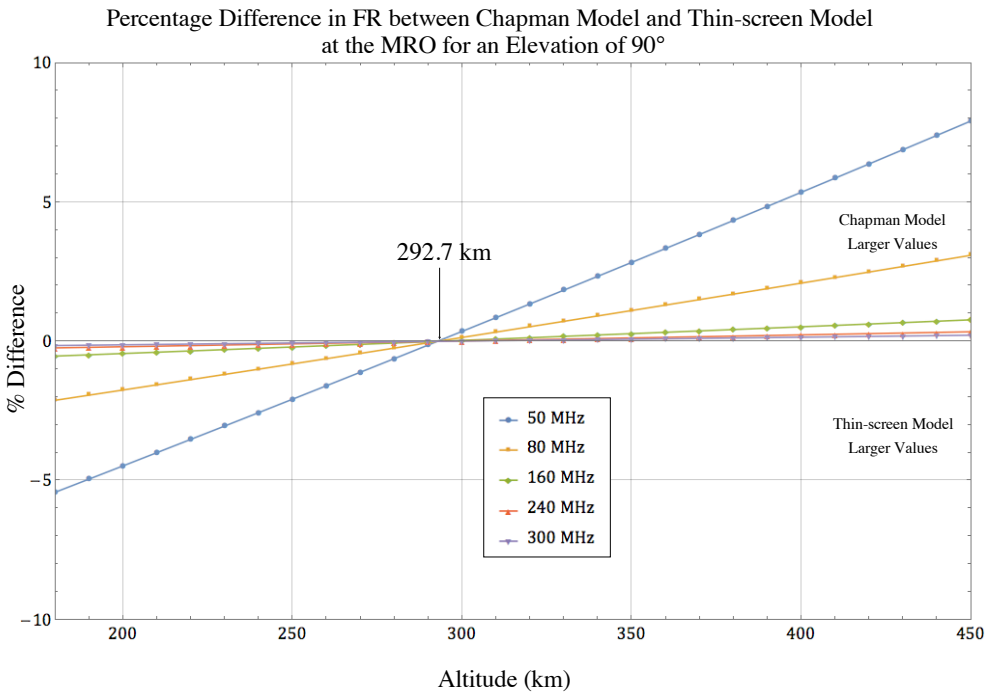


*Figure 4.31: Plot of values presented in Table 4.7. The difference between models falls to less than a value of 0.2% at a thin-shell altitude of 292.7 km.*

In each case, placing the thin-shell altitude at ~290 km was necessary to achieve closest agreement with a model based on a Chapman profile. This height stands in stark disagreement to the altitude at which thin-shell models typically place the ionospheric piercing point (IPP) of from 390 - 450 km.

### 4.2.5. Comparison of an Ionosphere Modelled Under the IRI-2012 Model and a Thin-shell Model.

Outputs of the differences between models were produced for a range of elevation angles (30°, 60° and 90°) and observation frequencies (50 MHz, 80 MHz, 160 MHz, 240 MHz and 300 MHz) and for each hour of the day (01:00 - 24:00 hours). Modelled coincidence altitudes between the thin shell model and the IRI-2012 model ionosphere are displayed in Figure 4.32. A series of tables (Tables 4.8-4.13) and plots (Figures 4.33-4.38) of the outcomes of this modelling work are also displayed.

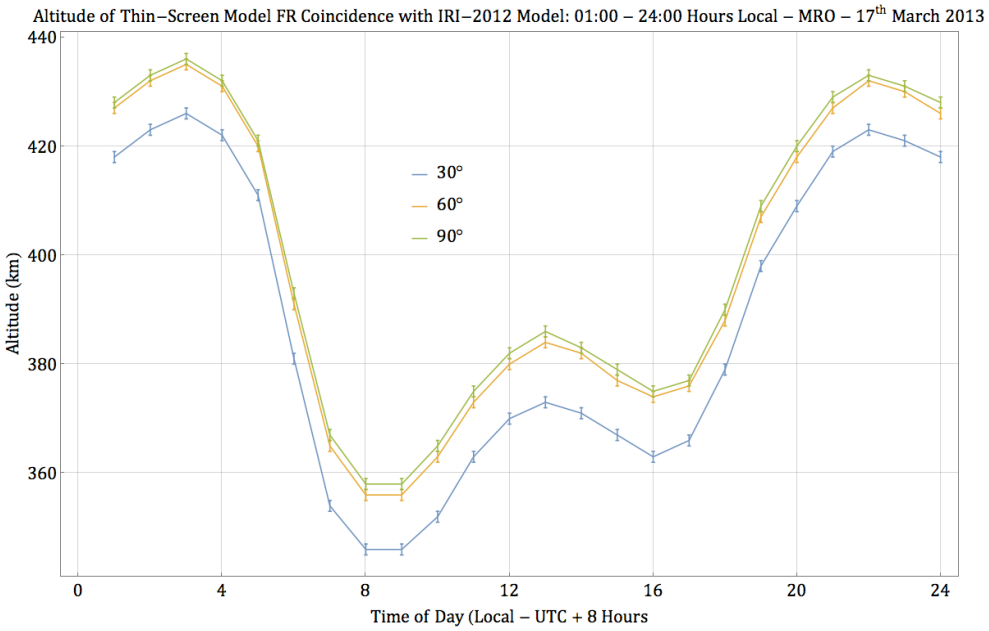


*Figure 4.32: Altitudes at which the thin-shell model profile and IRI-2012 model profile coincide with the same FR values.*

| **Elevation of 30° @ 04:00 Hours** | % Difference in FR at Observation Frequency (MHz) | | | | |
|---|---|---|---|---|---|
| Thin Shell Height (km) | 50 | 80 | 160 | 240 | 300 |
| 210 | -21.27 | -8.31 | -2.08 | -0.92 | -0.59 |
| 230 | -19.34 | -7.56 | -1.89 | -0.84 | -0.54 |
| 250 | -17.4 | -6.8 | -1.7 | -0.76 | -0.48 |
| 270 | -15.45 | -6.03 | -1.51 | -0.67 | -0.43 |
| 290 | -13.47 | -5.26 | -1.32 | -0.58 | -0.37 |
| 310 | -11.48 | -4.48 | -1.12 | -0.5 | -0.32 |
| 330 | -9.47 | -3.7 | -0.92 | -0.41 | -0.26 |
| 350 | -7.44 | -2.9 | -0.73 | -0.32 | -0.21 |
| 370 | -5.39 | -2.11 | -0.53 | -0.23 | -0.15 |
| 390 | -3.32 | -1.3 | -0.32 | -0.14 | -0.09 |
| 410 | -1.24 | -0.48 | -0.12 | -0.05 | -0.03 |
| 430 | 0.86 | 0.34 | 0.08 | 0.04 | 0.02 |

*Table 4.8: $FR_{IRI\text{-}2012\ Model}$ as a percentage of $FR_{Thin\ Shell}$ at an elevation of 30° at 04:00 local. Negative values correspond to higher values of $FR_{Thin\text{-}Shell}$.*

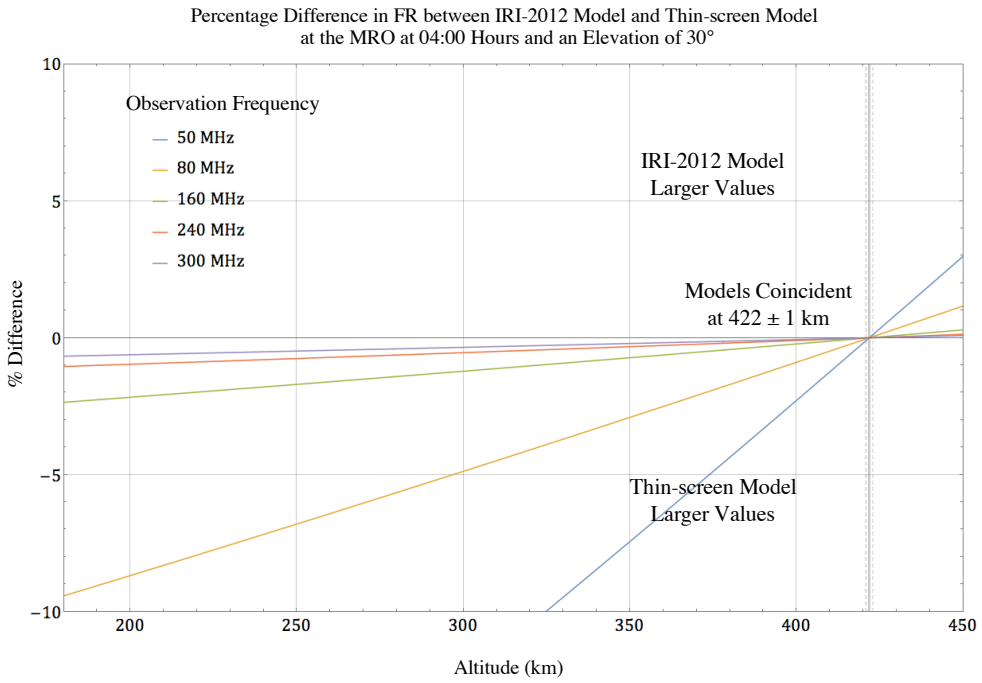


*Figure 4.33: Plot of values presented in Table 4.8 plus the altitude at which the two models' FR values coincide to an accuracy of +/- 1 km.*

| **Elevation of 30° @ 08:00 Hours** | % Difference in FR at Observation Frequency (MHz) | | | | |
|---|---|---|---|---|---|
| Thin Shell Height (km) | 50 | 80 | 160 | 240 | 300 |
| 210 | -14.55 | -5.68 | -1.42 | -0.63 | -0.4 |
| 230 | -12.47 | -4.87 | -1.22 | -0.54 | -0.35 |
| 250 | -10.36 | -4.05 | -1.01 | -0.45 | -0.29 |
| 270 | -8.23 | -3.22 | -0.8 | -0.36 | -0.23 |
| 290 | -6.09 | -2.38 | -0.59 | -0.26 | -0.17 |
| 310 | -3.93 | -1.53 | -0.38 | -0.17 | -0.11 |
| 330 | -1.74 | -0.68 | -0.17 | -0.08 | -0.05 |
| 350 | 0.46 | 0.18 | 0.04 | 0.02 | 0.01 |
| 370 | 2.68 | 1.05 | 0.26 | 0.12 | 0.07 |
| 390 | 4.92 | 1.92 | 0.48 | 0.21 | 0.14 |
| 410 | 7.18 | 2.81 | 0.7 | 0.31 | 0.2 |
| 430 | 9.46 | 3.7 | 0.92 | 0.41 | 0.26 |

*Table 4.9: $FR_{IRI\text{-}2012\ Model}$ as a percentage of $FR_{Thin\ Shell}$ at an elevation of 30° at 08:00 local time. Negative values correspond to higher values of $FR_{Thin\text{-}Shell}$.*

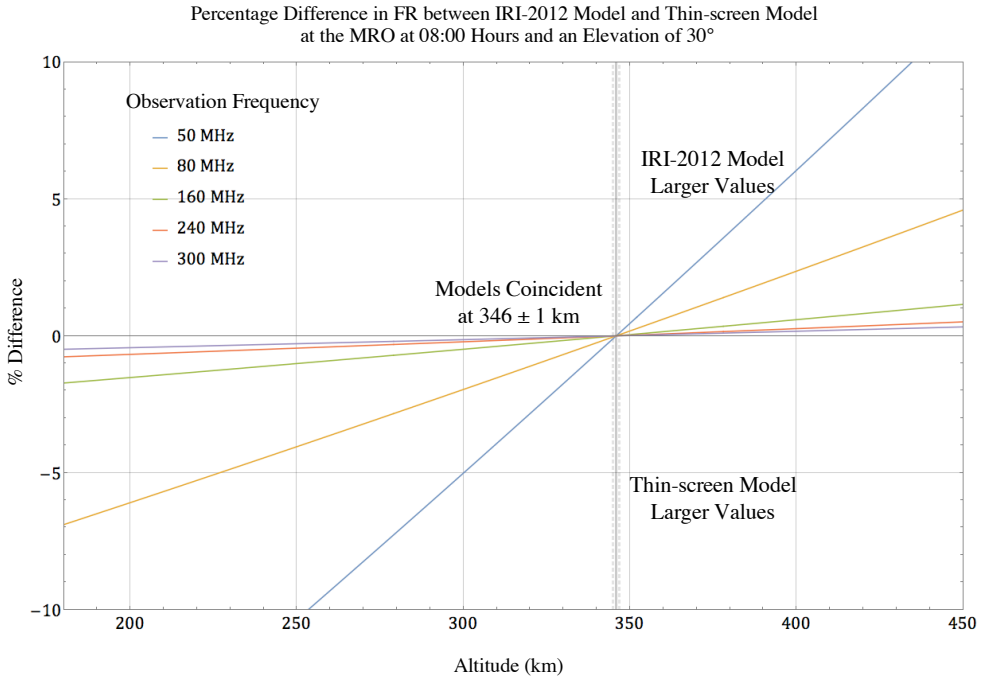


*Figure 4.34: Plot of values presented in Table 4.9 plus the altitude at which the two models' FR values coincide to an accuracy of +/- 1 km.*

| **Elevation of 60° @ 04:00 Hours** | % Difference in FR at Observation Frequency (MHz) | | | | |
|---|---|---|---|---|---|
| Thin Shell Height (km) | 50 | 80 | 160 | 240 | 300 |
| 210 | -11.93 | -4.66 | -1.16 | -0.52 | -0.33 |
| 230 | -10.89 | -4.25 | -1.06 | -0.47 | -0.3 |
| 250 | -9.84 | -3.84 | -0.96 | -0.43 | -0.27 |
| 270 | -8.78 | -3.43 | -0.86 | -0.38 | -0.24 |
| 290 | -7.71 | -3.01 | -0.75 | -0.33 | -0.21 |
| 310 | -6.64 | -2.59 | -0.65 | -0.29 | -0.18 |
| 330 | -5.56 | -2.17 | -0.54 | -0.24 | -0.15 |
| 350 | -4.47 | -1.75 | -0.44 | -0.19 | -0.12 |
| 370 | -3.37 | -1.32 | -0.33 | -0.15 | -0.09 |
| 390 | -2.27 | -0.88 | -0.22 | -0.1 | -0.06 |
| 410 | -1.15 | -0.45 | -0.11 | -0.05 | -0.03 |
| 430 | -0.03 | -0.01 | 0 | 0 | 0 |

*Table 4.10: $FR_{IRI\text{-}2012\ Model}$ as a percentage of $FR_{Thin\ Shell}$ at an elevation of 60° at 04:00 local time. Negative values correspond to higher values of $FR_{Thin\text{-}Shell}$.*

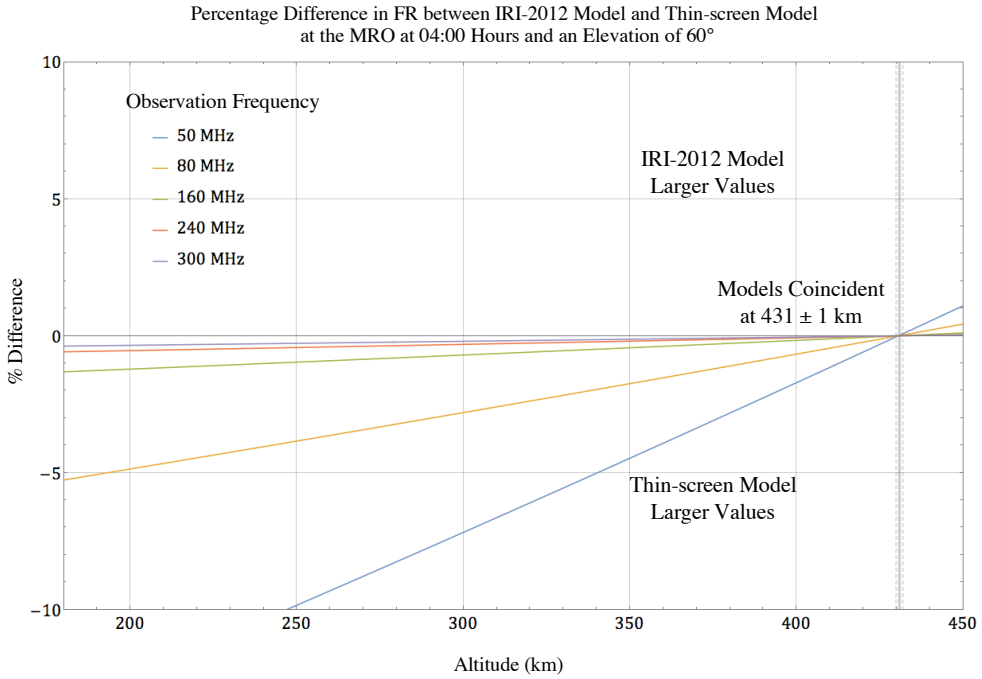


*Figure 4.35: Plot of values presented in Table 4.10. plus the altitude at which the two models' FR values coincide to an accuracy of +/- 1 km.*

| **Elevation of 60° @ 08:00 Hours** | % Difference in FR at Observation Frequency (MHz) | | | | |
|---|---|---|---|---|---|
| Thin Shell Height (km) | 50 | 80 | 160 | 240 | 300 |
| 210 | -8.15 | -3.18 | -0.8 | -0.35 | -0.23 |
| 230 | -7.06 | -2.76 | -0.69 | -0.31 | -0.2 |
| 250 | -5.96 | -2.33 | -0.58 | -0.26 | -0.17 |
| 270 | -4.86 | -1.9 | -0.47 | -0.21 | -0.13 |
| 290 | -3.75 | -1.46 | -0.37 | -0.16 | -0.1 |
| 310 | -2.63 | -1.03 | -0.26 | -0.11 | -0.07 |
| 330 | -1.5 | -0.59 | -0.15 | -0.07 | -0.04 |
| 350 | -0.36 | -0.14 | -0.04 | -0.02 | -0.01 |
| 370 | 0.78 | 0.3 | 0.08 | 0.03 | 0.02 |
| 390 | 1.93 | 0.75 | 0.19 | 0.08 | 0.05 |
| 410 | 3.09 | 1.21 | 0.3 | 0.13 | 0.09 |
| 430 | 4.26 | 1.66 | 0.42 | 0.18 | 0.12 |

*Table 4.11: $FR_{IRI\text{-}2012\ Model}$ as a percentage of $FR_{Thin\ Shell}$ at an elevation of 60° at 08:00 local time. Negative values correspond to higher values of $FR_{Thin\text{-}Shell}$.*

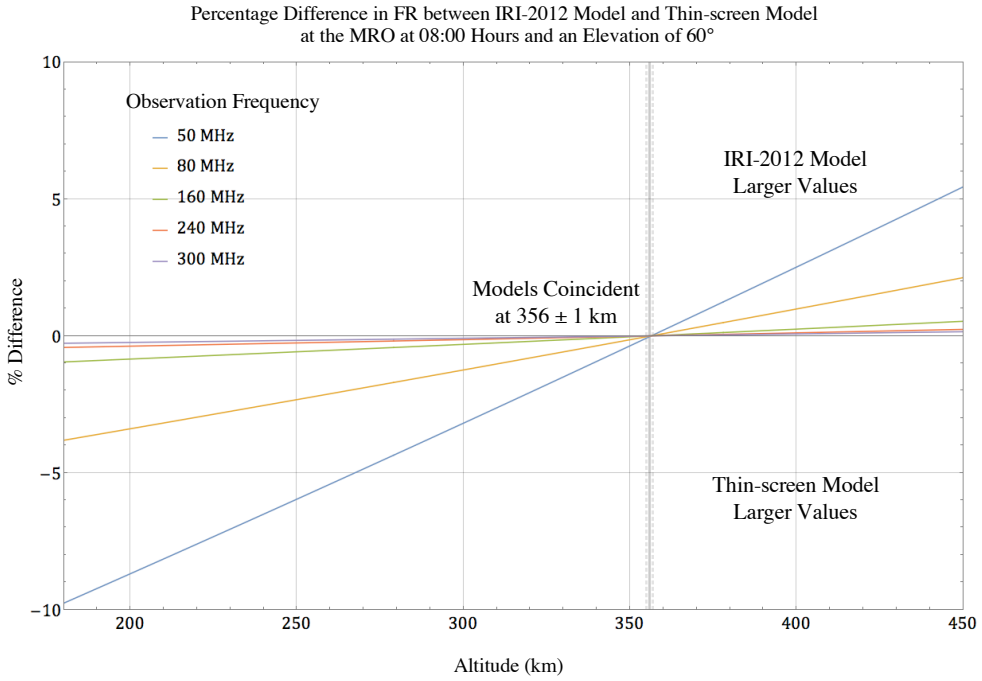


*Figure 4.36: Plot of values presented in Table 4.11 plus the altitude at which the two models' FR values coincide to an accuracy of +/- 1 km.*

| **Elevation of 90° @ 04:00 Hours** | % Difference in FR at Observation Frequency (MHz) | | | | |
|---|---|---|---|---|---|
| Thin Shell Height (km) | 50 | 80 | 160 | 240 | 300 |
| 210 | -10.27 | -4.01 | -1 | -0.45 | -0.29 |
| 230 | -9.38 | -3.66 | -0.92 | -0.41 | -0.26 |
| 250 | -8.48 | -3.31 | -0.83 | -0.37 | -0.24 |
| 270 | -7.57 | -2.96 | -0.74 | -0.33 | -0.21 |
| 290 | -6.66 | -2.6 | -0.65 | -0.29 | -0.18 |
| 310 | -5.74 | -2.24 | -0.56 | -0.25 | -0.16 |
| 330 | -4.81 | -1.88 | -0.47 | -0.21 | -0.13 |
| 350 | -3.88 | -1.52 | -0.38 | -0.17 | -0.11 |
| 370 | -2.95 | -1.15 | -0.29 | -0.13 | -0.08 |
| 390 | -2 | -0.78 | -0.2 | -0.09 | -0.06 |
| 410 | -1.05 | -0.41 | -0.1 | -0.05 | -0.03 |
| 430 | -0.1 | -0.04 | -0.01 | 0 | 0 |

*Table 4.12: $FR_{IRI\text{-}2012\ Model}$ as a percentage of $FR_{Thin\ Shell}$ at an elevation of 90° at 04:00 local time. Negative values correspond to higher values of $FR_{Thin\text{-}Shell}$.*

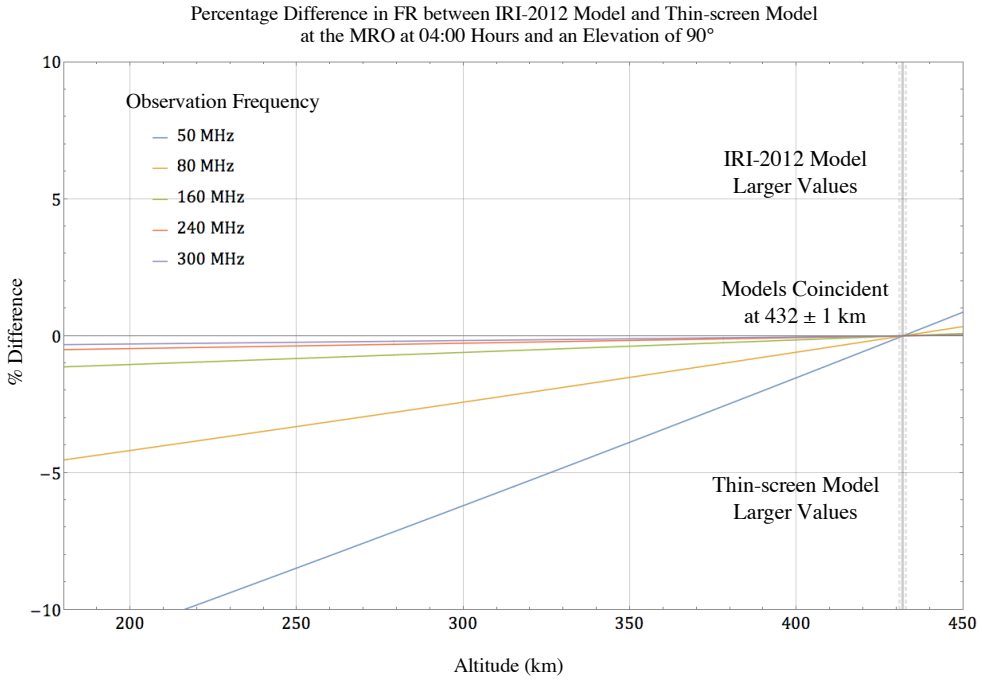


*Figure 4.37: Plot of values presented in Table 4.12 plus the altitude at which the two models' FR values coincide to an accuracy of +/- 1 km.*

| **Elevation of 90° @ 08:00 Hours** | % Difference in FR at Observation Frequency (MHz) | | | | |
|---|---|---|---|---|---|
| Thin Shell Height (km) | 50 | 80 | 160 | 240 | 300 |
| 210 | -7.01 | -2.74 | -0.68 | -0.3 | -0.19 |
| 230 | -6.09 | -2.38 | -0.59 | -0.26 | -0.17 |
| 250 | -5.15 | -2.01 | -0.5 | -0.22 | -0.14 |
| 270 | -4.21 | -1.65 | -0.41 | -0.18 | -0.12 |
| 290 | -3.27 | -1.28 | -0.32 | -0.14 | -0.09 |
| 310 | -2.31 | -0.9 | -0.23 | -0.1 | -0.06 |
| 330 | -1.36 | -0.53 | -0.13 | -0.06 | -0.04 |
| 350 | -0.39 | -0.15 | -0.04 | -0.02 | -0.01 |
| 370 | 0.58 | 0.23 | 0.06 | 0.03 | 0.02 |
| 390 | 1.56 | 0.61 | 0.15 | 0.07 | 0.04 |
| 410 | 2.54 | 0.99 | 0.25 | 0.11 | 0.07 |
| 430 | 3.53 | 1.38 | 0.34 | 0.15 | 0.1 |

*Table 4.13: $FR_{IRI\text{-}2012\ Model}$ as a percentage of $FR_{Thin\ Shell}$ at an elevation of 90° at 08:00 local time. Negative values correspond to higher values of $FR_{Thin\text{-}Shell}$.*

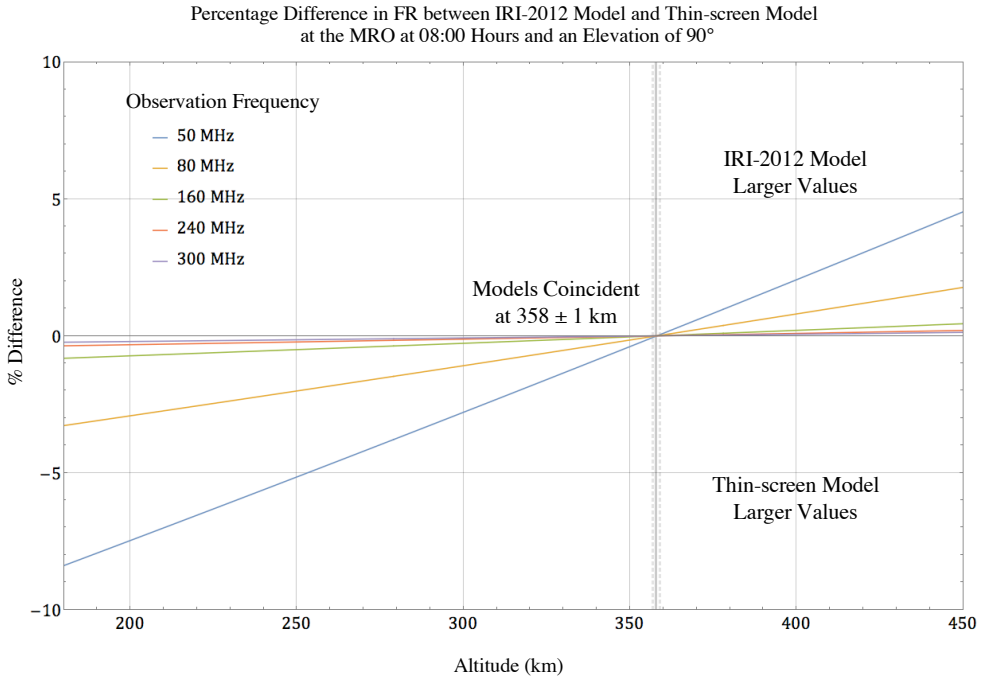


*Figure 4.38: Plot of values presented in Table 4.13 plus the altitude at which the two models' FR values coincide to an accuracy of +/- 1 km.*

Tables 4.8, to 4.13 give $FR_{IRI\text{-}2012\ Model}$ as a percentage of $FR_{Thin\text{-}shell}$. Negative values correspond to higher FR predicted by the thin-shell model. Figures 4.33, to 4.38 plot the corresponding values and demonstrate that at particular altitudes, $FR_{IRI\text{-}2012\ Model}$ and $FR_{Thin\text{-}shell}$ agree closely. However, selection of the appropriate thin-shell height is necessary to achieve close agreement.

The altitudes at which separately the Chapman model ionosphere and the IRI-2012 model ionosphere produce the same FR as the thin-shell model ionosphere differ. However, peak heights of the single Chapman profile agree closely with those produced by the IRI-2012 model at times during the day. The IRI-2012 model assigns a greater proportion of the ionosphere's electron content to the topside ionosphere, that region above the peak and also to a lower, E-layer. Figure 4.39 displays the results of an analysis of features in the data produced in this section.

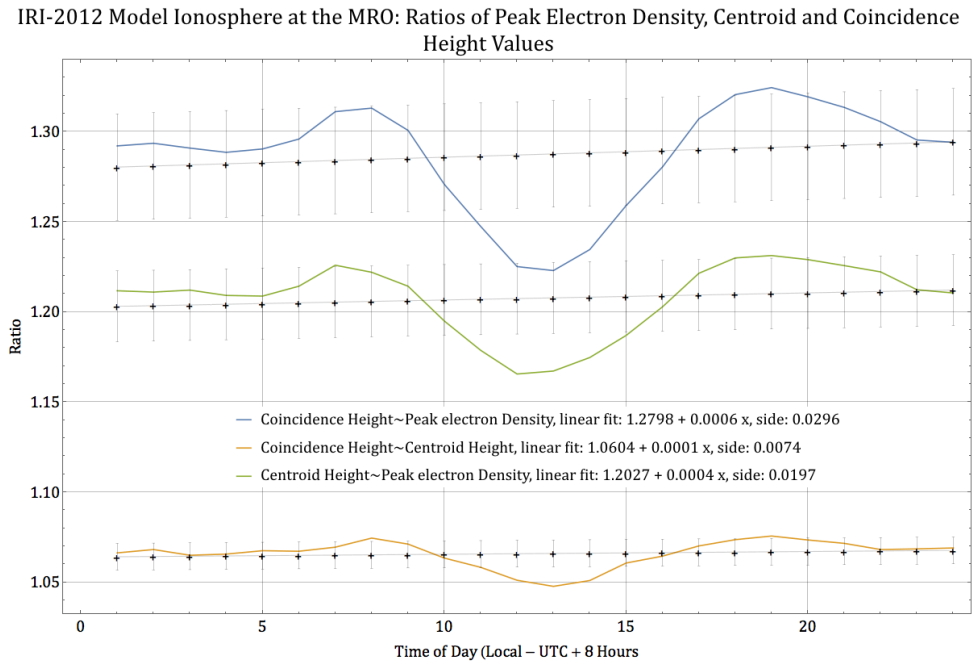


*Figure 4.39: Plot of the ratios of the IRI-2012 model peak electron density (PED), PED centroid and coincidence heights. A line fitted to the coincidence height~IRI-2012 PED centroid height displays a slope 0.33% and minimum and maximum values are separated by 2.60%.*

Two of the three curves present ratios of the heights of FR coincidence between the thin-screen model and either the IRI-2012 model PED height (blue trace) or the PED centroid height (amber trace). The third curve (green trace) presents the ratios of the IRI-2012 model PED heights and centroid heights. The curves demonstrate that there is a slightly better coincidence, as demonstrated by a ratio closer to unity and smaller standard deviation, between the IRI-2012 model PED data centroid height and the height of FR coincidence between the two models than there is between the IRI-2012 model peak height and the height of FR coincidence with a thin-shell model. This implies that perhaps the IRI-2012 model centroid height is the best determinant of where to place an equivalent thin-screen height and the obvious value to use.

In Chapter 6, the outputs of the IRI-2012 model are compared to GPS derived TEC at the location of the MRO over a period of several years. This comparison provides a test of the accuracy of an ionospheric climatological model against measured data. The major conclusion of this section however, is that a single height-value, thin-shell ionospheric model is incapable of producing accurate FR at all times of day for a given location but a variable height model is capable of agreeing closely with the IRI-2012 model (Figure 4.32) and a model based on a Chapman profile when the screen height is varied in altitude according to changes in the structure of the ionosphere..

### 4.2.6. Faraday Rotation Measured at the MRO.

We have attempted detection of time-varying ionospheric Faraday rotation over the MWA using the 150.012 MHz, linearly polarised emission from the radio beacon of one satellite (F15) of the Defence Meteorological Satellite Programme (DMSP) (Coster, Herne et al. 2012). These satellites are in nearly circular orbits at 840 km altitude in two sun-synchronous planes.

Observations were conducted during expeditions to the MRO in 2009 and 2011. On one high elevation pass on August 05th 2009 from 10:30 - 10:45 UT, Stokes parameters were observed for tiles 3 and 11 (of 32 tiles) and the signal polarisation determined over an interval of 50 s. This is shown in Figure 4.40 as that region between the dashed lines and which corresponds to the central part of the main lobe of the MWA antennas. Over this interval, the transmitted signal was 100% polarised.

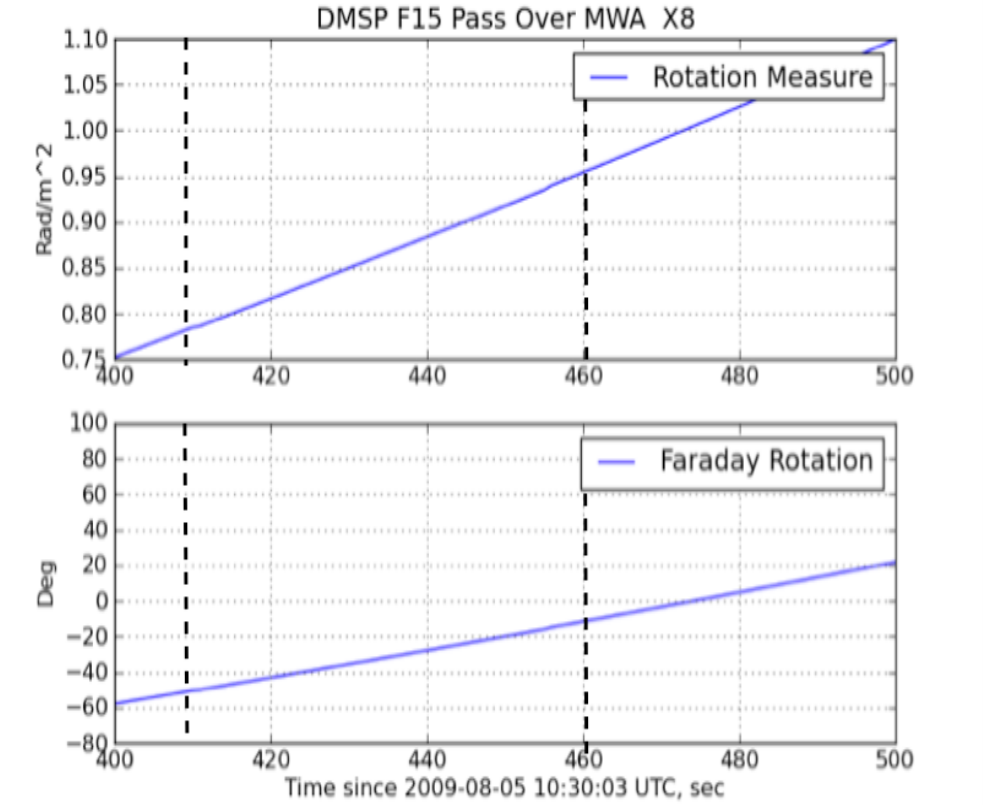


*Figure 4.40: Rotation Measure and Faraday Rotation estimated (Coster, Herne et al. 2012) The expression 'X8' in the label refers to expedition 8 of the MWA 'X'-series expeditions.*

During a pass, the DMSP F15 ephemerides were used to calculate azimuth and elevation when viewed from the MWA at each measurement step. The total Faraday rotation along the line of sight from the MWA to the DMSP F15 satellite was calculated. The International Geomagnetic Reference Field (IGRF) was used to model the terrestrial magnetic field strength and direction. The Rotation

measure (RM) and Faraday rotation thus computed by this model at 150.012 MHz for the DMSP F15 pass, where the Faraday rotation angle = $\lambda^2$RM, are shown in Figure 4.40. The rotation rate, signified by higher RMs in Figure 4.40 (upper panel), is faster for the later (northern) portion of the pass, although the range and hence the integration length is symmetric about its minimum value at the transit point. At the start of the pass, the Earth's magnetic field has a very significant tilt with respect to the low elevation line of sight to the satellite (magnetic aspect angle = 70 deg). As the satellite moves northwards on its near polar orbit, the Earth's line of sight to the satellite becomes more closely aligned with the local magnetic field and therefore provides a larger weight in the Faraday rotation integration.

The predicted Faraday rotation angle changes by ~40° (Figure 4.42 bottom panel). The estimated polarisation angle $\chi$ changed by ~45° in the same period. The two are in good agreement, showing similar curvature in their respective trends. We conclude that observed trends in the variation of $\chi$ are consistent with the expected signature of ionospheric Faraday rotation.

This activity demonstrated the utility of the MWA in detecting FR in a signal that falls within the instruments frequency range. As configured, the MWA is capable of returning relative TEC (as opposed to GPS derived aTEC values). Hence, a combination of GPS acquired aTEC and relative values returned from the DMSP F15 satellite, would provide a convenient and powerful technique for measuring the total FR imposed by the ionosphere.

## 4.3. Scintillation.

Scintillation comprises irregular fluctuations of wave phase, amplitude and polarisation. Scintillation is predominant in the northern and southern auroral ovals and in the vicinity of the magnetic dip equator

(Rawer 1993), which in latitude relative to the MRO, happen to lay further north than the geographical equator. The MRO has a magnetic latitude of -38° (Oberoi and Lonsdale 2012).

Scintillation measured with dual frequency GPS is returned in the form of a scintillation ($S_4$) index, which combines the phase and amplitude of received signals,

$$S_4 = \sqrt{\frac{\langle I^2 \rangle - \langle I \rangle^2}{\langle I \rangle^2}}, \tag{4.62}$$

where $\langle I \rangle = \langle uu^* \rangle$ and $u$ is the instantaneous complex amplitude, $\langle\ \rangle$ being the time averaged value.

Under weak scintillation conditions, in alignment with the Sellmeier dispersion formula, $S_4$ decreases according to a power law,

$$S_4 \propto f^{-n}, \tag{4.63}$$

where $n$ takes values relative to the expected level of scintillation, which at the mid-latitude location of the MRO was expected to be small and exhibit values typically of order $n$ = 1.5 (Hajkowicz 1994, Kennewell, Caruana et al. 2005, Herne, Kennewell et al. 2013), however, at GPS frequencies, scintillation would prove almost immeasurable regardless due to the very small amount of refraction imposed on radio waves at associated frequencies, as shown in Figure 4.41.

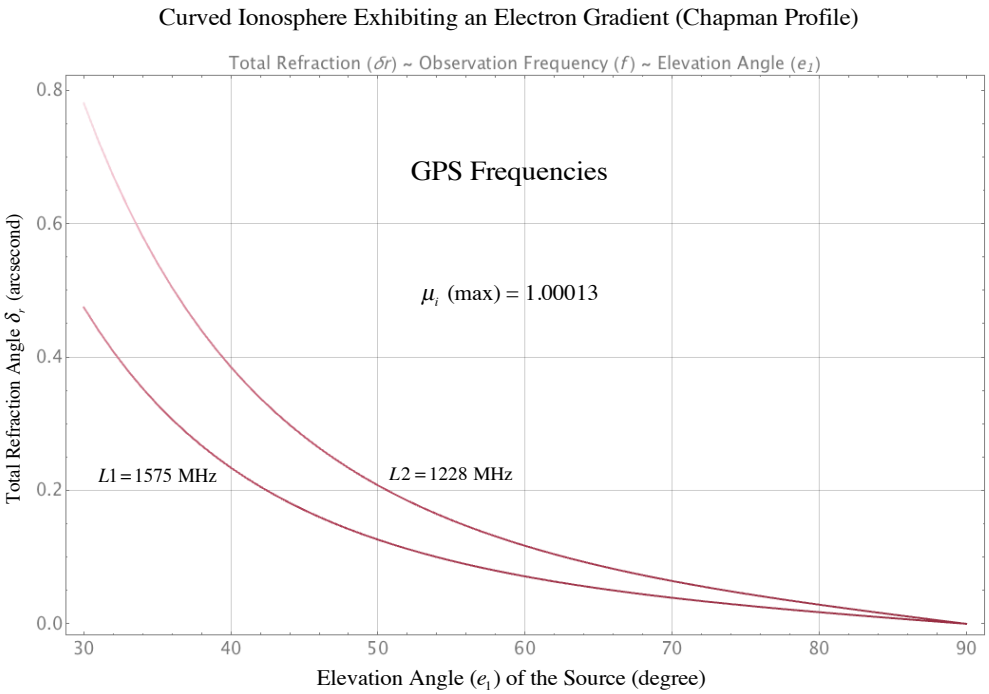


*Figure 4.41: Ionospheric refractive index at the two GPS, L1 and L2 frequencies over the MRO on 17th March 2013, employing a Chapman profile applied to GPS-derived TEC data. The $S_4$ index is computed using L1 only.*

Scintillations were measured using GPS observations and are presented in Chapter 6. Multi-path interference dominates the data, being of even greater significance due to the very small levels of scintillation measured.

## 4.4. Discussion.

Radio astronomy conducted at frequencies of tens to the low hundreds of megaHertz, presents challenges not encountered at higher frequencies. Issues of interest here exist in the calibration of an instrument against ionospheric effects. A static, array-based, imaging instrument faces various design challenges, including direction dependent antenna gain, sidelobe contamination, the provision of adequate *uv* coverage against necessary imaging resolution (which often calls for longer baseline lengths that introduce further uncertainty in calibration against ionospheric effects due to sources being imaged

through different parts of the ionosphere), high data rates at various stages of processing (the MWA is a petabyte per day instrument) and real-time imaging requirements. A discussion on the significance and impacts of refraction, FR and scintillation, each of which was studied in this chapter, follows

### 4.4.1. Ionospheric Refraction.

Seven cases were developed. The first two dealt with examples of a slab (flat-earth) approximation for the ionosphere featuring in the first instance, a homogeneous electron profile and in the second, an inhomogeneous profile. In each case, refraction of an incoming incident ray was shown to be absent and these cases were pursued no further. The following two cases assumed a curved ionosphere exhibiting a homogeneous and an inhomogeneous electron profile. The latter featured a profile derived from Chapman theory which determined also the ionosphere's peak altitude and depth. To more clearly observe the differing responses between curved ionospheres of equivalent electron contents, heights and depths but differing electron density profiles, a fifth case was developed. At a frequency of particular interest (182 hMz, a frequency at which observations by the MWA are cited in Chapter 6 that displayed large refractive offsets), the differences in refraction between the examples of a homogeneous and inhomogeneous ionosphere were between ~13.6% and ~12% greater in the latter over a range of elevations ($e_1$) from 50° to 85° for a TEC of 50 TECU. When processes in the ionosphere that involve refraction are considered therefore, the argument for utilising a model that allows for both curvature and an inhomogeneous electron content profile has been validated. The sixth case studied refraction in right ascension. Excursions in TEC in this direction are principally associated with travelling ionospheric disturbances (TIDs). The seventh case studied refraction in a perturbed ionosphere.

Calibration of the MWA is a real-world problem that requires an accurate knowledge of the relevant parameters and dynamics of the ionosphere. Modern computing, through increasing power, permits models of greater sophistication to provide inputs into the calibration process in place of less sophisticated, less accurate models. The IRI-2012, climatological model, as an example of the former, could be employed at least in setting an appropriate ionospheric screen height during calibration of the array. Interestingly, in Chapter 6 it will be demonstrated that even the IRI-2012 model experiences limitations to accuracy under some conditions in the ionosphere.

### 4.4.2. Faraday Rotation.

FR is a well understood phenomena (Oberoi and Lonsdale 2012). The value in presenting the relationship between FR and radio frequencies is in reminding the reader of the high sensitivity of linearly polarised, VHF radio waves to small changes in ionospheric electron content. At the lowest proposed MWA observing frequency (50 MHz) polarisation information is lost for a change of 1 TECU (eqn. 4.58, Table 4.4) at all elevations up to the zenith because FR exceeds $\pi$ radians. Conversely, rapid, small scale fluctuations in observed polarisation might provide a means of measuring changes in ionospheric free electron content to high time resolution (seconds). Over longer intervals, as sources track across the sky and their radio emissions are intercepted by the stationary antennas, direction dependant antenna gain and polarisation sensitivity due to changing effective antenna geometry, adds uncertainty to observed fluctuations. In Chapter 6, I propose the orbiting of a VHF, beacon equipped satellite (cubesat) that would assist in characterising the polarisation sensitivity of MWA antennas as their observation angles change (Section 6.5).

A common treatment of FR in radio astronomy involves the implementation of the ionosphere as an infinitely thin shell, in which

the ionospheric TEC is fully contained. A comparison of FR obtained under this schema against those modelled for an ionosphere based on both (1) a Chapman profile and (2) the IRI-2012 model was produced. It showed a close correspondence in FR values at particular thin-shell altitudes of ~292 km for the Chapman profile model and altitudes of between 345 km and 435 km for an ionosphere based on the IRI-2012 model. A range of altitudes was obtained in the latter case as the IRI-2012 model produced TEC profiles for each hour of the day that was modelled, as opposed to the Chapman profile model which produced a single profile. Ionospheric altitudes encountered in the literature typically take values of between 390 and 450 km, dependent on the time of day and result in up to 16% difference between thin-shell models and the ionosphere modelled using the aforementioned Chapman profile (at 30° elevation and 50 MHz observation frequency). Similar differences were found for the ionosphere modelled using IRI-2012.

For the single day modelled hourly under IRI-2012, a close correspondence was observed between the TEC data centroid at each interval and the altitude at which FR values showed close agreement with the thin shell model, i.e., the coincidence heights. A line fitted to the ratios of the IRI-2012 model TEC centroid and coincidence heights exhibits a slope of 0.33% and the minimum and maximum values are separated by 2.60% (Figure 4.39). If this relationship was demonstrated to be consistent, then the IRI-2012 model TEC centroid might provide a ready guide to the most appropriate altitude that should be assigned at any moment to a thin shell model, thus improving the accuracy of FR values determined. FR differences between those modelled under IRI-2012 and a thin-shell ionosphere were conducted for periods during nighttime hours and daytime hours (Table 4.8, Figure 4.33 - Table 4.13, Figure 4.38) but analysed as a single interval. In future work, separate intervals will be reported to better separate the daytime and nighttime ionospheres.

### 4.4.3. Scintillation.

Scintillation was expected to be quite low at the mid-latitude location of the MWA (Hajkowicz 1994, Kennewell, Caruana et al. 2005). Measurements by dual-frequency GPS systems on the site of the MRO, nearby and at a location ~500 km further south, have been dominated by multi-path effects (Chapter 6), with little to no scintillation observed. At frequencies used by dual-frequency GPS systems (1228 and 1575 MHz), refraction has been shown in this chapter to be negligible. In Section 6.6, an alternative methodology for measuring scintillation is discussed, employing satellite-borne, VHF beacons.

Arguments developed in this chapter are further discussed in Section 6.28.

## 4.5. Future Work.

A slowly varying ionosphere has been assumed in the analyses selected in this chapter. However, this work could be extended to accommodate a rapidly varying ionosphere that accounts for common disturbed modes such as sudden ionospheric disturbances (SIDs) travelling ionospheric disturbances (TIDs) and storm enhanced density fluctuations (SEDs). An example is discussed in Chapter 6.

## 4.6. Summary.

In this chapter, the following issues have been studied and outcomes summarised.

(1) The ionosphere's influence on transiting radio waves of varying frequencies have been investigated, from those impacting VHF radio astronomy and also the higher frequency GPS signals employed in studying the ionosphere itself.

(2) Model ionospheres were developed that were characterised by either a homogeneous profile, an inhomogeneous profile, an electron density profile after a Chapman model or a profile based on the IRI-2012 model, each of which was subsequently applied employing ionospheric TEC data captured by up to three field deployed dual-frequency GPS systems. Two GPS systems remain in use.

(3) Ionospheric refractive indices were determined from the ionospheric model, measured ionospheric electron concentrations and radio frequencies of interest. Figures display refractive indices for frequencies of typical interest to low-frequency (VHF) radio astronomy and the MWA in particular.

(4) The total refraction produced by a flat (slab) ionosphere, under a flat Earth model, was shown in both the instance of a homogeneous ionosphere and one demonstrating an electron gradient, to be zero. Therefore, use of such models in radio astronomy is without merit.

(5) The difference in FR behaviour of model ionospheres based on an infinitely thin-shell, a Chapman profile and one modelled after IRI-2012 have been investigated and the consequences discussed. The climatological IRI-2012 model is the most sophisticated of the three models and produced varying altitudes at which the thin-shell model returned identical FR. The advantage of employing a model based on Chapman theory is that one was able to perturb the model directly within Mathematica, which was not possible when using the web-based IRI-2012 model. The downloadable version might be accessible from Mathematica and such capability will be tested in future work.

(6) An example of a disturbed ionosphere was presented, in this case, perturbed by a sinusoidal function.

(7) Opportunities to expand on this modelling research include:

(i) A study of the perturbation induced by Earth's magnetic field on rays not confined to the vertical plane.

(ii) Assessing the feasibility of deploying dedicated VHF (hundreds of MHz), satellite beacons in the interrogation of the ionosphere at low-frequencies relevant to radio astronomy at MWA (and LOFAR) wavelengths. This possibility is discussed further in Chapter 6.

(iii) The application of inverse methods in producing a tomographic map of a realistic ionosphere, as others have attempted. This will require the design of a sophisticated approach to interrogating the ionosphere that can draw on disparate data, with for example, GPS signals and VHF satellite beacons or ionograms. Ionograms are physically limited by signal absorption and signal loss. The top-side ionosphere should be investigated separately to the bottom-side ionosphere for example.

# 5. Field Instrumentation and Data Processing.

Two fundamental aspects to this work were [1] conduct of an extensive field, experimental program involving the deployment of dual-frequency GPS systems and [2] modelling of physical processes in the ionosphere that impact the quality of images produced by the MWA. The latter activity was also a beneficiary of the former, which permitted modelling to make use of and be evaluated against, observations conducted on the MRO, at Boolardy homestead and at Meckering (Chapter 6).

The first experiment deployed on the MWA was a single tile of the MWA, on expedition 1T (Figure 2.8) in March 2007. At this time, there were no buildings, sealed roads, electricity, water or communications except satellite phones, which were the sole means of on-site communications. Power generation was by means of portable generators and where low-voltage (12 V) battery backed supplies were appropriate, sometimes by solar panels. Accomodation was provided at Boolardy homestead 40 km from the MRO. Roads became impassable in places following as little as 10 mm of rain. Due to the low regional topography, a river in flood might swell to over 20 km in width. Further, when roads were decreed 'closed' by local authorities, it was an offence to venture onto one. Therefore GPS systems, Novotel Model 4000B receivers coupled to Novotel model GPS-702 dual-frequency antennas, were deployed at first in a campaign based mode due to the lack of supporting infrastructure (2007-2009) and later as fixed installations (2012-2014) as infrastructure support improved.

Figure 5.1 shows a GPS receiver, monitor and computer at Boolardy homestead in March 2009. The pencil shaped device in front of and to the right of, the receiver is a temperature logger (http://www.lascarelectronics.com) for environmental monitoring. Maximum temperatures could exceed 50°C and approach 0°C minimums. The

antenna was located outdoors about 5 m from the building, the furthest separation allowed by the standard 10 m coaxial cable all systems employed. The temperature loggers were used to study possible GPS receiver temperature dependancies. Figures 5.7 and 5.9 demonstrate the benefit of these devices in understanding GPS system performance.


*Figure 5.1: A GPS receiver, monitor and computer at Boolardy homestead in March 2009. The pencil shaped device in front of and to the right of, the receiver is a temperature logger.*

The experimental campaign generated a total of 16.8 million readings for each of TEC and $S_4$ during the course of this study. These data are discussed in the following chapter.

GPS data were processed by a dedicated suite of programs written by Boston College's Charles Carrano under USAFOSR funding (Carrano, Anghel et al. 2009). I take this opportunity to acknowledge Charles' contribution. His program is known as the Scintillation Network Decision Aid (SCINDA). These were written for execution under the Linux operating system. I ported these to the MacIntosh operating system (OSX version 10) and they are available to anyone who is interested.

Modelling and data analysis were conducted with the aid of on-line tools and ~50 programs written under the program Mathematica. Some are presented in Appendix 9.1. All were written by the author. Activities that generated data are discussed in following sections.

## 5.1. Data Acquired from Curated Databases and On-line Modelling Tools.:

Data acquired from curated databases is often generated through a combination of observation and modelling. However, these sites are listed as providing data either through observation or through the application of well understood models and which output values that take into account specific geographic locations. These sites were accessed for some data used in this work.

(1) The Australian government, Ionospheric Prediction Service (http://www.ips.gov.au). Data retrieved include Australian Solar and Geophysical Summary reports (SAGS), scaled ionospheric data (*Iondata*), ionogram data, Australian magnetometer data, solar flux data from the Leamonth Solar Observatory, K-indices (K-Index) and associated A index, 10.7 cm flux (F10.7 Index) as an surrogate for solar electromagnetic output and T-indices.

(2) National Geophysical Data Centre (http://www.ngdc.noaa.gov/). Data retrieved included Kp and Ap indices.

(3) Astronomical sunrise and sunset times (at an altitude of 300 km) were acquired from the Astronomical Applications Department of the US Naval Observatory (http://aa.usno.navy.mil/index.php).

(4) Centre for Orbit determination in Europe (CODE) (http://www.aiub.unibe.ch/content/research/satellite_geodesy/code__research/index_neg.html). Data retrieved include global TEC data and GPS satellite biases.

(5) Wolfram (http://www.wolfram.com). Curated geospatial data . (http://reference.wolfram.com/language/).

(6) The International Reference Ionosphere (IRI-2012) (http://omniweb.gsfc.nasa.gov/vitmo/iri_vitmo.html) was used to generate ionospheric and ionosphere relevant atmospheric data.

(7) Earth's magnetic field data acquired with the World Magnetic Model (WMM), hosted in this instance by NOAA (http://www.ngdc.noaa.gov/geomag/WMM/limit.shtml).

(8) The online model MSIS-E-90 (http://omniweb.gsfc.nasa.gov/vitmo/msis_vitmo.html) was employed in modelling atmospheric components, such as the numbers of free molecular and atomic oxygen molecules in the ionosphere at the MRO on March 17th, 2013 in Figure 5.2.

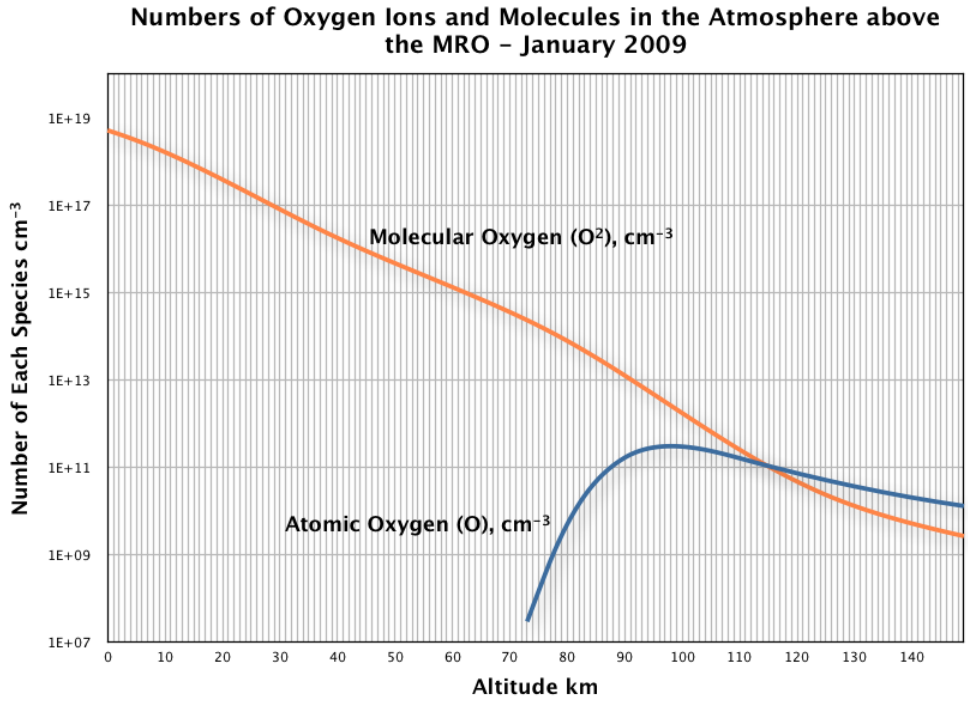


*Figure 5.2: Molecular and atomic oxygen molecules in the ionosphere at the MRO(-26.7° latitude, 116.7° longitude) on March 17th, 2013 as modelled by the author using* ***MSIS-E-90****.*

## 5.2. Probing the Ionosphere with Radio Waves

Due to the dispersive nature of the ionosphere, particularly at low radio frequencies (up to a few hundreds of megaHertz), radio signals provide a means of studying the ionosphere's physical properties through remote sensing, such as the reflection of radio waves transmitted and received by transceivers at ground level (ionosondes) and transionospheric radio waves transmitted by satellite mounted beacons (typically GPS). Ionosonde data were not used in this study, however, as ionosondes are important sources of TEC data and would likely contribute to future work, the technique is discussed here. Figure 5.3 displays a typical ionogram, which in this case displays considerable structure.

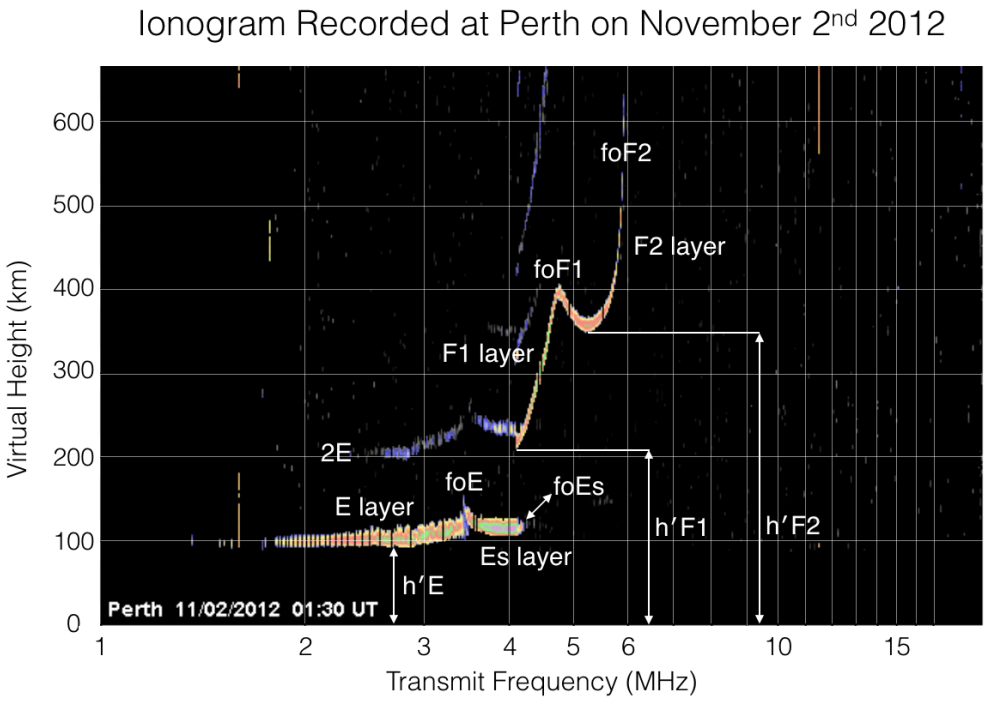


*Figure 5.3: A typical ionogram. Each ionogram is unique and displays features in the ionosphere that vary over time. In this ionogram, 4 regions of enhanced electron content are evident, the E layer, the sporadic E layer (Es) and two F layers. Virtual height is calculated as a product of the arrival times of a pulse reflected from the ionosphere and the speed of light in a vacuum. This result is later corrected for the actual value of c in the ionised medium and which is a much lower value, depending on the transmit frequency.*

Ionosondes, which are swept radio transmitter/receiver systems used to study the bulk electronic properties of the ionosphere, do not respond to very weakly ionised layers at frequencies below a particular cut-off frequency $f_1$ that corresponds in the D layer when present. When interpreting an ionogram, which is the output data produced by an ionosonde, a correction for the density of charged species in this layer should be applied (Titheridge 1986). Without such correction, one of the principal data products produced by an ionosonde, the height to the peak ionisation layers of the E and F layers, might be in error by several kilometres.

Ionosondes probe the ionosphere at low megaHertz frequencies (~1 - 30 MHz) and can access altitudes up to those corresponding to the F layer critical frequency (foF2). Associated virtual heights are ~500-600 km, corresponding to real heights of the order 300-400 km. The topside ionosphere, above the region of peak electron density, is not visible to ground-based ionosondes (Huang, Center for Atmospheric Research et al. 2002). The contribution of the topside ionosphere and higher plasmasphere is subsequently estimated using one or more models such as IRI-2007 or measured using signals transmitted through the ionosphere/plasmasphere to or from a satellite in communication with equipment on the surface of the earth, such as GPS systems.

In Figure 5.3, features of the reproduced ionogram include reflections from the E, Es, F1 and F2 regions of enhanced electron density. Frequencies foE, foEs, foF1 and foF2 are the ordinary ray frequencies of the highest stratification of the corresponding layer ( Wakai, Ohyama et al. 1987) and are known as the critical frequencies. Heights h'E, h'Es, h'F1 and h'F2 are the minimum virtual heights of the ordinary wave corresponding to the highest stable heights of layers, E, F1 and F2. Trace 2E is a second order reflection of the one corresponding to the E layer.

Benefits in the use of ionosondes are [1] the capture of not just TEC data but also ionospheric structure including transient features such Es,

spread F (not present in Figure 5.2) and the separate F1 and F2 layers and [2] readings are taken pointing to zenith. Satellite data are captured at slant angles and must be reinterpreted as VTEC, leading to greater uncertainty in results.

Dual frequency GPS satellites transmit at frequencies less useful to the study of scintillation, namely 1.57542 GHz (L1 band) and 1.2276 GHz (L2 band) but sample the entire ionosphere and plasmasphere from their orbital altitude of ~20,200 km. At least 6 satellites and up to 12 satellites are visible to a receiver at one time, providing as many ionospheric piercing points.

Satellite altimetry has also been used to measure ionospheric aTEC. Radar altimeters pointing toward nadir measure the time-of-flight for signals reflected from Earth's surface. Topex/Poseidon (launched 1992) and Jason-1 (launched 2001) carried dual-frequency altimeters. These spacecraft occupied identical circular orbits, at inclinations of 66° and altitudes of 1,336 km. The radar altimeters operated at frequencies of 5.3 GHz (C-band) and 13.6 GHz (Ku-band) and operate simultaneously. Topex carried a microwave radiometer, operating at 18 GHz, 21 GHz and 37 GHz, which was used to correct for atmospheric moisture induced transmission delays.

A subsequent mission, Jason-2, also known as the Ocean Surface Topography Mission (OSTM), was launched in 2008 on a mission that is ongoing. This spacecraft carries a very similar payload to Jason-1 but with better (lower) noise characteristics.

Alizadeh et. al (Alizadeh, Wijaya et al. 2013)found that in the Ku-band (12-18 GHz), range delay *dR* due to TEC is 2.2 mm/TECU and the precision for a one-second data average is 5 TECU (Alizadeh, Wijaya et al. 2013). Here,

$$VTEC_{alt} = -dR\frac{f_{Ku}^2}{40.3\cdot 10^{19}} \qquad [5.2]$$

where $f_{Ku}$ is the Ku-band carrier frequency and $dR$ is in mm.

For this study, 2 to 3 dual-frequency GPS systems operating at much lower frequencies (1227.60 MHz and 1575.42 MHz) were used to measure ionospheric TEC and scintillation. The use of these systems is discussed in following sections.

## 5.3. The Application of GPS Methods.

The global positioning satellite network (GPS), consists of a constellation of 32 spacecraft (space segment), of which one or more might be out of service while undergoing maintenance (currently numbering a single vehicle) and ground-based management infrastructure (control segment). Terrestrial based receivers (on land, at sea and in the air) comprise the third major component of the network (user segment). The spacecraft reside at altitudes of ~20,200 km on orbits inclined at ~55° and separated by 60° right ascension. One satellite orbit is completed in 11 hours 58 minutes, ½ of a sidereal day. Each satellite passes over approximately the same location on the surface of the Earth each day, during which time at least 6 satellites are visible from most locations.

The fundamental frequency in GPS is 10.23 MHz. This fundamental is multiplied by a factor of 154 to create the 1575.42 MHz L1 carrier and by a factor of 120 to generate the 1227.60 MHz L2 carrier. These are righthand and circularly polarised. The information on each band is carried by the P (or now the Y) code modulating the carrier at the fundamental frequency rate of 10.23 MHz.

These modulated wideband signals, in which the message bandwidth is considerably longer than the signal coherence bandwidth, can be used to calculate the ionosphere's *TEC*, found as:

$$TEC = \frac{(t_1 - t_2) f_1^2 f_2^2}{1.34 * 10^{-7} (f_2^2 - f_1^2)}. \qquad [5.1]$$

Here, *$t_1$ and $t_2$ are* the times at which the rising edges of the modulation signals occur on the measurement frequencies $f_1$ and $f_2$ respectively. In the case of GPS and the control/modelling software SCINDA (Section 5.3.3), data are captured on each GPS frequency at a rate of 50 samples per second and supplied to a model that generates an output at the rate of 1 set of readings per minute. This covers a satellite track across the sky of approximately 0.50°.

For this study, TEC and $S_4$ were determined using GPS satellite data and GPS receivers deployed under various configurations as discussed in relevant sections.

### 5.3.1. GPS Systems.

The GPS receivers deployed as principal data acquisition systems were dual-frequency, Novatel model 4000B receivers coupled to Novatel model GPS-702, dual-frequency antennas. As mentioned previously, these systems were deployed as opportunity permitted, at first in a campaign mode and later as fixed installations. Data collection continues at two sites, one of which is available continuously for data collection.

Outputs available for analysis included:

(1) Date/time.
(2) Observation azimuth and elevation.
(3) Ionosphere penetration latitude and longitude (assigned to 350 km altitude).
(4) $S_4$.
(5) Slant TEC and associated error.
(6) Vertical TEC and associated error.

(7) Satellite PRN.

The VTEC value [6] is computed for values at [3]. The satellite pseudo random noise number [7], is a recycled code that appears as noise but is reproducible and orthogonal to (very unlikely to be confused with) other current PRN values. This allows receivers to repetitively and unambiguously lock onto a particular satellite signal during a satellite pass.

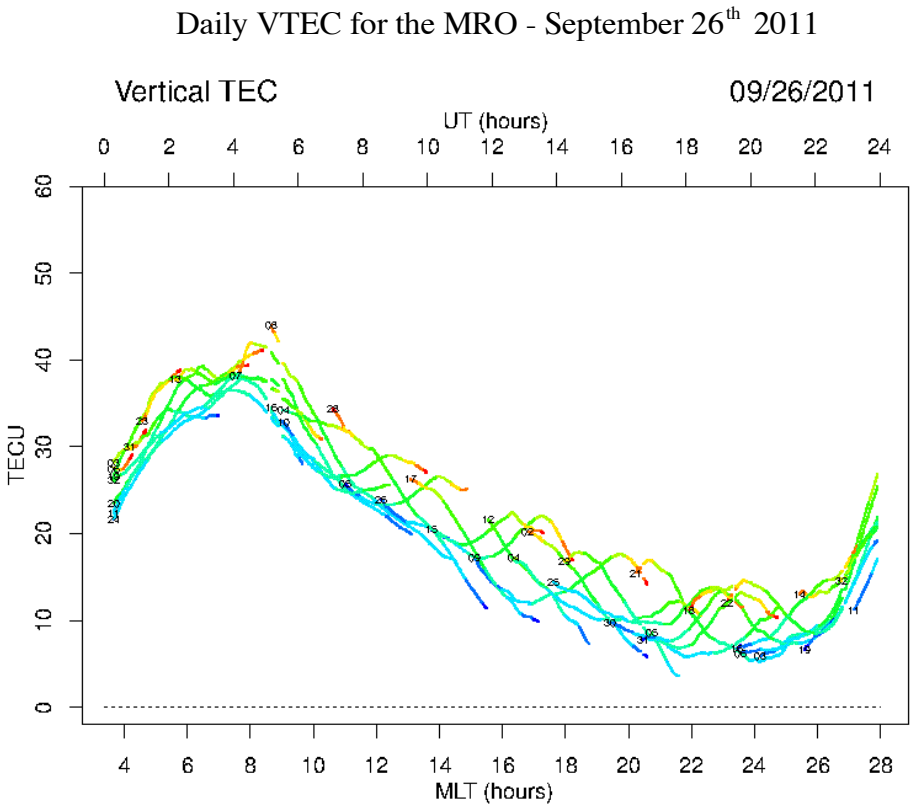


*Figure 5.4: Plot of VTEC for 26th September 2011 over a 24 hour cycle. Superimposed numbers are satellite PRN number and the colours for each trace range from low (blue) magnetic latitude (MLT) to high MLT (red).*

Figure 5.4 displays a daily plot of VTEC. In this plot, a single component curve (associated with a unique PRN), traces the movement of a satellite through its magnetic latitude (trace colour) and longitude (MLT hours). The computed VTEC at each increment in time (1 minute) is shown.

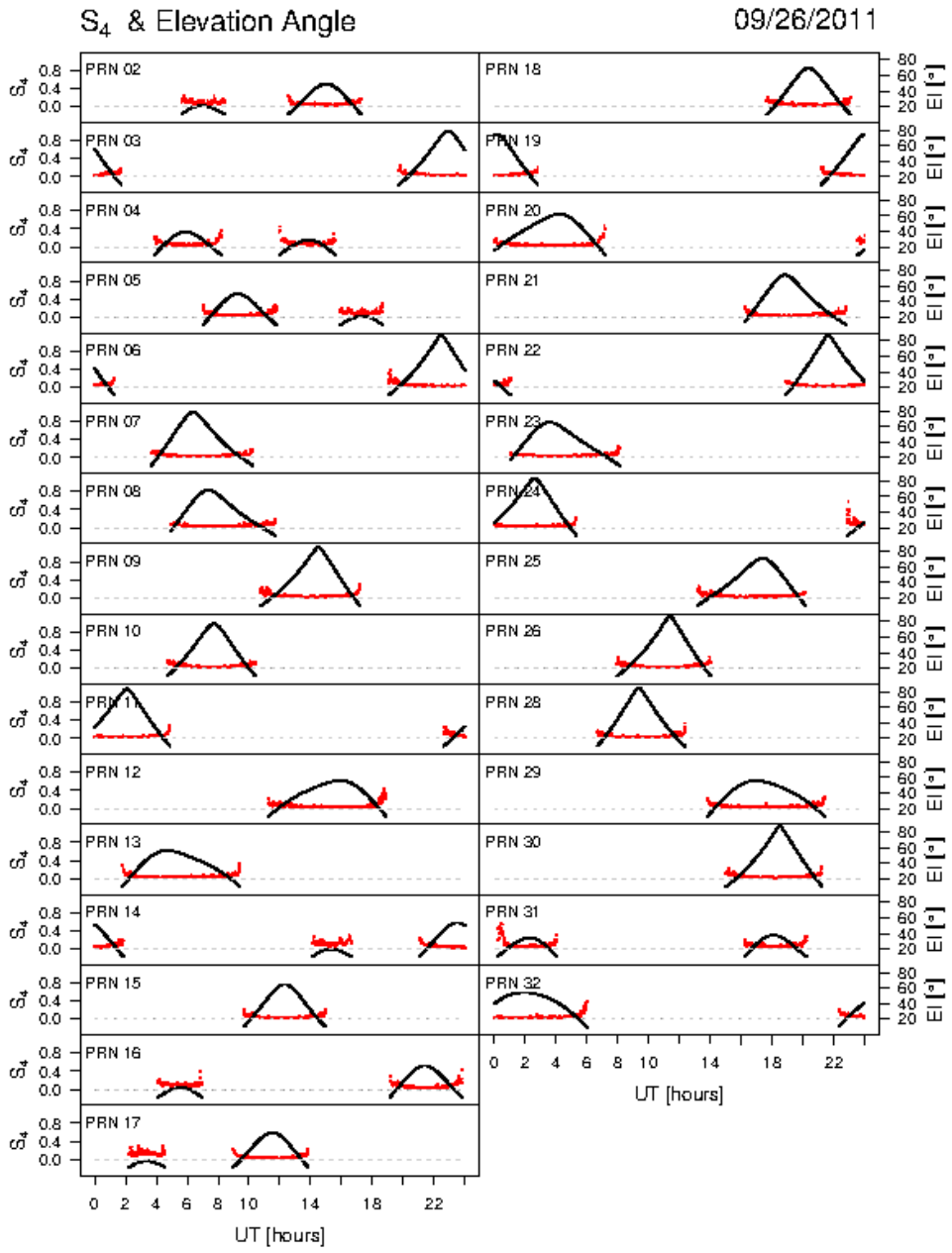


*Figure 5.5: Plots of GPS scintillation intensity at the MRO for 26th September 2011 (red curves) and elevation of the particular GPS satellite at the time $S_4$ was calculated (black curve).Negligible scintillation is observed except at very low elevations, at which data are excluded from calculations of TEC.*

Figure 5.5 displays plots of satellite elevation (black trace) against $S_4$ (red trace) for each satellite acquired during the day. In this instance, scintillation was not observed. Here, $S_4$ (from equation 4.6), rises above background levels (values close to 0) at the lowest elevations of a

satellite pass, at the beginnings and ends of the black curves. This plot and its implications are discussed in depth in Chapter 6.

Data captured by the two GPS systems used concurrently since 2012 at Boolardy and at Meckering were filtered to return results above 50° elevation to ensure that the regions of the ionosphere mapped by each ground receiver did not overlap (Figure 6.13) and duplicate data.

### 5.3.2. Deployment of GPS Receivers.

Each GPS system comprised an antenna, receiver, 10 m long coaxial cable and a host computer. The simplicity of this configuration permitted flexible deployment options, albeit hampered by the use of desktop-class, Dell computers, rather than notebook systems and which, under the typically unreliable power supply conditions encountered, proved an unnecessary handicap. Notebook computers, by virtue of their built-in battery, survive momentary power outages encountered frequently at the remote locations at which systems were deployed. Each system was equipped with uninterruptible power supplies that included back-up batteries, however, remarkably, these often exacerbated the problems encountered by dropping the voltage on the marginal line supply through the need to keep batteries charged.

Systems now have access to reliable, solar power supplies that my colleagues and I constructed for this project. Three battery-backed systems were produced, as shown in Figures 5.6 and 5.7. Each of the three trailers built host the following electrical hardware:

(1) Six Schott Poly multi-crystalline solar panels (5 shown in Figure 5.5).

(2) Six N70Gel batteries with capacities of 24 Vdc and 650 Ahr.

(3) One Tristar 60 A charge controller.

(4) One INTERvolt 24 V - 12 V inverter with a capacity of 30 A.

Each system is capable of supplying over 300 W continuously.

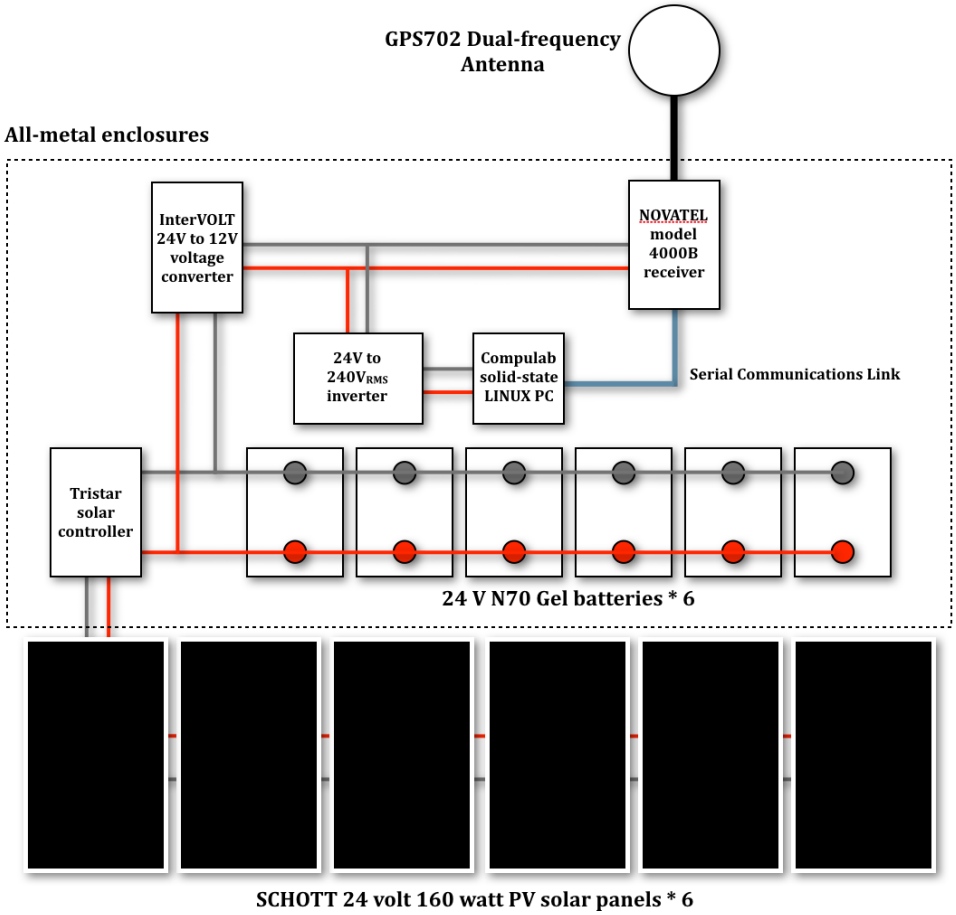


*Figure 5.6: System schematic, mobile, solar powered GPS systems. With the exception of the antenna, all RFI implicated system components are housed in metal enclosures (with unfiltered breakthroughs for solar panel DC power and the antenna coaxial cable). Components were supplied courtesy of Horizon Power Pty. Ltd. Perth, W.A.*


*Figure 5.7: One of 3 solar power supplies constructed by the author and colleagues. This is a current deployment on the Australian Space Academy campus at Meckering and is returning data in real-time over a 3G cell connection. Electrical components were supplied courtesy of Horizon Power Pty. Ltd. Perth, W.A.*

### 5.3.3. SCINDA

GPS data acquisition was managed by the software package *Scintillation and Network Decision Aid* (SCINDA), written by Charles Carrano of Boston College (Carrano, Anghel et al. 2009). SCINDA is also the name given to a network of GPS systems deployed worldwide that employ this software. Outputs include a measure of ionospheric scintillation as the $S_4$ index and aVTEC. This software models the ionosphere as a thin-shell constrained to an altitude of 350 km. Satellite biasses were retrieved from the CODE database. Receiver biasses are estimated locally within the SCINDA software. Each of these aspects to the operation of the SCINDA software are discussed.

The following discussion of TEC measurement is based on the SCINDA user documentation (AFRL-VS-TR-2007-0000) and describes the particular implementation employed in this study.

In the weakly ionised plasma of the ionosphere, permeated by the Earth's magnetic field, radio waves experience a group delay ($\Delta t$ s) that is proportional to the ionosphere's TEC encountered along the line-of-sight ($TEC_{LOS}$) to the satellite, calculated as:

$$\Delta t = \frac{40.3 TEC_{LOS}}{cf^2}, \qquad [5.2]$$

where $f$ is the signal frequency in Hertz. $TEC_{LOS}$ can be estimated by measuring the group delay or a second phenomenon, carrier phase advance, imparted by the ionosphere on the two GPS carrier signals (L1 and L2). The first involves pseudorange measurements on L1 and L2, found as:

$$TEC_P = A\,[[P_2\text{-}P_1] - [B_R\text{+}B_S] + D_P\text{+}E_P], \qquad [5.3]$$

where $P_1$ is the pseudorange on L1 (ns), $P_2$ is the pseudorange on L2 (ns), $B_R$ is the receiver differential code bias (ns), $B_S$ is the satellite differential code bias (ns), $D_P$ is the differential pseudorange multipath error (ns) and $E_P$ is the differential pseudorange measurement noise (ns). A pseudorange is the time (ns) from the space segment to the receiver on each channel and therefore is frequency dependent. An actual, frequency independent range is later computed together with uncertainties derived from $D_p$ and $E_p$. The constant $A$ gives $TEC_P$ in units of TECU and takes the value:

$$A = 2.854\ TECU\ \text{ns}^{-1}. \qquad [5.4]$$

Estimating TEC using pseudoranges requires the determination of satellite and receiver hardware differential code biasses ($B_R$ and $B_S$) and subtracting them from the differential pseudorange measurements. This method however, is often subject to substantial multipath and other measurement noise errors. The effects of these can be discerned in Figures 6.4 - 6.12 as sloping lines from the upper-left corner to the lower-right corner in the plots, corresponding to multipath and other non time-of-day measurement errors.

The second method makes use of signal carrier phases on L1 and L2 and takes the form:

$$TEC_L = B(L_1 - \frac{f_1}{f_2} L_2) - (N_1 - \frac{f_1}{f_2} N_2) + D_L + D_L \qquad [5.5]$$

where $L_1$ is the carrier phase on L1 (cycles), $L_2$ is the carrier phase on L2 (cycles), $N_1$ is the integer ambiguity of the L1 phase (cycles), $N_2$ is the integer ambiguity of the L2 phase (cycles), $D_L$ is the differential phase multipath error (cycles) and $E_L$ is the differential phase measurement noise (cycles). The constant $B$ gives $TEC_L$ in units of TECU and takes the value:

$$B = 1.812 \text{ TECU/L1 cycle.} \qquad [5.6]$$

Estimating TEC using this method exhibits smaller multipath error and measurement noise, which improves precision. However, the integer numbers of accumulated cycles of phase ($N_1$ and $N_2$) for each frequency are unknown and change after each cycle slip.

In real-time operation, SCINDA calculations are based on the phase method [5.5] and ignore the multipath and noise terms. Pseudoranges are used to estimate the unknown number of accumulated phase cycles.

TEC is determined as :

$$TEC = TECR_R - A\ (B_R + B_S), \qquad [5.7]$$

where $TECR_R$ is the relative TEC, $B_R$ is the receiver differential code bias and $B_S$ is the satellite differential code bias. $TECR_R$ is found as:

$$TECR_R = DCP + \langle DPR - DCP \rangle_{ARC}, \qquad [5.8]$$

where the term inside $\langle\rangle_{ARC}$ is an average taken over a phase connected arc between successive cycle slips and the differential carrier phase, $DCP$ and the differential pseudorange, $DPR$, are found as:

$$DCP = B(L_1 - \frac{f_1}{f_2} L_2) \qquad [5.9]$$

and

$$DPR = A(P_2 - P_1). \quad [5.10]$$

Equation [5.7] is the calibrated value of the number of electrons along the line-of-sight between the receiver and satellite.

### 5.3.4. Calibration of Systems.

During deployments in 2007 and 2008, I ran two trials with collocated GPS systems to study differences among these systems when operating in close proximity. The first (T1) was in November 2007 during the expedition on which the 32T radio telescope was installed. The three GPS systems were deployed in a single location, with the antennas all within ~300 mm of each other and the receivers housed together. Antennas were housed in white polymer, lidded buckets out of the direct sunlight. The receivers were housed in a shaded and insulated, un-airconditioned van. The antenna coaxial cables were exposed to direct sunlight. Figure 5.8 is a plot of the results of this trial.

Each coloured trace in the lower panel represents the difference in TEC between the maximum and minimum values of the three GPS systems. The upper panel displays the ambient shaded air temperature recorded on the site during the trial. Regions *A* highlight temperature fluctuations near midday due to intermittent cloud cover. In this environment, patchy clouds develop locally as the day warms, produced from atmospheric moisture, by evaporation and the transpiration of foliage. The temperatures experienced were high, even for the time of year at this location. The air temperature ranged over the 5 days (including the latter part of November 12$^{th}$) between a low of ~20 °C and a high of ~52 °C.

Regions *B* correspond to midnight UTC, 08:00 local time (LT), at which time receiver biasses are updated. New receiver biasses, for estimating GPS receiver differential code biasses, are estimated daily using data

acquired between 03:00-06:00 LT. Assumptions made in the estimation of biases are:

(1) That the ionosphere is most uniform and least turbulent over this period.

(2) That the ionosphere treated as a thin-screen is a valid input to the model used for calibrating the GPS systems under SCINDA.

(3) That slant TEC is a function of elevation only. This assumes that a thin-screen ionospheric model is valid and depends, in part, on assumptions (1) and (2) being valid.

(4) The computed vertical TEC (VTEC) for each satellite is the same across the field of view, which depends on assumptions (1), (2) and (3) being valid.

Region *C* corresponds to a brief period of missing data.

SCINDA employs a thin-screen ionosphere height of 350 km. Satellite biasses are accessed from the CODE database. Applying these to calculations of TEC essentially resets that model. The previously larger and increasing differences in TEC indicated by trend lines *D* immediately drop to lower values when new biasses are applied. Each coloured curve rises from a minimum value to a peak and then falls again to a minimum. This mirrors the corresponding elevation of the satellite pass. This form of curve is indicative of differences caused by receiver bias offsets (Cornely 2013). The greatest error in TEC measurement occurs when the satellite being tracked is highest in the sky and exhibits a negative temperature coefficient, being greater as the temperature falls and a minimum at the hottest point in the day. The rates of change in the GPS TEC differences match closely the inverse rates of change in temperature. I would not have expected this outcome were errors due to multi-path interference as the GPS systems experience the least disturbed line-of-site to the satellite when it is highest in the sky and closest to the observer.

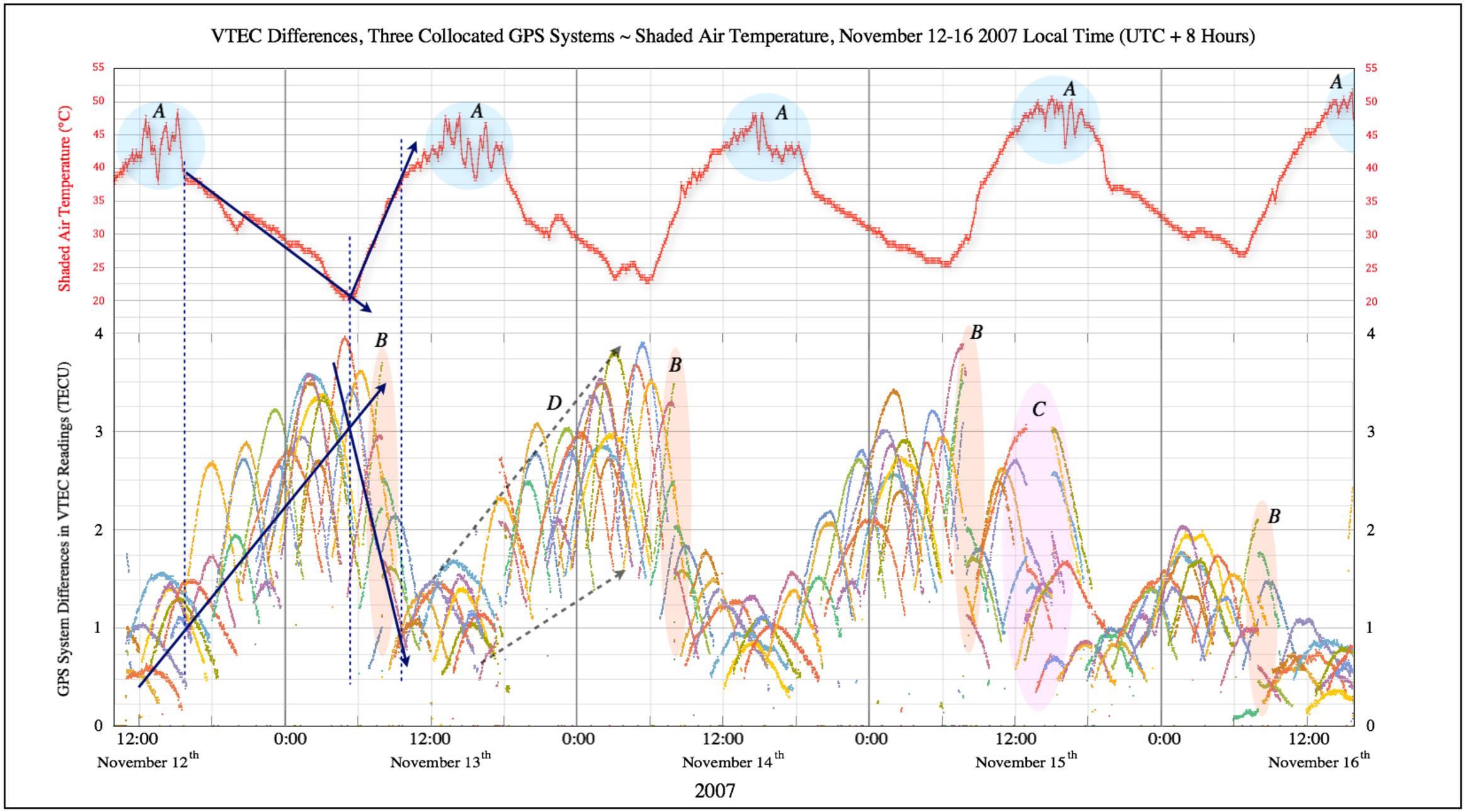


*Figure 5.8: Plots of the maximum excursion in aVTEC readings amongst three, colocated GPS systems for individual, colour-coded GPS satellites over a period of 4 days in November 2007, against the shaded air temperature for the period. The times shown are local (UTC + 8 hours). Each system's antenna was situated within approximately 300 mm of the other antennas and housed in a white polymer enclosure. System receivers were collocated in an un-airconditioned van that was shaded by rooftop solar panels and in which air was circulated by a small fan. Coaxial cables of 10 m length were exposed outside the van to full sunlight. Each coloured curve represents the maximum excursion between 3 GPS systems of TEC for a unique satellite. Readings of air temperature are displayed with error bars representing the manufacturer's published accuracy for these transducers. Regions of the plots* $A$, $B$ *and* $C$ *represent respectively, the effects of cloud shading, differences in retrieved satellite biasses over daily boundaries and an excursion in the data that includes the loss of data from a single receiver for a short period. Dashed arrows* $D$ *outline the increasing trend of differences between systems as the day progresses. Solid blue arrows represent trends in data (TEC and temperatures for a single day).*

Cornell (2013) used a subset of my data (without temperature data) to draw the same conclusion.

During the second trial (T2) of collocated GPS systems, in April 2008, the systems were laid out as shown in Figure 5.9. TEC differences observed are presented in Figure 5.10.

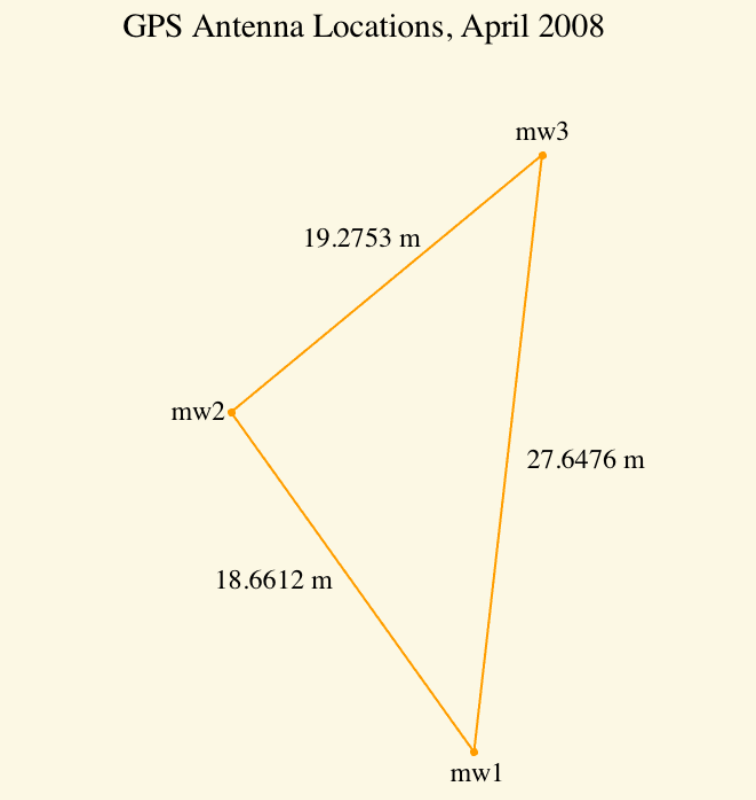


*Figure 5.9: Locations of the three GPS systems in close proximity during testing in April 2008.*

Whereas data presented a similar structure to the previous trial and displayed the same features, the magnitudes of the differences between systems were up to half of those the previously encountered and the temperature coefficient positive.

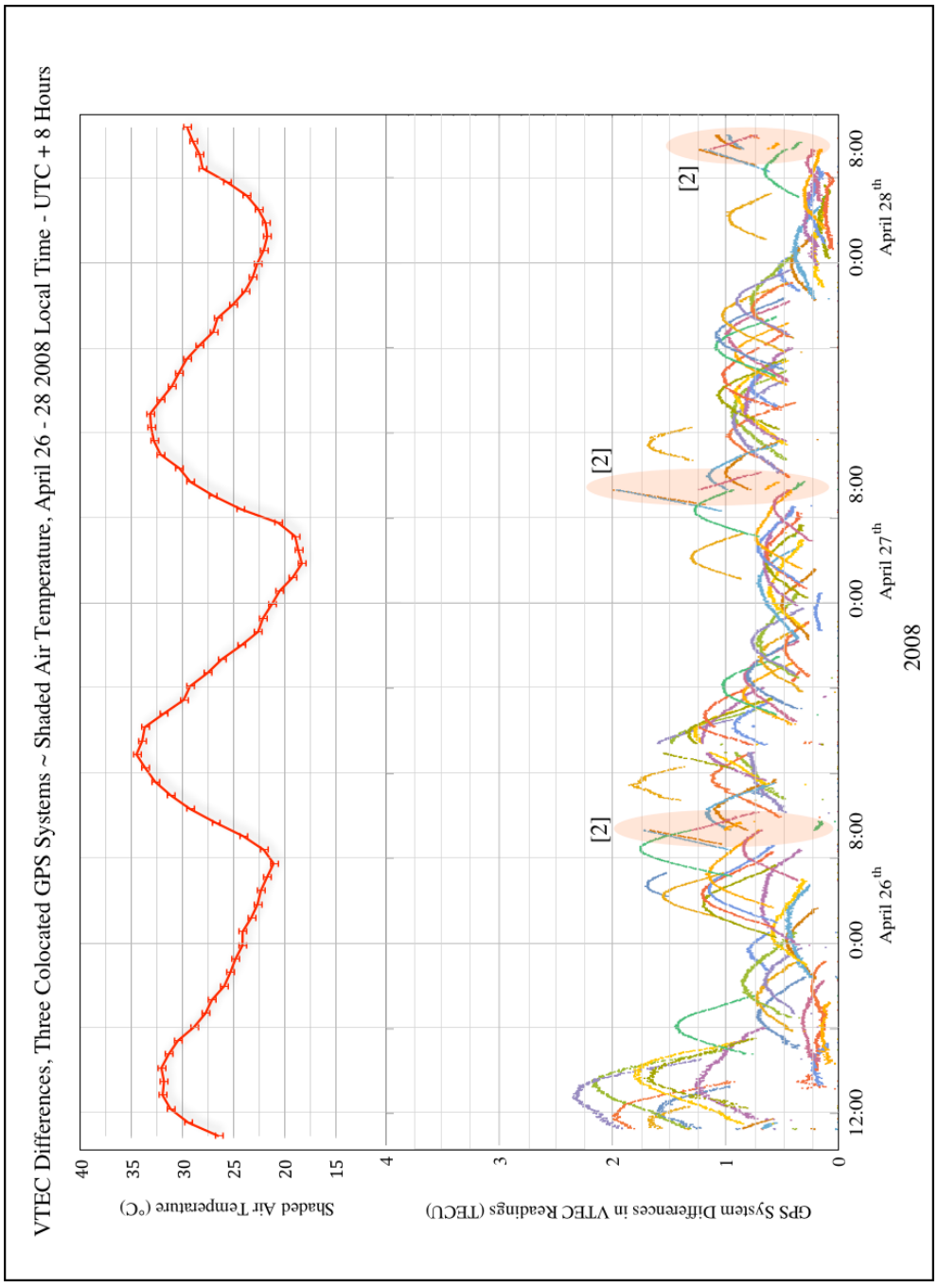


*Figure 5.10: Plots of the maximum excursion in VTEC readings (absolute) between three, collocated GPS systems for individual GPS satellites over a period of 4 days in April 2008. Local time is shown on the abscissa.*

At the time of this trial, the receiver biasses exhibited a positive temperature coefficient. A notable feature of this data is the lower temperatures encountered in the second trial. This might explain the lower peak TEC values attained in this trial. A trial conducted where

collocated receivers are maintained at a constant temperature is highly desirable.

In all instances, the individual curves of TEC differences between GPS systems are remarkably smooth. This feature of the data, together with the trend of increasing amplitudes of the excursions in data from the beginning of the day (UTC), regardless of temperature and the disconnect in curves at midnight (UTC), at which point differences drop substantially, leads me to conclude that the observed differences in TEC readings between systems is the result of systematic errors, most likely in receiver biasses.

### 5.3.5. GPS Observations over Several Years.

Following these foregoing and other brief campaign-based deployments, a period of fixed installation of 3 identical systems, annotated mw1, mw2 and mw3, commenced in 2009. Systems were deployed as shown in Figure 5.11.

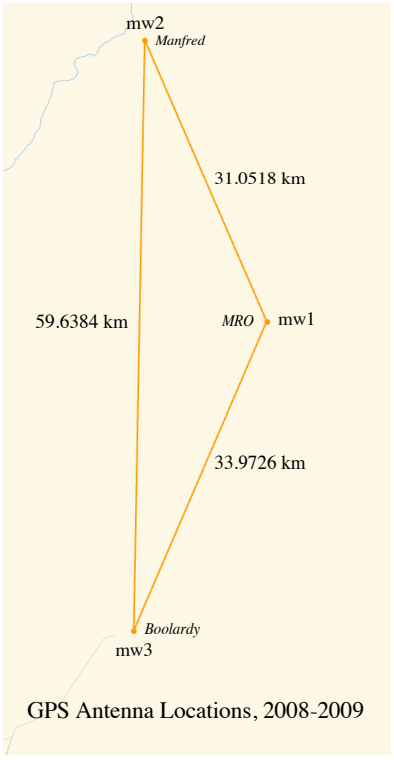


*Figure 5.11: Dual frequency GPS systems, were deployed at 3 sites from 2009 as shown.*

GPS systems were later returned to the USAFOSR later in 2009 for temporary redeployment elsewhere in Australia, after which two systems were returned and deployed as shown in Figure 5.12. All subsequent TEC data was returned from these two sites.

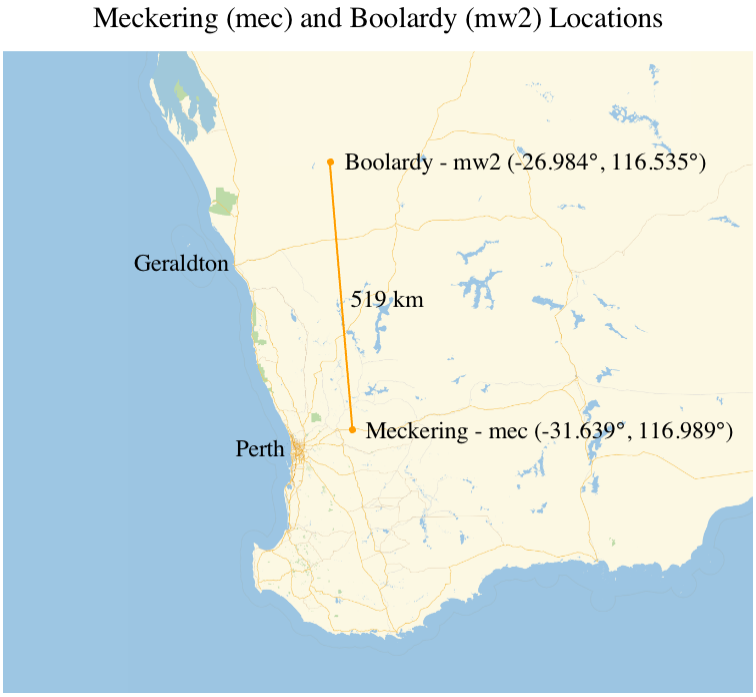


*Figure 5.12: Dual frequency GPS systems, identified as mw1 and mec were deployed at 2 sites, Boolardy homestead and at the Australian Space Academy campus at Meckering respectively, from 2012 as shown.*

The addition of the Australian Space Academy (ASA) site at Meckering enabled mapping of the ionosphere to the south of the MRO, as shown in Figure 5.13. Data from this site contributed to the detection of TIDs propagating from the southern polar vortex during a significant geomagnetic storm (Figure 6.19, Section 6.3).

When comparing the two sites, TEC data for each were constrained to observations above 50° elevation so that the ionosphere represented by each would be unique to that site (Figure 6.13).

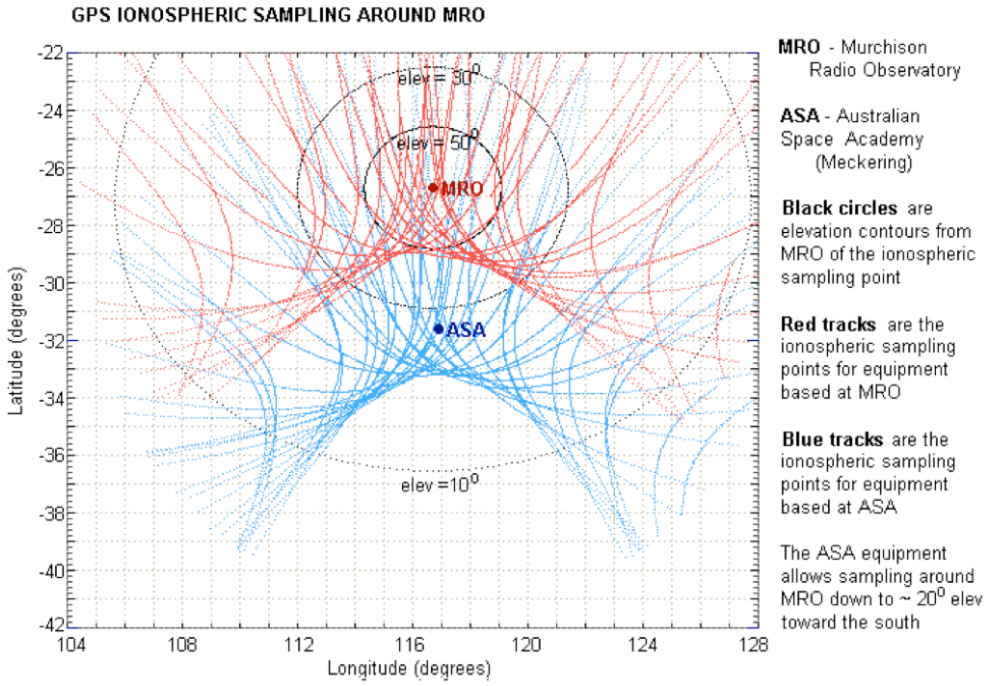


*Figure 5.13: Extended coverage over the MRO provided by deployment of a GPS system on the Australian Space Academy campus at Meckering (blue traces). Image courtesy of Dr John Kennewell.*

TEC values were computed under control of the software package SCINDA, as discussed in Section 5.5.3.

## 5.4. Experimental Electromagnetic Compatibility.

Any experiment conducted at a radio observatory is expected to meet strict electromagnetic compatibility standards. MRO site managers (CSIRO) require that the experiment must not contribute to the local *radio frequency interference* (RFI) environment. Self-generated RFI would in all likelihood, be detected by any experiments including the one that was generating the RFI as either an overwhelming signal at particular frequencies (narrowband) or at many frequencies (broadband) or as an elevated background radio frequency noise. Either is unacceptable. RFI studies conducted at Hat Creek Radio Observatory in California (Bower 2002) in preparation for construction of the Allen Telescope Array (ATA) demonstrate this issue convincingly. An observatory present at the site, the Berkeley Illinois Maryland

Association millimetre wave interferometer (BIMA), was shown to contribute significant self-generated RFI across a wide spectrum of frequencies (from less than 500 MHz to approximately 3.0 GHz). This observatory was decommissioned after a final observing run on June 7th, 2004 and merged with Caltech's Owens Valley Radio Observatory millimetre array to form CARMA at Cedar Flat, in the Inyo Mountains of California.

Once the MWA became operational, RFI was strictly regulated throughout a 40 km wide zone around the MRO, within which radio emissions were forbidden. From this time, operation of GPS systems took place outside this region.

### 5.4.1. Self-Generated RFI

The GPS receivers and antennas are housed in enclosures that minimise the leakage of RFI. However, associated computing systems are not specially hardened. The enclosures produced for use with the solar power trailers that we produced are designed for RFI mitigation, which is currently not fully implemented.

## 5.5. Summary.

The purpose of this chapter was to provide details of the field, data acquisition program undertaken and initial data processing. The following activities and outcomes were achieved.

(1) Initially, 3 identical dual-frequency GPS systems (annotated mw1, mw2 and mw3) and later 2 systems (annotated mec and mw2) were deployed in locations shown in Figures 5.11 and 5.12 respectively, to collect ionospheric TEC and scintillation ($S_4$) data.

(2) In the earliest deployments, during campaign based field programs when supporting infrastructure had not yet been

established, the initial 3 GPS systems were deployed on 2 occasions such that their relative performances could be compared. In the first instance (T1), the 3 systems were collocated such that the antennas were sited within 300 mm of one another and the receivers and their control computers were housed adjacent to one another in a shaded, though un-airconditioned van. An analysis of the comparative performance of the systems under this configuration is presented in Figure 5.8. For the second trial (T2), the 3 systems were deployed within tens of metres of one another, as shown in Figure 5.9. Observations arising from these trials include:

(i) During T1, the TEC between the 3 systems varied by as much as ~4 TECU. During T2, the maximum excursion in TEC difference between the 3 systems was ~2.5 TECU. Most values however, did not exceed ~1TECU.

(ii) A significant environmental difference between the 2 trials was the much lower temperature range experienced during T2, where maximum temperatures did not exceed ~35 °C. During T1, maximum temperatures regularly ranged between 35 °C and 50 °C.

(iii) During T1, the receivers exhibited negative temperature coefficients, returning lower differences in readings as the day warmed and lower readings as the day cooled. During T2, the systems experienced both negative and positive temperature coefficients, which implicates receiver bias resets during the trial changing their polarity, as calibration values can be positive or negative.

(3) GPS TEC and $S_4$ observations were conducted over several years. During E1, data were collected from July 2008 to October 2009. During E2, data were collected from February 2012 over Boolardy homestead and from August 2012 at the ASA, Meckering. Capture

continued until recently but are reported until May 2014 at mw2 and August 2014 for mec. A loss of facilities has halted readings being taken at mw2 and a failure of equipment has halted readings at mec.

(4) Installation of a GPS system at the ASA (mec) has enabled the detection of TIDs propagating from the south (Section 6.3) and mapping of ionospheric TEC and $S_4$ over a much larger area than possible previously (Figure 5.13).

(5) The installation of a GPS system at the ASA was engendered by our construction of self-contained, trailer mounted, solar power supplies (3 units), of which one is located with mec (Figures 5.6 and 5.7). Units are capable of supplying over 300 W each.

(6) GPS systems are controlled using the software package *Scintillation and Network Decision Aid* (SCINDA - Section 5.3.3), written by Charles Carrano of Boston College (Carrano, Anghel et al. 2009) TEC and $S_4$ values are computed using the same software package.

# 6. Analysis, a Southern, Mid-latitude, Continental Ionosphere.

Whereas research into the nature of the ionosphere over continental Australia has been undertaken over many decades (Komesaroff 1960, Bowman 1981), into recent times (Kennewell, Caruana et al. 2005, Harris, Cervera et al. 2012, Cervera and Harris 2014), particular recent impetus attended the development of a site for hosting the SKA. Following selection of a site in the Murchison region of Western Australia for the MRO, the MWA as a low frequency radio telescope array and SKA precursor instrument (Tingay, Goeke et al. 2012) provided opportunity for further study of the local ionosphere. Subsequently, given requirements for proper calibration of the instrument, a new generation of researchers has renewed interest in the ionosphere over Australia and mid-west Western Australia in particular (Mitchell, Greenhill et al. 2008, Oberoi and Lonsdale 2012).

The purpose of this chapter is to provide an analysis of the important physical characteristics and dynamics of the ionosphere relevant to VHF radioastronomy (e.g. the MWA and SKA-low). This is accomplished through the interpretation of GPS-derived TEC and scintillation data that I have collected over several years (2008-present), the incorporation of ancillary data drawn from external sources and through the modelling of atmospheric and ionospheric physical properties and processes. The period covered encompasses one-half of one solar cycle from a period of minimal solar activity in 2008/09 to one of maximal activity in 2013/14.

Analysis proceeds from a discussion of recent findings by other researchers regarding the nature and dynamics of the ionosphere, through novel outcomes of this work, including the observation of TIDs, which have been implicated as possible causes of radio-image degrading scintillation (Booker 1979). The chapter concludes with the

examination of aspects of ionospheric dynamics relevant to the MRO and MWA in particular.

## 6.1. Recent Modelling and Analysis.

A paper published in the Journal of Astronomy and Astrophysics titled *Calibrating high-precision Faraday rotation measurements for LOFAR and the next generation of low-frequency radio telescopes* (Sotomayor-Beltran, Sobey et al. 2013), demonstrates the acute interest of the international community of low-frequency (VHF) radio astronomers in issues of instrument calibration. This paper is particularly important due to recent publication and authorship by eighty astronomers of core issues in VHF radio astronomy. These include ionospheric electron content, calibration of FR and the southern extent of the equatorial ionisation anomaly, which are relevant to the siting of recently established and planned facilities such as LOFAR, the MWA and the SKA. This paper is notable too in the assumptions that underly the author's analysis, such as use of a thin-shell model of the ionosphere and the use of widely dispersed GPS receivers in providing ionospheric total electron content data.

In their paper, Sotomayor et. al. (S-B) introduce a model, **ionFR**, that is intended to '*calculate the amount of ionospheric Faraday rotation*' and provide a means of unwinding this ionospheric induced effect. Several aspects of the problem are addressed, including the structure of a modelled ionosphere and the global behaviour of ionospheric TEC. S-B draws upon a database managed by the Centre for Orbit Determination in Europe (CODE) for provision of GPS derived TEC data. These data are derived from approximately 200 GPS receivers distributed globally, although non-uniformly. Data are interpolated onto a grid at spacings of 5° in longitude and 2.5° in latitude and 2 hour intervals temporally. (Authors indicate that interpolation is used to more finely resolve time intervals down to hourly scales where required.) An ensemble of 12

maps of global TEC is presented, covering the course of a single day, the 11th of April, 2011 (S-B Figure 2). Vertical TEC (VTEC) values are displayed. However, the resulting maps display ionospheric VTEC values that are inverted by latitude and therefore provide an incorrect interpretation of global TEC and associated dynamics. A VTEC value mapped for a particular latitude in the northern hemisphere is actually the value for the corresponding latitude in the southern hemisphere. The mapping is also incorrectly registered with the underlying geographic mapping. I produced a program in Mathematica to read the CODE global ionospheric map (GIM) data and produce corresponding global TEC maps. The GIM data, in a format known as *ionosphere map exchange format* (IONEX), is readily interpreted with little risk of ambiguity and yet the major error remained undetected by the authors and the paper's reviewers with publication of the S-B paper.

In response to errors in the paper, I wrote a rebuttal in the form of a Letter (successful in peer review) which was submitted to Astronomy and Astrophysics. Although the Letter was given referee support, A&A declined publication in favour of an S-B author produced Corrigendum (Sotomayor-Beltran, Sobey et al. 2015). The contribution of my thesis advisors and I in detecting the error was noted in the Acknowledgment section of the corrigendum. A single map from Figure 2 for 06:00 UTC is shown in Figure 1. Each map exhibited at least two fundamental errors. As noted above, the S-B maps are inverted by latitude, resulting in a given value of VTEC in the southern hemisphere actually applying to a northern hemisphere location and visa-versa. A second error resulted in the VTEC maps also being displaced by another ~10 degrees in a north/south direction, as peak values for the northern hemisphere appear displaced further north by an amount that corresponds to a southerly shift for southern hemisphere values. As a consequence, the EIA was shown erroneously to pass directly over both the site in Western Australia that was chosen for hosting the SKA, the Murchison region in Western Australia and the site in Southern Africa, in the Karoo region of

South Africa. This representation is totally incorrect. The correct interpretation of the CODE data for 11th April 2011 at 06:00 UTC is given in Figure 6.2 below.

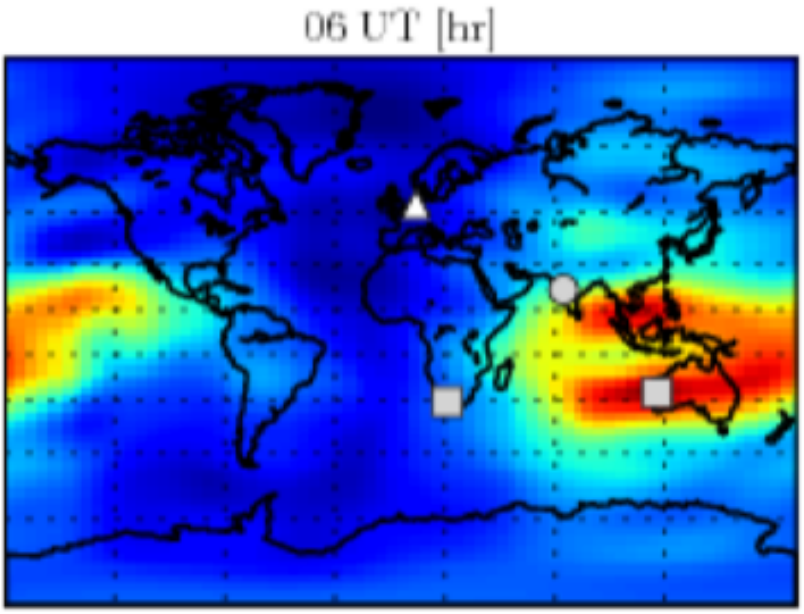


*Figure 6.1: A global ionospheric map (GIM) extracted from Figure 2 of a paper by Sotomayor-Beltran et. al., (Sotomayor-Beltran, Sobey et al. 2013) that displays their incorrect mapping of global TEC for 06:00 UTC, April 11th, 2011. This map is inverted by latitude and stretched north/south by approximately 10°.*

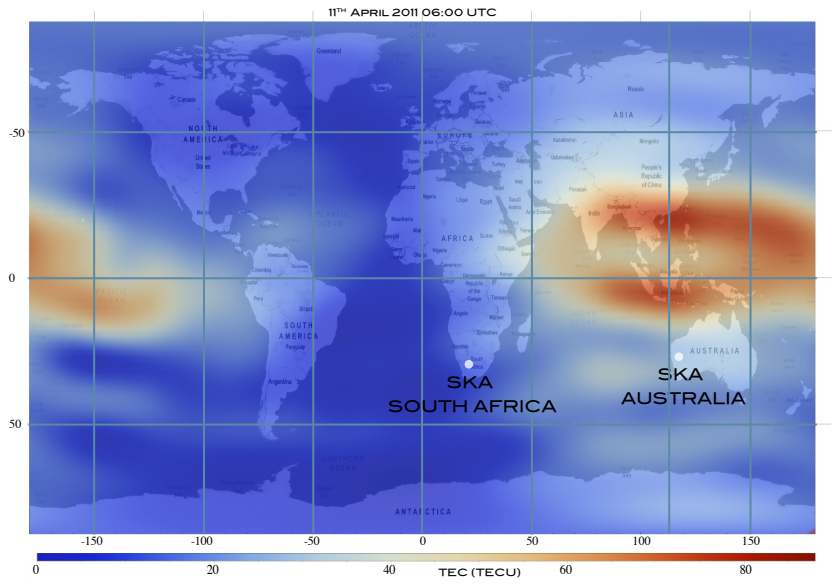


*Figure 6.2: Vertical TEC values produced by the author, using IONEX data produced by the Centre for Orbit Determination Europe (CODE) at 06:00 UTC, 11th April 2011.*

Conclusions drawn directly from the GIMs in the S-B paper are particularly unfortunate in their potential to mislead the radio astronomy community regarding what are actually excellent locations in the southern hemisphere chosen to host the SKA. On page 5 of S-B (2013), the authors made the statement that:

'*it is evident from Fig. 2 that the ionosphere above the two sites chosen for the SKA are subject to the Equatorial Ionisation Anomaly (EIA). These two regions of enhanced plasma density are located approximately 15 degrees north and south of the magnetic dip equator (McDonald et al. 2011) and are the result of the equatorial fountain effect (Appleton 1946). We note that the SKA will suffer far higher levels of ionospheric Faraday rotation than at the LOFAR sites, as the southern component of the EIA can pass directly above both locations*'.

Further, in the conclusions on page 13, the authors stated that '*given that the ionospheric equatorial anomaly sometimes passes directly over the two sites in South Africa and Western Australia, it will be crucial to have a robust and accurate calibration procedure in place to take full advantage of what the SKA has to offer*'.

These statements were drawn either from an incorrectly reproduced map of global VTEC or from erroneous ionFR model output. The southern, mid-latitude ionosphere has been studied extensively over many years, (Bowman 1981, Hajkowicz 1994, Lynn, Gardiner-Garden et al. 2008, Harris, Cervera et al. 2012, Cervera and Harris 2014). When therefore, recommendations were sought regarding suitable locations in Australia for siting of the SKA, the region in the mid-west of Western Australia that was eventually chosen was expected to exhibit a stable ionosphere, well clear of the EIA (Kennewell, Caruana et al. 2005). Our measurements confirm this (Herne, Kennewell et al. 2013). We also note that in a report (Willis et al. 2013, unpublished) by a group reviewing rotation measure (RM) and polarisation (Polarisation Sky Survey of the Universe's Magnetism - POSSUM) plans for the CSIRO's

Australian SKA Pathfinder (ASKAP), a 36 dish radio telescope on the MRO, the authors stated that there was a clear discrepancy between slant TEC and RM values measured by ALBUS and by the ionFR package of S-B. Two packages they investigated provided comparable values of TEC that were quite different ('*about half*') of those obtained using ionFR. The POSSUM report also recommends that '*the SKA needs to set up its own GPS network in order to accurately correct for low frequency ionospheric Faraday rotation effects*.' Finally, a local researcher studying Faraday rotation on polarised astrophysical sources (E. Lenc, private communication) has advised that when using ionFR, he needs to flip the sign of the ionospheric contribution. He has also used the ALBUS software and noted a discrepancy.

In conclusion, a figure (S-B 2013 Figure 2) presented in a paper published in this journal (S-B), incorrectly portrayed the global structure of ionospheric TEC for a particular day, April 11th 2011. The authors of S-B 2013proceeded to caution the reader over the suitability of such sites to host VHF radio observatories. The correct map, in revealing the errors, supports the original, carefully formulated decision of the SKA site selection committee and their conclusion that the sites in the Murchison in Western Australia and the Karoo in South Africa are excellent locations for the conduct of radio astronomy.

Clearly, the most significant implication to low frequency radio astronomy of the incorrect representation of global VTECs presented in S-B Figure 2, is the implication that the respective sites chosen for locating the MWA and the SKA are from time-to-time severely degraded by the ionospheric equatorial anomaly (Bhuyan and Bhuyan 2007, England, Immel et al. 2010). The site of the MWA is not impacted by the anomaly. The same is true of the site in southern Africa chosen to co-host the SKA.

Regarding Faraday rotation, Oberoi and Lonsdale (2012), in a recent paper state that:

*'The task of calibration is made more difficult by the Faraday rotation (FR) of polarised flux as it passes through the magnetised plasma of the ionosphere, the plasmasphere, the magnetosphere, and the heliosphere.'*

The local ionosphere imposes constraints on image quality, therefore, Earth-bound VHF radio astronomy signals require an appreciation of the disposition, dynamics and appropriate correction for the impact of the ionosphere. The outcomes of the present research are presented in the following sections.

## 6.2. Introduction to the Ionosphere over the Murchison Radio Observatory.

I have measured ionospheric aTEC and scintillation at the MRO and at other locations at intervals over a period of approximately 7 years, beginning in 2007 and spanning over ½ of the current solar cycle (Cycle 24 - Figure 6.3).

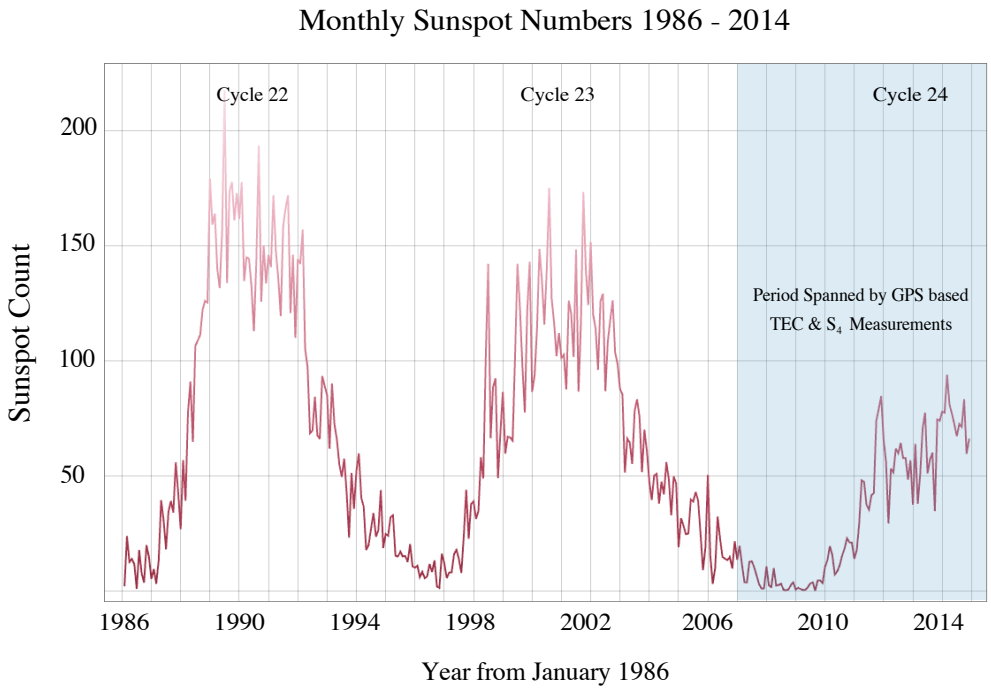


*Figure 6.3: Solar cycles from January 1986 until December 2014 as determined from the index of sunspot numbers (SSN). Reproduced from data compiled by NOAA. Source: WDC-SILSO, Royal Observatory of Belgium, Brussels.*

Over much of this interval, data were collected as opportunity permitted on an expeditionary basis, as permanent facilities to support data acquisition on what is now known as the Murchison Radio Observatory did not exist. Data were captured initially during expeditions to the wholly unimproved site. Early years truly comprised a period of expeditionary radio astronomy.

Later, as infrastructure improved, full-time data acquisition took place. Figures 6.4 to 6.12 present TEC and scintillation ($S_4$) data captured over the duration of the present study and earlier and associated analytical outputs. Data are displayed as "waterfall" plots at 6 minute intervals each day, therefore resulting in one year's data comprising up to 365/366 days (abscissa) of 240 values each (ordinate).

Gaps in the record were due, at first, to the expeditionary basis of measurements. Later, when systems were deployed permanently, failure of either equipment (confined in almost all instances to the vulnerable coaxial cable between antennas and receivers) or failure of power generation equipment (frequently) was the cause of data losses. Uninterruptible power supplies that also filtered power were employed though seldom provided backup power for long enough to compensate for mains power outage time. Interestingly, the UPS system deployed at one site, Manfred station (26.4460° S, 116.5465° E) where only a low-capacity solar system and diesel generator were available, degraded mains voltage level due to the current it drew to maintain backup charge levels and contributed to power failures until it was decommissioned.

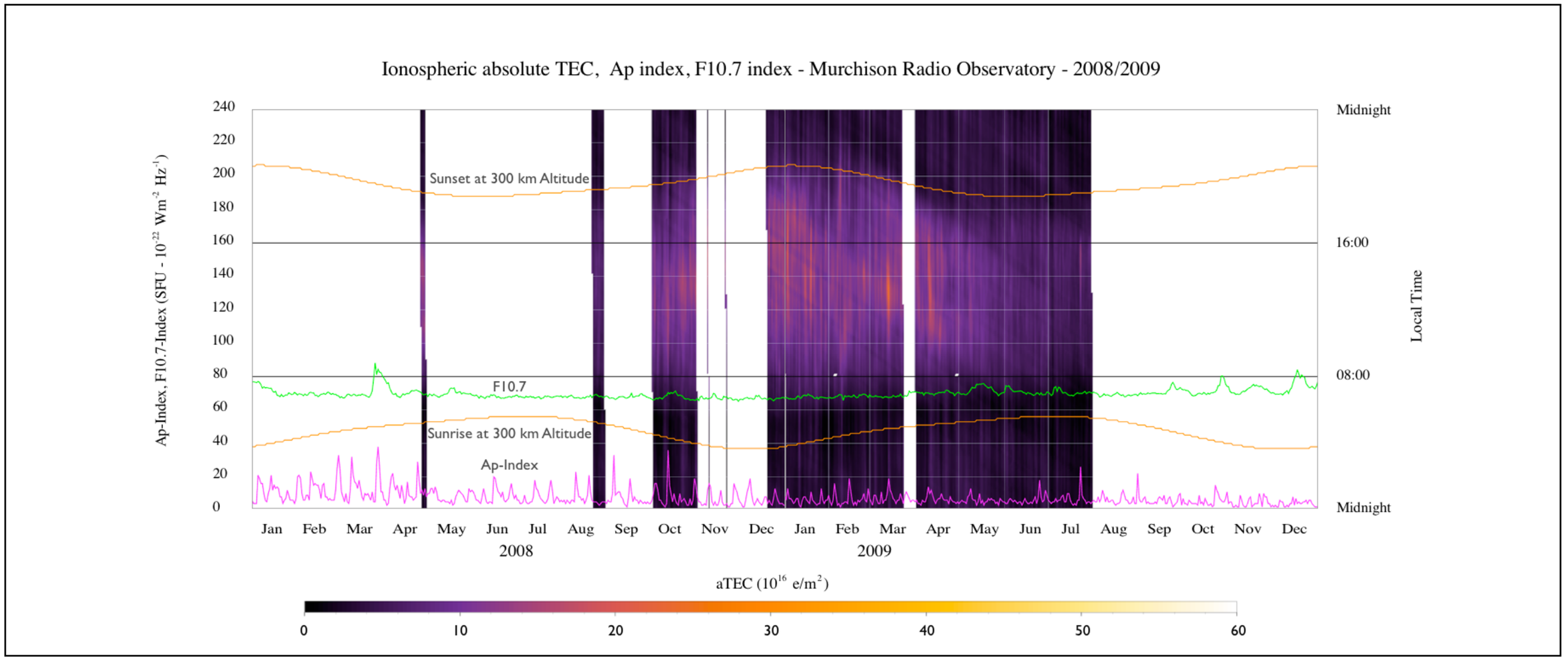


*Figure 6.4: Absolute TEC values produced from data acquired on the MRO over the interval 2008-2009. Waterfall plots display daily readings at intervals of 6 minutes. The F10.7 (10.7 cm - 2800 MHz) data, in units of SFU ($10^{-22}$ $Wm^{-2}$ $Hz^{-1}$), are provided as an analogue to solar photoionising electromagnetic flux. The $A_p$ index is a daily averaged, planetary-wide interpretation of the $K_p$ three-hourly index, which is measure of the horizontal magnetic activity at the Earth's surface. Over this interval, only about 500 readings over a value of 30 TECU were captured.*

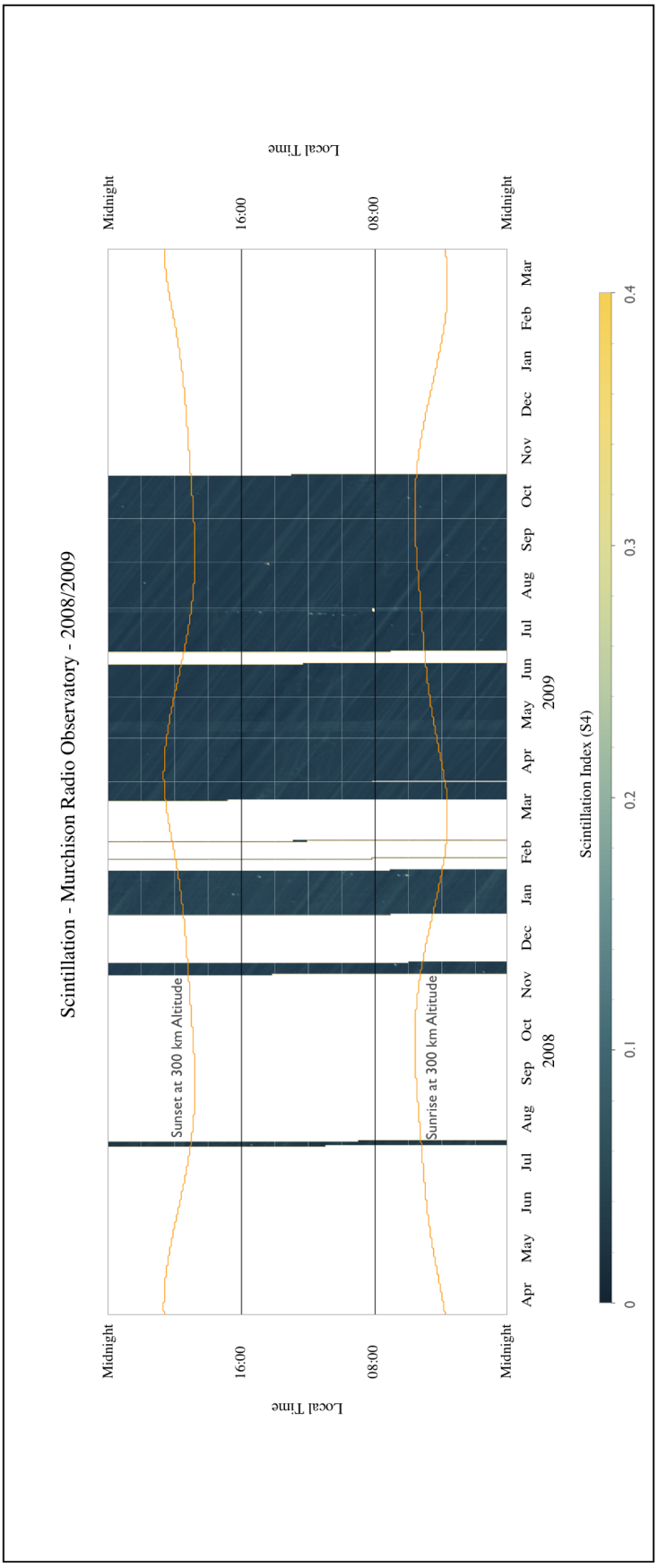


*Figure 6.5: Scintillation ($S_4$) values produced from data acquired on the MRO over the interval 2008-2009, reproduced over 10 minutes intervals.*

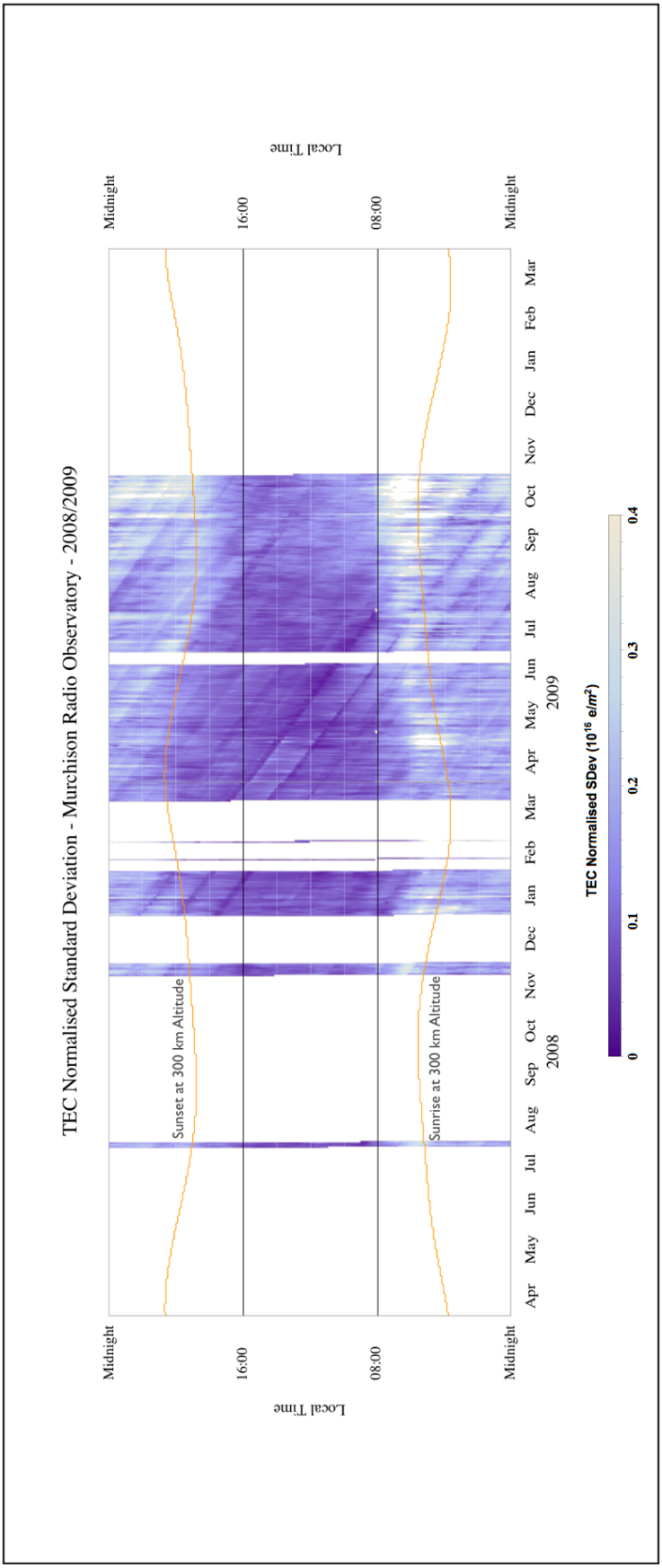


*Figure 6.6: TEC normalised standard deviations produced from data acquired on the MRO over the interval 2008-2009, reproduced over 10 minutes intervals.*

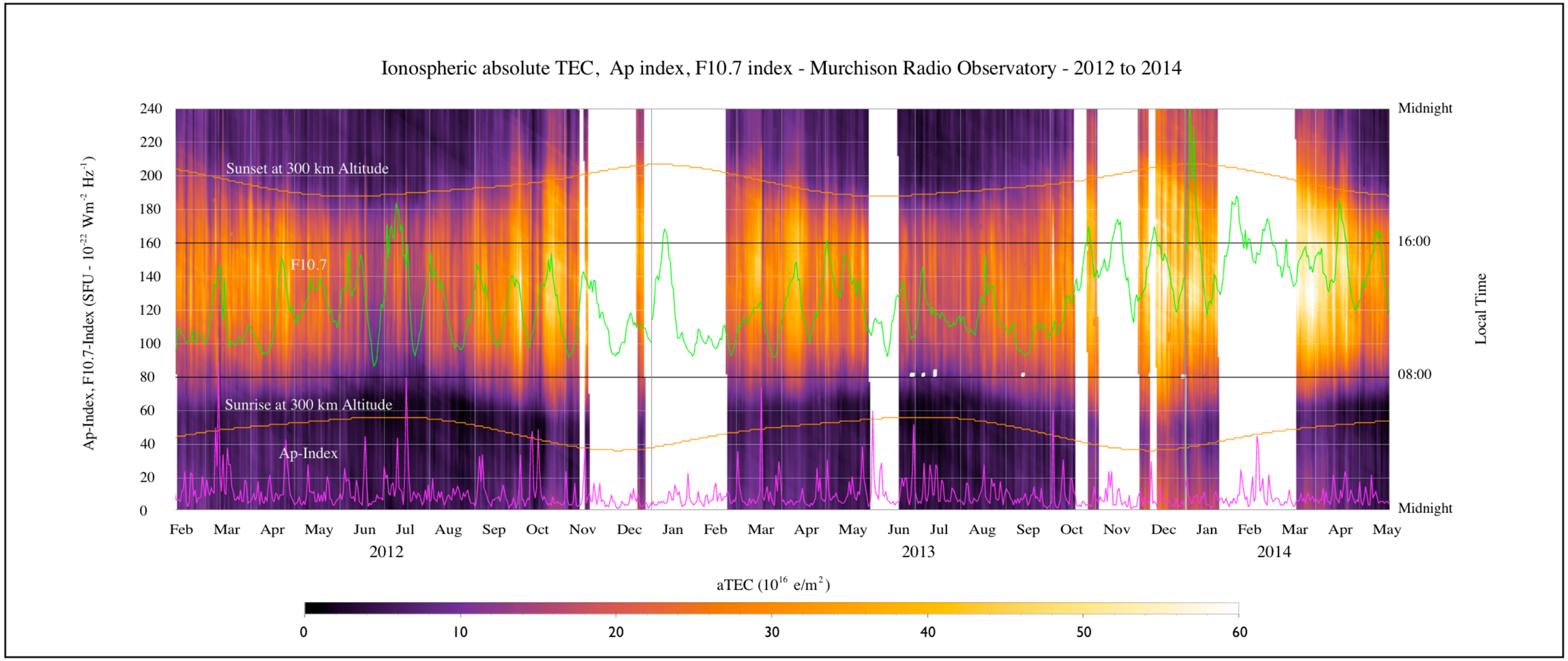


*Figure 6.7: Absolute TEC values produced from data acquired on the MRO over the interval 2012-2014. Waterfall plots display daily readings at intervals of 6 minutes. The F10.7 (10.7 cm - 2800 MHz) data, in units of SFU ($10^{-22}$ $Wm^{-2}$ $Hz^{-1}$), data are provided as an analogue to solar photoionising electromagnetic flux. The $A_p$ index is a daily averaged, planetary-wide interpretation of the $K_p$ three-hourly index, which is measure of the horizontal magnetic activity at the Earth's surface. Over this interval, about 500 readings over a value of 80 TECU were captured.*

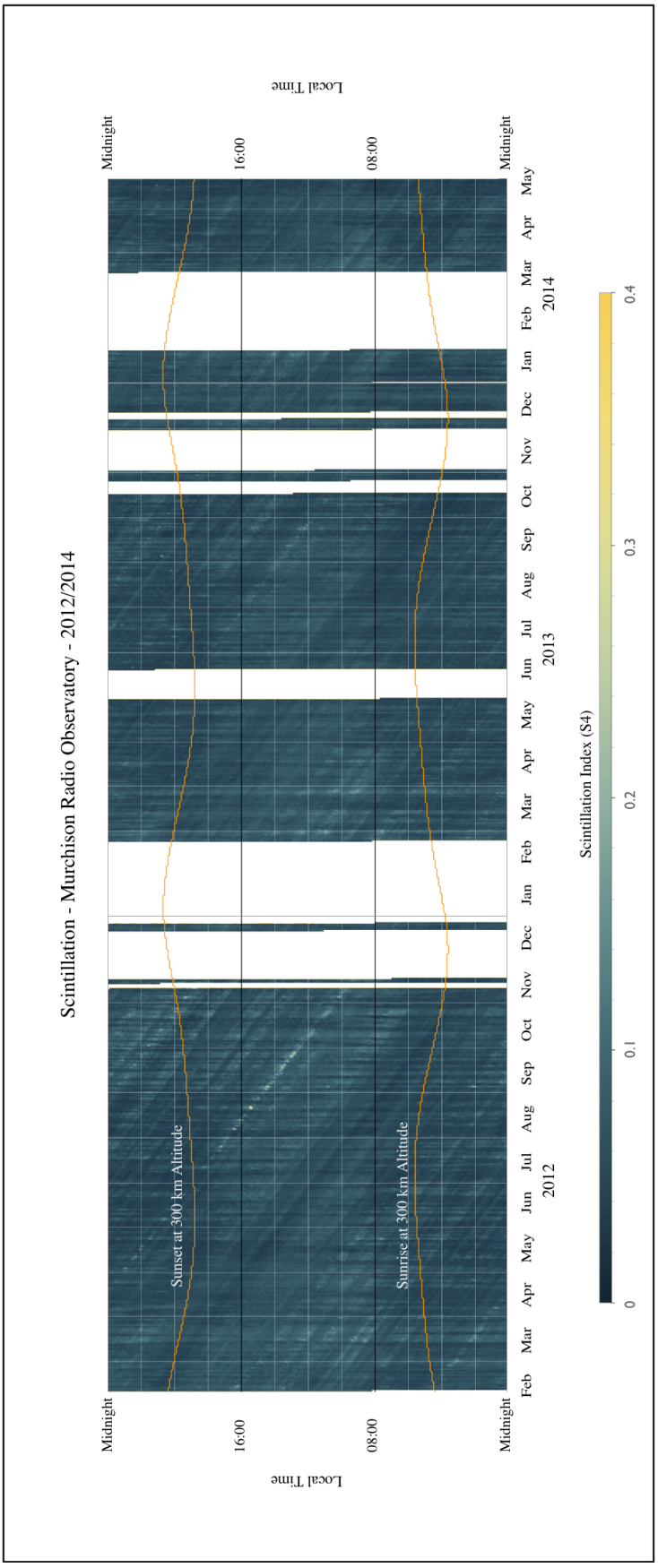


*Figure 6.8: Scintillation ($S_4$) values produced from data acquired on the MRO over the interval 2012-2014, reproduced over 10 minutes intervals.*

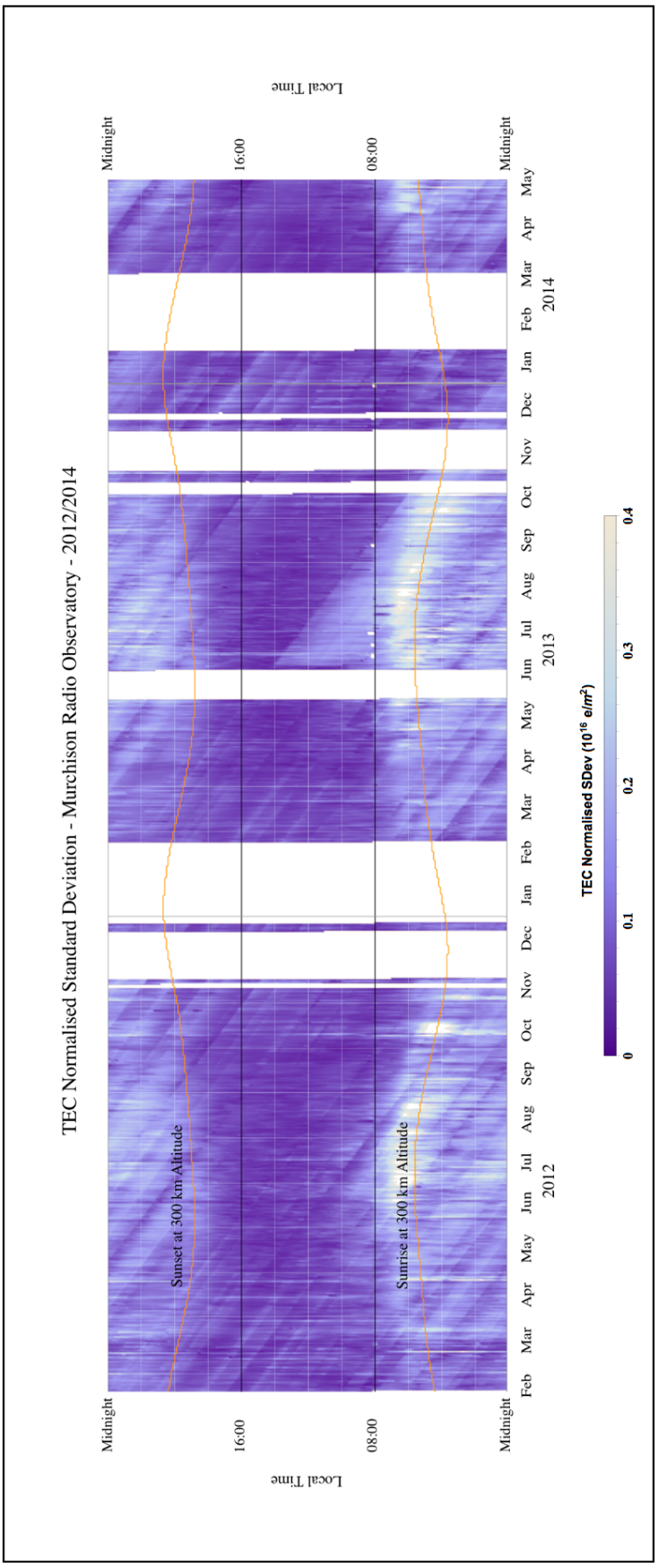


*Figure 6.9: TEC normalised standard deviations produced from data acquired on the MRO over the interval 2012-2014, reproduced over 10 minutes intervals.*

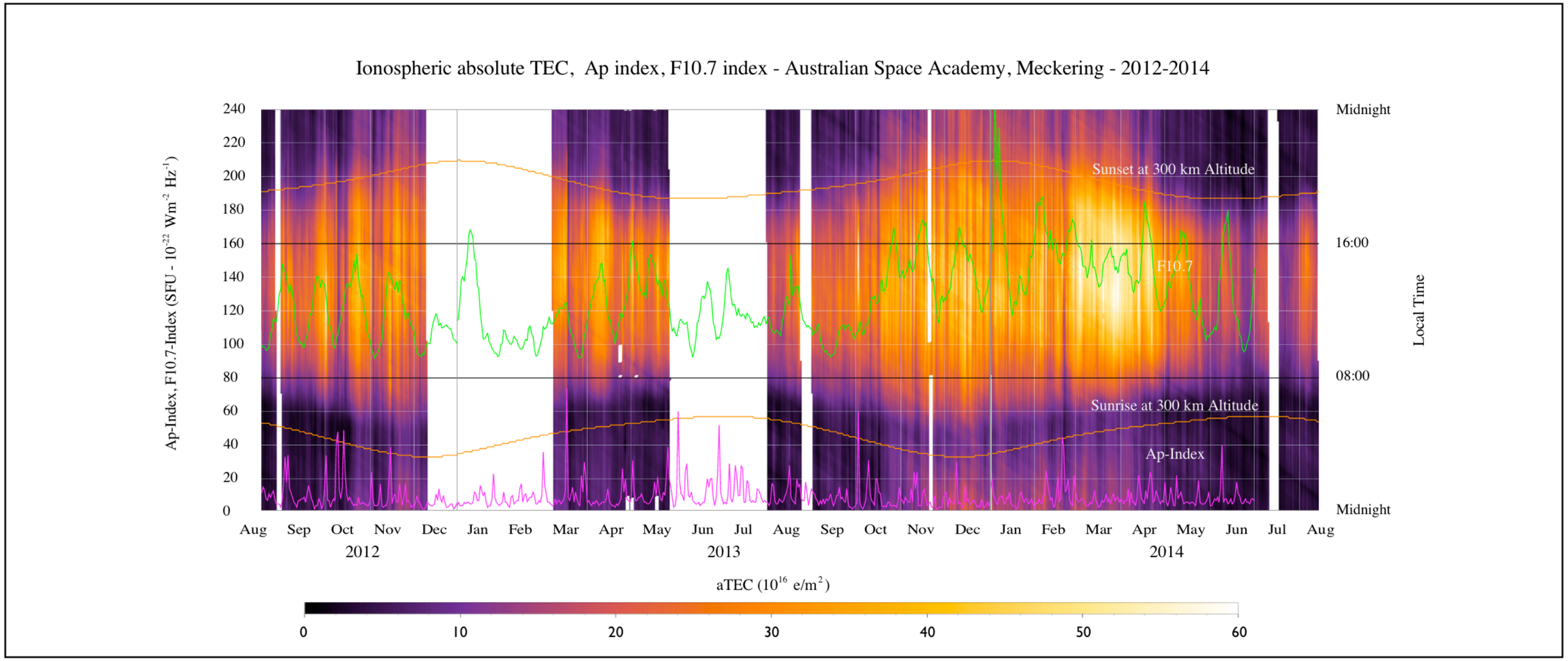


*Figure 6.10: Absolute TEC values produced from data acquired on the Australian Space Academy campus at Meckering over the interval 2012-2014. Waterfall plots display daily readings at intervals of 6 minutes. The F10.7 (10.7 cm - 2800 MHz) data, in units of SFU ($10^{-22}$ $Wm^{-2}$ $Hz^{-1}$), data are provided as an analogue to photoionising solar electromagnetic flux. The $A_p$ index is a daily averaged, planetary-wide interpretation of the $K_p$ three-hourly index, which is measure of the horizontal magnetic activity at the Earth's surface. Over this interval, only about 200 readings over a value of 70 TECU were captured.*

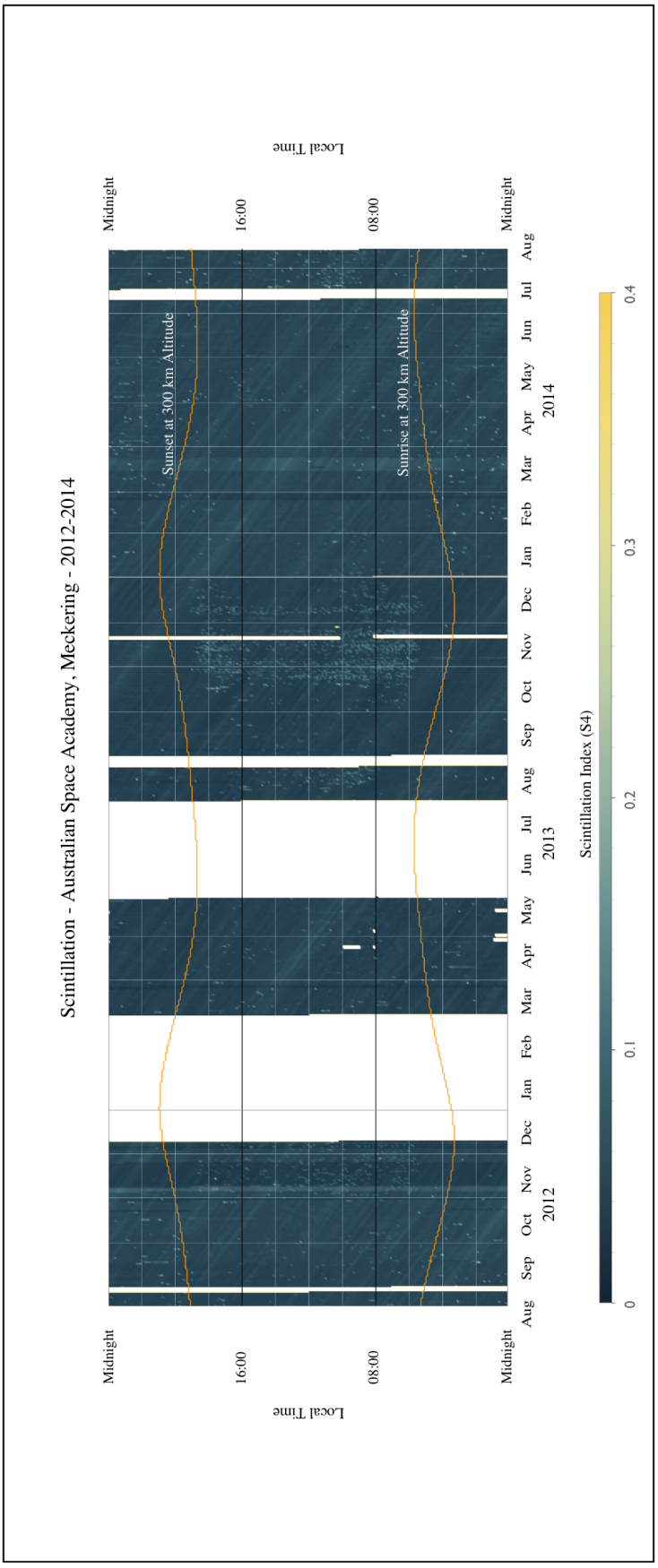


*Figure 6.11: Scintillation ($S_4$) values produced from data acquired at Meckering over the interval 2012-2014, reproduced over 10 minutes intervals.*

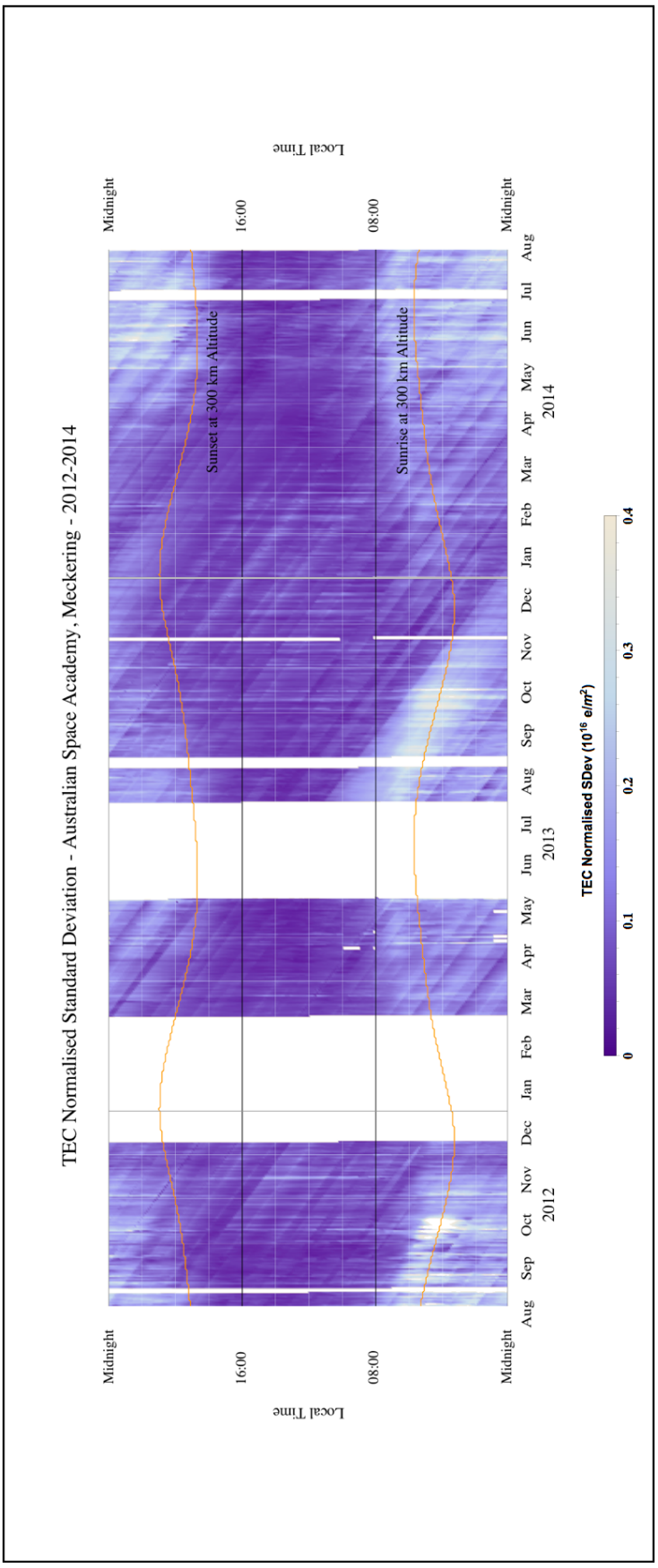


*Figure 6.12: TEC normalised standard deviations produced from data acquired at Meckering over the interval 2012-2014, reproduced over 10 minutes intervals.*

TEC observations at Meckering and the MRO, as mentioned previously, were constrained to those above 50° elevation so that the area of the ionosphere that contributed to each site was unique and didn't overlap the other, as shown in Figure 6.13.

Ionosphere viewed from the MRO (blue) and Meckering (red) at 350 km altitude for an observation elevation of 50°


*Figure 6.13: TEC observations on the MRO and at Meckering were constrained to 50° elevation, ensuring that the ionospheric observations (at 350 km altitude) by each GPS receiver didn't overlap.*

### 6.2.1. Epochs

GPS data acquisition took place during solar cycle 24, over 2 distinct epochs, as illustrated in Figure 6.14.

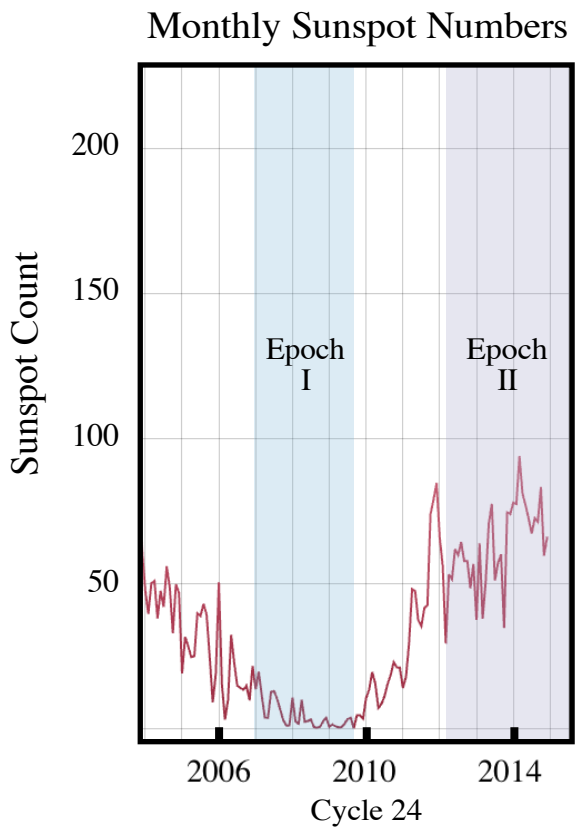


*Figure 6.14: Epochs over which GPS-derived TEC and $S_4$ readings were acquired. Epoch I comprised a period of low sunspot activity corresponding to a transition from solar cycle 23 to cycle 24. Epoch II comprised a period of maximum sunspot activity during cycle 24.*

(1) Epoch I (E1) spanned a transition into cycle 24, during which smoothed sunspot numbers (SSN) were at a minimum. During the period of this study, SSN fell from a high of 12.0 in January, 2007, to a low of 1.7 in November and December 2008 (SILSO data/ image, Royal Observatory of Belgium, Brussels). Measurements were conducted initially during site visits as opportunity permitted, typically for periods of less than 7 days. Later, systems were deployed over extended periods but suffered power and equipment failures under harsh conditions. Stanley Solomon et. al. (Solomon, Woods et al. 2010) demonstrated that solar activity as indicated by the flux of solar extreme-ultraviolet radiation, was anomalously low over the interval 2007 - 2009, a period that corresponds to that over which the entire GPS data set collected for the early part of this study was obtained.

(2) Epoch II (E2) spanned the peak of the current solar cycle. Over this period, SSN climbed to a high value of 82.0 in April, 2014. Two GPS systems were installed and monitored on a full-time basis over this interval. However, due to infrequent opportunities to visit either site, data loss due to equipment failure was often not rectified immediately. Accordingly, GPS system maintenance at Boolardy was provided on a volunteer basis by the MWA Solar Heliospheric Ionospheric (SHI) team at Curtin and members of MWA engineering staff during their routine visits to the site.

### 6.2.2. Perturbations.

Five factors that contributed to the stimulation or perturbation of the ionosphere were tracked and discussed in this thesis, being:

(1) Day length.

Daylight hours were mapped at an altitude of 300 km, the approximate height at which the ionosphere is exposed to sunlight. This altitude is a defining quantity in an investigation of the variability of TEC in the ionosphere (Section 6.2.4).

(2) F10.7 index.

This is an index of solar electromagnetic output at a wavelength of 10.7 cm (2800 MHz). This serves as an surrogate to solar EUV, the principal ionosphere electromagnetic ionising vector. This index is presented in units of Solar Flux Units (SFU) ($10^{-22}$ $Wm^{-2}$ $Hz^{-1}$).

(3) Ap index.

The Ap index is a daily averaged, planetary-wide interpretation of the Kp three-hourly index, which is measure of the horizontal magnetic activity at the Earth's surface.

(4) Geomagnetic data.

Local geomagnetic data which were retrieved from data captured at the Ionospheric Prediction Service (IPS), Learmonth on the mid-north coast of Western Australia.

(5) TID propagation.

TIDs which were detected in data and studied in depth (Section 6.3).

### 6.2.3. TEC Variability Across Two Epochs.

During each of the epochs studied, TEC and scintillation records are incomplete over the span of a single year. However, over a period of several years, a fairly complete annual record was produced over the peak of cycle 24 for both Meckering and Boolardy sites. This combined record is represented in the statistical analyses that follow. E1 is less-well represented, however, both the period of peak TEC and minimum TEC are either well represented or sampled and demonstrate clearly the lower TEC values year round that are typical of a solar cycle transition/ minimum.

E1 TEC data comprised 2,557,552 values captured between July 2008 and October 2009. Of these, 99.0% of readings fell in the range 1-20 TECU. The maximum TEC values returned were of order 34 TECU, with a single 35 TECU example. Approximately 91.4% of values fell in the range 1-15 TECU.

E2 TEC data comprised 2,937,272 values for Boolardy over an annual cycle from February 2012 to May 2014 and 3,403,944 values for Meckering, the record for which was missing 10 days of a complete annual cycle. At Meckering, the TEC record covers the period August 2012 to August 2014. At Boolardy, 99.5% of readings were a maximum of 60 TECU. At Meckering, 98.1% of readings ranged to 50 TECU to a maximum of less than 70 TECU.

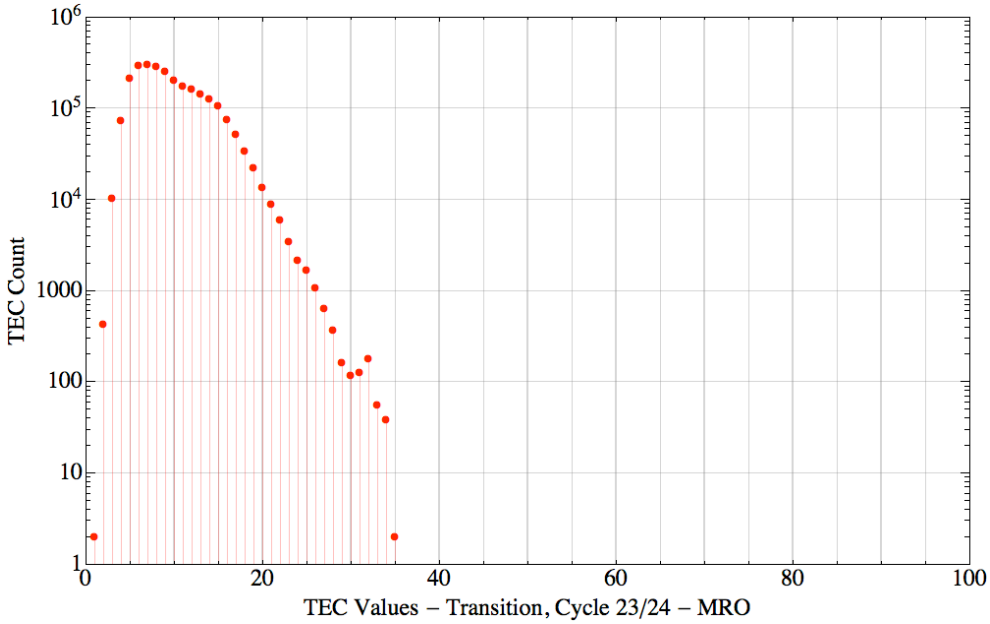


*Figure 6.15: The numbers of GPS TEC values captured on the MRO over the period from July 2008 to October 2009, during the transition of solar cycle 23 into cycle 24. The total number of each TEC value (TEC Count) are plotted on a logarithmic scale against the associated TEC value.*

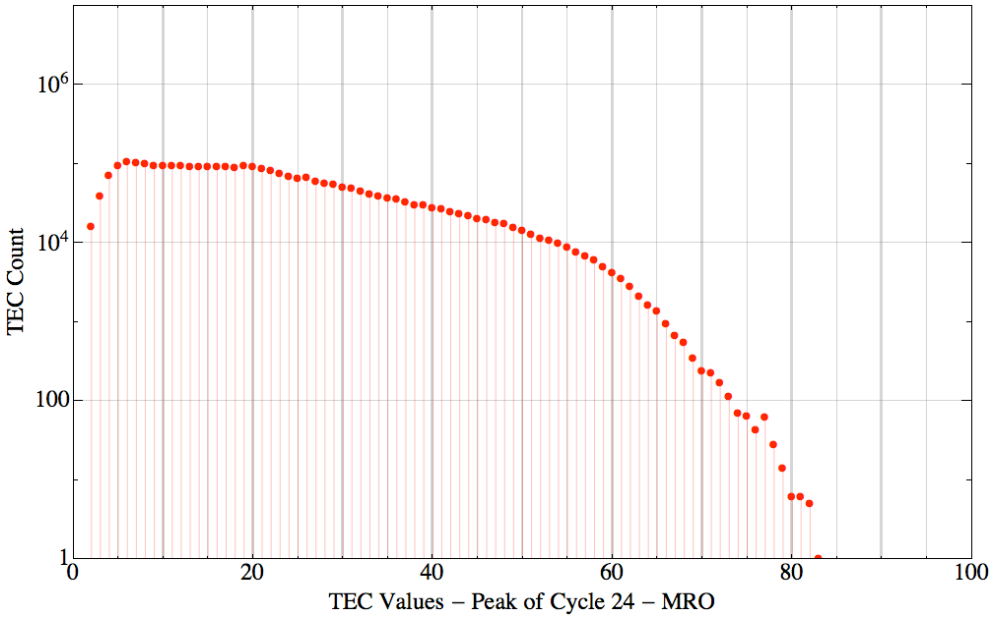


*Figure 6.16: The numbers of TEC values calculated from GPS data captured at Boolardy over the period from February 2012 to May 2014, during the peak of solar cycle 24. The total number of each TEC value (TEC Count) are plotted on a logarithmic scale against the associated TEC value.*

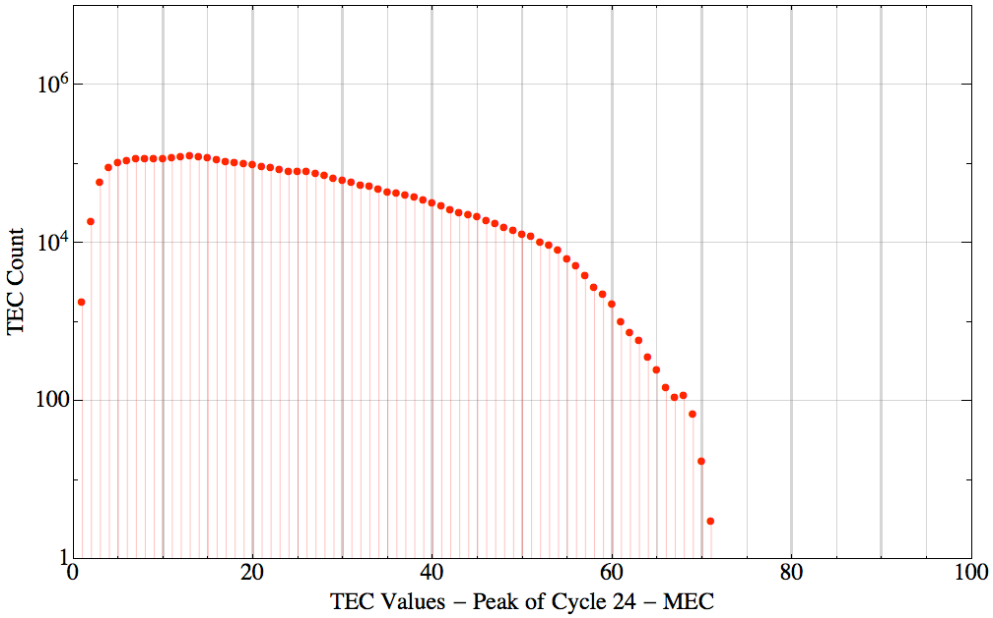


*Figure 6.17: The numbers of TEC values calculated from GPS data captured at Meckering over the period from August 2012 to August 2014, during the peak of solar cycle 24. The total number of each TEC value (TEC Count) are plotted on a logarithmic scale against the associated TEC value.*

Figures 6.15-6.17 present semi-logarithmic plots of (log) TEC counts against TEC values. These clearly demonstrate the very much lower levels of TEC exhibited during the transition to cycle 24 compared to the peak of cycle 24 and the noticeably lower values experienced at Meckering, 519 km south of Boolardy.

### 6.2.4. TEC Variability Across the Ionosphere.

The standard deviation in TEC between all GPS satellites at any instant is a measure of the variability of TEC across the accessible sky, as satellites are observed in differing directions. TEC readings (Figures 6.4, 6.7 and 6.10) were binned over 6 minute intervals. Standard dev iations were calculated for all readings in each bin and normalised.

Hence, where SD was lowest, TEC variability across the sky was lowest. Conversely, larger SD indicated greater variability in TEC (Figure 6.18).

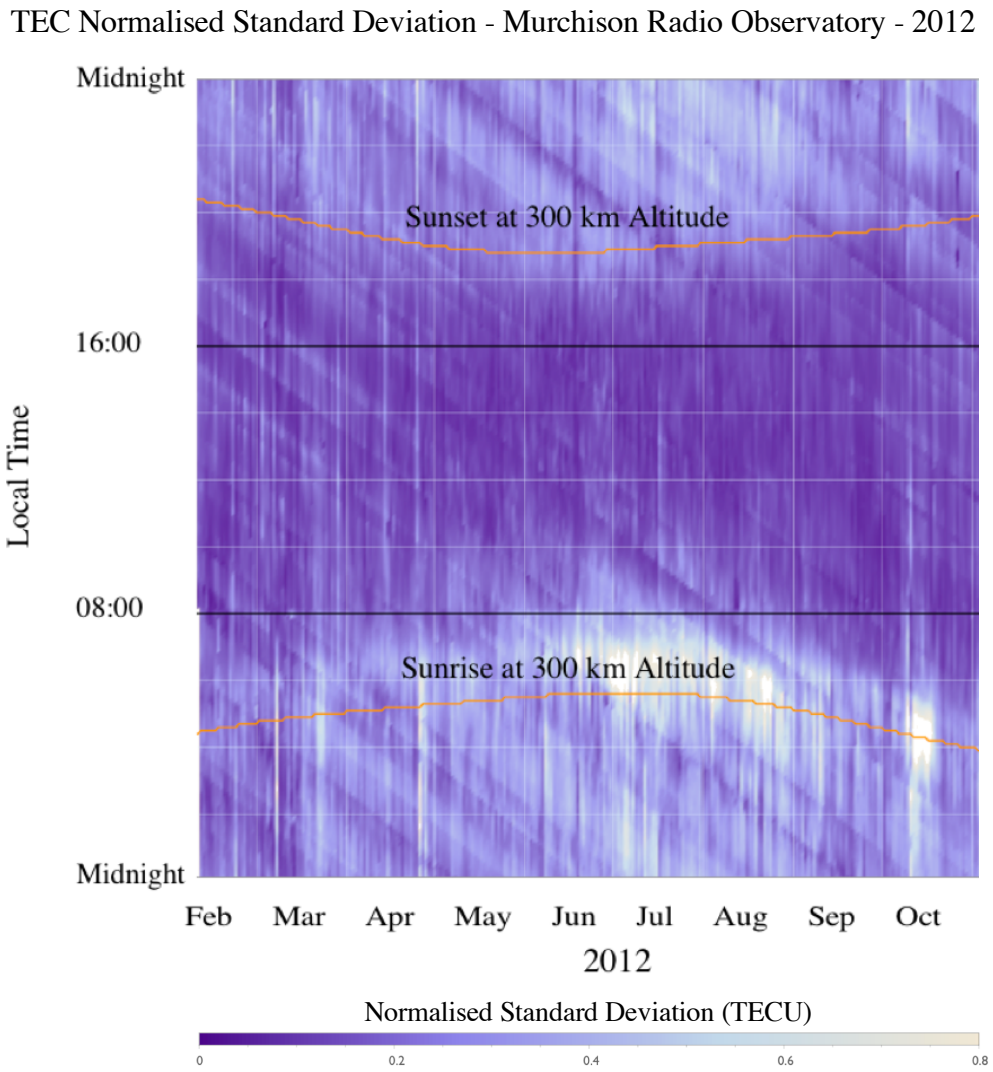


*Figure 6.18: Normalised standard deviation of TEC readings for the months February to October, 2012 at the MRO. Dark areas represent lower standard deviation and therefore, lower variability of TEC across the sky. The brightest regions exhibit the highest TEC variability across the field of view.*

Over most of the year during both E1 and E2, the largest TEC SD occurred during the ~90 minutes between astronomical sunrise (sunrise at 300 km altitude) and local dawn. The variability of TEC across the telescope's field of view is an important issue in calibration of the instrument and in observation quality (Helmboldt, Lazio et al. 2012).

The TEC SD between satellites can be calculated quickly and might prove a valuable input to an observer's ionosphere quality index, discussed later in this chapter (Section 6.5.1).

### 6.2.5. TEC Response to Perturbation by Enhanced Solar, Electromagnetic Radiation.

The dominant driver of elevated TEC was solar EUV radiation, which varied throughout the year with the change of seasons and with the onset of transient events such as solar flares. At the winter solstice, the MRO received ~10 hours and 18 minutes of sunlight (Figure 6.18). At the summer solstice, the MRO received ~13 hours and 59 minutes of daylight, a difference of 3 hours and 43 minutes, or 36%. However, the effect was exaggerated by the difference in the solid angle that the Earth produces with the Sun's emissions due to eccentricity in the Earth's orbit. The Earth experiences 7% greater irradiation during the southern, summer solstice with respect to the southern winter solstice due to closer proximity to the Sun alone.

Significant features were observed in the ionosphere that aligned with levels and changes in levels of solar flux. During E2, from October to April (2013-2014) inclusive, elevated TEC continued through the evening and declined to minimum values in the time between astronomical and terrestrial sunrise. This corresponded to lower standard deviations in TEC across the whole day. This outcome is significant to classes of MWA observations for which TEC variability is a significant issue (Mitchell, Greenhill et al. 2008).

From May to September, peak TEC values fell quickly after sunset to minimums also between astronomical sunrise and terrestrial sunrise. Lower TEC standard deviation values were observed during daylight hours than at night.

The F10.7 index is a measure of solar 10.7 cm, 2800 MHz, electromagnetic radiation that correlates well with both sunspot number and EUV emissions. This quantity has been measured since 1947 in Canada (http://spawx.nwra.com/spawx/f10.html). Measurements in units of SFU ($10^{-22}$ $Wm^{-2}$ $Hz^{-1}$), are made at ground level in all

weather conditions. The F10.7 index however, is normalised to a reading equivalent to that which would be observed at a constant 1 astronomical (AU) unit from the Sun.

During E2, over the entire period that TEC was observed and mapped (Feb 2012-August 2014; Figure 6.7), strong periodicity was observed in the F10.7 index. Over the interval March-October 2012 inclusive, where the periodic nature was least ambiguous, the F10.7 index period was 25.6 days with a standard deviation of 3.0 days. The peak extent of daily TEC corresponded well with the peak values of the F10.7 index. These observations suggest that peaks in 10.7 cm radiation corresponded to the prolonging of daytime TEC levels into the late evening/early morning. The nighttime ionosphere ascends to higher altitudes due to the longer mean lifetime of ionised particles at higher altitudes, due in turn to an exponential decrease in neutral density. Peaks in the F10.7 index did not necessarily correspond to locally higher TEC readings however.

Over the interval February 2012 to November 2013, the RMS of F10.7 was ~120 SFU. November saw a rise in RMS F10.7 to ~145 SFU. This started to decline in May 2014.

Over E1, the F10.7 index periodicity was subdued and peaky. the RMS of F10.7 values ranged between 60-70 SFU.

Daily minimum TEC values persistently occurred in the ~90 minutes between astronomical sunrise and terrestrial sunrise, at which time the highest variability in TEC across the sky was encountered (Figures 6.4, 6.7 and 6.10). This is to be expected, as the ionosphere at higher altitudes first comes under solar radiation and later, lower altitudes comes under increasing solar influence.

### 6.2.6. TEC Response to Perturbation by Geomagnetic Activity.

The Sun's magnetic field interacts constantly and variably with Earth's magnetosphere, with consequences for the electron content of the plasmasphere and ionosphere. Open magnetic field lines have been shown to extend from the lower corona to Earth orbit and act as channels for relativistic electron jets to impact the magnetosphere (Rust, Haggerty et al. 2008). The effects of the solar magnetic field impinging the magnetosphere are detectable at the Earth's surface and are constantly monitored by magnetometers. One index of geomagnetic activity is the K index, which is a measure of the 3 hourly change in the horizontal magnetic components of the Earth's magnetic field at a particular location. The index is interpreted uniquely for each site, depending on the magnitude of magnetic field changes that are experienced at that site. The Kp index is a planetary index of mean values from sites worldwide. The Ap index is the daily mean of the nine, three-hourly Kp index values. The Ap index (purple trace on Figures 6.4, 6.7 and 6.10) used in this thesis is that generated by NOAA, Boulder, Colorado (Section 5.1(7)). There is also magnetometer data available closer to the MWA, captured at the Learmonth Solar Observatory, 560 km NW of the MRO. Magnetometer readings used in the study of the March 17$^{th}$, 2013 geomagnetic storm (Figures 4.2 and 6.19) were recorded at Learmonth.

Due to geomagnetic activity, electrons spiral along field lines, impinging the ionosphere at polar latitudes and often resulting in Aurora. However, episodes during which the Sun ejects large amounts of coronal plasma, threaded by magnetic field lines, might if large enough, induce strong geomagnetic effects. These coronal mass ejections (CMEs) are considered to be the primary drivers of interplanetary disturbances (Liu, Manchester et al. 2007) and result in geomagnetic storms in the Earth's magnetosphere, with consequences for the ionosphere.

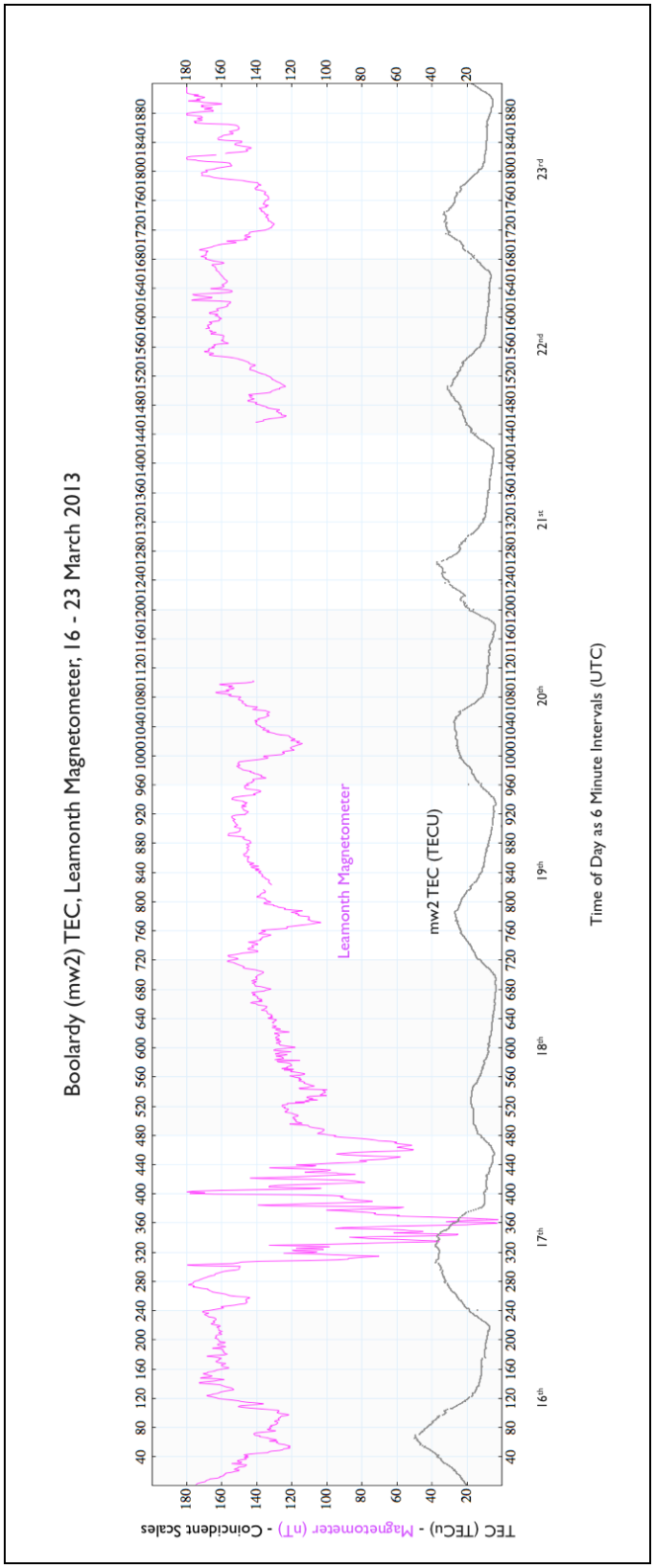


*Figure 6.19(a): Plot of TEC values measured either side of the event of March 17th, 2013. TEC values were depressed for several days following the event, particularly on the 18th and recovered slowly. Magnetometer data was captured at the Leamonth Solar Observatory.*

On March 17th, 2013 (local time; see Figures 6.7 and 6.10) a geomagnetic storm created by a CME, which originated from active region AR1692, induced a fluctuation of almost 180 nT (Figure 6.19) in the magnetometer located at Learmonth (Section 5.1(1)). A rapid drop in aTEC followed (Figures 6.19 (a) and (b)). Several days of subdued aTEC readings followed. The TEC did not recover its pre-storm value until March 21st. This event generated interest worldwide (Bernard V. Jackson, private communication). Figure 6.19(a) displays TEC readings from the MRO (mw2) and magnetometer data from the Leamonth solar observatory for the period 16th - 23rd March 2013. Figure 6.19(b) focusses on the day of the event in greater detail.

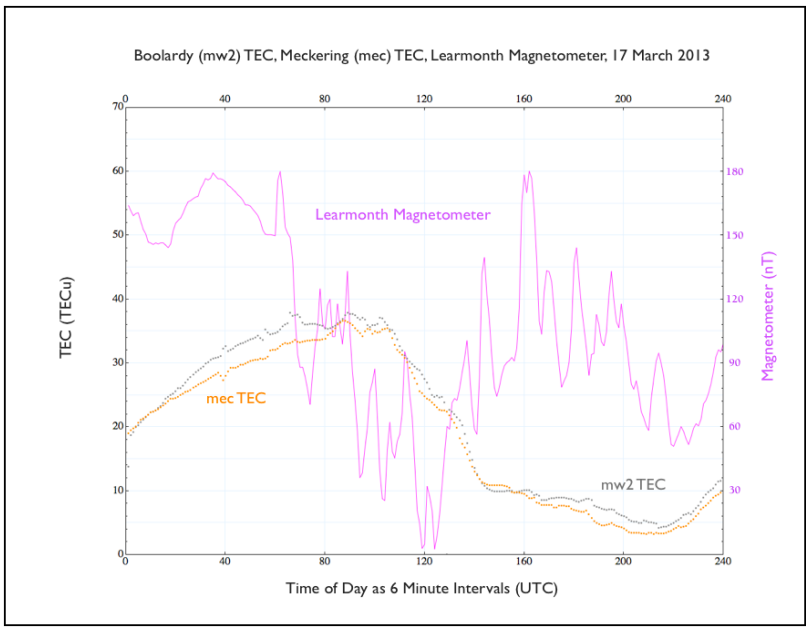


*Figure 6.19(b): Ionospheric TEC measured over two locations, at Meckering (-31.639°, 116.989°) and Boolardy (-26.984°, 116.535°) during a severe geomagnetic storm. Magnetometer data were captured at the Learmonth Solar Observatory.*

This event, preceded by a now well studied CME originating on 15th March (Xiao, Yang et al. 2014, Li, Hudson et al. 2015) will be shown in Chapter 6 to be particularly useful in highlighting phenomena in the ionosphere that are relevant to this study and to the operation of the MWA, such as TIDs (Section 6.3). Similar, previous events have been studied closely (Sojka, Rice et al. 2004, Mannucci, Tsurutani et al. 2008).

TEC readings at the MRO remained depressed for several days following the CME event, before slowly recovering. As a consequence of this event, large-scale TIDs were observed in the GPS measured TEC record and were studied in detail in this thesis (Section 6.3).

### 6.2.7. Multi-path Artefacts in GPS TEC

The effects of multi-path interferences were evident in TEC data at very subdued levels. These were not given special consideration in the processing and analysis of TEC data. Figure 6.20, an extract of Figure 6.7, illustrates the barely discernible effect on readings.

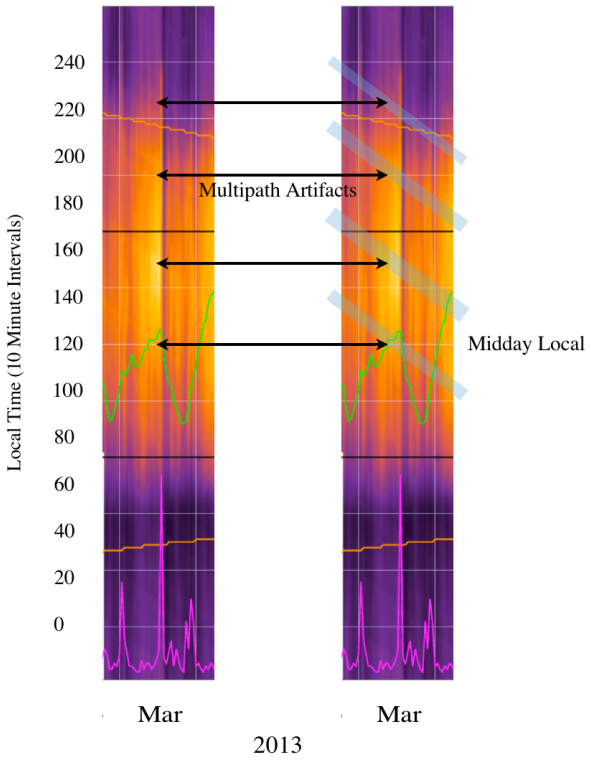


*Figure 6.20: Evidence for multi-path interference in TEC data recorded at Boolardy manifest as angled features that slope at the same rate as satellite precession, 4 minutes daily. In TEC readings, these were subdued.*

### 6.2.8. Scintillation ($S_4$).

Scintillation at MWA frequencies at the location of the MRO was expected to be negligible. In their report to the CSIRO as part of the Australian SKA proposal, Kennewell and Caruana (Kennewell, Caruana et al. 2005) produced maps of expected ionospheric scintillation modelled under WBMOD, the wideband ionospheric scintillation model curated by Northwest Research Associates (http://spawx.nwra.com/ionoscint/wbmod.html). These maps, reproduced here (Figures 6.21, 6.22, 6.23), display $S_4$ expected over three intervals at 100 MHz. These are polar plots of elevation~azimuth, with north toward the top. The first displays the least scintillation. The elevated readings between 50° and 60° elevation corresponds to the magnetic dip angle of the station.

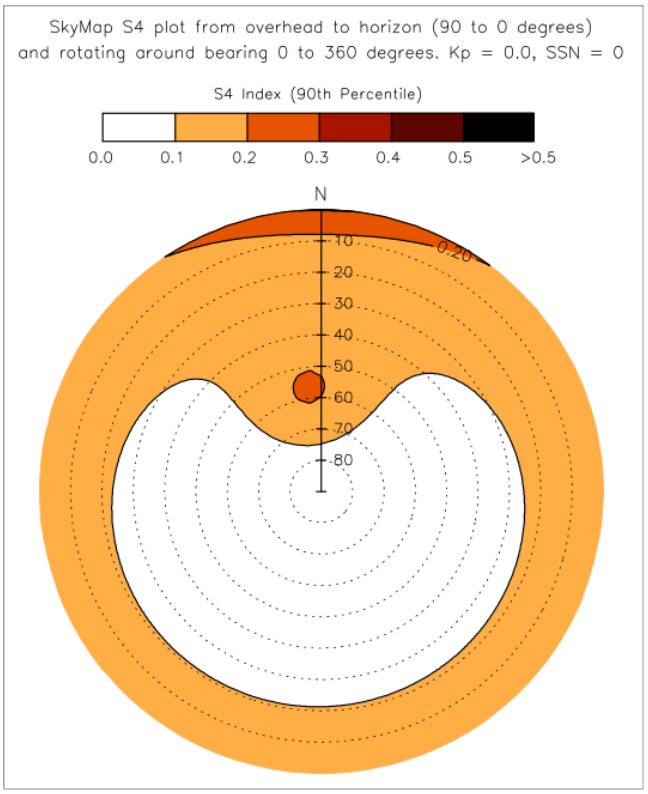


*Figure 6.21: Expected scintillation at the MRO for a SSN=0 and Kp=0 modelled under WBMOD. Reproduced from (Kennewell, Caruana et al. 2005).*

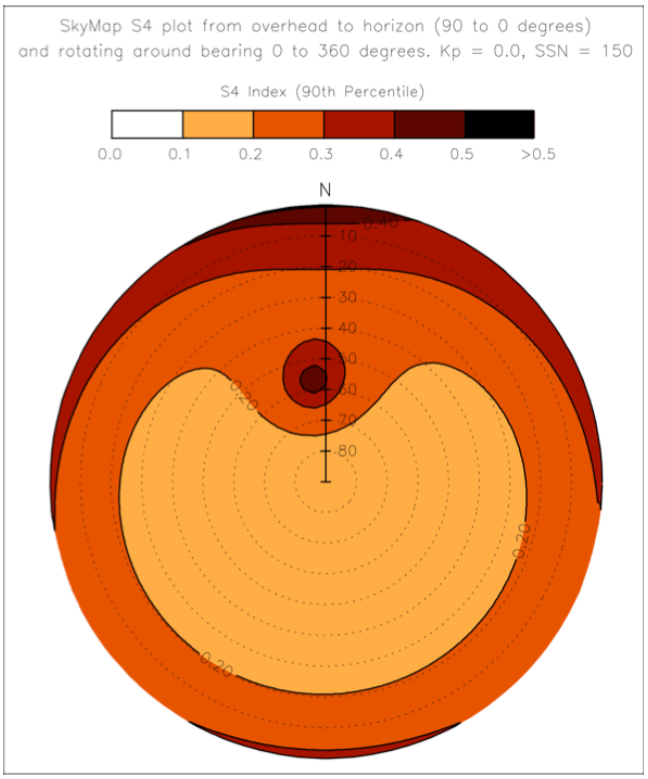


*Figure 6.22: Expected scintillation at the MRO for a SSN=150 and Kp=0 modelled under WBMOD. Reproduced from (Kennewell, Caruana et al. 2005).*

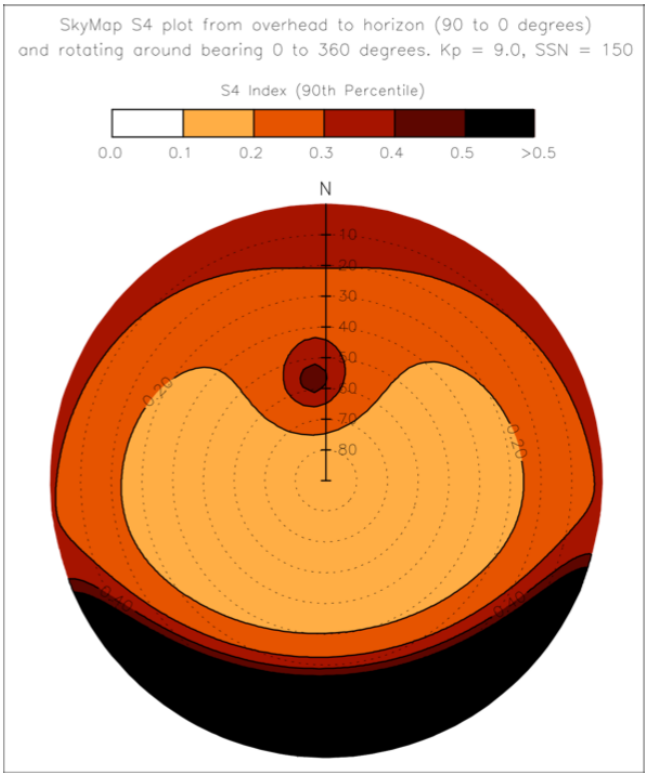


*Figure 6.23: Expected scintillation at the MRO for a SSN=150 and Kp=9 modelled under WBMOD. Reproduced from (Kennewell, Caruana et al. 2005).*

Kennewell et. al found that the worst case result, given in Figure 6.23 of scintillation approaching levels greater than 0.5 below 30° elevation, occurs less than 0.1% of the total time.

My observations however, were conducted at GPS frequencies. Typically, over both E1 and E2, features in the data were aligned with the GPS satellite precession rate as shown in plots for select individual satellites (for clarity) over two intervals in Figures 6.24 and 6.25.

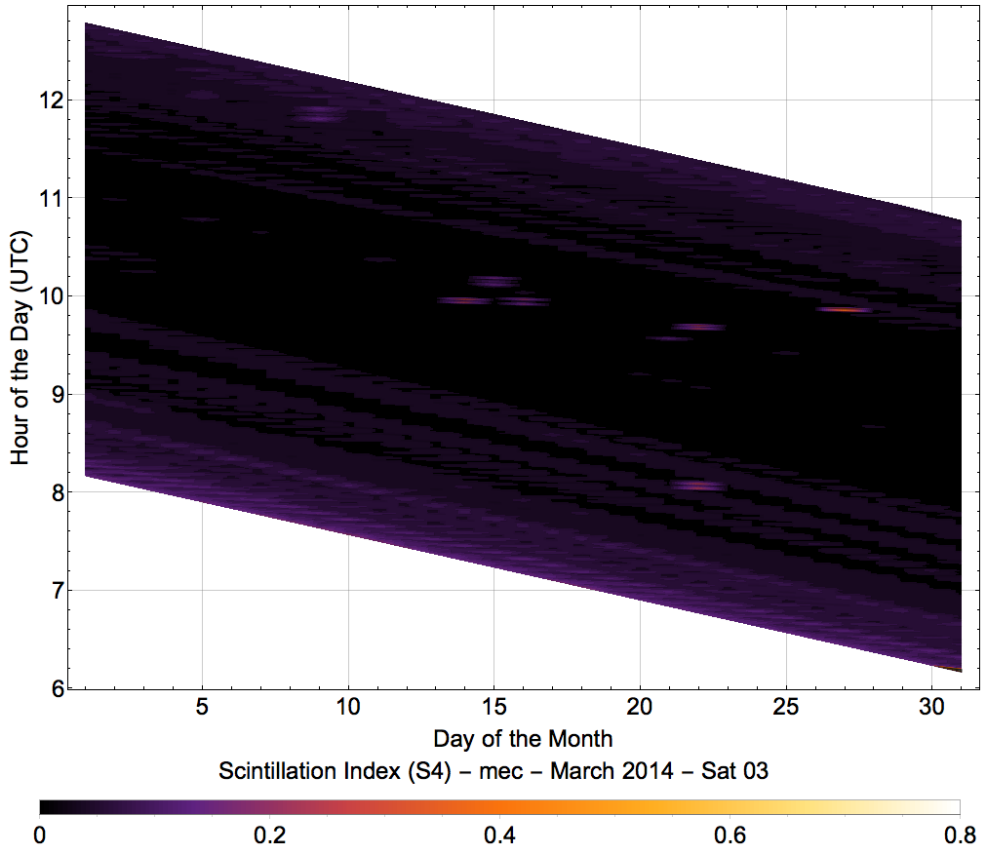


*Figure 6.24: $S_4$ measured with a single GPS satellite, PRN 03, at Meckering over the month of March, 2014.*

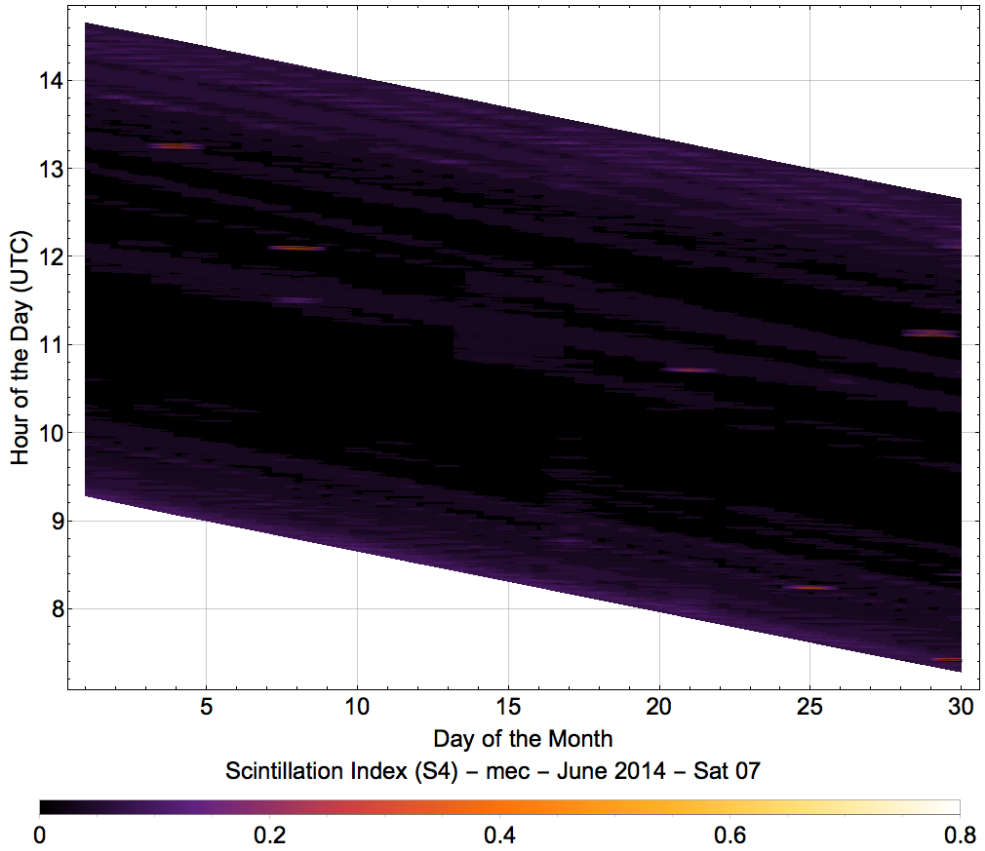


*Figure 6.25: $S_4$ measured with a single GPS satellite, PRN 07, at Meckering over the month of June, 2014.*

Elevated readings at the beginning and end of each satellite record result from an additional effect. Scintillation readings are typically higher at lower satellite elevations, resulting in brighter, inclined bands that run from the left to right following the slope of the waterfall plots. Other elevated readings cannot be attributed to elevated $S_4$ values and many also precess.

Figure 6.26 demonstrates the fixed locations of features (data) over time. Each plot from the top down (a through f) presents data captured 2 days later than the previous plot. In each subsequent plot, time moves through the image, traversing 8 minutes, or ~4 minutes daily, equivalent to the precession rate of a GPS satellite. Therefore, features that remain aligned are the result of multi-path interferences, as are the majority of recurring features as these are stationary in the landscape regardless of the time of day. Non-recurring features can result from temporary interferers such as the movement of vehicles nearby.

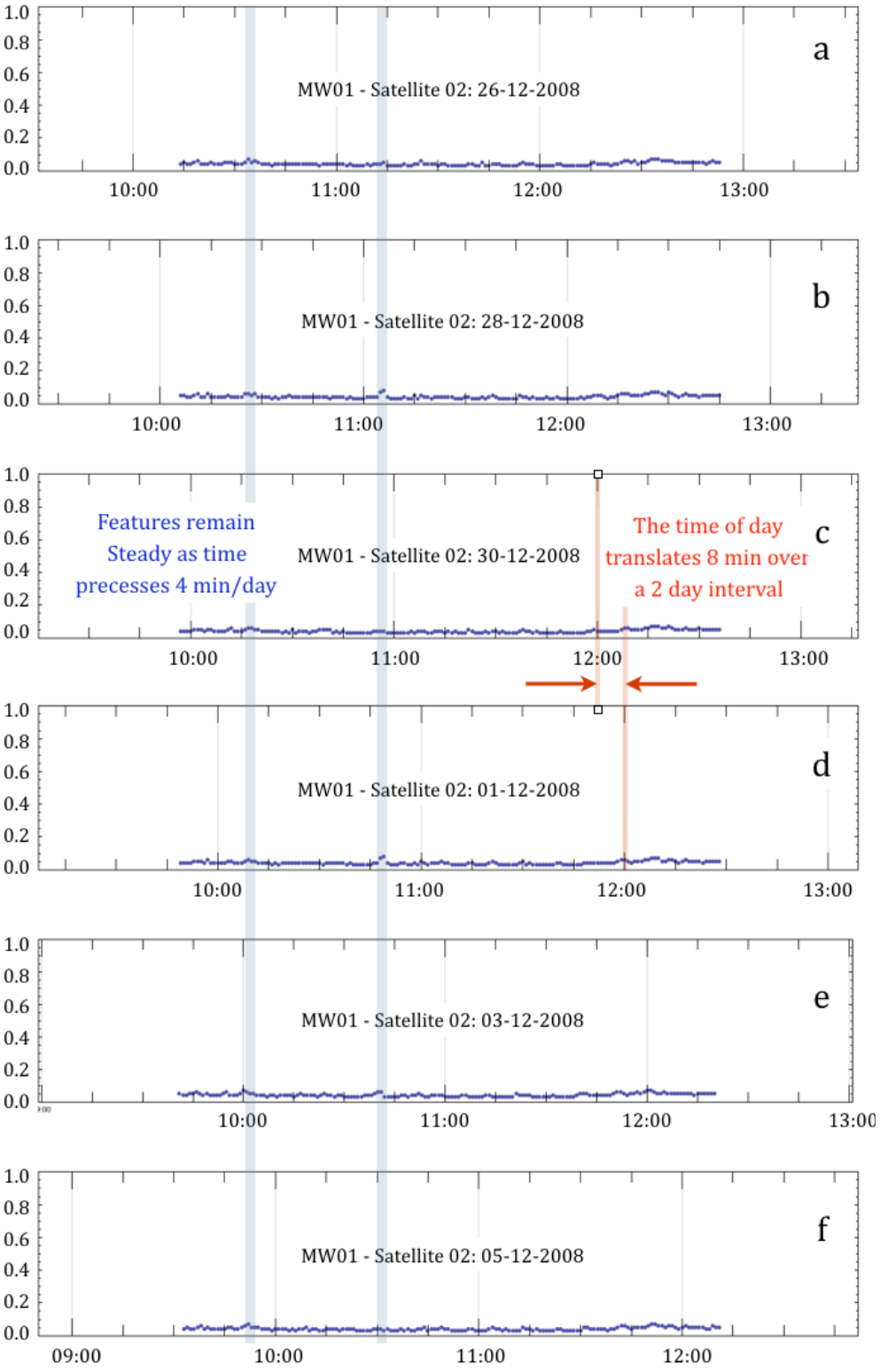


*Figure 6.26: Six plots of $S_4$, acquired at the MRO from a single satellite, separated in time by 2 days each from the top to the bottom plots. Time moves through subsequent plots an amount equivalent to the precession rate of GPS satellites, ~4 minutes per day.*

Occasional excursions in $S_4$ however, observed in data returned by all satellites visible over a particular interval but not repeated on following

days, cannot be eliminated as legitimate scintillation events. Figure 6.27 displays one such sequence of $S_4$ readings captured by the 4 GPS satellites that were visible over an interval on April 26th, 2009.

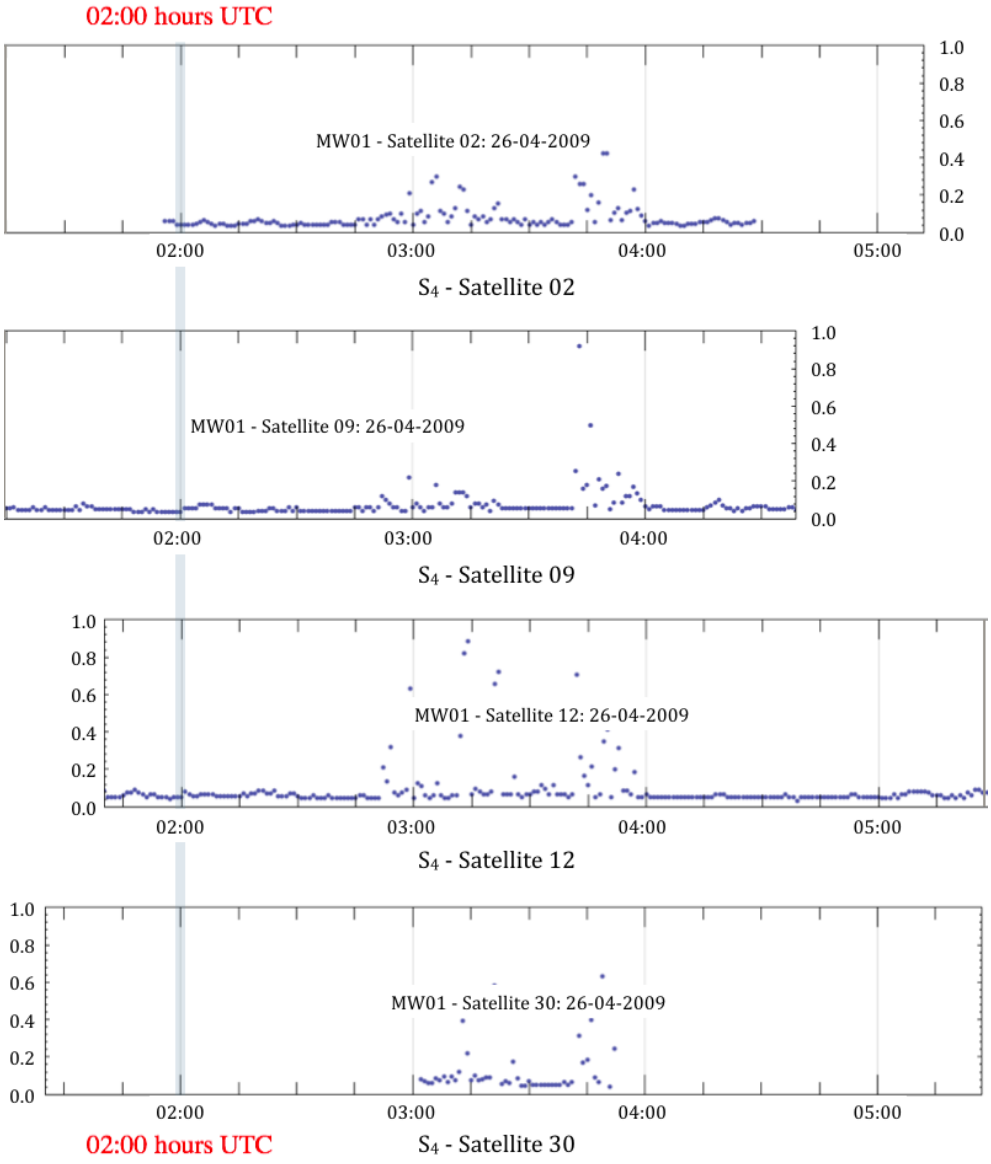


*Figure 6.27: The $S_4$ index for 4 satellites aligned over a common interval on April 26th, 2009 at the MRO display possible scintillation at GPS frequencies. These were the sole readings at these levels over the extent of E1.*

Events discussed as occurring on this day included a magnetospheric substorm (Kubyshkina, Sergeev et al. 2011) and observations of plasma bubbles using the 53MHz MST radar located at Gadanki, India (13.5 °N, 79.2 °E, 6.5 °N magnetic latitude) (Patra and Pavan Chaitanya 2014). The former included observations using the fluxgate magnetometer on

the THEMIS spacecraft, however, each was conducted at much higher latitudes than the location of the MWA. The event shown in Figure 6.27 was unique for the epoch.

In conclusion, modelling conducted specifically for the location of the MRO under known environmental parameters, predicted that very low levels of $S_4$ would be encountered. My GPS satellite-generated scintillation data show no evidence of $S_4$ other than occasional, events with values displayed typically falling in the range 0.0 to <<0.1.. Measurement of scintillation with VHF, satellite mounted beacons (Section 6.6) would compliment the work reported here.

## 6.3. Observations of Travelling Ionospheric Disturbances.

I have observed TIDs in GPS TEC data captured on March 17$^{th}$, 2013 with systems deployed at Boolardy homestead (mw2) and Meckering (mec) (Section 6.3). Due to a severe geomagnetic storm, a rapid drop in TEC was experienced (Figures 6.19 (a) and (b)), followed by several days of subdued TEC readings. GPS satellite data revealed wave-like oscillations in ionospheric TEC of up to 3 TECU for up to three contiguous propagating wave cycles. Each of these oscillations was evident in records acquired at Meckering (mec) and Boolardy (mw2) and were clearly coupled. Of particular interest was an interval spanning the hours 06:00-12:00 UTC (14:00-20:00 local time, March 17$^{th}$ 2013), although instances of such behaviour were observed out to approximately 16:00 UTC (24:00 local time). Figures 6.28 and 6.29 highlight those intervals over which TIDs reported here were evident.

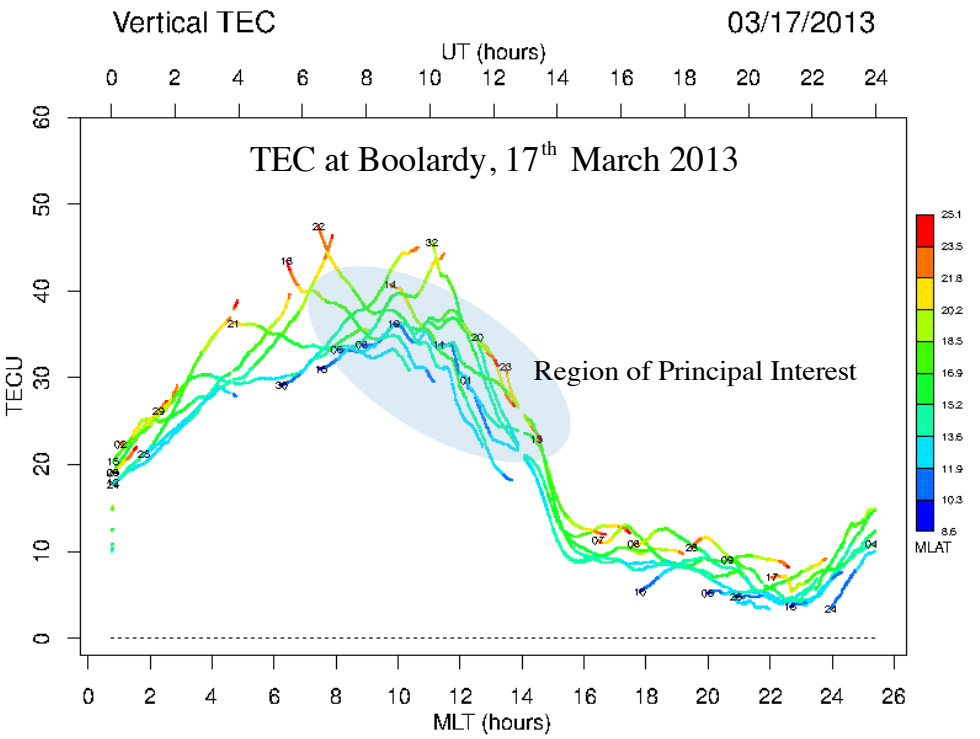


*Figure 6.28: GPS TEC record for a number of GPS satellites for March 17th, 2013 at Meckering (mec). Each trace reveals the TEC during the satellite pass and the MLAT location (by colour) at the time readings were taken.*

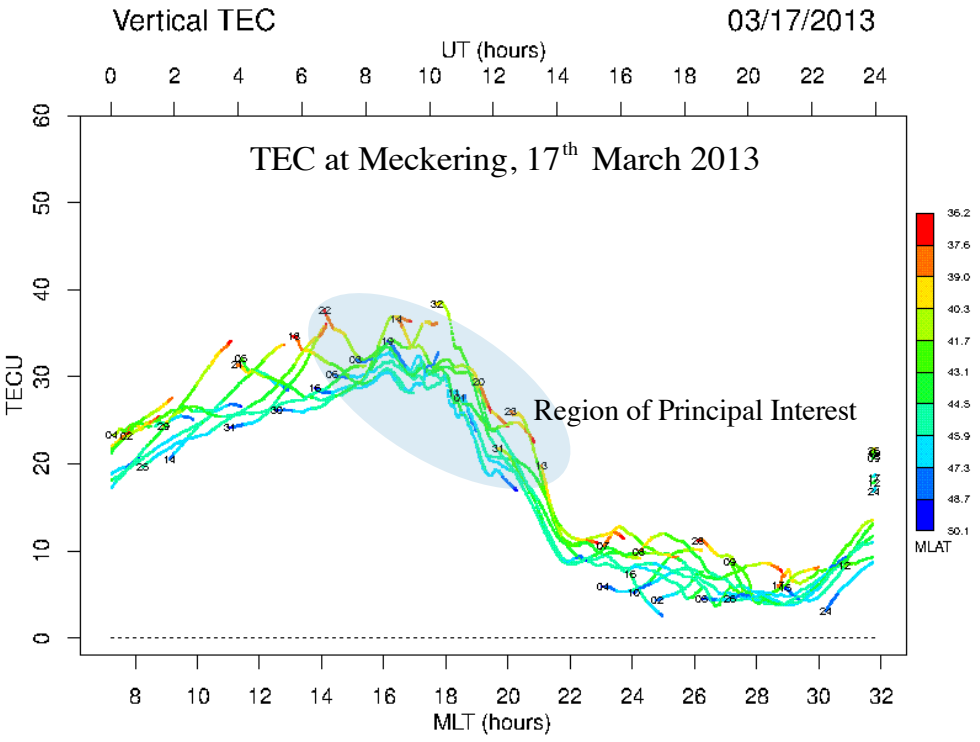


*Figure 6.29: GPS TEC record for a number of GPS satellites March 17th, 2013 at Boolardy (mw2). Each trace reveals the TEC during the satellite pass and the MLAT location (by colour) at the time readings were taken.*

Plasma redistribution occurs orthogonal to TEC isoclines at velocities of order 100 $ms^{-1}$, although measured up to 1000 $ms^{-1}$ (Afraimovich, Astafyeva et al. 2008) during a geomagnetic storm of similar magnitude to the one discussed in this thesis. Velocities of 180 $ms^{-1}$ have been observed (MacDougall, Abdu et al. 2009). MacDougall et. al used the SD of ΔNmF2/NmF2 as a measure of the magnitude of TIDs in a paper that discusses phenomena close to the sunrise terminator (MacDougall and Jayachandran 2011). Conjugate terminator effects have been found in GPS derived TEC data (E. L. Afraimovich, S. V. Voyeikov et al. 2009). This phenomenon is a candidate for future study.

Astronomical sunset (sunset at 300 km altitude) occurred at 11:30 hours UTC on March 17$^{th}$, 2013 at Meckering and at 11:40 hours at Boolardy.

### 6.3.1. Method Applied to the Determination of the Properties of Observed TIDs.

In the first instance, the TIDs reported here were observed through a visual inspection of daily GPS derived TEC data (Figure 6.30). However, once detected, a rigorous method, discussed here, was applied to the determination of their properties.

Figure 6.30 displays six corresponding TEC records for mec and mw2. Three distinct regimes are present during the interval of interest, where TEC was increasing (satellite 16), where TEC values overall were approximately stationary (satellites 03 and 06) and where TEC was falling (satellites 18, 19 and 22). In each case, TEC changes at Meckering preceded those at Boolardy and average values were lower. Numbers (1 through 3 or 4) mark points in each plot that were used in determining physical properties of the associated TID, such as velocity.

The steps that I took to determine the properties of TIDs suggested in Figure 6.30 are described next.

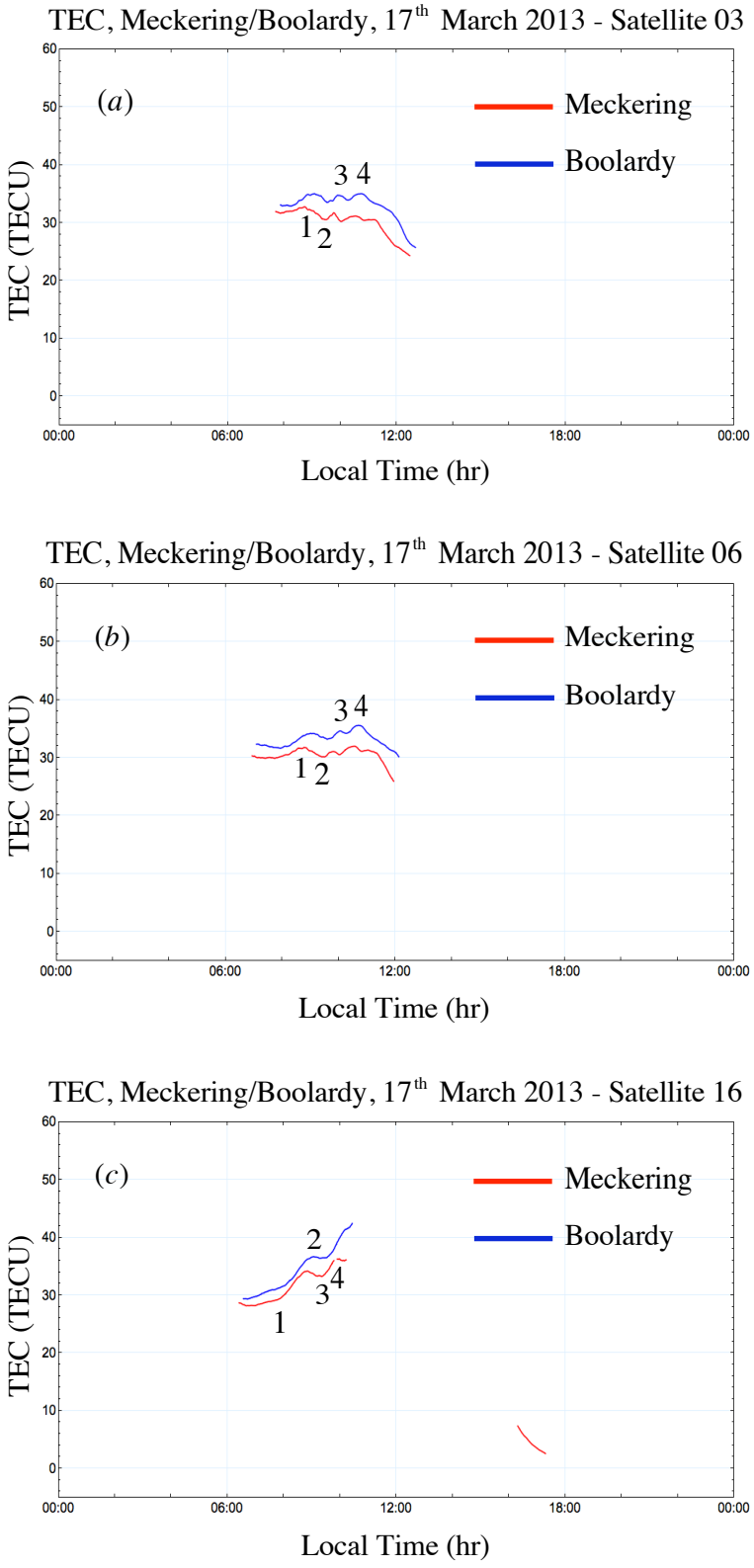


*Figure 6.30 (a, b, c): VTEC observations for individual GPS satellites for corresponding passes seen from both Meckering and Boolardy. Features used in measuring differences in timing for events at respective locations are numbered. The uncertainty in feature locations were measured and used in calculating final TID parameter uncertainties.*

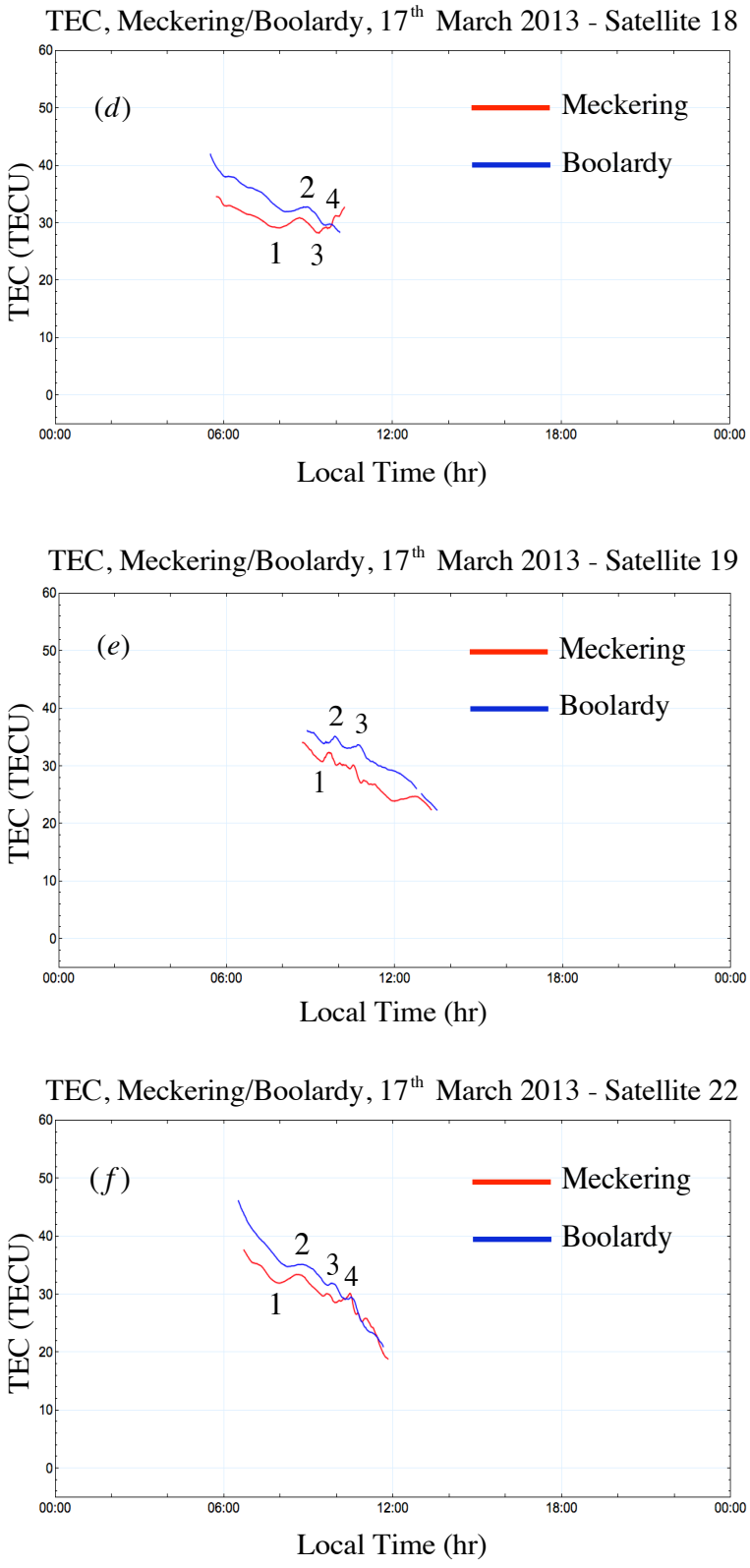


*Figure 6.30 (d, e, f): VTEC observations for individual GPS satellites for corresponding passes seen from both Meckering and Boolardy. Features used in measuring differences in timing for events at respective locations are numbered. The uncertainty in feature locations were measured and used in calculating final TID parameter uncertainties.*

(1) Delay in TID onset between mec and mw2.

The delay in the onset of each TID between mec and mw2 and the wave period was found by computing the distance correlation coefficient between TEC values returned from each site, found as:

$$DCC[u,v] = 1 - \frac{(u-\overline{u})(v-\overline{v})}{\left\|(u-\overline{u})\right\|\left\|(v-\overline{v})\right\|}, \tag{6.1}$$

where $DCC[u,v]$ is the the distance correlation coefficient (DCC) between vectors $\overline{u}$ and $\overline{v}$ (Székely and Rizzo 2012). TEC values for either mec or mw2 were shifted in one minute steps against the other over a predetermined interval, ensuring that the two time series always overlapped and the DCC was recalculated. The wave delay was taken as the time corresponding to the minimum of each curve, that is, when the 2 time series were as closely in phase as possible. Figure 6.31 displays DCCs for six satellites that were transiting at the time of the TID and which provided the times at which peak readings of the DCC occurred at each site. The extracted transit times are displayed in Figures 6.32 - 6.35.

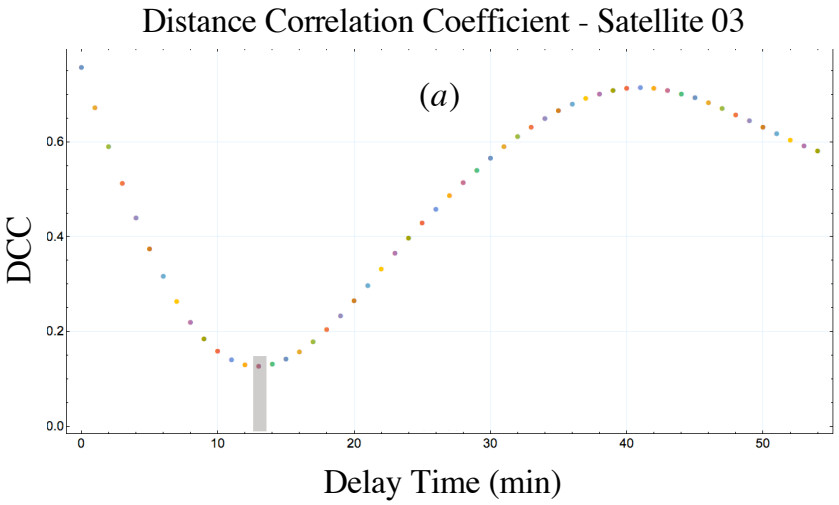


*Figure 6.31(a): Plot of the output of distance correlation coefficient operations on mec and mw2 TEC data for satellite PRN 01, to identify corresponding onset delays between the two sites for a transiting TID.*

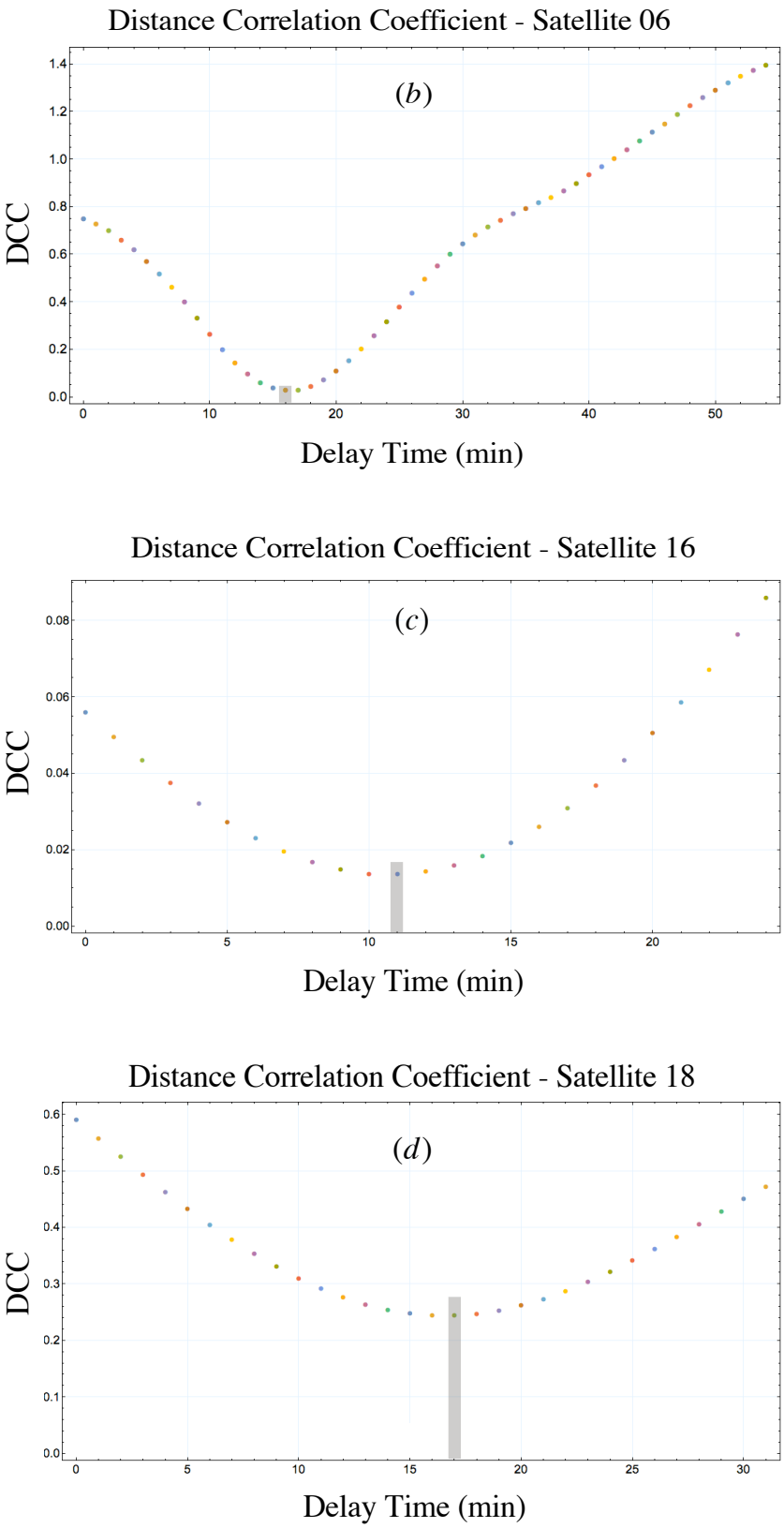


*Figure 6.31(c, d, e): Plot of the output of distance correlation coefficient operations on mec and mw2 TEC data for satellites PRN 06, 16 and 18, to identify corresponding onset delays between the two sites for a transiting TID.*

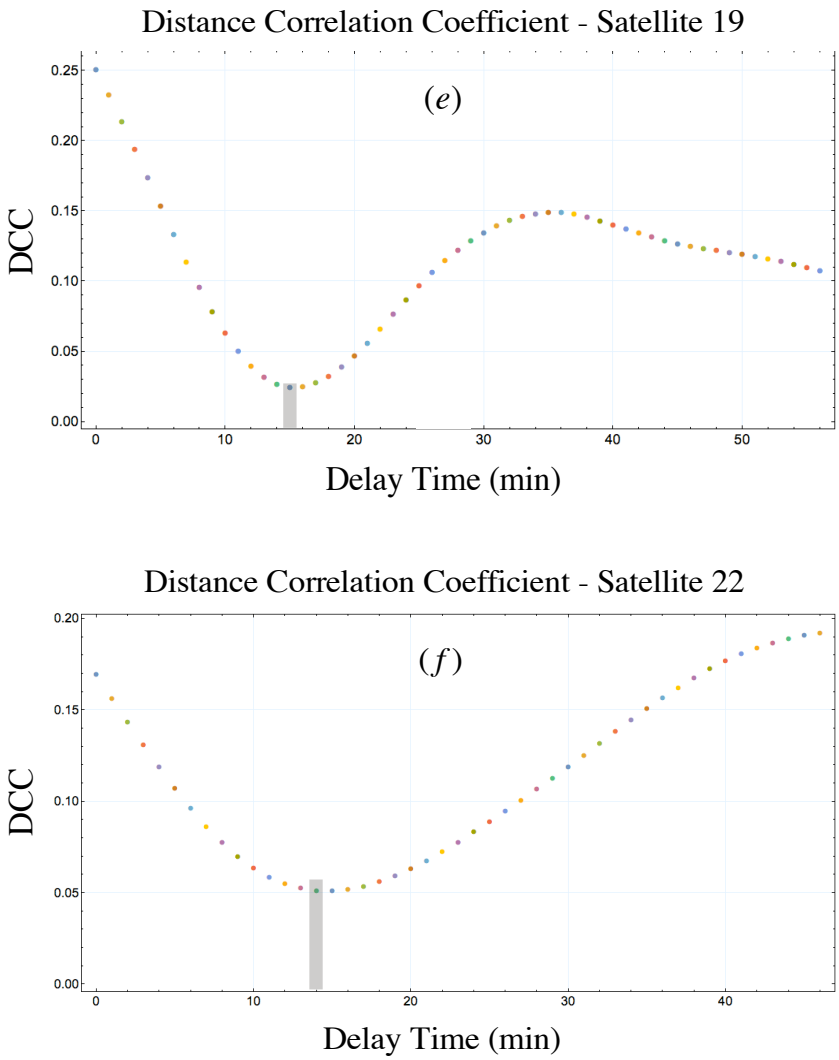


*Figure 6.31(e and f): Plot of the output of distance correlation coefficient operations on mec and mw2 TEC data for satellites PRN 19 and 22, to identify corresponding onset delays between the two sites for a transiting TID.*

(2) Corresponding ionosphere piercing points.

The coordinates of the 350 km altitude ionospheric piercing points and corresponding times were retrieved from the data associated with each satellite's ephemeris. Both latitudes and longitudes were plotted in Figures 6.32 to 6.35. Uncertainties in positions of the piercing points were determined from records corresponding to uncertainties in the timing of events. Uncertainties in the timing of each event are best estimates based on the minimum of each curve in Figure 6.3 of the corresponding curve.

(3) Determination of TID direction.

The rates of change in location of the transiting TID events (peaks) were found as linear models of time of occurrence~position, both for latitude and longitude. Figures 6.32-6.35 present the results of the linear regressions separately for time~latitude and time~longitude for each event. In respect of latitude for each event, the slope for each is positive, indicating a northward progression of the TID in each case (see Fig. 6.32 and 6.34). In respect of longitude, the slope of the regression line is negative in the case of the first event (see Fig. 6.33), indicating a westward progression and positive in the second case (see Fig. 6.35), indicating an eastward progression. The vectors for progression of the TID in latitude and longitude in each case were summed to produce the final speed and bearing of each TID.

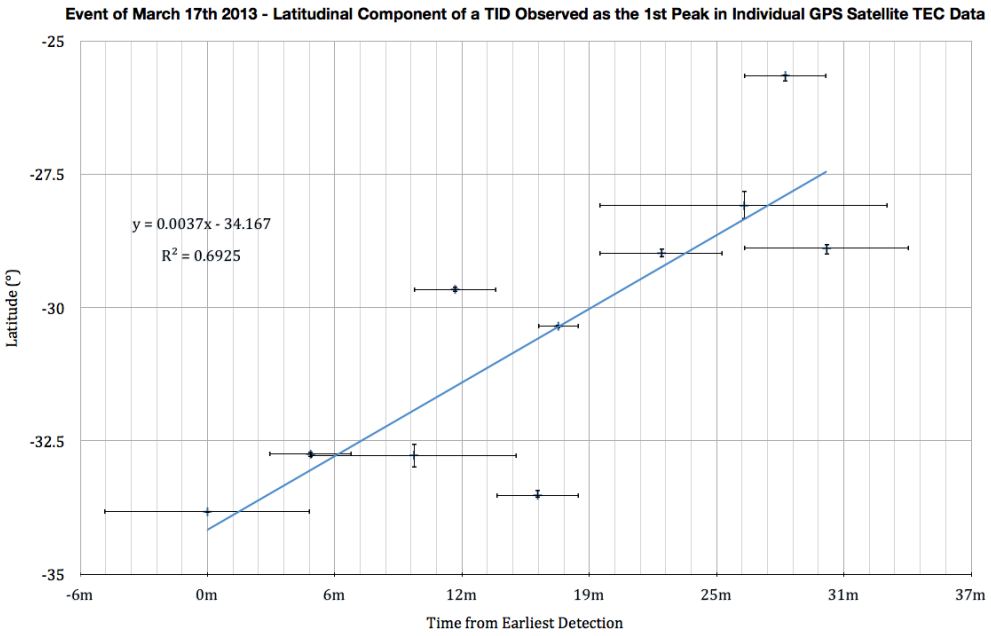


*Figure 6.32:Plot of the output of a linear regression performed on relative time-of-onset ~ latitude data for two sites, Meckering and Boolardy, used to determine the northward pointing vector of the phase speed of the first observed TID.*

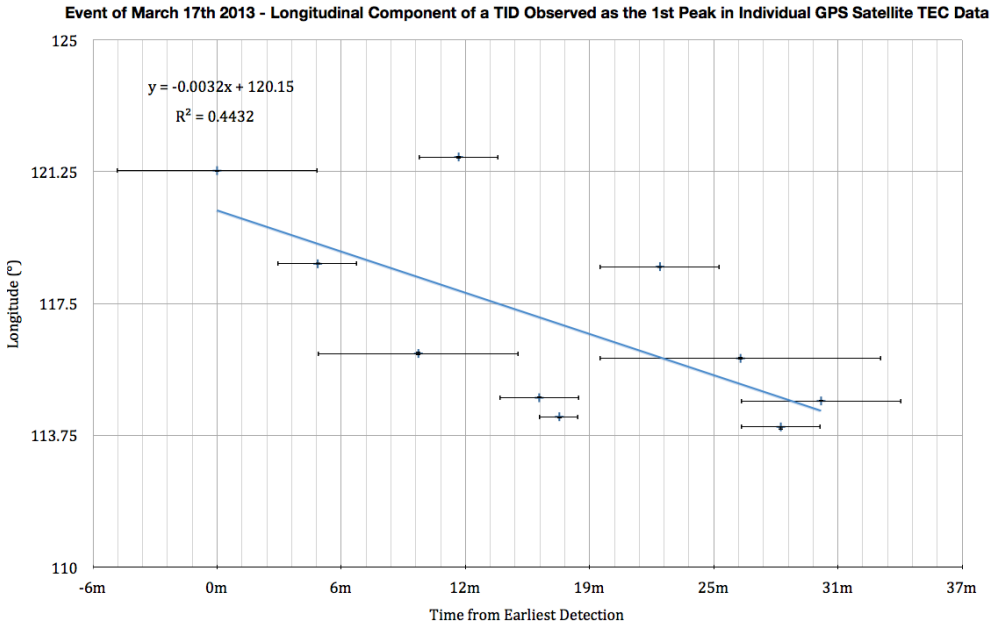


*Figure 6.33: Plot of the output of a linear regression performed on relative time-of-onset ~ longitude data for two sites, Meckering and Boolardy, used to determine the northward pointing vector of the phase speed of the first observed TID.*

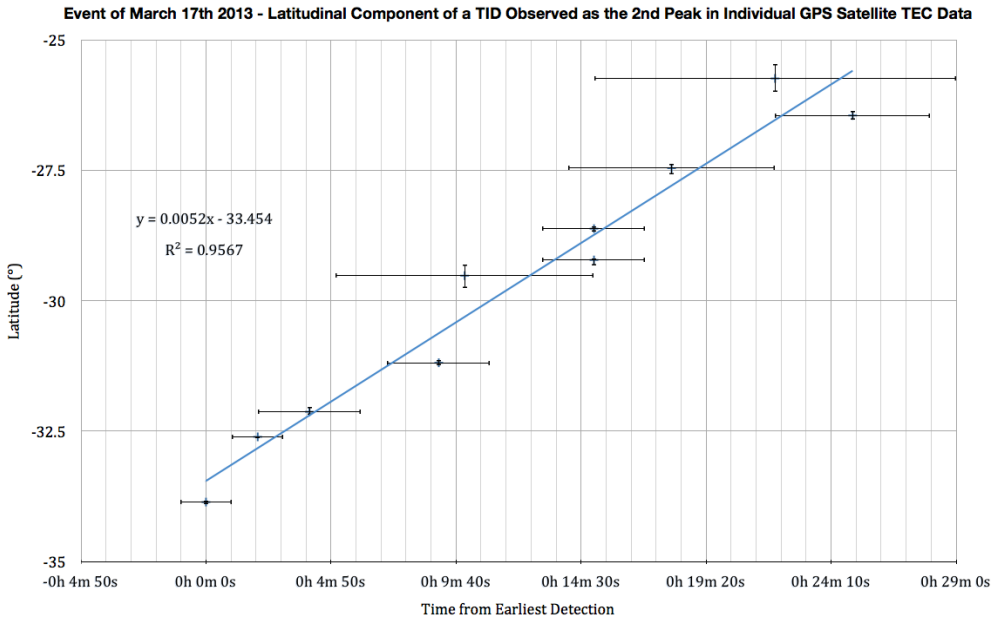


*Figure 6.34: Plot of the output of a linear regression performed on relative time-of-onset ~ latitude data for two sites, Meckering and Boolardy, used to determine the northward pointing vector of the phase speed of the second observed TID.*

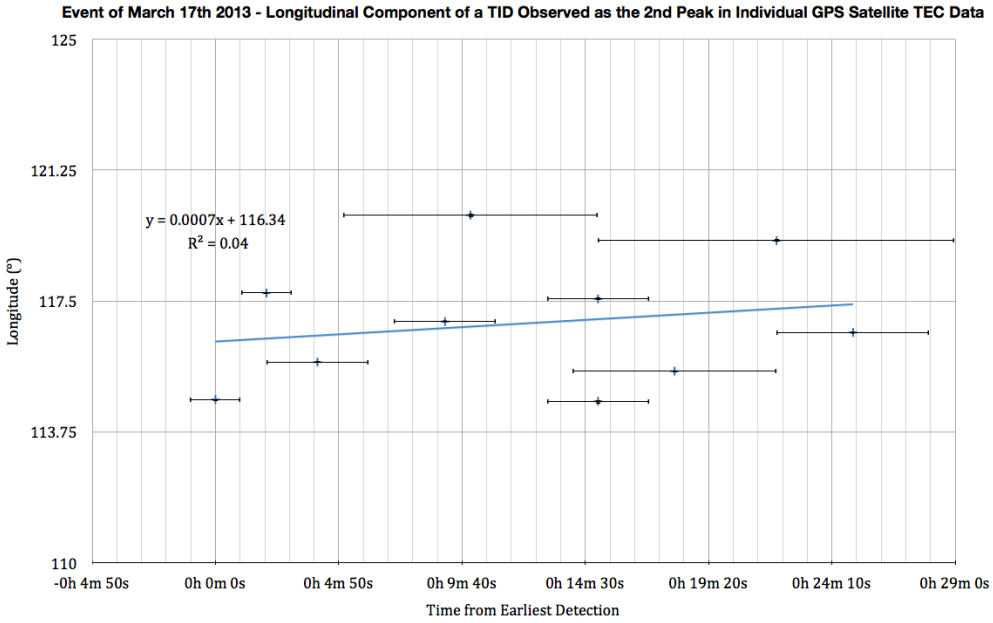


*Figure 6.35: Plot of the output of a linear regression performed on relative time-of-onset ~ longitude data for two sites, Meckering and Boolardy, used to determine the northward pointing vector of the phase speed of the second observed TID.*

At an altitude of 350 km, 1° of latitude equates to an arc length of 117.05 km and at 30°S, 1° of longitude equates to an arc length of 102.51 km. These were employed in converting angular results into distances.

### 6.3.2. Observed TIDs.

Figures 6.36 and 6.37 display the TIDs and associated parameters for successive wavefronts. Table 6.1 provides a summary of TID parameters and associated uncertainties.

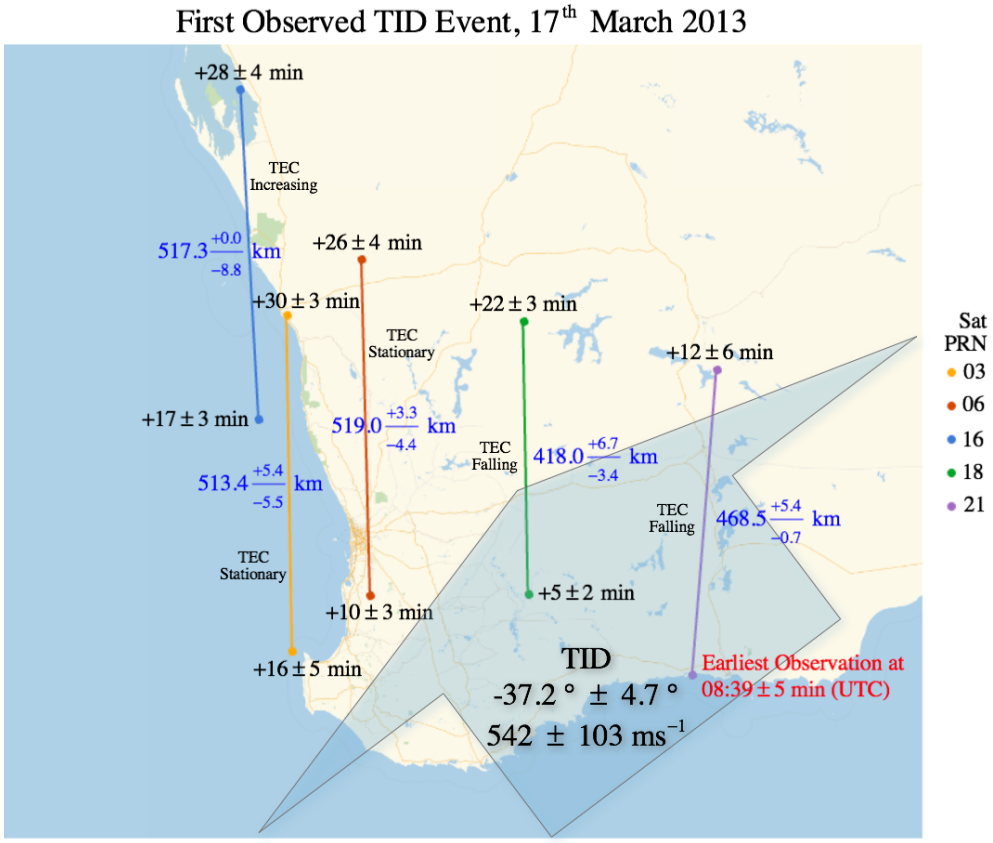


*Figure 6.36: First TID observed in GPS-derived TEC data on 17th March 2013 during onset of a geomagnetic storm. The time shown against the lower endpoint of each coloured transect (except PRN 21) is the delay from the time of earliest observation. The time against the upper endpoint of each transect is also the delay from the time of earliest observation. The difference in the two times for each transect is the time taken for the TID to propagate the length of the transect, shown in blue text, except for PRN 21, in which the propagation time is the upper time shown (12 +/- 6 min). Regression analysis of the data produced a TID velocity of 542 +/- 103 ms-1 in the direction of -37.2 +/- 4.7 ° (where north is 0.0 °).*

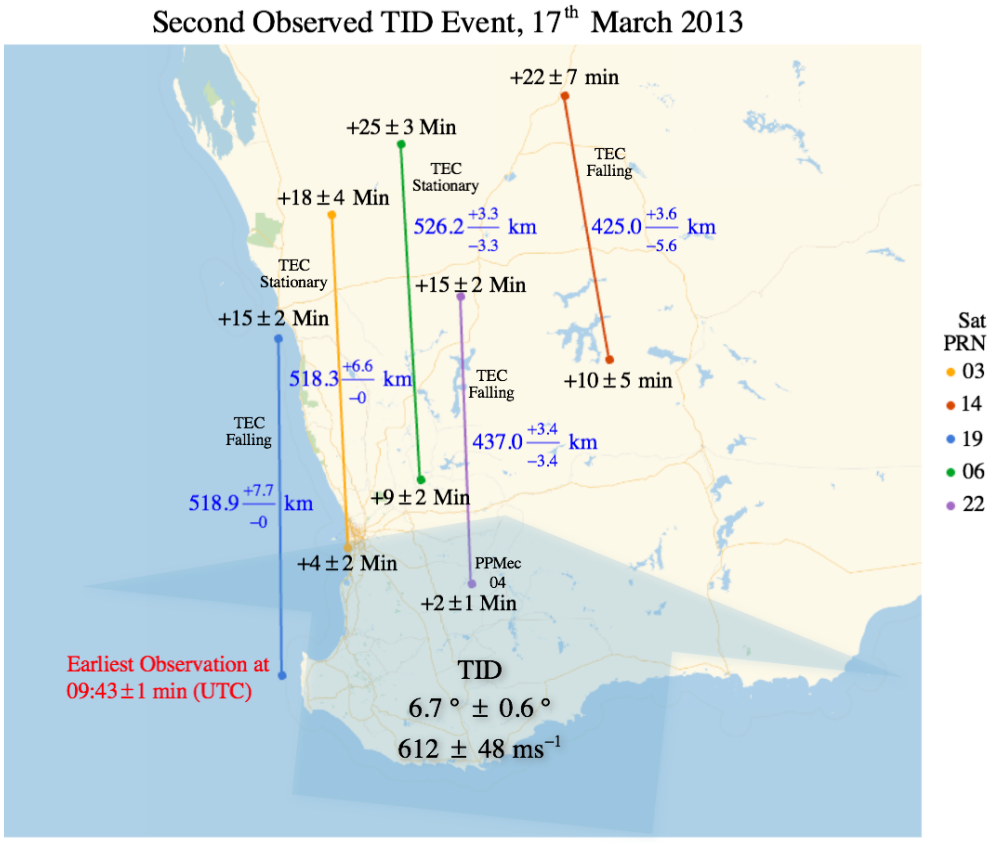


*Figure: 6.37: Second TID observed in GPS-derived TEC data on 17th March 2013 during onset of a geomagnetic storm. The time shown against the lower endpoint of each coloured transect (except PRN 19) is the delay from the time of earliest observation. The time against the upper endpoint of each transect is also the delay from the time of earliest observation. The difference in the two times for each transect is the time taken for the TID to propagate the length of the transect, shown in blue text, except for PRN 19, in which the propagation time is the upper time shown (12 +/- 6 min). Regression analysis of the data produced a TID velocity of 612 +/- 48 ms-1 in the direction of 6.7 +/- 0.6 °.*

Each coloured line segment (Figures 6.36, 6.37) joins corresponding ionospheric piercing points (IPP) for mec and mw2 at 350 km altitude, at which height the ionosphere is treated under SCINDA as a thin shell, the model used to determine TECs. The final uncertainties in the direction of each TID indicate that they could not coincide and are likely separate waves of enhancement/depletion. Intervals displayed mark the delay at each associated location of the onset of peak TEC against the earliest time associated with the TID (red text). The speeds and

periods of these TIDs fall within regimes broadly associated with medium scale travelling ionospheric disturbances (MSTIDs) (Waldock and Jones 1987, van Velthoven and Spoelstra 1992), although their classification as such by Waldock et. al would have implied lower velocities of order <350 $ms^{-1}$.

Table 6.1 summarises parameters of the two TID events observed in data at mw2 and mec for March 17th, 2013.

| Measure | TID 1 | TID 2 |
|---|---|---|
| Group velocity ($ms^{-1}$) | 542 ± 103 | 612 ± 48 |
| Bearing (° E of N) | -37.2 ± 4.7 | 6.7 ± 0.6 |
| Period [SDev] (min) | 58 [6.1] | 43 (2.4) |

*Table 6.1: Parameters for TIDs of March 17th, 2013. The group velocity and period were derived from the delay in the onset of respective features in TEC data at mw2 after mec and the delay between corresponding features (marked as 1 to 3 or 4 in Figure 6.30) in the data used to calculate parameters.*

Van Velthoven et. al (Van Velthoven, Mercier et al. 1990) observed TID periods of tens of minutes out to order 40-50 minutes. Group velocities an order of magnitude lower than those observed here have been observed (Shiokawa, Mori et al. 2013). Indeed, many references to the properties of MSTIDs involve phase velocities of the order 300 $ms^{-1}$ or less, however. Hence, when classified by period, the TIDs described here fit conservatively into the class MSTID, whereas by phase velocity they can also fall into a classification of large scale TID (LSTID) (Parkinson and Dyson 1998). Equator-ward propagating storm-induced wave packets have been observed during several geomagnetic storms displaying mean wavelengths of 2000 km, mean periods of 59 min and phase speeds of 684 $ms^{-1}$ (Borries, Jakowski et al. 2009). These authors also noted large TID activity in GPS derived TEC data during

geomagnetic storm events. Danilov noted that geomagnetic disturbances of the order observed here drive the strongest response in the ionospheric F-region (Danilov 2013).

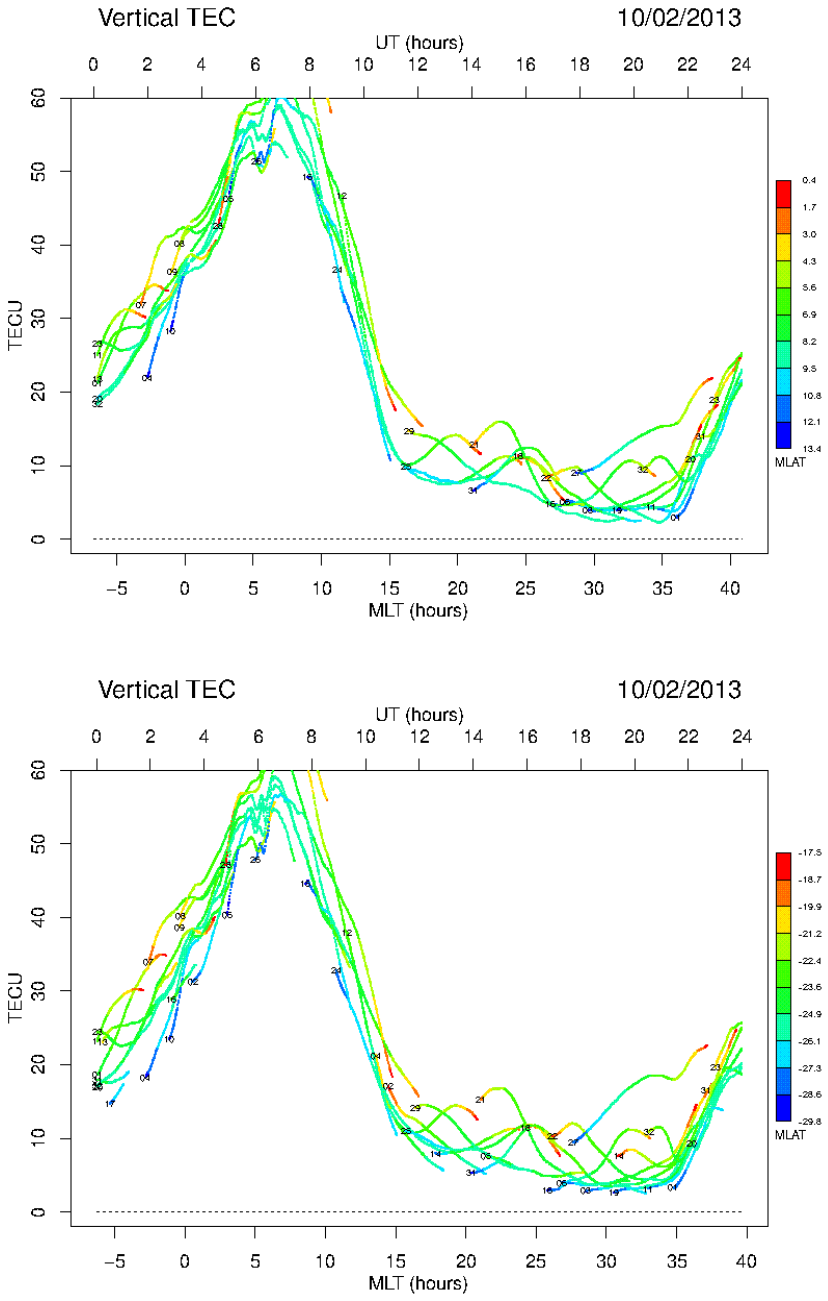


*Figure 6.38: TIDs were evident during a brief period (a single day) of elevated VTEC. The upper plot shows TEC readings for Meckering, the lower plot, Boolardy.*

The TIDs (Table 6.1)were observed separated in time by 65 minutes and display distinctly differing properties, leading to the conclusion that they probably resulted from separate events in the south polar, auroral

oval. In these regions, during significant geomagnetic storm events, Sieradzki et. al (Sieradzki, Cherniak et al. 2013) observed TEC rates of change associated with the northern polar auroral oval of up to 5 TECU $min^{-1}$.

Whereas the TIDs discussed here occurred during the onset of a significant geomagnetic storm., TIDs have been observed under very different conditions, as shown in Figures 6.38-6.40.

TEC at both Meckering and Boolardy were elevated significantly over a single 24 hour period, as shown in Figure 6.39. Also elevated at the time was the $A_p$ index, which demonstrates that this index isn not under all circumstances relevant to processes taking place in the local magnetosphere.

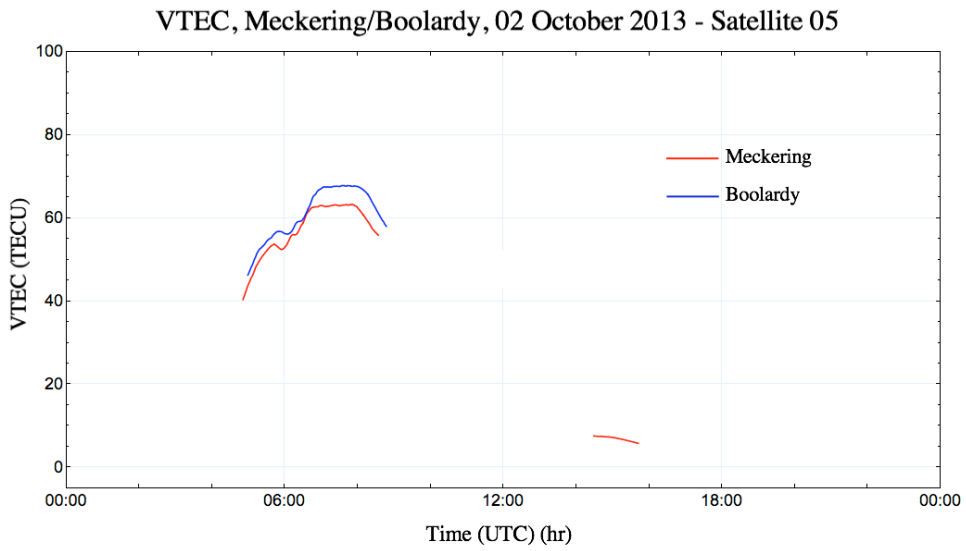


*Figure 6.39: TID of October 2nd, 2013 during a period of elevated VTEC. The high readings were encountered over a single 24 hour period.*

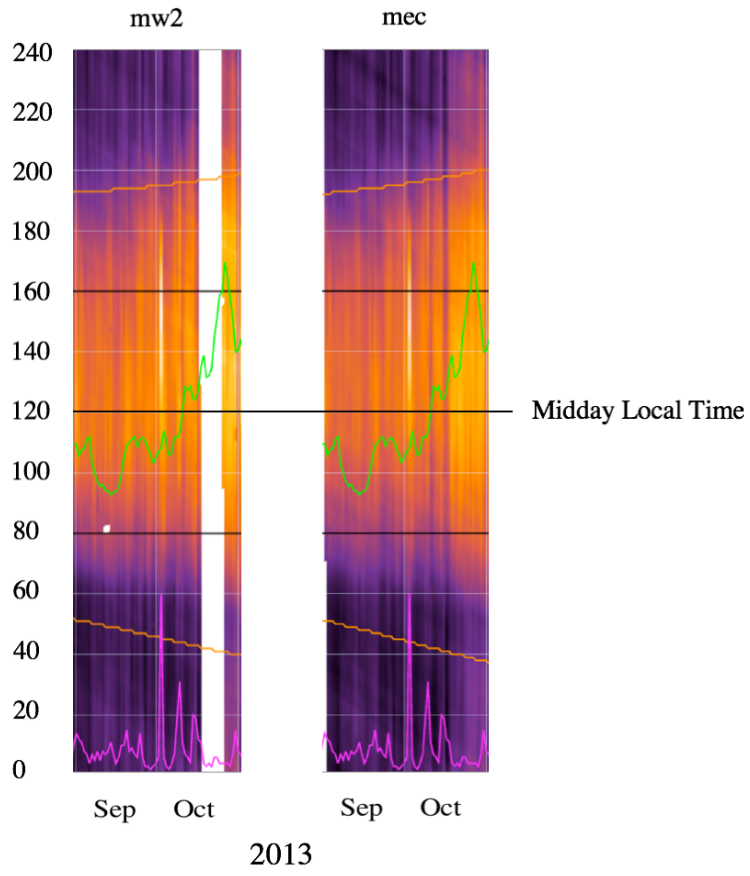


Figure 6.40: Briefly elevated TEC at mec and mw2 (vertical white patches, which in Figure 6.38 are TEC readings off-scale, on October 2nd at both sites).

### 6.3.3. The Scales of TIDs Detected by GPS methods.

TIDs were detected at varying scales, as displayed in Figure 6.41.

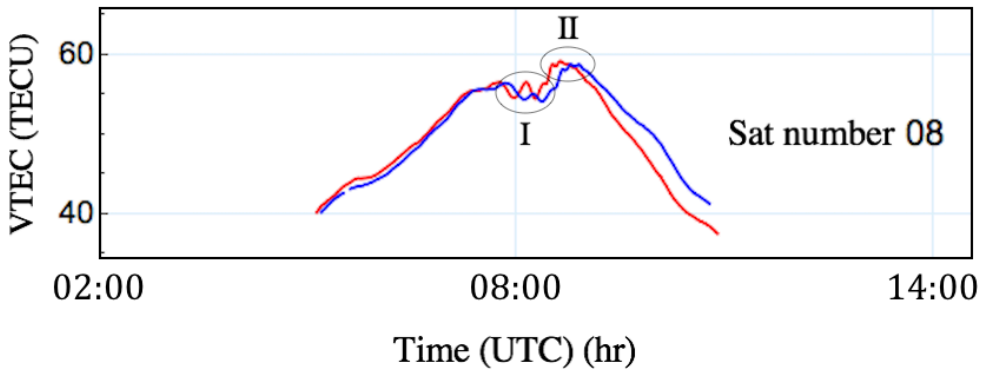


*Figure 6.41: TIDs at varying scales observed as subsequent events at Meckering (red trace) and Boolardy (blue trace) for October 2nd, 2013. Event sequence I exhibits peak values and wavelengths up to an order of magnitude greater than event sequence II.*

At Meckering (red Trace), TID (I) exhibited a peak magnitude of ~2 TECU and a period of ~25 minutes. TID (II) exhibited a peak magnitude ~0.5 TECU and a period of ~7 minutes.

GPS is sensitive to TID related TEC variations at fractional TECU levels. Absolute accuracy however is dependent on calibration of GPS satellite transmitters (space segment biasses) and receivers ( user segment biasses).

### 6.3.4. Sources and Magnitudes of Uncertainties.

As mapping each TID required the accurate spatial and temporal location of corresponding TEC values across sites and satellites, the largest uncertainty resulted from identifying points in common on each satellite trace. Some curves were unambiguous, being represented by smoothly varying TEC values (e.g.. Fig. 6.30(b)) and these were assigned smaller uncertainties. Others were either broad or degraded, possibly due to local conditions and these were assigned appropriate uncertainties (e.g.. Fig. 6.30(d)). Uncertainty in latitude and longitude were derived from uncertainties in timing. The magnitude of these depended on the rate at which a satellite's latitude or longitude were changing at the time, resulting in values from 0 km to maxima of +7.7/-8.8 km.

### 6.3.5. Conclusion.

TIDs were observed in GPS-derived TEC data. The two TIDs mapped propagated in a direction away from the south pole, towards the equator.

There is no fundamental impediment to the method described here being automated and providing parameters to systems employed in, for

example, the provision of an ionosphere quality index, as discussed in following sections.

## 6.4. The Ionosphere Interpreted at Two Locations Separated by 519 km on a North/South Transect.

TEC was measured at both Meckering and Boolardy (Figure 5.9) over E2, the peak of cycle 24 (Figure 6.14). The two sites displayed very similar ionospheric structure and dynamics as interpreted by TEC.

Histograms in Figures 6.16 and 6.17 display counts of TEC values at each site over this period. Each has a very similar distribution of TEC readings up to ~55 TECU. Counts at higher values fall more rapidly at Meckering to ~100 readings above 70 TECU. At Boolardy, there were ~50 readings above 80 TECU.

Figure 6.42 highlights differences in time coincident TEC readings at Boolardy (mw2) and Meckering (mec) over E2. The difference in TEC at the two sites was found as:

$$\Delta TEC = TEC_{mw2} - TEC_{mec} \tag{6.2}$$

Each location suffered data outages at differing times, therefore the overlapping Δ*TEC* record is slightly smaller than each site record.

The majority of Δ*TEC* values fall within the range -5 TECU (larger mec TEC) to +5 TECU (larger mw2 TEC). Values of Δ*TEC* that exceed ~+10 TECU are often grouped as features that change daily in alignment with the precession rate of GPS satellites and are therefore likely to have resulted from interferences in readings (multi-path etc). Differences in TEC between the sites therefore are typically small. Meckering exhibited slightly higher evening TEC as autumn progressed into winter and the incomplete record suggested that over E2 might have exhibited slightly higher TEC during daylight hours also. Boolardy typically exhibited

higher TEC during daylight hours over much of the year and over evening hours too during spring into summer.

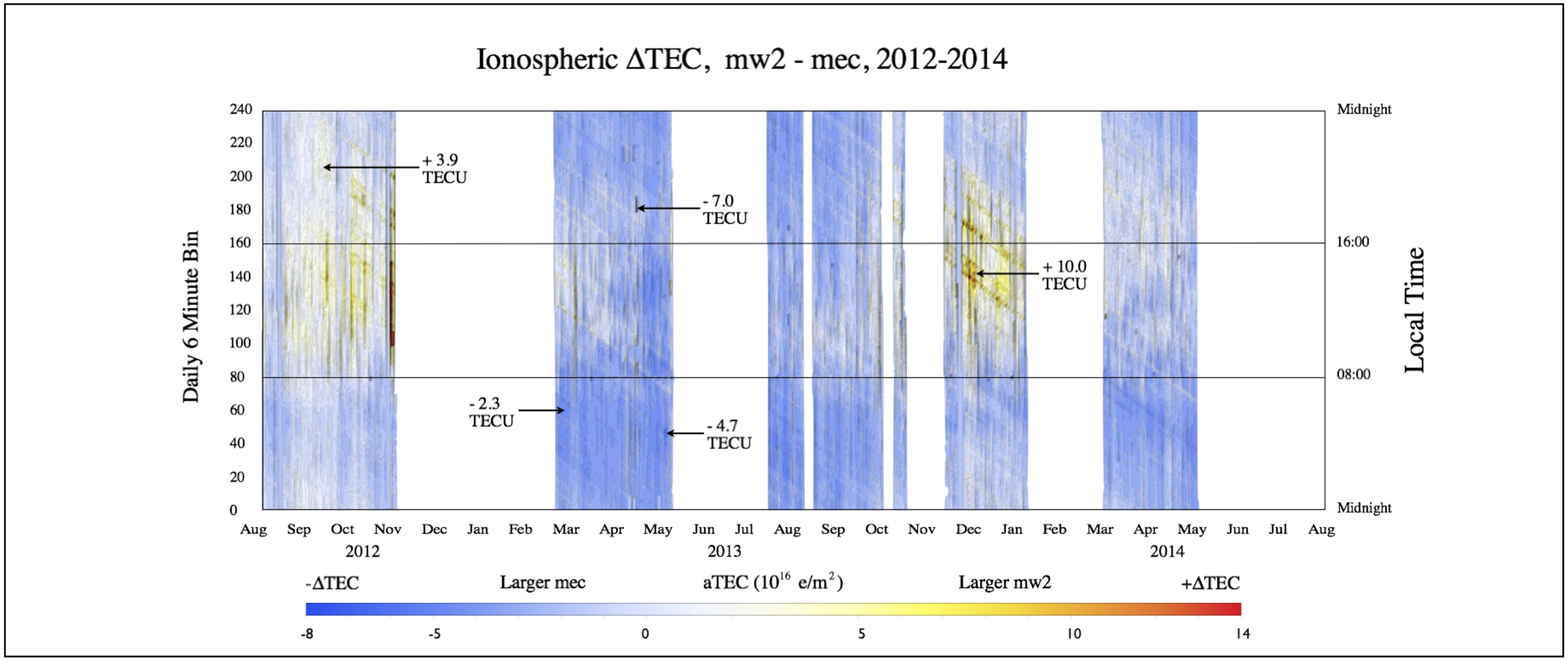


*Figure 6.42: Differences in TEC readings at mw2 and mec over the interval August 2012 - May 2014. Many of the strongest features precess with the GPS satellites, indicating that these features are caused by multi-path interference captured in the original data from mw2 and mec.*

## 6.5. Comparison of GPS Derived TEC at the MRO Against IRI-2012 Modelled TEC.

Having captured TEC readings over an extended period on the MRO, I now compare these observations with outputs of the IRI-2012 model. Comparison is conducted on an hourly and monthly basis over E1 and E2 with a result included from the intermediate period in September 2011. Each plot (Figures 6.43 and 6.44) consists of the hourly output of the IRI-2012 model for the 15$^{th}$ day of the month (red trace) plotted together with GPS TEC readings recorded above 50° elevation for each hour of every day of the month. Hence, a range of values represented by a column of data (orange bars) at each time division (hourly) represents the range of TECs recorded for that hour for each day of the month.

Tables 6.2 and 6.3 present the RMS differences (*ΔRMS*) between the IRI-2012 model outputs and GPS TEC values for each month. Table 6.2 presents results for the beginning of the current solar cycle (24), Table 6.3 presents results for the peak of the current cycle.

| Year/Month | *ΔRMS (TECU)* | Year/Month | *ΔRMS (TECU)* |
|---|---|---|---|
| 2008-04 | *1.29* | 2009-02 | *1.17* |
| 2008-08 | *1.23* | 2009-03 | *1.31* |
| 2008-09 | *2.34* | 2009-04 | *1.49* |
| 2008-10 | *1.08* | 2009-05 | *1.03* |
| 2008-11 | *1.65* | 2009-06 | *1.04* |
| 2008-12 | *1.57* | 2009-07 | *1.10* |
| 2009-01 | *1.10* | 2011-09 | *1.66* |

*Table 6.2: RMS differences in monthly TEC modelled under IRI-2012 and GPS generated TEC for Epoch 1 and an intermediate period, September 2011.*

| Year/Month | *ΔRMS (TECU)* | Year/Month | *ΔRMS (TECU)* |
|---|---|---|---|
| 2012-02 | *2.16* | 2013-04 | *4.10* |
| 2012-03 | *3.61* | 2013-05 | *3.30* |
| 2012-04 | *4.27* | 2013-06 | *1.70* |
| 2012-05 | *4.50* | 2013-07 | *1.71* |
| 2012-06 | *2.75* | 2013-08 | *2.06* |
| 2012-07 | *2.36* | 2013-09 | *5.22* |
| 2012-08 | *1.98* | 2013-10 | *2.84* |
| 2012-09 | *2.53* | 2013-11 | *5.83* |
| 2012-10 | *4.70* | 2013-12 | *9.61* |
| 2012-11 | *3.10* | 2014-01 | *8.94* |
| 2012-12 | *5.52* | 2014-03 | *13.07* |
| 2013-02 | *1.32* | 2014-04 | *6.51* |
| 2013-03 | *2.96* | 2014-05 | *5.60* |
| | | 2014-07 | *3.25* |

*Table 6.3: RMS differences in monthly TEC modelled under IRI-2012 and GPS generated TEC for Epoch 2.*

The data demonstrate that, over a period of low SSN, the IRI-2012 climatological model was capable of predicting daily ionospheric TEC with remarkable accuracy. Over E1 (April 2008 - July 2009), the mean *ΔRMS* (TECU) between the IRI-2012 model and GPS derived TEC =1.34 TECU.

Over a period of elevated SSN, such as the peak of a solar cycle and its vicinity, The IRI-2012 model was less capable of predicting daily ionospheric TEC. Over E2 (February 2012 - July 2014), the mean *ΔRMS* between the IRI-2012 model and GPS derived TEC = 4.28 TECU. However, over the peak of E2 in 2014, the mean *ΔRMS* = 7.47 TECU.

These results contrast to those of Kumar (Kumar, Priyadarshi et al. 2012), who found that the IRI-2012 model often overestimated TEC by up to 26 TECU and underestimated by as much as 21 TECU. The GPS stations that Kumar used in his study however, were either affected (severely) by the EIA ( Singapore, Thailand and China) or were at high latitudes (Mongolia and Russia). My study however, has employed GPS systems at locations directly relevant to the study undertaken (Boolardy HS and Meckering), located at mid-latitudes which are recognised to exhibit lower levels of variance. The disparity though, highlights the need to conduct high-quality TEC measurements close to the environment in which the results are to be used and to provide a measure against which modelling can be compared.

Table 4.4 shows that at the lowest MWA observational frequency of 50 Hz, FR information is lost (FR > 1π radians) for a 1 TECU change at all elevations. For the month of highest RMS difference in TEC, March 2014, all FR information is lost at an observation frequency of 240 MHz at up to 60° elevation.

| **FR integrity for *ΔRMS TEC* of 13.07 TECU** | Observation Frequency (MHz) | | | | |
|---|---|---|---|---|---|
| Observation Elevation (°) | 50 | 80 | 160 | 240 | 300 |
| 30 | FR lost | FR lost | FR lost | FR lost | FR lost |
| 45 | FR lost | FR lost | FR lost | FR lost | |
| 60 | FR lost | FR lost | FR lost | FR lost | |
| 75 | FR lost | FR lost | FR lost | | |
| 90 | FR lost | FR lost | FR lost | | |

*Table 6.4: Loss of FR information for the month of March 2014, where the RMS difference in TEC between measured and that produced by the IRI-2012 model reached 13 TECU.*

The implications of these outcomes are discussed in Section 6.5.1.

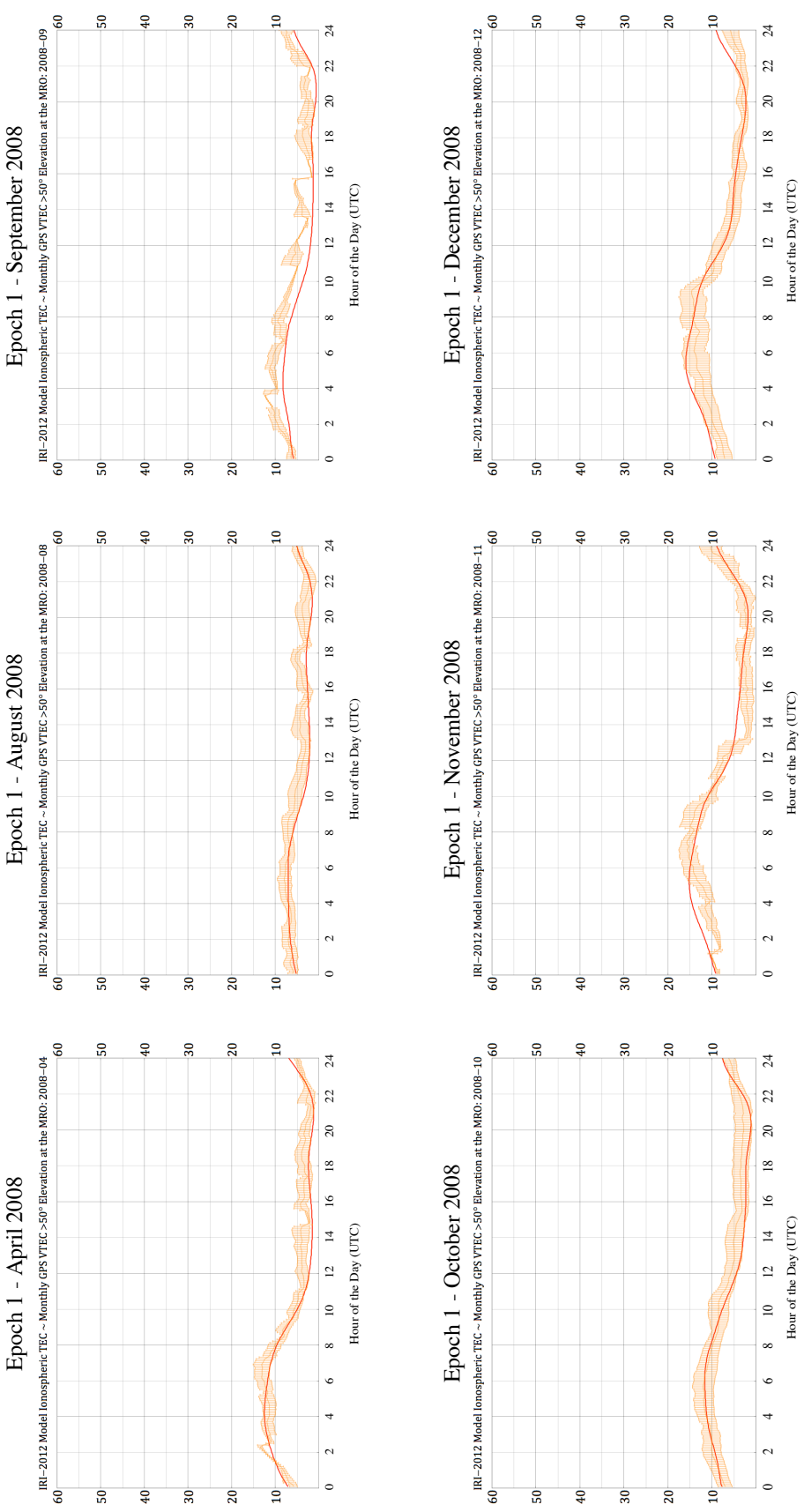


*Figure 6.43 (i):Hourly TEC for each day of the month (orange columns) compared to the output of the IRI-2012 model (red) for part of Epoch 1, April 2008 - December 2008.*

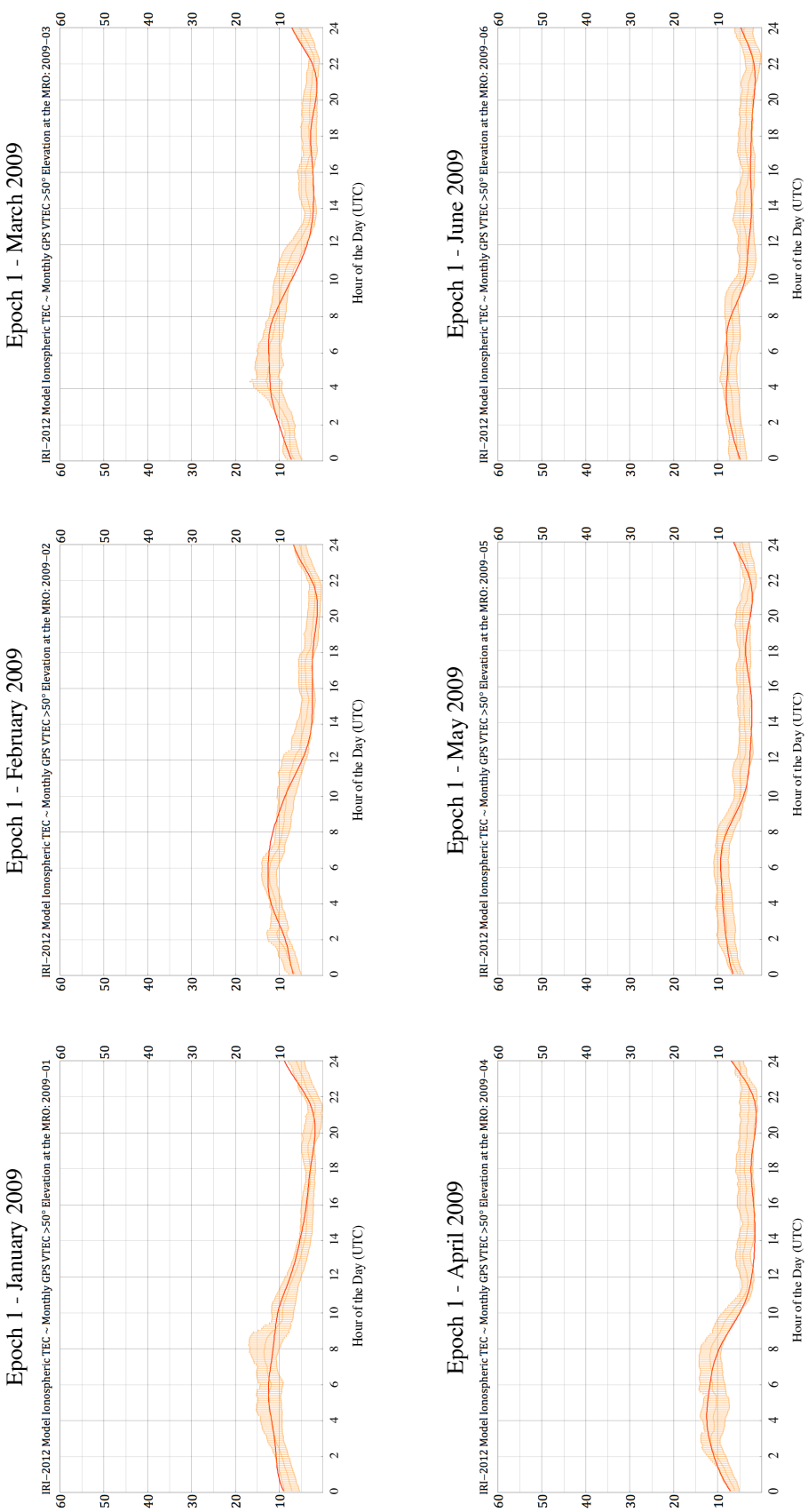


*Figure 6.43 (ii):Hourly TEC for each day of the month (orange columns) compared to the output of the IRI-2012 model (red) for part of Epoch 1, January 2009 - June 2009.*


*Figure 6.43 (iii):Hourly TEC for each day of the month (orange columns) compared to the output of the IRI-2012 model (red) for part of Epoch 1, July 2009 and for Sep 2011.*

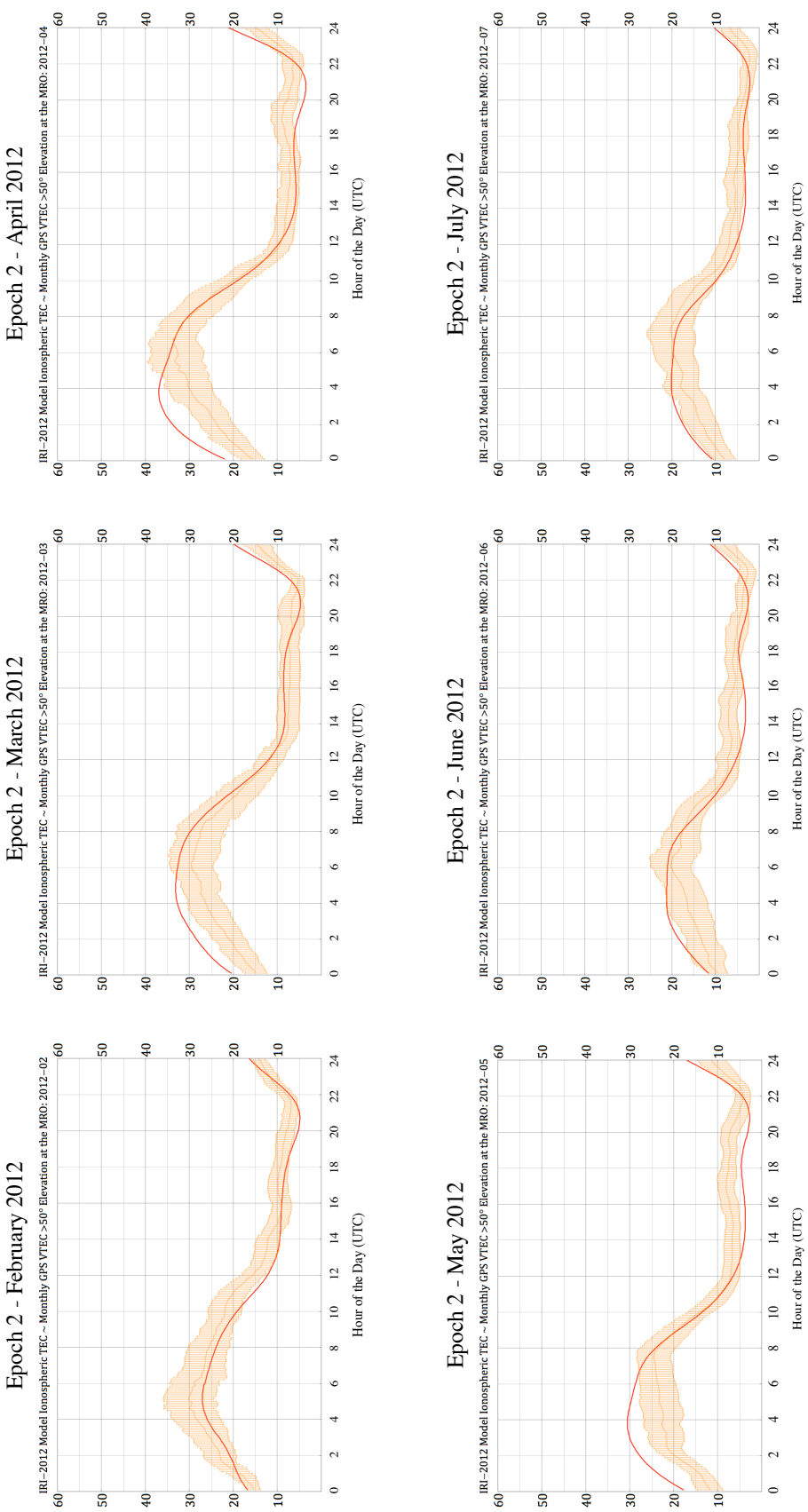


*Figure 6.44 (i):Hourly TEC for each day of the month (orange columns) compared to the output of the IRI-2012 model (red) for part of Epoch 2, February 2012 - July 2012.*

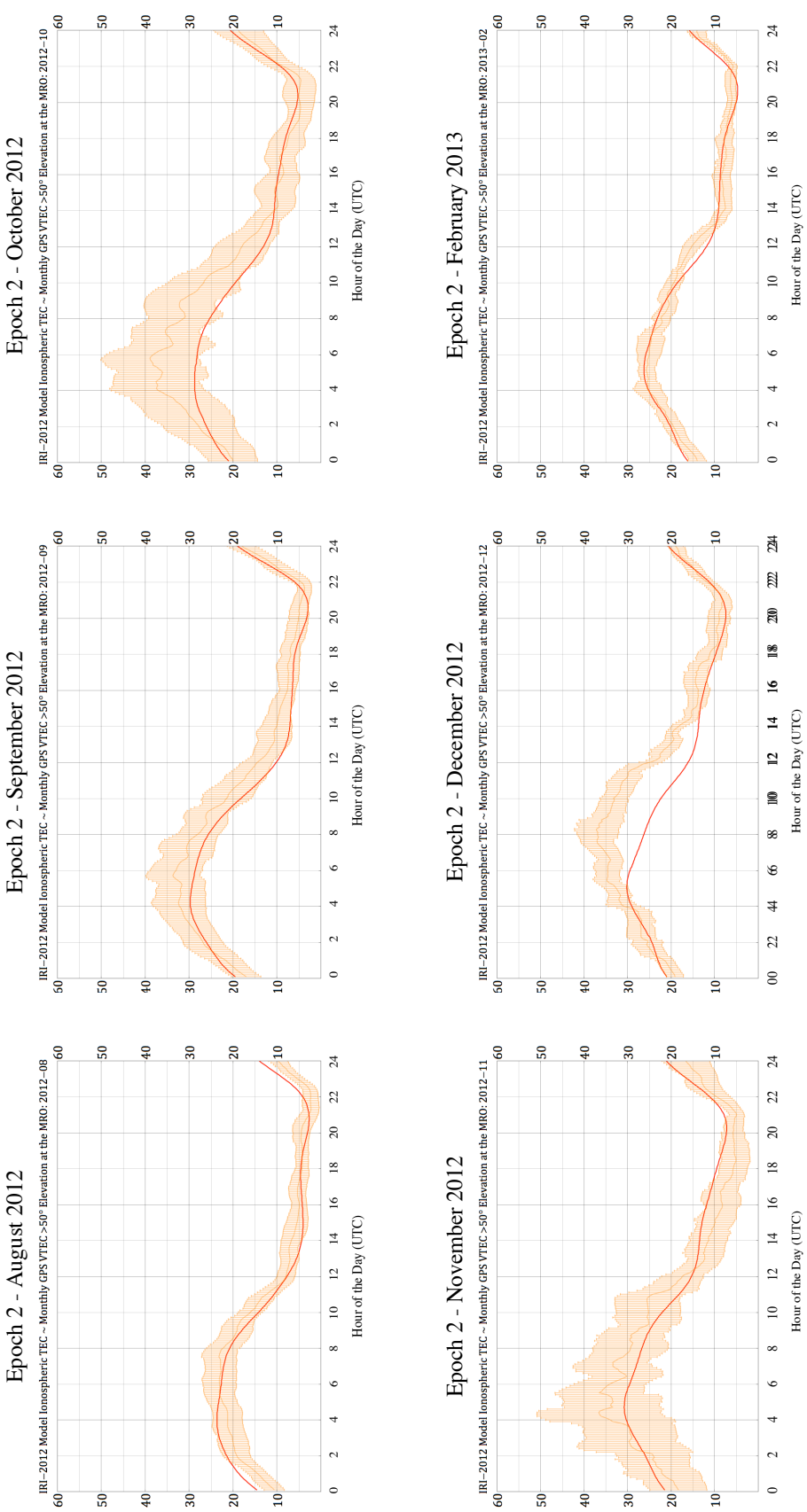


*Figure 6.44 (ii):Hourly TEC for each day of the month (orange columns) compared to the output of the IRI-2012 model (red) for part of Epoch 2, August 2012 - February 2013.*

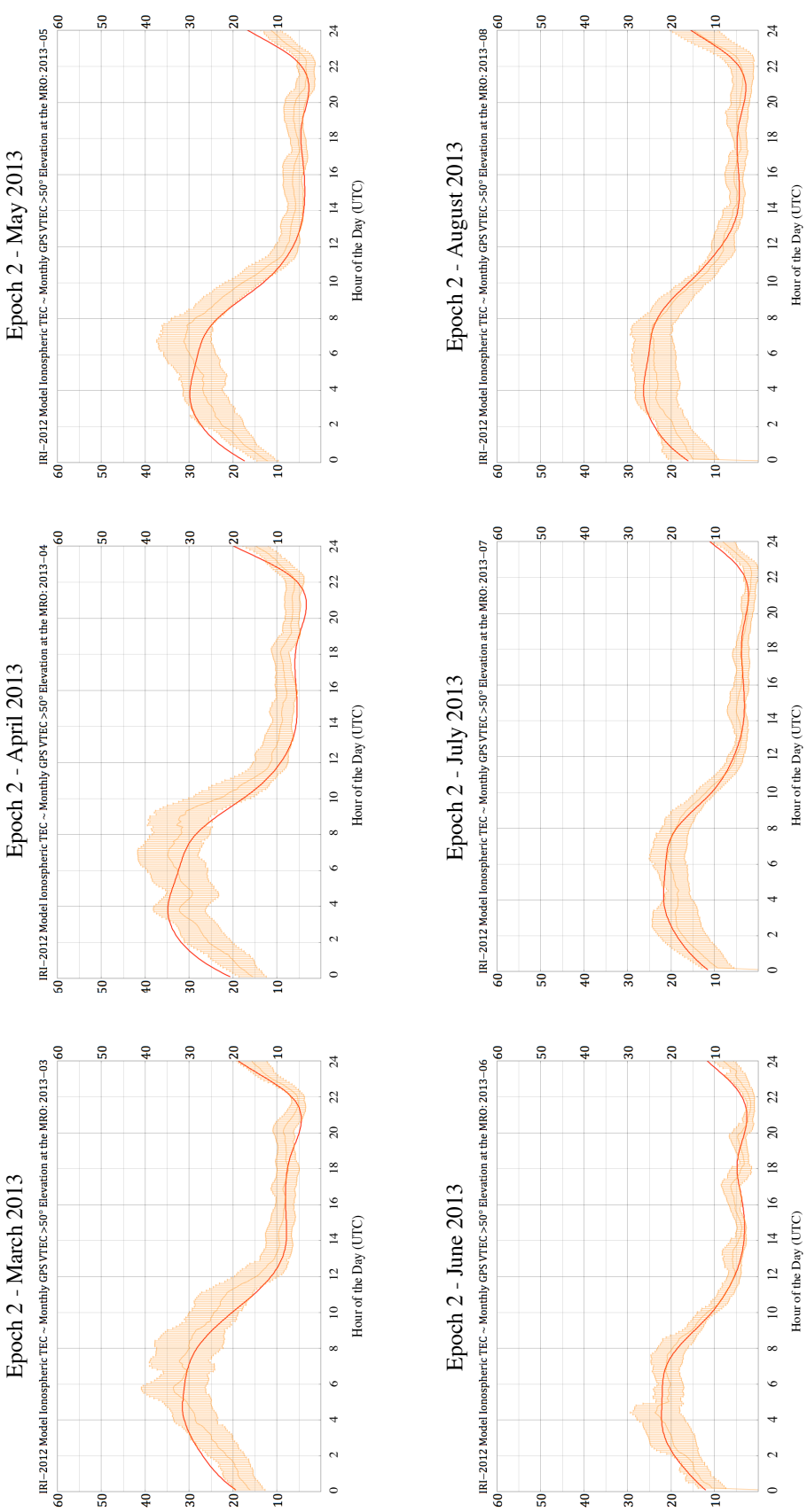


*Figure 6.44 (iii):Hourly TEC for each day of the month (orange columns) compared to the output of the IRI-2012 model (red) for part of Epoch 2, March 2013 - August 2013.*

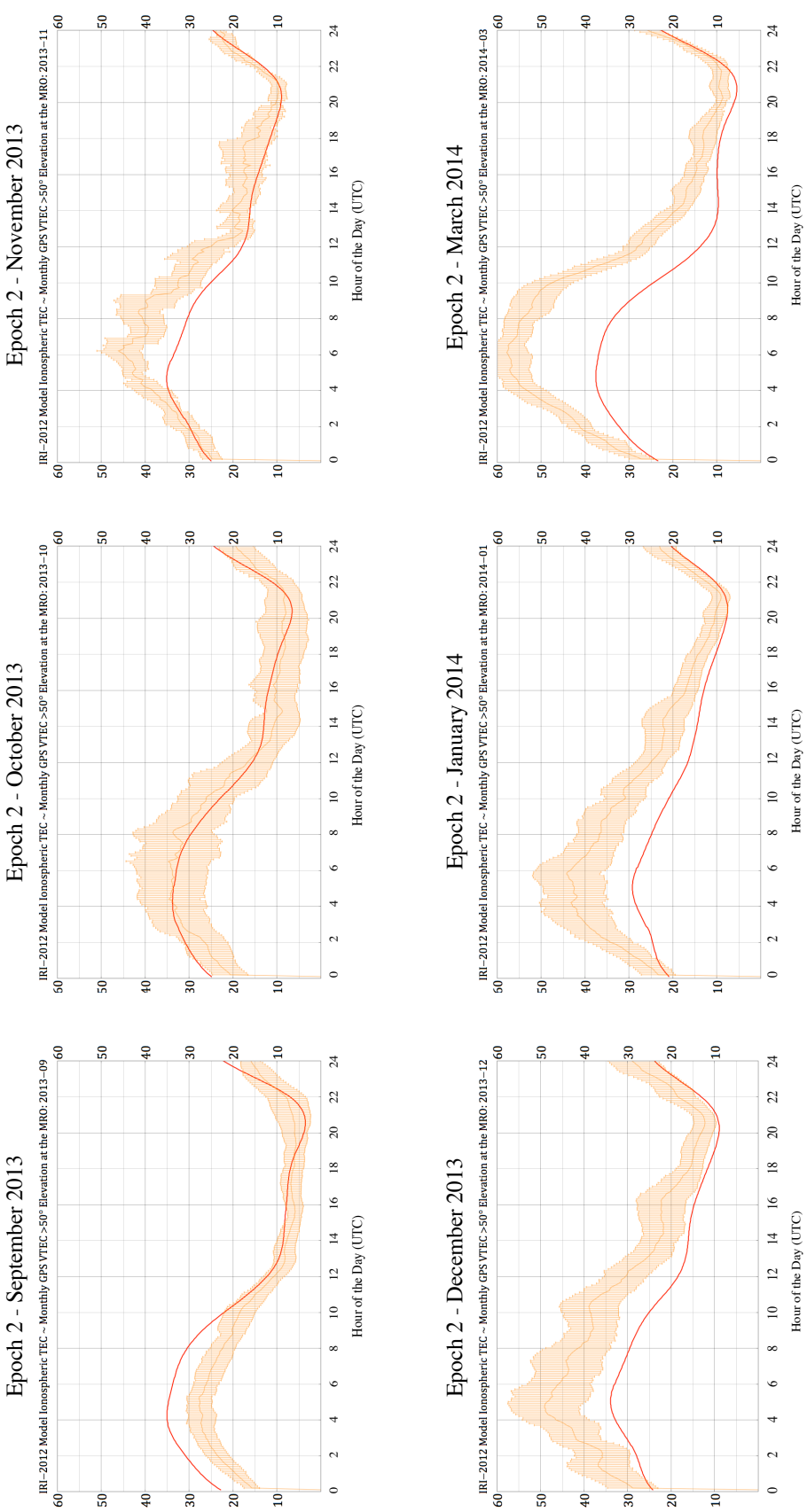


*Figure 6.44 (iv):Hourly TEC for each day of the month (orange columns) compared to the output of the IRI-2012 model (red) for part of Epoch 2, September 2013 - March 2014.*

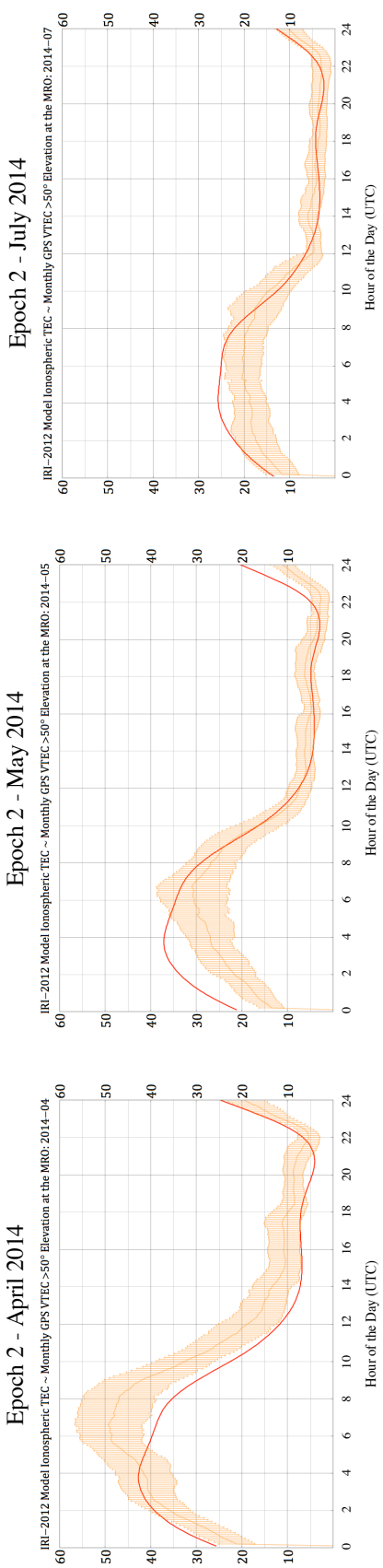


*Figure 6.44 (v):Hourly TEC for each day of the month (orange columns) compared to the output of the IRI-2012 model (red) for part of Epoch 2, April 2014 - July 2014.*

## 6.6. An Ionosphere Quality Index (IQI).

The outcomes of Section 6.5 might guide the formulation of an observer's Ionosphere Quality Index (IQI). Post processing of imaging data would benefit from knowledge of how well models used in calibration of an instrument performed. Another factor of possible interest would be the rate of change of TEC. Elevated TEC that is changing slowly over time can more readily be factored than TEC that is rapidly changing in value when there is likely to be greater ionospheric turbulence encountered.

The implications of the differences in $\Delta RMS$ TEC between measured and the IRI-2012 model (Tables 6.2 and 6.3) are significant when one uses the model in the calibration of a telescope. Previously, Section 4.2.4 demonstrated the effects on FR estimates of differences between a thin-shell ionosphere and a more sophisticated model, such as that based on a Chapman profile. Section 6.5 has demonstrated that differences in ionospheric model estimates of TEC and recorded values compounds the problem of accurately estimating ionospheric TEC.

The possibility of formulating an IQI will be pursued in future work.

## 6.7. A Triple VHF Beacon Equipped Cubesat.

Renewed interest in VHF radio astronomy and the growth of major LF radio telescopes on four continents, including LOFAR in Europe, the MWA and SKA-low (SKA VHF component) in Australia and the LWA in the USA, has spurred renewed interest in calibration requirements (Chapter 2.7). Ionospheric turbulent electron density structure plays the parallel role in radio astronomy that atmospheric turbulence does in degrading optical astronomy. Hence, an understanding of ionospheric electron dynamics is necessary to perform accurate calibration of LF radio telescopes. Modelling (Chapter 4) and observations (this chapter)

have demonstrated the profound affect that the ionosphere has on LF radio waves in particular and the fidelity required of calibration. Probing the ionosphere therefore with the same low frequencies will provide opportunities to study phenomena that are inaccessible to much higher frequency GPS methods. These include FR (Section 4.4.2) and scintillation (Section 4.4.3)). A triple, VHF beacon equipped cubesat will provide the opportunity to momentarily illuminate observatories with radio signals within their frequency range of interest, from outside the bulk of the ionosphere (around 800 km altitude). Techniques applied by GPS satellites to the determination of ionospheric TEC (Sections 5.2 and 5.3) would be provided by these satellites also. Studies have previously been undertaken into mission goals and architectures, such as:

(1) 'On Monitoring the State of the Ionosphere Using a Multifrequency Beacon on the Next generation of AUSSAT Satellites', E. A. Essex, Proceedings of the Third National Space Engineering Symposium, Canberra, 30 June - 2 July 1987, page numbers 60-63.

(2) 'A CubeSat Radio Beacon Experiment: CUBECON – a beacon test of designs for the future', M. Cousins. CubeSat Developers Workshop, San Luis Obispo. California, April 23 2010.

(3) 'An Australian Geosynchronous Satellite Radio Beacon', J. A. Kennewell. Proceedings of the Third National Space Engineering Symposium, Canberra, 30 June - 2 July 1987, page numbers 64-69. Several oceanographic satellites used VHF beacons and communications systems and had ionospheric monitoring ability, including for example, TOPEX/Poseidon.

More recently, we (Herne, Lynch and Kennewell) proposed a triple LF beacon equipped cubesat (TFBC) to a national meeting (Astrosats 2014, Mount Stromlo Observatory, http://rsaa.anu.edu.au/news-events/astrosats-2014-astronomy-satellites-workshop) featuring the architecture presented in this Chapter. Our proposal received equal highest ranking amongst those presented.

### 6.7.1. Role.

Several roles would be performed by the proposed TFBC. These include:

(1) Providing the opportunity to measure ionospheric TEC and scintillation at frequencies relevant to the new generation of LF radio telescopes.

(2) Provide the means of measuring direction dependant properties of telescope antennas, including gain and polarisation sensitivity across the sky (as a function of the satellite's orbit overhead). As array antennas physically point always to zenith, the antenna geometry changes constantly as a source (in this case, the TFBC) moves across the sky.

(3) A TFBC equipped with a dual-frequency GPS receiver would provide a means of differentiating between the TEC of the ionosphere and that above the satellite's orbit, which would encompass the plasmasphere and above and could also perform radio-occultation ionospheric profiling.

(4) Evaluate cost-effective technologies that could be applied, with the provision of a ground segment, to the probing of the ionosphere of Mars.

### 6.7.2. Beacon Architecture.

The satellite component would follow an architecture, proposed by J. A. Kennewell:

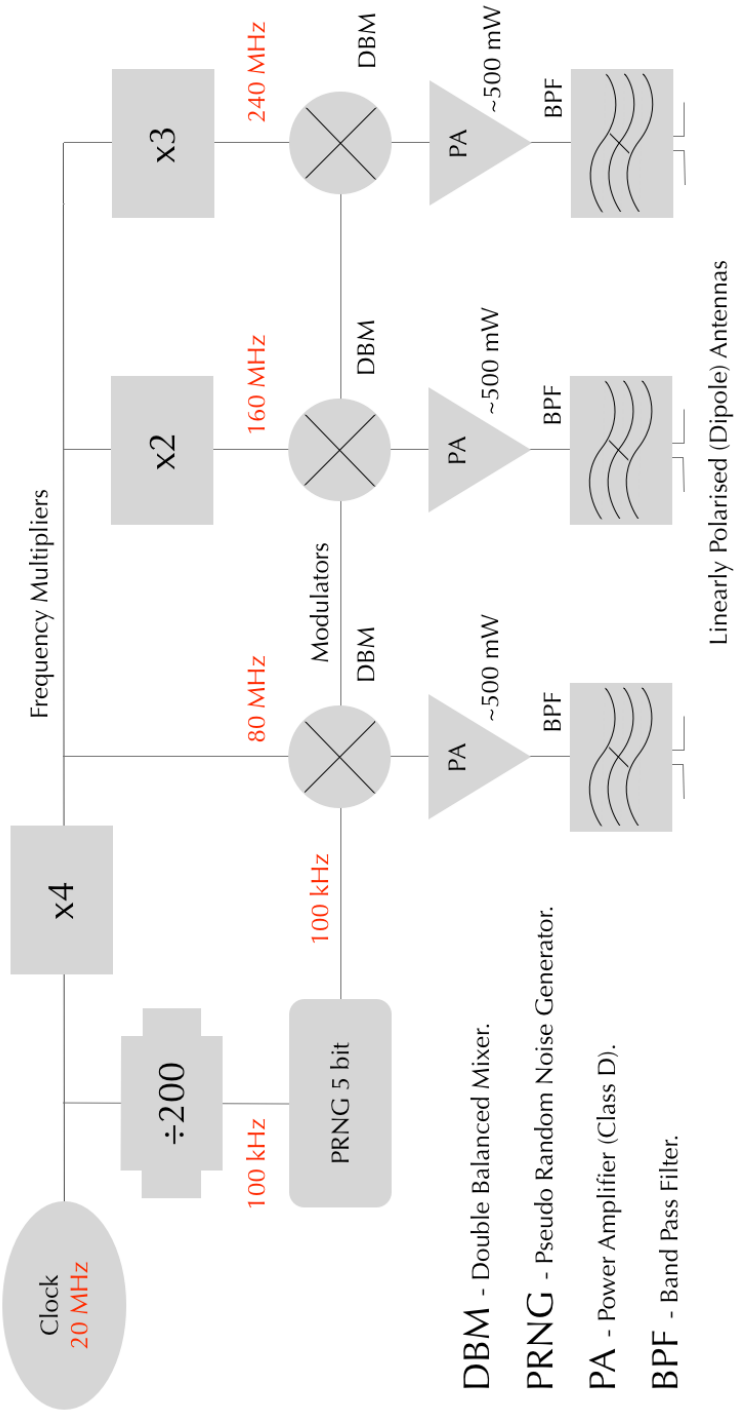


*Figure 6.45: Cubesat radio beacon architecture after a reference design by J. Kennewell.*

### 6.7.3. Receiving Station Architecture.

The user component would follow an architecture, proposed by J. A. Kennewell:

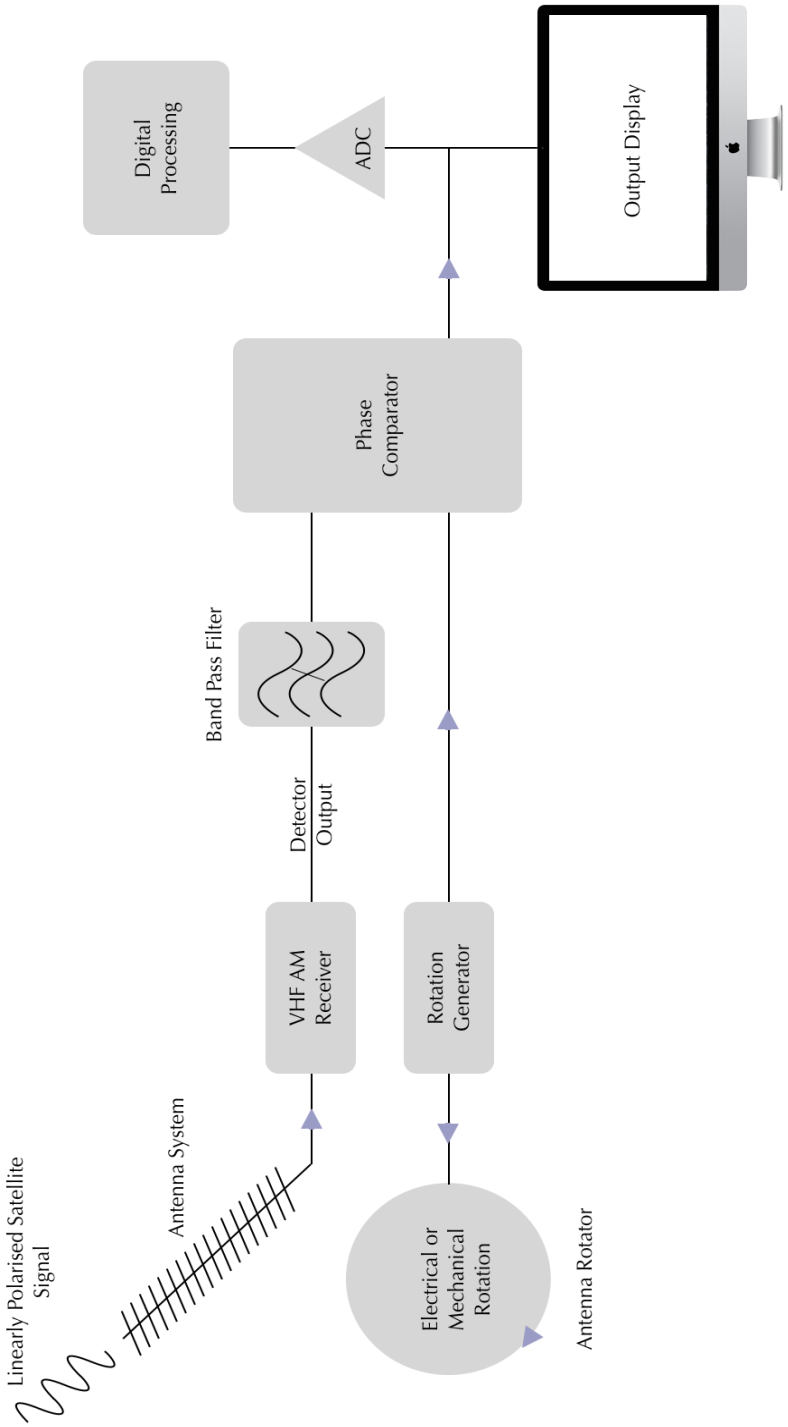


*Figure 6.46: Cubesat receiving station architecture after a reference design by John Kennewell.*

### 6.7.4. Conclusions.

A cubesat mounted, triple VHF beacon will prove to be a viable, cost-effective system capable of fulfilling roles in VHF radio astronomy that currently cannot be duplicated. This proposal will continue to be pursued through every available means.

## 6.8. Summary

(1) The disposition and dynamics of a southern, mid-latitude, continental ionosphere has been studied closely, with data captured at the point of greatest interest, on or near the MRO, over one-half of one full solar cycle.

(2) A Letter that addressed shortcomings in a paper published in 2013 (Sotomayor-Beltran, Sobey et al. 2013), received peer review support for publication but was declined by the host journal. The original paper contained a number of factual and theoretical errors.

(3) A paper was published by the author under peer review (Herne, Kennewell et al. 2013) that addresses the subject of ionospheric dynamics with respect to VHF radio astronomy.

(4) Ionospheric TEC and scintillation data were captured at the MRO over the period 2008-2009, at the beginning of solar cycle 24. The data are represented in waterfall plots (Figures 6.4 to 6.6).

(5) Ionospheric TEC and scintillation data were captured near the MRO at Boolardy homestead and at the Australian Space Academy campus at Meckering over the period 2012-2014, over the peak of solar cycle 24. The data are represented in waterfall plots (Figures 6.7 to 6.12).

(6) The TEC variability in the ionosphere was analysed and presented over two epochs, over the beginning of and the peak of solar cycle 24.

(7) The response of the local ionosphere to a significant CME on March 17th, 2013 was studied and presented (Figures 6.19 (a) and (b)). Resulting TIDs were observed and analysed in detail, resulting in the detection and interpretation of the dynamics of 2 TIDs (Figures 6.36 and 6.37).

(8) Scintillation as $S_4$ was studied alongside the studies of TEC. The failure to detect $S_4$ at GPS frequencies was discussed in concert with the low expectation of scintillation activity at the southern, mid-latitude location of the MRO (Figures 6.21 to 6.25).

(9) An event in the ionosphere on October 2nd, 2013 was studied and discussed. The observation of TIDs at varying scales during this event was presented (Figures 6.39 and 6.42).

(10) The disposition of the ionosphere interpreted at two locations 519 km apart (mw2 and mec) was discussed and differences in local TEC coincident in time presented (Figure 6.42).

(11) A comparison of the levels of TEC predicted by the model IRI-2012 for the MRO with measured TEC was undertaken and the results presented (Tables 6.2 and 6.3, Figures 6.43 and 6.44). The study covered the two period from the beginning of solar cycle 24 (E1) to the peak of the cycle (E2). The model was compared with hourly TEC levels measured for every hour of every day on a monthly basis. The model clearly demonstrated the ability to predict TEC levels to high accuracy under conditions of low SSN (mean $\Delta TEC$ = 1.34 TECU over E1). The model performed quite poorly at times during periods of high SSN (mean $\Delta TEC$ = 4.28 TECU over E1, rising to mean $\Delta TEC$ = 7.47 TECU over the peak of E2).

(12) The possibility and benefits of developing an Ionosphere Quality Index (IQI) was briefly discussed. This work is the subject of possible future work.

(13) The benefits of orbiting a triple VHF beacon equipped cubesat was presented. The architecture of a satellite borne transmitter and the ground segment (receiver) was described (Figures 6.45 and 6.46). The role and benefits such a satellite would present both to the MWA (calibration) and ionospheric science was discussed.

# 7. Conclusions and Further Work.

Over the period of this research (2007-2014), the ionosphere above the mid-west and south-west of Western Australia was studied and the implications for VHF (50-300 MHz) radio astronomy in particular reported. Radio telescopes such as the MWA are highly susceptible to degrading effects of the ionosphere, a dispersive and refractive medium. This work investigates the nature of the mid-latitude, continental ionosphere and endorses the original decision to promote the site's selection as a high quality candidate for the SKA instrument. The MRO is confirmed, by the present research effort, to be an excellent location from which to conduct low-frequency (VHF) radio astronomy.

The Thesis opened with descriptions of the design and operational requirements of the MWA (Chapter 2), an instrument that I helped construct. Discussion continued with a description of the ionosphere (Chapter 3) with particular attention paid to aspects relevant to VHF radio astronomy. Research conducted was both theoretical (Chapter 4) and experimental (Chapters 5 and 6). Mathematica scripts were used for data reduction, analysis and for all modelling. I am willing to share programs, of which I was sole author, with any researcher who might find them useful.

Findings resulted from each activity and are drawn to a conclusion in this chapter together with recommendations for further work. Finally, I also highly recommend that GPS TEC measurements continue at both the MRO (or vicinity) and at the Australian Space Academy campus at Meckering and that these studies be undertaken using multiple, colocated systems (Section 5.3.4). I recommend too, that systems be placed east of the MRO to accommodate research into refraction in right ascension, as discussed in Section 4.1.11.

## 7.1. Modelling of the Ionosphere in Respect of VHF Radio Astronomy.

The objective of this section was to explore essential requirements of models that describe the response of VHF (50-300 MHz) radio waves to the ionosphere, so that such models will be useful in support of instrument calibration.

The simplest instance of a model ionosphere that could be deduced from first principles, after Chapman theory, was discussed in detail and a model of the ionosphere formulated as a Chapman profile (Section 4.1.4). The ionosphere was modelled also after the empirical model IRI-2012 (Section 4.2.1). Profiles were produced for each hour of 17th March 2013, during a significant geomagnetic storm, under this model (24 cases - Figures 4.27 and 4.29). I demonstrated that:

(1) Slab ionospheres featuring either a uniform or non-uniform electron profile do not produce refraction (Sections 4.15-4.16).

(2) In a curved ionosphere that conforms to the curvature of the Earth, refraction differs in an ionosphere that features a uniform electron profile against one featuring an inhomogeneous electron profile with equal TEC (Section 4.1.7-4.1.9).

(3) Refraction in right ascension (Section 4.1.11) is subject, to a first order, on changes in TEC in an east-west direction and that TEC excursions in this direction are principally associated with TIDs (Figure 4.21).

(4) One advantage of a model ionosphere derived from theory, such as the one here derived from Chapman theory, is that it may be arbitrarily perturbed (Figure 4.25) and deeper relationships investigated.

(5) Refraction observed in images captured on the evening of 15th October, 2013 was shown to require a refracting surface, that is, a

significant change in electron density, to produce observed effects. Cases of spherical and lenticular regions of enhanced density were studied that required regions one order of magnitude more dense than the indigenous region to produce the observed effect.

(6) The ionosphere modelled after Chapman theory assigned 63.9% of the ionosphere to the topside. The ionosphere derived from the (hourly) IRI-2012 model assigned between 68.4% - 78.1% to the topside.(Section 4.2.1). This resulted in slight differences between the two models when estimating FR due to the ionosphere.

FR in the ionosphere at MWA frequencies is very sensitive to changes in TEC. When studying FR, (Section 4.2), I discovered that:

(7) A thin-shell ionosphere can return FR values that correspond closely to those produced by an ionosphere modelled after either Chapman theory (Section 4.2.4) or IR-2012 (Section 4.2.5). However, the screen height must be carefully chosen (Figure 4.34). This discovery has implications for all models that employ a thin-shell ionosphere in the calibration of low-frequency radio telescopes. A thin-shell is a computationally efficient form of ionosphere and is used by most models.

(8) The ratios of the IRI-2012 model TEC centroid across an entire day and coincidence heights (the heights at which the thin-shell model produces the same FR as the IRI-2012 model), are in an almost one-to-one relationship, displaying a slope of 1.064 and a standard deviation of 0.007. This result (Section 4.2.5) has implications for thin-shell height selection when based on the IRI-2012 model, resulting in a computationally efficient determination.

(9) Computed FR was compared against FR that we measured over the MRO (Section 4.2.6) and found good agreement.

I studied the slowly varying ionosphere. This work could be extended to:

(10) Accommodate a rapidly varying ionosphere, accounting for common disturbed modes such as sudden ionospheric disturbances (SIDs), travelling ionospheric disturbances (TIDs) and storm enhanced density fluctuations (SEDs).

(11) Apply inverse methods to produce a tomographic map of the realistic ionosphere.

## 7.2. Structure and Variability of the Ionosphere over the Southern, Mid-Latitude, Murchison Radio Observatory.

The objective of this section was to describe the structure and dynamics of the ionosphere at the MRO over an extended period of time and discuss implications for the site as home to the MWA and SKA low-frequency (VHF) observatory.

The disposition of a southern, mid-latitude, continental ionosphere was described over two separate epochs, one of low solar activity at the beginning of cycle 24 (E1) and the other during a period of high solar activity over the peak of cycle 24 (E2) (Figure 6.13). Conclusions arising from this work include:

(1) I demonstrated (Figures 5.8 and 5.10) that GPS systems can produce TEC values that differ by several TECU even when colocated, depending on ambient temperature and the biases applied to individual receivers (Section 5.3.4).

(2) Data collected over E1 and E2 (Section 6.2.1) displayed markedly differing TEC values. Over E1 at the MRO, readings fell within the range 1-35 TECU., with 99.0% in the range 1-20 TECU. Over E2 at the MRO, readings fell within the range 1-84 TECU with 99.5% below 60 TECU. At Meckering, readings fell within the range 1-73 TECU with 98.1% less than 50 TECU.

(3) Scintillation, computed as $S_4$ was reliably undetectable. Background $S_4$ readings over E1 and E2 were very similar. Signal noise that precessed daily at the same rate as the GPS satellites (4 minutes earlier each day) was higher at the MRO during E2 than over E1. This can be attributed to higher $S_4$ noise levels close to the horizon (Section 6.2.4). Scintillation at GPS frequencies was measured at background (noise) levels with occasional excursions that, even if valid, did not exceed quiet sky conditions except for the occasional bands of readings that precessed at the GPS satellite rate and could therefore not be distinguished from multi-path effects.

(4) Solar EUV flux, measured as 10.7 cm (2800 MHz) radiation, ranged between 60-80 SFU over E1 and ranged between 90-180 SFU over E2.

(5) Ap index values ranged to ~20 over E1 with excursions to 40. Over E2, the index ranged to ~40 with a maximum excursion observed of ~90.

(6) TEC consistently fell to the lowest levels locally in the ~90 min between astronomical sunrise (sunrise at 300 km altitude) and local dawn (sea level) (Figures 6.4, 6.7 and 6.10). This was the result of a gradual depletion overnight of free electrons by recombination in the absence of solar EUV.

(7) TEC exhibited the greatest variability across the whole sky in the ~90 min between astronomical sunrise (sunrise at 300 km altitude) and local dawn (sea level) (Figures 6.6, 6.9 and 6.12). This was a consequence of the TEC displayed being produced as the average of TEC readings returned by all satellites, some of which were exposed to daylight while others were in darkness. Therefore, parts of the ionosphere had experienced solar EUV and the consequent rise in free electron content while other parts had not.

(8) TEC exhibited the lowest variability across the sky during daylight hours over all months annually (Section 6.2.3, 6.2.4).

(9) A ~25.6 variability in TEC was evident over E2 in mec and mw2 data except where elevated nocturnal TEC masked the feature. This could not be discerned in this data over E1. This period is not consistent with solar rotation of ~27 days and is likely the result of solar plage on different parts of the sun generating higher levels of EUV. Smaller peaks in the F10.7 plots provide further evidence of the complex nature of this emission.

(10) Peaks in 10.7 cm radiation corresponded to elevated daytime TEC readings and the prolonging of daytime TEC levels into the early evening.

(11) The response of the ionosphere at 2 locations (mec and mw2) was studied during a significant CME event on March 17$^{th}$, 2013. TEC was observed to drop suddenly upon onset of the event and take several days to recover (Figure 6.19 a and b). During this event, strong TIDs were observed .

(12) TIDs (Section 6.6) were detected at varying temporal and spatial scales (Figures 6.22, 6.26 and 6.28), illustrating GPS' ability to map small (<1.0 TECU) excursions in TEC. Two large TIDs associated with the geomagnetic storm of 17$^{th}$ March, 2013 were detected and shown to be propagating in a direction away from the southern polar vortex (Figures 6.23 and 6.24). The directions of these TIDs were calculated with ±12% and ±9% uncertainty and their speeds to ±19% and ±8% accuracy respectively.

(13) The difference in observed TEC between mec and mw2 over the period August 2012 to May 2014 was presented on a daily basis, where coincident readings were available. Whereas TEC levels at Meckering were typically very close in value to those at Boolardy, background levels at the latter over E2 often ranged a little higher (by a few TECU).

(14) A comparison of GPS-derived TEC was compared with TEC levels predicted by the IRI-2012 model (Section 6.5). The difference in output of this model with measured TEC values over E1 and E2 was studied and reported. E1 incorporated a period of time at the very beginning of solar cycle 24 (2008-2009) and E2, the peak of the cycle (2012-2014). The mean RMS difference between the model output over E1 was low (1.34 TECU) and over E2 was less accurate (4.28 TECU). Over the peak of the cycle in 2014, the mean RMS difference was considerably higher (7.47 TECU). The climatological IRI-2012 model did not predict observed TEC values well during periods of high sunspot number (SSN). The model cannot predict and therefore, accurately account for, the SSN experienced on a day-to-day basis.

(15) The system architecture and benefits to the MWA and other VHF radio telescopes obtained by orbiting a triple, VHF beacon equipped satellite (in a cubesat form factor) are outlined and discussed. The outcomes of this study are discussed in Section 7.4.

(16) A paper published recently that incorrectly mapped the ionosphere over mid-latitude Australia, resulting in the assertion that the ionosphere over the MRO was subject to the EIA, was corrected (Section 6.1). A corrigendum by the paper's authors is awaiting publication.

## 7.3. Future Activities.

This work has opened many opportunities for further work, including that which would lead to the following.

### 7.3.1. An Observer's Ionosphere Quality Index.

The objective of this section was to explore the formulation of one or more indices that will assist observers in deciding which observations are most likely to provide images to the highest fidelity.

(1) The relevance of differences in $\Delta RMS$ TEC between measured and the IRI-2012 model (Tables 6.2 and 6.3) were shown to be significant when one uses the model in the calibration of a telescope.

(2) Section 4.2.4 demonstrated the effects on FR estimates of differences between a thin-shell ionosphere and a more sophisticated model, such as that based on a Chapman profile. Section 6.5 demonstrated that differences in ionospheric model estimates of TEC and recorded values compounds the problem of accurately estimating ionospheric TEC.

### 7.3.2. Satellite Based, VHF Beacon.

The objective of this section was to explore the possibility of employing a VHF beacon equipped cubesat in more accurate determinations of FR and MWA tile response.

(1) Determine the feasibility of using a VHF beacon equipped satellite (cubesat) in probing the ionosphere at MWA relevant frequencies to permit both the study of FR in the ionosphere and aid in characterising antenna response, which is currently inaccessible in the far-field.

(2) A satellite would fulfil several roles (Section 6.7.1), such as:

(a) providing the opportunity to measure ionospheres TEC and scintillation at frequencies relevant to the MWA.

(b) Provide a means of measuring direction-dependent properties of telescope antennas.

(c) When suitably equipped with a high-fidelity GPS receiver, measure upper-ionospheric TEC.

(d) Evaluate cost-effective technologies that could be applied to studying the Martian ionosphere *in situ*.

# 8. Publications

## 8.1. Publications as First Author

(1) **David Herne**, John Kennewell, Mervyn Lynch, Charles Carrano (2013). **Ionospheric Phenomena and Low-Frequency Radio Astronomy**. Proceedings of the Australian Space Science Conference (ASSC), Sydney, Australia, 30th September-2nd October 2013. (Peer reviewed.)

(2) **David Herne**, Mervyn Lynch, John Kennewell, Charles Carrano, Keith Groves, Anthea Coster, Divya Oberoi (2011). **Characterisation of the ionosphere over the Murchison Radio Astronomy Observatory**. AGU Fall Meeting, December 5-9 2011, San Francisco; Session SA07.

(3) **David Herne**, Mervyn Lynch, Anthea Coster, Charles Carrano, Keith Groves, John Kennewell, Jennifer Williams, Divya Oberoi (2011), **Characterisation of the ionosphere over the Murchison Radio Astronomy Observatory**. Path to SKA-low Workshop - Perth, Western Australia, 6th-9th September 2011.

(4) **David E. Herne**, M.J. Lynch, (2010), **Remote sensing of the Ionosphere over the Murchison Radio Observatory, Murchison, Western Australia, Leading to an Understanding of Fine Scale Behaviour**. AGU Fall Meeting, December 13-17 2010, San Francisco; Session SA07. Poster session.

(5) **David E. Herne**, M.J. Lynch,(2009), **Characterisation of the Ionosphere over the Murchison Radio Observatory, Murchison, Western Australia**. AGU Fall Meeting, December 14-18 2009 San Francisco; Paper Number: SA23A-1460.

# Characterisation of the Ionosphere over the Murchison Radio Observatory, Murchison, Western Australia.


**David E. Herne**

**Curtin Institute of Radio Astronomy, Curtin University of Technology, Perth, Western Australia**

david.herne@student.curtin.edu.au



**AGU Fall Meeting, December 14-18 2009 San Francisco; Paper Number: SA23A-1460**



## Abstract

The Murchison Radio Observatory (MRO) is the future home of radio astronomy in Australia. Projects are currently under development at the MRO, including a low-frequency instrument, the Murchison Widefield Array (MWA). The MWA is an aperture synthesis, imaging array that when complete will comprise approximately 8,000 dipole antennas, operating in the frequency range, 80 to 300 MHz.

Signals in the frequency range of interest reaching the MWA are subject to distortions caused by the ionosphere. The effects of scintillation and faraday rotation degrade image quality. Self-calibration techniques compensate for scintillation and in the process, provide accurate relative total electron content (TEC) measures of the ionosphere (milli-TEC). However, to 'unwind' faraday rotation effects, the absolute TEC (aTEC) of the ionosphere must be determined. This step is necessary in order to study processes in space involving magnetism.

Over a period of two years, absolute TEC measurements have been made over the MRO using high-precision, dual-frequency GPS systems. Continuous measurements have been performed over the past year and campaign-based measurements prior to that. This paper presents results from those studies, which are providing insights into the nature of the ionosphere over a previously poorly understood, mid-latitude region of the southern hemisphere. This work too, is laying a foundation for the accurate characterisation of the ionosphere over the MRO which is also the possible future site of the Square Kilometre Array (SKA).


## The Murchison Radio Observatory

Located in the Murchison Shire of Western Australia, the **Murchison Radio Observatory (MRO)** is the future site of radio astronomy observatories in Australia. Currently, two projects are under active development, the CSIRO's ***Australian Square Kilometre Array Prototype (ASKAP)*** and the ***Murchison Widefield Array***, radio telescope ***(MWA)***. ASKAP is a ***Square Kilometre Array (SKA)*** prototype, multi-gigahertz, dish-based antenna array. It is currently in the earliest stages of construction at the MRO.


Image: CSIRO Simulation

Image: David Herne

The MWA is a low-frequency, aperture-synthesis, tile-based array that when complete, will comprise 8,192 crossed-dipole antennas mounted on 512 tiles arrayed in a dithered Reuleaux formation. This observatory is currently producing images from a 32 tile, 512 dipole build and is due for completion in 2010/2011.

Other significant radio experiments that have employed the facility include the ***Precision Array to Probe the Epoch of Reionization*** (***PAPER***), led by the University of California, Berkeley and the National Radio Astronomy Observatory (NRAO) and ***EDGES***, led by Haystack Observatory and JPL.

The MRO is located in one of the most sparsely inhabited, accessible, regions of Australia, a region with a population of up to 160 people occupying approximately 50,000 square kilometres.

## Ionospheric Dependancies of Low-Frequency Radio Astronomy

The MWA operates in the frequency regime **80 - 300 Mhz**. To these frequencies, the ionosphere is both refractive and birefringent, leading to pronounced scintillation and the imparting of significant Faraday rotation on impinging radio signals (Rawer, 1993). Therefore, images produced by telescopes operating at susceptible frequencies must be calibrated at either or both of two levels in order to produce images of the highest fidelity. Further, the ionosphere, being a phenomenon that is itself susceptible to forcing over various time scales, imposes the need on observers to perform regular calibration of instruments so to maintain their image fidelity. Understanding therefore, timescales in the ionosphere is necessary also.

Although both positively charged species (positive ions) and negatively charged species (electrons) exist in the ionosphere and magnetosphere, it is the electrons in the ionosphere that are principally responsible for the phenomena that require mitigating, due to their intrinsic coupling frequency. The relevant metric therefore, is the **total electron content (TEC)** of the ionosphere.

## Calibration of the MWA

The MWA is strongly susceptible to the image degrading effects of the ionosphere. However, it is capable of removing the effects of refraction in the ionosphere by a process of self-calibration know as *peeling* (D. A. Mitchell et. al., 2008). Peeling in this implementation is a real-time, interferometric technique that has been observed to perform well under various ionospheric conditions. The calibration system of the MWA measures the apparent angular offsets of calibrators that are induced by the ionosphere. Models of the ionosphere and of instrument response are fitted to the image to remove offsets. This process takes place in real-time, with a cadence of 8 seconds as data streaming from the array is not stored due to the volume involved (19 Gb $s^{-1}$ from the correlator). This process produces a corresponding map of the *relative total ionospheric content* (TEC) of the ionosphere. Interestingly, this capability also promotes use of the MWA as a sensor capable of mapping the ionosphere (Coster et. al., 2008).

However, the self-calibration process lacks the ability to 'unwind' faraday rotation, which is necessary if one intends studying magnetic field dependant processes, which is important in many modern studies, such as those of pulsars for example. The faraday effect is that whereby the plane of polarisation of an electromagnetic wave is caused to rotate as the wave traverses a bi-refringent medium, due to differing group delays of the wave's 'o' and 'e' waves (being also a frequency dependant metric). Unwinding faraday rotation requires knowledge of the *absolute* total electron content (aTEC) of the ionosphere and magnetosphere. Therefore, an external method of determining aTEC is necessary and the results fed into the calibration chain. Over a period of two years, such a method has been studied on the MRO, that of employing high-precision, differential GPS systems.

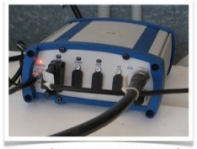

Pictured above are the 3 components of a GPS system, the antenna, receiver and computer.

## Characterising the Ionosphere Over the MRO

For the purposes of radio astronomy, a first order, full calibration of the ionosphere is possible if the absolute total electron content (aTEC) is known in the line of sight of the instrument when producing an image. Absolute TEC takes the value of the number of electrons per square metre. Vertical TEC (VTEC), which is the assumed quantity in this discussion, takes the TEC value looking vertically overhead. One TEC unit (TECU) is equivalent to $10^{16}$ electrons $m^2$. However, the ionosphere is dynamic at varying timescales (Kennewell et. al., 2005). Therefore, a knowledge of time scales of the dynamic structure of the ionosphere is necessary in order to perform calibrations at appropriate intervals. Three high-precision, dual frequency GPS systems, provided by the United States, Air Force Research Laboratory (Dr. Keith Groves), have been deployed over the past two years in a campaign mode and when facilities were accessible, in a continuous mode, with which to probe the ionosphere. After post-processing, using a Kalman filter technique (Carrano et. al., 2009), values of aTEC and scintillation index (S4) are returned together with other parameters. Readings are returned on a time-scale (epoch) of 1 minute, although much more highly time-wise resolved data is availabl

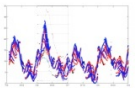

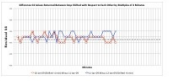

Plot - Charles Carrano

Graphs - David Herne

The graph above is a typical plot of aTEC returned by the systems. Diurnal variation can clearly be seen in the readings. Overlain on the data for day 316, although hard to distinguish, is the graph of ionosonde readings produced by the Learmonth Solar Observatory, located approximately 500 km to the northwest for that day. Most recently, these systems have been deployed in the configuration shown below, at separations useful to observing dynamic features of the ionosphere, such as traveling ionospheric disturbances (TIDs). These are density ripples that travel through the ionosphere, driven by atmospheric processes.

The Locations of GPS systems used in this study.

The plot centre top shows the S4 index for a single hour (12:00 - 13:00 hrs Universal) on three successive days returned by a single satellite. At first glance, there is structure to the data, although over a small range. However, once the daily 4 minute precession of this single satellite is taken into account (pointed out in a feature of the data by the green arrows, a local maxima) and residuals calculated, the S4 index on this occasion is seen to be quite subdued (plot top right).

## Other Analyses and Techniques

The Australian government's Ionospheric Prediction Service (IPS) provides very useful data into the process, through modelling of the nature and behaviour of the ionosphere over Australia and through provision of acquired data, such as ionogrammes, examples of each of which are shown in the images below. The ionogramme was produced at the Learmonth Solar Observatory.

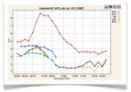

## References


(1) Rawer K.; *Wave Propagation in the Ionosphere*, 1993, Kluwer Academic Publishers, P.O. Box 17, 3300 AA Dordrecht, The Netherlands.

(2) Mitchell D. A., Greenhill L. J., Wayth R. B., Sault R. J., Lonsdale C. J., Cappallo R. J., Morales M. F., Ord S. M., 2008, *Real-Time Calibration of the Murchison Widefield Array*, arXiv:0807.1912v2

(3) Coster A., Erickson P., Herne D., Oberoi D., Salah J., 2008, *The Murchison Widefield Array (MWA): A New Ionospheric Sensor*, IES 2008.

(4) Kennewell J., Caruana J., Terkildsen M., Wu J., Wilkinson P., Cole D., Mitchel K., To V., 2005, *The Australian Ionosphere*, report prepared for CSIRO by IPS Radio and Space Services.

(5) Carrano C. S., Anghel A., Quinn R. A., Groves K. M., 2009, *Kalman filter estimation of plasmaspheric total electron content using GPS*, Radio Sci., 44, RS0A10, doi:10.1029/2008RS004070.


*Figure 8.1: Poster - Characterisation of the Ionosphere over Murchison Radio Observatory, Murchison, Western Australia, AGU Fall Meeting, San Francisco, December 2009.*

# Remote sensing of the Ionosphere over the Murchison Radio Observatory, Western Australia, Leading to an Understanding of Fine Scale Behaviour.

**David Herne[1,6], Mervyn Lynch[1], Anthea Coster[2], Charles Carrano[3], Keith Groves[4], John Kennewell[1], Jennifer Williams[5], Divya Oberoi[2].**

[1] Curtin Institute for Radio Astronomy, International Centre for Radio Astronomy Research, [2] MIT Haystack Observatory, [3] Boston College, [4] United States Airforce, Office of Scientific Research. Airforce Research Laboratory, [5] Siena College, [6] To whom correspondence should be addressed. david.herne@student.curtin.edu.au

**AGU Fall Meeting, December 13-17 2010 San Francisco; Paper Number: SA43B-1764**

## Abstract

The Murchison Radio Observatory (MRO) is the home of radio astronomy in Australia. Projects currently under development at the MRO include a low-frequency instrument, the Murchison Widefield Array (MWA). The MWA is an aperture synthesis, imaging array that when complete will comprise approximately 8,000 dipole antennas operating in the frequency range, 80 to 300 MHz. Signals in this frequency range are subject to distortions caused by the ionosphere. The effects of scintillation and Faraday rotation degrade image quality. In order to 'unwind' Faraday rotation, the distribution of the electron content in the ionosphere must be determined. Knowledge of the absolute total electron content (TEC) provides information about this distribution. This step is necessary in order to study processes in space involving magnetism.

Over a period of two years, TEC measurements have been made over the MRO using high-precision, dual-frequency, GPS systems. Continuous measurements were performed for 12 months and campaign-based measurements at other times, due to the remote location of the MRO. The determination of the GPS receiver biases used to calculate TEC were studied with respect to changing temperatures. TEC measurements are compared to the results of modelling conducted previously (Kennewell et. al. 2005) as part of Australia's bid to host the Square Kilometre Array radio telescope (SKA). Further, due to the fine grained nature of measurements (on the order of 0.01-0.03 TEC units), fine-scale structure can be resolved in the behaviour of the ionosphere in both temporal and spatial domains and is discussed.

This work too, is laying a foundation for the accurate characterisation of the ionosphere over the MRO which is also the possible future site of the SKA. Plans to extend this work and the implementation of useful new measurement regimes are discussed, enabled by facilities currently being established as part of Australia's ongoing commitment to radio astronomy on the MRO.

## The Murchison Radio Observatory

Located in the Murchison Shire of Western Australia, the **Murchison Radio Observatory (MRO)** is the future site of radio astronomy observatories in Australia. Currently, two projects are under active development, the CSIRO's ***Australian Square Kilometre Array Prototype (ASKAP)*** and the ***Murchison Widefield Array***, radio telescope ***(MWA)***. ASKAP is a ***Square Kilometre Array (SKA)*** prototype, multi-gigahertz, dish-based antenna array. It is currently in the earliest stages of construction at the MRO.


*Image:* CSIRO Simulation  Image: David Herne

The MWA is a low-frequency, aperture-synthesis, tile-based array that when complete, will comprise 8,192 crossed-dipole antennas mounted on 512 tiles arrayed in a dithered Reuleaux formation. This observatory is currently producing images from a 32 tile, 512 dipole build and is due for completion in 2011.

Other significant radio experiments that have employed the facility include the ***Precision Array to Probe the Epoch of Reionization (PAPER)***, led by the University of California, Berkeley and the National Radio Astronomy Observatory (NRAO) and ***EDGES***, led by Haystack Observatory and JPL.

The MRO is located in one of the most sparsely inhabited, accessible, regions of Australia, a region with a population of up to 160 people occupying approximately 50,000 square kilometres.

## Ionospheric Dependancies of Low-Frequency Radio Astronomy

The MWA operates in the frequency regime **80 - 300 Mhz**. To these frequencies, the ionosphere is both refractive and birefringent, leading to pronounced scintillation and the imparting of significant Faraday rotation on radio signals (Rawer, 1993). Therefore, images produced by telescopes operating at susceptible frequencies must be calibrated at either or both of two levels in order to produce images of the highest fidelity. Further, the ionosphere, being a phenomenon that is itself susceptible to forcing over various time scales, imposes the need on observers to perform regular calibration of instruments so to maintain their image fidelity. Understanding therefore, timescales in the ionosphere is necessary also.

Although both positively charged species (positive ions) and negatively charged species (electrons) exist in the ionosphere and magnetosphere, it is the electrons in the ionosphere that are principally responsible for the phenomena that require mitigating, due to their intrinsic coupling frequency. The relevant metric therefore, is the **total electron content (TEC)** of the ionosphere, a measure of the total numbers of electrons along line-of-sight paths between the observing instrument and object under investigation.

## Calibration of the MWA

The MWA is strongly susceptible to the image degrading effects of the ionosphere. However, it is capable of removing the effects of refraction in the ionosphere by a process of self-calibration know as *peeling* (D. A. Mitchell et. al., 2008). Peeling in this implementation is a real-time, interferometric technique that has been observed to perform well under various ionospheric conditions. The calibration system of the MWA measures the apparent angular offsets of calibrators that are induced by the ionosphere. Models of the ionosphere and of instrument response are fitted to the image to remove offsets. This process takes place in real-time, with a cadence of 8 seconds as data streaming from the array is not stored due to the volume involved (19 Gb $s^{-1}$ from the correlator). This process produces a corresponding map of the *relative total ionospheric content* (TEC) of the ionosphere. Interestingly, this capability also promotes use of the MWA as a sensor capable of mapping the ionosphere (Coster et. al., 2008).

However, the self-calibration process lacks the ability to 'unwind' Faraday rotation, which is necessary if one intends studying magnetic field dependant processes, which is important in many modern studies, such as those of pulsars for example. The Faraday effect is that whereby the plane of polarisation of an electromagnetic wave is caused to rotate as the wave traverses a bi-refringent medium, due to differing group delays of the wave's 'o' and 'e' waves (being also a frequency dependant metric). Unwinding Faraday rotation requires knowledge of the *absolute* total electron content (aTEC) of the ionosphere and magnetosphere. Therefore, an external method of determining aTEC is necessary and the results fed into the calibration chain. Over a period of two years, such a method has been studied on the MRO, that of employing high-precision, differential GPS systems.

## Characterising the Ionosphere Over the MRO

For the purposes of radio astronomy, a first order, full calibration of the ionosphere is possible if the absolute total electron content (aTEC) is known in the line of sight of the instrument when producing an image. Absolute TEC takes the value of the number of electrons per square metre. Vertical TEC (VTEC), which is the assumed quantity in this discussion, takes the TEC value looking to the zenith. One TEC unit (TECU) is equivalent to $10^{16}$ electrons $m^2$. However, the ionosphere is dynamic at varying timescales (Kennewell et. al., 2005). Therefore, a knowledge of time scales of the dynamic structure of the ionosphere is necessary in order to perform calibrations at appropriate intervals. Three high-precision, dual frequency GPS systems, provided by the United States, Air Force Research Laboratory (Dr. Keith Groves), were deployed in a campaign mode and when facilities were accessible, in a continuous mode, with which to probe the ionosphere. After post-processing, using a Kalman filter technique (Carrano et. al., 2009), values of aTEC and scintillation index (S4) are returned together with other parameters. Readings are returned on a time-scale (epoch) of 1 minute, although much more highly time-resolved data is available (50 Hz).

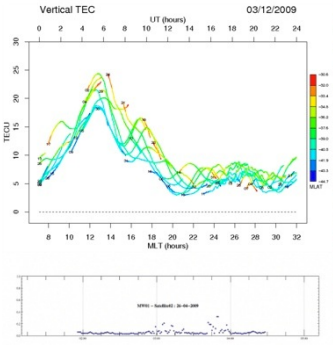


The image, left upper, is a plot of typical aTEC readings returned by a GPS system over the interval of a single day. Local time is ahead of UT by 8 hours, which places the peak reading of approximately 25 TECU at 2PM local. The minimum value is reached at around 11PM local. The image, left lower, is of scintillation indices (S4) returned by a single satellite pass. Two possible excursions in the data may be observed. To date, data have been acquired during an extensive period of solar minimum conditions. However, as the Sun enters a period of heightened activity, data collection will continue and will be provided to the MWA in real time for calibration purposes. These systems were deployed in the configuration shown below, at separations useful to observing dynamic features of the ionosphere, such as traveling ionospheric disturbances (TIDs). These are density ripples that travel through the ionosphere, driven by atmospheric processes.

The Locations of GPS systems used in this study.

## GPS - Embracing the Ionosphere and Plasmasphere

Recognising the potential for the plasmasphere, that region of Earth's near space environment that contains non-negligible numbers of charged species, the behaviour of which is dominated by the Earth's magnetic field, to contribute to the TEC observed by GPS ground components, Charles Carrano and colleagues employed techniques that estimate plasmaspheric TEC contribution through the application of Kalman filter techniques (Carrano et. al. 2009). Due to the significantly greater path length of signals in the plasmasphere compared to the ionosphere, it was estimated that under commonly encountered conditions, the contribution to TEC of each can be comparable. Estimating the plasmasphere's contribution reduced the uncertainty in estimates of satellite and receiver instrumental biases and the ionosphere's contribution, which at different latitudes would have resulted in either an under estimation or an over estimation of TEC.

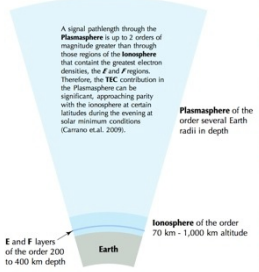


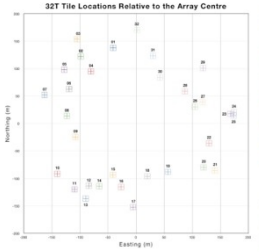


## Receiver Temperature

A member of this project, Jennifer Williams, has looked closely at the effects of temperature on the estimates of receiver biasses (Williams et. al., 2010). Ms. Williams has met with success in detrending data and continues to pursue a deeper understanding of the impact of temperature mediated uncertainties in receiver biasses. Environmental temperatures in the order of 50°C are not uncommon in the Murchison region of Western Australia.

## The MWA as an Ionospheric Sensor

The Murchison Wide Field Observatory will provide excellent ionospheric sensing, leading to finely resolved determinations of dynamic TEC and scintillation indices (S4). The MWA is inherently a multi-element receiving system (8,000 antennas in its final configuration), has a wide field of view that provides a window of approximately 175 square kilometres (Coster et. al., 2008) and exhibits high spectral purity and fidelity at operating frequencies (80 - 300 MHz). Measurements will be made on short timescales with a cadence of 8 seconds and deliver finely resolved TEC measurements of less than 0.01 TECU. Differential TEC values will be produced at kilometre scales as part of a self-calibration procedure. Together with the fine temporal resolution of the imaging process, detailed knowledge of traveling ionospheric disturbances (TIDs), and TEC gradients, storm enhanced density effects (SEDs) and dynamic S4 behaviour will be finely resolved. The image, left lower, shows the prototype arrangement of antenna tiles (each of which comprises 16 full stokes antennas) that comprises 512 dipole antennas. Behaviours of interest will be studied at many frequencies and in many directions (32 currently) concurrently, allowing temporal and energy sensitive signatures to be resolved.

## Additional Data Sources

The Australian government's Ionospheric Prediction Service (IPS) provides very useful data through modelling of the nature and behaviour of the ionosphere over Australia and through provision of acquired data, such as ionograms. Spectrograms and ionograms are contributed to the study by the Learmonth Solar Observatory.

## Conclusions

A rigorous approach to study of the ionosphere over the Murchison Radio Observatory through the deployment of conventional instrumentation employing GPS systems and as yet unconventional instrumentation, the MWA telescope and an equally rigorous approach to accurate instrumental bias estimations has provided an excellent opportunity for improving our knowledge of the systematics of the ionosphere over southern hemisphere, continental mid-latitudes. Should the fullest capabilities of each of the aforementioned instrumental approaches be realised, unprecedented fine-scale knowledge of the ionosphere will be enhanced.

## References

Rawer K., *Wave Propagation in the Ionosphere*, 1993, Kluwer Academic Publishers, P.O. Box 17, 3300 AA Dordrecht, The Netherlands.

Mitchell D. A., Greenhill L. J., Wayth R. B., Sault R. J., Lonsdale C. J., Cappallo R. J., Morales M. F., Ord S. M., 2008, *Real-Time Calibration of the Murchison Widefield Array*, arXiv:0807.1912v2

Coster A., Erickson P., Herne D., Oberoi D., Salah J., 2008, *The Murchison Widefield Array (MWA): A New Ionospheric Sensor*, IES 2008.

Kennewell J., Caruana J., Terkildsen M., Wu J., Wilkinson P., Cole D., Mitchel K., To V., 2005, *The Australian Ionosphere*, report prepared for CSIRO by IPS Radio and Space Services.

Carrano C. S., Anghel A., Quinn R. A., Groves K. M., 2009, *Kalman filter estimation of plasmaspheric total electron content using GPS*, Radio Sci., 44, RS0A10, doi:10.1029/2008RS004070.

Williams J., Coster A., Herne D., Erickson P., Weatherwax A., Oberoi D., Groves K., Carrano C., (2010), *GPS Receiver Bias Temperature Dependence and its Implications for the Murchison Widefield Array (MWA)*. CEDAR, June 2010. Poster Session.

*Figure 8.2: Poster - Remote Sensing of the Ionosphere over Murchison Radio Observatory, Western Australia, Leading to an Understanding ofFine Scale Behaviour, AGU Fall Meeting, San Francisco, December 2010.*

# Characterisation of the ionosphere over the Murchison Radio Astronomy Observatory

David Herne[1,5], Mervyn Lynch[1], Anthea Coster[2], Charles Carrano[3], Keith Groves[3], John Kennewell[1], Jennifer Williams[4], Divya Oberoi[2].

[1]Curtin Institute for Radio Astronomy, International Centre for Radio Astronomy Research, [2]MIT Haystack Observatory, [3]Boston College, [4]Siena College, [5]To whom correspondence should be addressed. david.herne@student.curtin.edu.au

Path to SKA-low Workshop - Perth, Western Australia, 6th-9th September 2011

## Abstract

Projects currently under development at the Murchison Radio Observatory (MRO) include a low-frequency instrument, the Murchison Widefield Array (MWA). The MWA is an aperture synthesis, imaging array operating over the frequency range 80 to 300 MHz. Signals in this range are subject to distortions caused by the ionosphere. The effects of scintillation and Faraday rotation degrade image quality. Historical measurements and models have long shown that the mid-latitude ionosphere has very low scintillation activity. TEC measurements we have made of the ionosphere over the MRO using high-precision, dual-frequency, GPS systems support this belief. Fine grained measurements (of the order 0.01-0.03 TEC units) have permitted fine-scale ionospheric structure to be resolved. These findings are reported and discussed. We review plans to extend this work with the implementation of mobile solar-powered instrumentation that will permit deployment of various GPS configurations that will collect TEC data during the forthcoming period of expected higher solar activity.

## The Murchison Radio Observatory

Located in the Murchison Shire of Western Australia, the **Murchison Radio Observatory (MRO)** is the future site of radio astronomy observatories in Australia. Currently, two projects are under active development, the CSIRO's ***Australian Square Kilometre Array Prototype (ASKAP)*** and the ***Murchison Widefield Array***, radio telescope ***(MWA)***. ASKAP is a ***Square Kilometre Array (SKA)*** prototype, multi-gigahertz, dish-based antenna array. It is currently in the earliest stages of construction at the MRO.

An MWA tile of 16 antennas.


CSIRO radio dishes on the MRO. Image: CSIRO Simulation.

The MWA is a low-frequency, aperture-synthesis, tile-based array that when complete, will comprise 8,192 crossed-dipole antennas mounted on 512 tiles arrayed in a dithered Reuleaux formation. This observatory is currently producing images from a 32 tile, 512 dipole build and is due for completion in 2011.

Other significant radio experiments that have employed the facility include the ***Precision Array to Probe the Epoch of Reionization*** (***PAPER***), led by the University of California, Berkeley and the National Radio Astronomy Observatory (NRAO) and ***EDGES***, led by Haystack Observatory and JPL.

The MRO is located in one of the most sparsely inhabited, accessible regions of Australia, which has a population of up to 160 people occupying approximately 50,000 square kilometres.

## Ionospheric Dependancies of Low-Frequency Radio Astronomy

The MWA operates in the frequency regime **80 - 300 Mhz**. To these frequencies, the ionosphere is both refractive and birefringent, leading to pronounced scintillation and Faraday rotation of radio signals (Rawer, 1993). Therefore, images produced by telescopes operating at susceptible frequencies must be calibrated in order to produce images of the highest fidelity. Further, the ionosphere, being a phenomenon that is itself susceptible to forcing over various time scales, imposes the need on observers to perform regular calibration of instruments so to maintain their image fidelity.

Although both positively charged species (positive ions) and negatively charged species (electrons) exist in the ionosphere and magnetosphere, it is the electrons in the ionosphere that are principally responsible for the phenomena that require mitigating, due to their coupling frequency. The relevant metric therefore, is the **total electron content (TEC)** of the ionosphere, a measure of the total numbers of electrons along line-of-sight paths between the observing instrument and object under investigation.

## Calibration of the MWA

The MWA is strongly susceptible to the image degrading effects of the ionosphere. However, it is capable of removing the effects of refraction in the ionosphere by a process of self-calibration know as *peeling* (D. A. Mitchell et. al., 2008). Peeling in this implementation is a real-time, interferometric technique that has been observed to perform well under various ionospheric conditions. The calibration system of the MWA measures the apparent angular offsets of calibrators that are induced by the ionosphere. Models of the ionosphere and of instrument response are fitted to the image to remove offsets. This process takes place in real-time, with a cadence of 8 seconds as data streaming from the array is not stored due to the volume involved (19 Gb $s^{-1}$ from the correlator). This process produces a corresponding map of the *relative total ionospheric content* (TEC) of the ionosphere. Interestingly, this capability also promotes use of the MWA as a sensor capable of mapping the ionosphere (Coster et. al., 2008).

However, the self-calibration process lacks the ability to 'unwind' Faraday rotation, which is necessary if one intends studying magnetic field dependant processes, which is important in many modern studies, such as those of pulsars for example. The Faraday effect is that whereby the plane of polarisation of an electromagnetic wave is caused to rotate as the wave traverses a bi-refringent medium, due to differing group delays of the wave's 'o' and 'e' waves (being also a frequency dependant metric). Unwinding Faraday rotation requires knowledge of the *absolute* total electron content (aTEC) of the ionosphere and magnetosphere. Therefore, an external method of determining aTEC is necessary and the results fed into the calibration chain. Over a period of two years, such a method has been studied on the MRO, that of employing high-precision, differential GPS systems.

## Characterising the Ionosphere Over the MRO

For the purposes of radio astronomy, a first order, full calibration of the ionosphere is possible if the absolute total electron content (aTEC) is known in the line of sight of the instrument when producing an image. Absolute TEC takes the value of the number of electrons per square metre. Vertical TEC (VTEC), which is the assumed quantity in this discussion, takes the TEC value looking to the zenith. One TEC unit (TECU) is equivalent to $10^{16}$ electrons $m^2$. However, the ionosphere is dynamic at varying timescales (Kennewell et. al., 2005). Therefore, a knowledge of time scales of the dynamic structure of the ionosphere is necessary in order to perform calibrations at appropriate intervals. Three high-precision, dual frequency GPS systems, provided by the United States, Air Force Research Laboratory (Dr. Keith Groves), were deployed in a campaign mode and when facilities were accessible, in a continuous mode, with which to probe the ionosphere. After post-processing, using a Kalman filter technique (Carrano et. al., 2009), values of aTEC and scintillation index (S4) are returned together with other parameters. Readings are returned on a time-scale (epoch) of 1 minute, although much more highly time-resolved data is available (50 Hz).

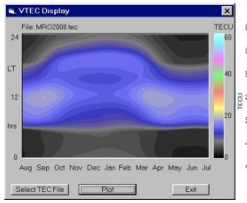


Image: Dr. John Kennewell.

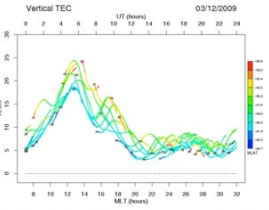


A plot of typical, mid-latitude daily TEC values returned by GPS.

The image, upper left, is the output of a TEC model run over 12 months for a typical mid-latitude, southern hemisphere site. The model bins TEC values into 6 minute intervals, giving a resolution for this image of 240, six minute intervals per day (pixels) by 365 pixels (days per non-leap year). The image, upper right, is of typical daily, TEC behaviour also for a southern, mid-latitude site. The behaviour observed is typical of daily fluctuations in TEC

TEC and S4 readings have been taken at the site of the MRO for a period of two years, both in a campaign mode and from fixed installations as continuous data at sites shown below. These are currently being analysed and together with readings currently being planned using mobile, self-contained GPS systems, will provide a highly resolved probe of the behaviour of the ionosphere in the Murchison region of Western Australia.

## The MWA as an Ionospheric Sensor

The Murchison Wide Field Observatory will provide excellent ionospheric sensing, leading to finely resolved determinations of dynamic TEC and scintillation indices (S4). The MWA is inherently a multi-element receiving system (8,000 antennas in its final configuration), has a wide field of view that provides a window of approximately 175 square kilometres (Coster et. al., 2008) and exhibits high spectral purity and fidelity at operating frequencies (80 - 300 MHz). Measurements will be made on short timescales with a cadence of 8 seconds and deliver finely resolved TEC measurements of less than 0.01 TECU. Differential TEC values will be produced at kilometre scales as part of a self-calibration procedure. Together with the fine temporal resolution of the imaging process, detailed knowledge of traveling ionospheric disturbances (TIDs), and TEC gradients, storm enhanced density effects (SEDs) and dynamic S4 behaviour will be finely resolved. The image, left lower, shows the prototype arrangement of antenna tiles (each of which comprises 16 full stokes antennas) that comprises 512 dipole antennas. Behaviours of interest will be studied at many frequencies and in many directions (32 currently) concurrently, allowing temporal and energy sensitive signatures to be resolved.

## Further Studies

Due to the nature of satellite orbital mechanics, a region of the ionosphere close to and south of the MRO is not sampled by instrumentation located on the MRO (image below, left). Therefore, it is beneficial to place a receiver well south of the MRO in order to better sample a relevant volume of the ionosphere. Hence, we have begun construction trailer mounted of solar power systems (below right) that will permit remote operation of GPS systems over long intervals One trailer is nearing completion, two more will follow shortly.

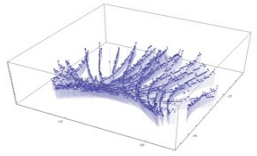

Satellite tracks over the MRO (lat/long), which is at the centre of this image, for a period of one day.

A solar powered trailer for GPS remote operation.

## Conclusions

A rigorous approach to study of the ionosphere over the Murchison Radio Observatory through the deployment of conventional instrumentation employing GPS systems and as yet unconventional instrumentation, the MWA telescope and an equally rigorous approach to accurate instrumental bias estimations has provided an excellent opportunity for improving our knowledge of the systematics of the ionosphere over southern hemisphere, continental mid-latitudes. Should the fullest capabilities of each of the aforementioned instrumental approaches be realised, unprecedented fine-scale knowledge of the ionosphere will be promoted.

## References

Rawer K., *Wave Propagation in the Ionosphere*, 1993, Kluwer Academic Publishers, P.O. Box 17, 3300 AA Dordrecht, The Netherlands.

Mitchell D. A., Greenhill L. J., Wayth R. B., Sault R. J., Lonsdale C. J., Cappallo R. J., Morales M. F., Ord S. M., 2008, *Real-Time Calibration of the Murchison Widefield Array*, arXiv:0807.1912v2

Coster A., Erickson P., Herne D., Oberoi D., Salah J., 2008, *The Murchison Widefield Array (MWA): A New Ionospheric Sensor*, IES 2008.

Kennewell J., Caruana J., Terkildsen M., Wu J., Wilkinson P., Cole D., Mitchel K., To V., 2005, *The Australian Ionosphere*, report prepared for CSIRO by IPS Radio and Space Services.

Carrano C. S., Anghel A., Quinn R. A., Groves K. M., 2009, *Kalman filter estimation of plasmaspheric total electron content using GPS*, Radio Sci., 44, RS0A10, doi:10.1029/2008RS004070.

Williams J., Coster A., Herne D., Erickson P., Weatherwax A., Oberoi D., Groves K., Carrano C., (2010), *GPS Receiver Bias Temperature Dependence and its Implications for the Murchison Widefield Array (MWA)*. CEDAR, June 2010. Poster Session.

*Figure 8.3: Poster - Characterisation of the Ionosphere over Murchison Radio Observatory, Path too SKA-low Workshop, Perth, Western Australia, September 2011.*

# CHARACTERIZATION OF THE IONOSPHERE OVER THE MURCHISON RADIO OBSERVATORY

**David Herne[1,6], Mervyn Lynch[1], Anthea Coster[2], Charles Carrano[3], Keith Groves[3], John Kennewell[1], Jennifer Williams[5], Divya Oberoi[2].**

[1] Curtin Institute for Radio Astronomy, International Centre for Radio Astronomy Research, [2] MIT Haystack Observatory, [3] Boston College, [4] United States Airforce, Office of Scientific Research. Airforce Research Laboratory, [5] Siena College, [6] To whom correspondence should be addressed. david.herne@icrar.org

AGU Fall Meeting, December 5 - 9 2011 San Francisco; Paper Number: SA21A-1867

## Abstract

The Murchison Radio Observatory (MRO), home of radio astronomy in Australia, is located in mid-latitude Western Australia. Projects currently under development at the MRO include a low-frequency instrument, the Murchison Widefield Array (MWA). The MWA is an aperture synthesis, imaging array operating over the frequency range 80 to 300 MHz. Signals in this range are subject to distortions caused by the ionosphere. The effects of scintillation and Faraday rotation degrade image quality. Historical measurements and models have long shown that the mid-latitude ionosphere has very low scintillation activity. TEC measurements we have made of the ionosphere over the MRO using high-precision, dual-frequency, GPS systems support this belief. Fine grained measurements (of the order 0.01-0.03 TEC units) have permitted fine-scale ionospheric structure to be resolved. These findings are reported and discussed. We review plans to extend this work with the implementation of mobile solar-powered instrumentation that will permit deployment of various GPS configurations that will collect TEC data during the forthcoming period of expected higher solar activity.

## The Murchison Radio Observatory

Located in the Murchison Shire of Western Australia, the **Murchison Radio Observatory (MRO)** is the future site of radio astronomy observatories in Australia. Currently, two projects are under active development, the CSIRO's ***Australian Square Kilometre Array Prototype (ASKAP)*** and the ***Murchison Widefield Array***, radio telescope ***(MWA)***. ASKAP is a ***Square Kilometre Array (SKA)*** prototype, multi-gigahertz, dish-based antenna array. It is currently in the earliest stages of construction at the MRO.

*Prototype antennas of the MWA.* *Image: David Herne*

The MWA is a low-frequency, aperture-synthesis, tile-based array that when complete, will comprise 8,192 crossed-dipole antennas mounted on 512 tiles arrayed in a dithered Reuleaux formation. This observatory is currently producing images from a 32 tile, 512 dipole build and is due for completion in 2011.

Other significant radio experiments that have employed the facility include the ***Precision Array to Probe the Epoch of Reionization*** (***PAPER***), led by the University of California, Berkeley and the National Radio Astronomy Observatory (NRAO) and ***EDGES***, led by Haystack Observatory and JPL.

The MRO is located in one of the most sparsely inhabited, accessible, regions of Australia, a region with a population of up to 160 people occupying approximately 50,000 square kilometres.

## Calibration of the MWA

The MWA is strongly susceptible to the image degrading effects of the ionosphere. However, it is capable of removing the effects of refraction in the ionosphere by a process of self-calibration know as *peeling* (D. A. Mitchell et. al., 2008). Peeling in this implementation is a real-time, interferometric technique that has been observed to perform well under various ionospheric conditions. The calibration system of the MWA measures the apparent angular offsets of calibrators that are induced by the ionosphere. Models of the ionosphere and of instrument response are fitted to the image to remove offsets. This process takes place in real-time, with a cadence of 8 seconds as data streaming from the array is not stored due to the volume involved (19 Gb s$^{-1}$ from the correlator). This process produces a corresponding map of the *relative total ionospheric content* (TEC) of the ionosphere. Interestingly, this capability also promotes use of the MWA as a sensor capable of mapping the ionosphere (Coster et. al., 2008).

However, the self-calibration process lacks the ability to 'unwind' Faraday rotation, which is necessary if one intends studying magnetic field dependant processes, which is important in many modern studies, such as those of pulsars for example. The Faraday effect is that whereby the plane of polarisation of an electromagnetic wave is caused to rotate as the wave traverses a bi-refringent medium, due to differing group delays of the wave's 'o' and 'e' waves (being also a frequency dependant metric). Unwinding Faraday rotation requires knowledge of the *absolute* total electron content (aTEC) of the ionosphere and magnetosphere. Therefore, an external method of determining aTEC is necessary and the results fed into the calibration chain. Over a period of two years, such a method has been studied on the MRO, that of employing high-precision, differential GPS systems.

## Characterising the Ionosphere Over the MRO

For the purposes of radio astronomy, a first order, full calibration of the ionosphere is possible if the absolute total electron content (aTEC) is known in the line of sight of the instrument when producing an image. Absolute TEC takes the value of the number of electrons per square metre. Vertical TEC (VTEC), which is the assumed quantity in this discussion, takes the TEC value looking to the zenith. One TEC unit (TECU) is equivalent to $10^{16}$ electrons m$^2$. However, the ionosphere is dynamic at varying timescales (Kennewell et. al., 2005). Therefore, a knowledge of time scales of the dynamic structure of the ionosphere is necessary in order to perform calibrations at appropriate intervals. Three high-precision, dual frequency GPS systems, provided by the United States, Air Force Research Laboratory (Dr. Keith Groves), were deployed in a campaign mode and when facilities were accessible, in a continuous mode. After post-processing, using a Kalman filter technique (Carrano et. al., 2009), values of aTEC and scintillation index (S4) are returned together with other parameters. Readings are returned on a time-scale (epoch) of 1 minute, although much more highly time-resolved data is available (50 Hz).

As part of the initial site selection process, TEC and scintillation were modelled at the location of the MWA. Under conditions of low sunspot number, which existed at the time of this initial study (as opposed to current conditions, under which this study is continuing) TEC values were expected to be quite low and smooth, up to 20 TECU over an annual cycle. Corresponding scintillation was expected to be virtually non-existent, or at least, displaying extremely low activity. Each of these expectations was supported by observations. In the images below, modelled VTEC values over the interval **August 2008 - July 2009** are displayed, followed by actual VTEC readings. The two exhibit a remarkable correspondence, particularly in the range of TEC values exhibited.

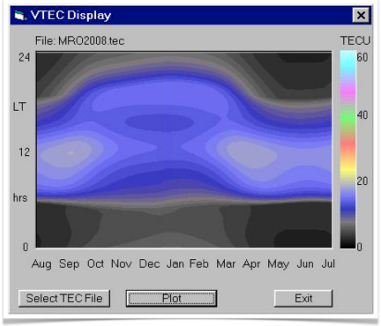


*Output of TEC model for the Murchison at the location of the MWA.* *Image: Dr. John Kennewell.*

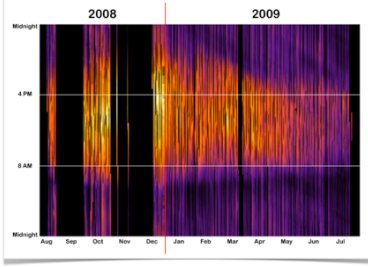


*A plot of typical, mid-latitude daily TEC values returned by GPS.*

| Counts of TEC Values (bins of 1 TECU) acquired using GPS receivers over a period of 12 months (above right) | | | | | | | | | | | | | | | | | | | | | | | | | | |
|---|---|---|---|---|---|---|---|---|---|---|---|---|---|---|---|---|---|---|---|---|---|---|---|---|---|---|
| TEC Value | 1 | 2 | 3 | 4 | 5 | 6 | 7 | 8 | 9 | 10 | 11 | 12 | 13 | 14 | 15 | 16 | 17 | 18 | 19 | 20 | 21 | 22 | 23 | 24 | 25 | 26 | 27 |
| Count | 6 | 11406 | 3255 | 6473 | 10691 | 5283 | 9644 | 4896 | 3622 | 2697 | 3616 | 3384 | 2926 | 2717 | 1272 | 776 | 383 | 193 | 80 | 57 | 49 | 42 | 16 | 5 | 2 | 4 | 2 |
| % Total | 0.0 | 49.8 | 1.8 | 4.8 | 8.1 | 4.7 | 3.3 | 2.8 | 2.2 | 2.1 | 2.1 | 1.9 | 1.4 | 1.2 | 0.7 | 0.4 | 0.2 | 0.1 | 0.0 | 0.0 | 0.0 | 0.0 | 0.0 | 0.0 | 0.0 | 0.0 | 0.0 |

*Table of VTEC counts returned over the 12 month interval above.*

Ionosonde data, provided by the Australian government's Ionospheric Prediction Service (IPS), is employed in partitioning TEC in the ionospheric column, providing after analysis, Chapman profiles for each of the E and F layers in the ionosphere. This, combined with GPS derived absolute TEC values, will provide the basis for an understanding of particular mechanisms responsible at each moment for observed TEC counts. This in turn, will provide the opportunity for a first pass at ionospheric tomography.

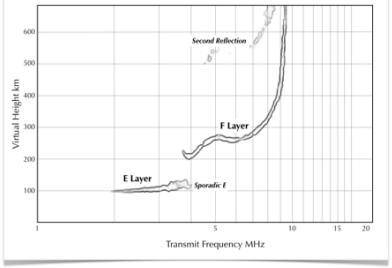


*Cleaned, edge-detected ionogram displaying distinct reflections from the ionosphere E and F layers.*

## Continuing Studies

Due to the nature of satellite orbital mechanics, a region of the ionosphere close to and south of the MRO is not sampled by instrumentation located on the MRO (image below, left). Therefore, it is beneficial to place a receiver well south of the MRO in order to better sample a relevant volume of the ionosphere. Hence, we have concluded the construction trailer mounted of solar power systems that will permit remote operation of GPS systems over long intervals.

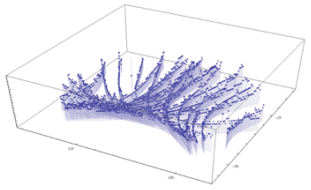

*Satellite tracks over the MRO (lat/long), which is at the centre of this image, for a period of one day.*

*One of three solar power units that will support remote, readily re-deployable GPS operations.*

## Conclusions

A rigorous approach to study of the ionosphere over the Murchison Radio Observatory through the deployment of conventional instrumentation employing GPS systems and as yet unconventional instrumentation, the MWA telescope and an equally rigorous approach to accurate instrumental bias estimations has provided an excellent opportunity for improving our knowledge of the systematics of the ionosphere over southern hemisphere, continental mid-latitudes. Should the fullest capabilities of each of the aforementioned instrumental approaches be realised, unprecedented fine-scale knowledge of the ionosphere will be enhanced.

## References

Rawer K., *Wave Propagation in the Ionosphere*, 1993, Kluwer Academic Publishers, P.O. Box 17, 3300 AA Dordrecht, The Netherlands.

Mitchell D. A., Greenhill L. J., Wayth R. B., Sault R. J., Lonsdale C. J., Cappallo R. J., Morales M. F., Ord S. M., 2008, *Real-Time Calibration of the Murchison Widefield Array*, arXiv:0807.1912v2

Coster A., Erickson P., Herne D., Oberoi D., Salah J., 2008, *The Murchison Widefield Array (MWA): A New Ionospheric Sensor*, IES 2008.

Kennewell J., Caruana J., Terkildsen M., Wu J., Wilkinson P., Cole D., Mitchel K., To V., 2005, *The Australian Ionosphere*, report prepared for CSIRO by IPS Radio and Space Services.

Carrano C. S., Anghel A., Quinn R. A., Groves K. M., 2009, *Kalman filter estimation of plasmaspheric total electron content using GPS*, Radio Sci., 44, RS0A10, doi:10.1029/2008RS004070.

Williams J., Coster A., Herne D., Erickson P., Weatherwax A., Oberoi D., Groves K., Carrano C., (2010), *GPS Receiver Bias Temperature Dependence and its Implications for the Murchison Widefield Array (MWA)*. CEDAR, June 2010. Poster Session.

*Figure 8.4: Poster - Characterisation of the Ionosphere over Murchison Radio Observatory, AGU Fall Meeting, San Francisco, December 2011.*

# IONOSPHERIC VARIABILITY OVER THE MURCHISON RADIO OBSERVATORY

David Herne[1,4], John Kennewell[1], Mervyn Lynch[1], Anthea Coster[2], Charles Carrano[3], Keith Groves[3].

[1] Curtin Institute for Radio Astronomy, International Centre for Radio Astronomy Research, [2] MIT Haystack Observatory, [3] Boston College,
[4] To whom correspondence should be addressed. david.herne@icrar.org

MWA Project Meeting, November 28 - December 01 2012 Geraldton, Western Australia

## Introduction

The Murchison Radio Observatory (MRO), home to radio astronomy in Australia, is located in mid-latitude Western Australia. Projects currently under development at the MRO include a low-frequency instrument, the Murchison Widefield Array (MWA). The MWA is an aperture synthesis, imaging array operating over the frequency range 80 to 300 MHz. Signals in this range are subject to distortions caused by the ionosphere. The effects of scintillation and Faraday rotation degrade image quality. Historical measurements and models have long shown that the mid-latitude ionosphere has very low scintillation activity. TEC measurements we have made of the ionosphere over the MRO using high-precision, dual-frequency, GPS systems support this belief. Data captured during a period of low solar activity and a period of high solar activity are reported and discussed. We review plans to extend this work with the implementation of mobile solar-powered instrumentation that has permitted deployment of an additional GPS configuration that is collecting TEC data and will continue to do so during the forthcoming period of expected higher solar activity.

## Equipment and Deployment

High fidelity, dual-frequency GPS systems running under the control of a purpose written application, SCINDA (Charles Carrano author) provide ionospheric absolute total electron content (aTEC) and scintillation index (S4) values computed on the fly. These systems, which correct for slant angle and the contribution of the plasmasphere to aTEC, together with potential sources of error such as satellite and receiver biasses, are deployed strategically in respect of the Murchison Widefield Array (MWA) project. Systems are currently deployed on Boolardy Station at the boundary of the Murchison Radio Observatory (MRO) and on the Australian Space Academy (ASA) site at Meckering, east of Perth and due south of the MRO. Under previous deployments, 3 systems were operated on or near the MRO, as shown in Figure 2.0. While providing finely resolved, separate data transects, Figure 2.1, none of these systems interrogated the ionosphere very far south of the MRO, Figure 3.0. Under current deployment, single GPS systems at Boolardy and at the ASA provide readings over the MRO but also well south, a distance of 540 km as shown in Figure 3.1. Readings over the MRO benefit further by the formation of separate, distinct transects produced over the observatory site from the southern deployment on the ASA, effectively increasing the density of measurements.

*Figure 1.0: - Horizon Power sponsored solar power trailer powering GPS system on the ASA, Meckering WA*

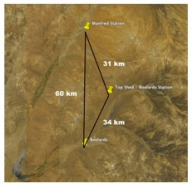


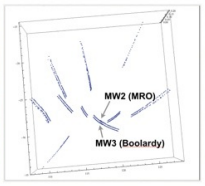


*Figure 2.0/2.1: - Three GPS systems on and near the MRO and the proximity of satellite transects for two of these systems. The transects in the second figure are separated by 34 km.*

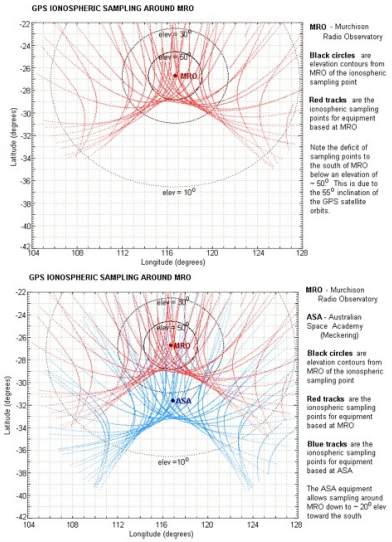


*Figure 3.0/3.1: - During the period of low solar activity, circa 2008, all GPS systems were deployed on or near the MRO. Currently, a single unit is deployed near the MRO and another on the ASA, Meckering, 540 km to the south*

## Data

Absolute TEC and scintillation values have been computed from captured data over extended periods under conditions of low solar activity and increasing-to-high solar activity. GPS systems are susceptible to errors caused by such effects as multi-path signal reception. As the GPS satellite repeats a particular ground track every day but at a precession rate of 4 minutes due to the satellite's sidereal day orbit, interferences manifest along a slanted path in plots such as the waterfall plots shown here that exhibit a 4 minute slope, seen quite clearly in Figures 4.0 - 4.4. This phenomenon aids in the interpretation of data.

All computed data products, including slant TEC, ionosphere penetration latitude and longitude, satellite elevation and azimuth, uncertainties and date/time stamps are archived and available for interrogation. These systems are capable of pushing data over the Internet and is being considered.

## Conclusions

•Over extended periods of time, during periods of both low and high solar activity, the scintillation index (S4) of the ionosphere over the MRO has remained very low, with readings dominated by low-level, interference generated noise.

•Absolute TEC readings have increased during daylight hours in the interval spanning a period of low solar activity to the present period of increasing-to-high solar activity.

## Solar Minimum Ionosphere

Figure 4.0 below displays absolute TEC values over the MRO for a 12 month period during an interval of **low solar activity**, circa 2008. Figure 4.1, bottom, displays corresponding scintillation, S4 values. Features observed in this data are discussed in the previous section.

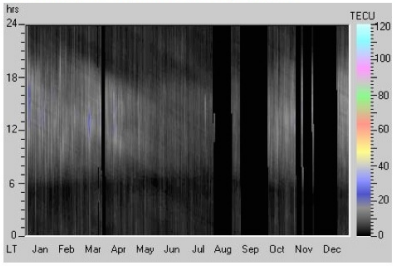


*Figure 4.0/4.1: - Absolute TEC and scintillation readings during a period of low solar activity, circa 2008.*

•Dual frequency GPS observations permit the production of statistically well sampled absolute TEC and S4 databases throughout the solar cycle.

• These databases provide information on ionospheric activity including, for example, transient ionospheric events [eg Travelling Ionospheric Disturbances (TIDS); ionospheric scintillation,..].

•The statistical information in a TEC database provides is an important tool for planning the viability / suitability of future radio observing experiments at that site.

•TEC information permits the researcher to use data quality filters on their research datasets to reject experimental data acquired during periods of high ionospheric activity.

## MWA Support

Current and future activities will provide ionospheric support for radio astronomy through:

- **climatology**, which will support project planning.
- an **archival database**, which will provide values of aTEC and S4, will provide quicklook graphs and detailed time-series data, will help in assessing data quality and will aid data reduction and analysis.
- will provide **dedicated support** for specific projects, LUNASAKA and high accuracy VLBI.

## Solar Maximum Ionosphere

Figure 4.2 below displays absolute TEC values over the MRO for a 12 month period during an interval of **increasing-to-high solar activity** during 2012. Figure 4.3, bottom, displays corresponding scintillation, S4 values. Features observed in this data are discussed in the previous section.

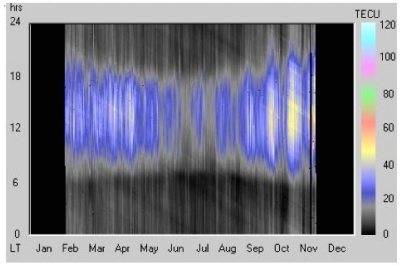


*Figure 4.2/4.3: - Absolute TEC and scintillation readings during a period of high solar activity during 2012.*

## References

Rawer K., *Wave Propagation in the Ionosphere*, 1993, Kluwer Academic Publishers, P.O. Box 17, 3300 AA Dordrecht, The Netherlands.

Mitchell D. A., Greenhill L. J., Wayth R. B., Sault R. J., Lonsdale C. J., Cappallo R. J., Morales M. F., Ord S. M., 2008, *Real-Time Calibration of the Murchison Widefield Array*, arXiv:0807.1912v2

Coster A., Erickson P., Herne D., Oberoi D., Salah J., 2008, *The Murchison Widefield Array (MWA): A New Ionospheric Sensor*, IES 2008.

Kennewell J., Caruana J., Terkildsen M., Wu J., Wilkinson P., Cole D., Mitchel K., To V., 2005, *The Australian Ionosphere*, report prepared for CSIRO by IPS Radio and Space Services.

Carrano C. S., Anghel A., Quinn R. A., Groves K. M., 2009, *Kalman filter estimation of plasmaspheric total electron content using GPS*, Radio Sci., 44, RS0A10, doi:10.1029/2008RS004070.

## Acknowledgements

This project is very, very grateful to **Mark Winstanley** for leading the construction of the solar power trailers and to **David Emrich** for GPS support in the field. Without the support of these gentlemen, the project in this form would not have been viable. The project acknowledges and thanks **Horizon Power** for supply of solar hardware and associated electronics and to the US Air Force Research Laboratories for supply of the specialised GPS receivers.

*Figure 8.5: Poster - Ionospheric Variability over Murchison Radio Observatory, MWA Project Meeting, Geraldton, November 2012.*

# Ionospheric Phenomena and Low-frequency Radio Astronomy.

David Herne[1], John Kennewell[1], Mervyn Lynch[1], Charles Carrano[2].

[1]Curtin Institute for Radio Astronomy (CIRA), International Centre for Radio Astronomy Research (ICRAR), [2]Boston College david.herne@icrar.org

13th Australian Space Science Conference September 30 - October 2, 2013, University of New South Wales.

## Abstract

The Murchison Widefield Array radio telescope (MWA), situated on the Murchison Radio Observatory (MRO) in Western Australia, has recently commenced operations. This instrument, which operates over the frequency range 80-300 MHz, is susceptible to scintillation caused by rapid, small-scale fluctuations in ionospheric plasma density and Faraday rotation of incoming signals caused by the interaction of low-frequency radio waves with dissociated electrons in the ionosphere. Observations of these parameters over several years, across periods of both subdued and elevated solar activity, have demonstrated markedly differing regimes. High-precision GPS systems, combined with purpose-written data acquisition software (SCINDA), has allowed investigation of various phenomena including the effect of solar storms on the ionosphere at highly resolved time-scales. We report on aspects of phenomena observed and their significance to low-frequency radio astronomy.

## The Murchison Widefield Array (MWA)

The Murchison Widefield Array radio telescope (MWA), is located on the Murchison Radio Observatory (MRO) in the shire of Murchison, Western Australia. The MWA is a low-frequency, aperture-synthesis, tile-based array that comprises 2,048 crossed-dipole antennas mounted on 128 tiles (Fig. 1) arrayed in a dithered Reuleaux formation, (Tingay, Goeke et al. 2012). The MWA achieved first light with an array of three tiles located on Mileura Station in March 2005 (Bowman, Barnes et al. 2007), (Bhat, Wayth et al. 2007).

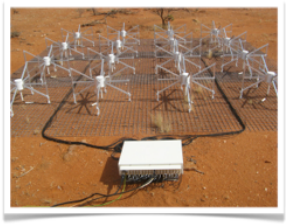

*Figure 1: A single tile of the 128 tile, Murchison Widefield Array radio telescope (MWA). Each tile hosts 16 dipole antennas capable of full Stokes imaging.*

Design parameters and performance measures for the MWA are given in Table 1 below.

| Parameter | Value |
|---|---|
| Frequency range (MHz) | 80 - 300 |
| Number of tiles (N) | 128 |
| Number of antennas | 2048 dual polarisation |
| Total collecting area (m²) | 2752 @ 150 MHz / 2534 @ 200 MHz |
| Field of view (deg²) | 610 @ 150 MHz / 375 @ 200 MHz |
| Receiver Temperature (K) | 50 @ 150 MHz / 25 @ 200 MHz |
| Instantaneous Bandwidth (MHz) | 30.72 MHz |
| Spectral channels | 1024 (30 kHz spectral resolution) |
| Temporal resolution (cadence) | 0.5 s uncalibrated / 8.0 s calibrated |
| Polarisation | Full Stokes |
| Array voltage beams | 32 |
| Angular resolution 1.5 km array | 3' @ 150 MHz / 2' @ 200 MHz |
| Angular resolution 3 km array | 2' @ 150 MHz / 1' @ 200 MHz |
| Broadband survey speed | 1.5 x 10⁵ deg²/hr (31 MHz, 10 mJy) |
| Narrowband survey speed | 190 deg²/hr (0.04 MHz, 10 mJy) |

*Table 1: Operational parameters of the MWA.*

## Radio Telescope Ionospheric Calibration

The MWA requires the ionospheric contribution to image degradation be mitigated through accurate calibration. Self-calibration is sufficient for certain classes of observation, (Mitchell, Greenhill et al. 2008). Absolute calibration, which requires an accurate knowledge of the ionospheric, absolute TEC (aTEC) content, is required for other important classes of observation, in particular those involving measures of Faraday rotation such as galactic magnetic field studies (Bowman, Cairns et al. 2013). The polarization angle of incoming radio signals is rotated in transiting the ionosphere, proportional to frequency of the signal and ionospheric aTEC.

$$\delta\phi \propto f^{-1}(TEC) \qquad (1)$$

where $\delta\phi$ is the incoming radio signal phase rotation (Faraday rotation) by free electrons along the line of sight, $f^{-1}$ is the observation frequency and *TEC* is the absolute total electron content in units of $10^{16}$ m$^{-2}$. Therefore, knowledge of the free electron content of the ionosphere is required in order to determine the ionosphere's contribution to measure signal Faraday rotation. Absolute TEC measured by us over several years is shown in Figures 3(a) and 3(c). However, the sky visible to the MWA exhibits varying qualities across a large field of view (610 deg² @ 150 MHz). Rapid, small-scale (sub-metre) fluctuations in electron density over short time intervals (seconds) induce amplitude and phase variations in signals received at the observatory (Kung Chie and Chao-Han 1982). Scintillation measured by dual-frequency GPS systems over the same interval as above, are shown in Figures 3(b) and 3(d). These are calculated as the normalised variance of the intensity signal received:

$$S_4 = \sqrt{\frac{\langle I^2\rangle - \langle I\rangle^2}{\langle I\rangle^2}} \qquad (2)$$

and known as the $S_4$ index. The levels detected by our GPS systems were persistently negligible in the context of low-frequency radio astronomy.

Irregularities in the ionosphere conspire to cause position errors in observed phenomena, such as shown in Figure 2 for an actual observation conducted with the MWA precursor instrument, the MWA 32 Tile Array (32T). Vectors effectively display the magnitude of the positional offset of observed sources when compared to a known catalogue, the Molonglo Reference Catalogue.

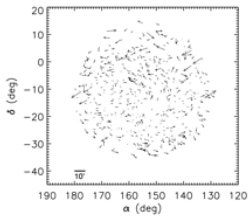


*Figure 2: Spatial offsets between the position of sources imaged by the MWA (32T) and sources for which matches were found in the Molonglo Reference Catalogue (MRC). These vectors effectively demonstrate the variability in the scene attributable substantially to the effect of the ionosphere on incoming radio signals (Williams, Hewitt et al. 2012).*

## The Southern, Mid-latitude Ionosphere

The southern, mid-latitude ionosphere has been studied over an extensive period, (Bowman 1981), (Hajkowicz 1994). When therefore, recommendations were sought regarding suitable locations in Australia for siting of the Square Kilometre Array (SKA) radio telescope, the region in the mid-west of Western Australia that was eventually chosen was expected to exhibit very low levels of scintillation (Kennewell, Caruana et al. 2005) and such is our experience. However, the total electron content of the ionosphere varies markedly not only over the course of a day but annually and over a solar (activity) cycle, as displayed below (Fig 3).

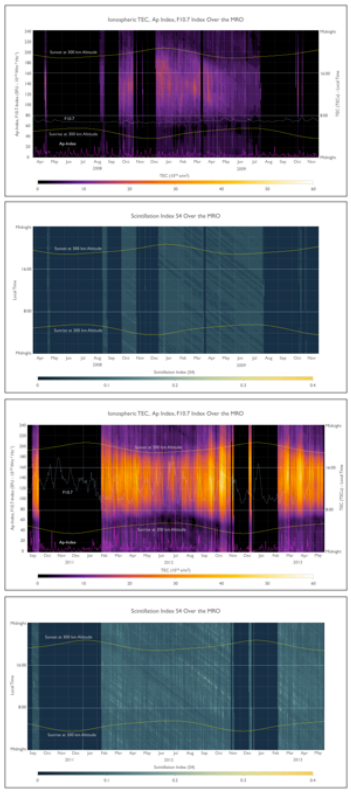

*Figures 3(a), (b), (c), (d): Absolute total electron content (aTEC) and scintillation indices ($S_4$) of the ionosphere above the Murchison Radio Observatory (MRO) for two epochs, (3a, 3b) during a period of low solar activity over the period 2008-2009 and (3c, 3d) high solar activity over the period 2012-2013 (continuing into the present). The index F10.7 is a measure of the sun's electromagnetic activity at wavelengths that produce photoionisation of the ionosphere, the index Ap is the daily equivalent of the index Kp, which is a three-hourly measure of geomagnetic activity.*

Whereas a great deal of fine structure is observed in the plots in Figure 3, variation in parameters over much smaller scales than those discernible here occur from moment to moment over the course of a single day or a few days (Fig. 4).

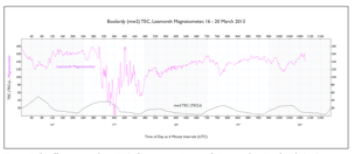

*Figure 4: The effect on ionospheric TEC of a geomagnetic storm that occurred on March 17th, 2013. Geomagnetic activity was responsible for depletion of the ionospheric plasma on March 18th.*

Through the use of distributed, high-fidelity GPS systems, the propagation of ionospheric disturbances are detectable. Two dual-frequency systems running special software (SCINDA), (Carrano, Anghel et al. 2009), situated approximately 400 km apart on a north-south transect, recorded the effect on ionospheric TEC of the March 17th event (Fig. 5).

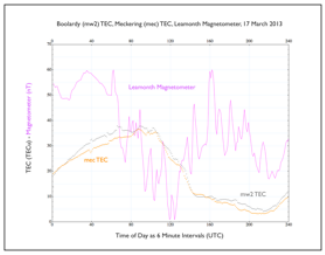


*Figure 5: Absolute TEC values recorded at two widely separated locations (about 400 km apart) using high-fidelity GPS systems employing purpose written software (SCINDA) superimposed with magnetometer readings captured at the Learmonth Solar Observatory, Learmonth, Western Australia, indicating a significant geomagnetic storm event.*

## Discussion

The MWA is a low-frequency radio array that boasts a wide field of view, high spatial and temporal resolution and simultaneous imaging capabilities, allowing high time-resolution imaging of transient events, daily observations of the sun with unprecedented capability (Oberoi, Matthews et al. 2011) and long integration time science, as required by epoch of re-ionisation (EOR) studies. In order however, to fully achieve the observatory's potential, careful attention must be paid to the behaviour of the local ionosphere over both short (seconds) and long (days) intervals and be equipped to remove the degrading effects of the ionosphere's free electrons.

To this end, measurements of ionospheric electron content (aTEC) and behaviour and scintillation are continuing and will in all likelihood be expanded.

## References

Bhat, N. D. R., R. B. Wayth, et al. (2007). "Detection of Crab Giant Pulses Using the Mileura Widefield Array Low Frequency Demonstrator Field Prototype System." The Astrophysical Journal 665: 618-627.

Bowman, G. G. (1981). "The nature of ionospheric spread-F irregularities in mid-latitude regions." Journal of Atmospheric and Terrestrial Physics 43(1): 65-79.

Bowman, J. D., D. G. Barnes, et al. (2007). "Field Deployment of Prototype Antenna Tiles for the Mileura Widefield Array Low Frequency Demonstrator." The Astronomical Journal 133: 1505-1518.

Bowman, J. D., I. Cairns, et al. (2013). "Science with the Murchison Widefield Array." PASA - Publications of the Astronomical Society of Australia 30.

Carrano, C. S., A. Anghel, et al. (2009). "Kalman filter estimation of plasmaspheric total electron content using GPS." Radio Sci. 44: RS0A10.

Hajkowicz, L. A. (1994). "Types of ionospheric scintillations in southern mid-latitudes during the last sunspot maximum." Journal of Atmospheric and Terrestrial Physics 56(3): 391-399.

Kennewell, J., J. Caruana, et al. (2005). The Australian Ionosphere - Report to CSIRO by IPS Radio and Space Services.

Kung Chie, Y. and L. Chao-Han (1982). "Radio wave scintillations in the ionosphere." Proceedings of the IEEE 70(4): 324-360.

Mitchell, D. A., L. J. Greenhill, et al. (2008). "Real-Time Calibration of the Murchison Widefield Array." Selected Topics in Signal Processing, IEEE Journal of 2(5): 707-717.

Oberoi, D., L. D. Matthews, et al. (2011). "First Spectroscopic Imaging Observations of the Sun at Low Radio Frequencies with the Murchison Widefield Array Prototype." The Astrophysical Journal Letters 728: L27.

Tingay, S. J., R. Goeke, et al. (2012) "The Murchison Widefield Array: the Square Kilometre Array Precursor at low radio frequencies." ArXiv e-prints 1206, 6945.

Williams, C. L., J. N. Hewitt, et al. (2012) "Low Frequency Imaging of Fields at High Galactic Latitude with the Murchison Widefield Array 32-Element Prototype." ArXiv e-prints 1203, 5790.

## Acknowledgements

We acknowledge and thank Dr. Ron Caton and the U.S.A.F. Research Laboratories for provision of the high-fidelity GPS systems employed in the measurement of ionospheric TEC and scintillation.

We take this opportunity to thank engineering staff of ICRAR who have assisted in the deployment and maintenance of a GPS system employed in this study, in particular, Mr. David Emrich, Mr. Brian Crosse and Mr. David Pallot.

We acknowledge the contribution made to this project by **Horizon Power** in provision of electrical components, including solar panels, required for the construction of 3 solar power trailers.

*Figure 18.6: Poster - Ionospheric Phenomena and Low-frequency Radio Astronomy, 13th Australian Space Science Conference, Sydney, October 2013.*

## 8.6. All Publications

(1) **David Herne**, John Kennewell, Mervyn Lynch, Charles Carrano (2013). **Ionospheric Phenomena and Low-Frequency Radio Astronomy**. Proceedings of the Australian Space Science Conference (ASSC), Sydney, Australia, 30th September-2nd October 2013. (Peer reviewed.)

(2) S. J. Tingay, D. L. Kaplan, B. McKinley, F. Briggs, R. B. Wayth, N. Hurley-Walker, J. Kennewell, C. Smith, K. Zhang, W. Arcus, N. D. R. Bhat, D. Emrich, **D. Herne**, N. Kudryavtseva, M. Lynch, S. M. Ord, M. Waterson, D. G. Barnes, M. Bell, B. M. Gaensler, E. Lenc, G. Bernardi, L. J. Greenhill, J. C. Kasper, J. D. Bowman, D. Jacobs, J. D. Bunton, L. deSouza, R. Koenig, J. Pathikulangara, J. Stevens, R. J. Cappallo, B. E. Corey, B. B. Kincaid, E. Kratzenberg, C. J. Lonsdale, S. R. McWhirter, A. E. E. Rogers, J. E. Salah, A. R. Whitney, A. Deshpande, T. Prabu, N. Udaya Shankar, K. S. Srivani, R. Subrahmanyan, A. Ewall-Wice, L. Feng, R. Goeke, E. Morgan, R. A. Remillard, C. L. Williams, B. J. Hazelton, M. F. Morales, M. Johnston-Hollitt, D. A. Mitchell, P. Procopio, J. Riding, R. L. Webster, J. S. B. Wyithe, D. Oberoi, A. Roshi, R. J. Sault, and A. William **On The Detection and tracking of Space Debris using the Murchison Widefield Array, I. Simulations and Test Observations Demonstrate Feasibility**. The Astronomical Journal, 146:103 (9pp), October 2013.

(3) **David Herne**, Mervyn Lynch, John Kennewell, Charles Carrano, Keith Groves, Anthea Coster, Divya Oberoi (2011). **Characterisation of the ionosphere over the Murchison Radio Astronomy Observatory**. AGU Fall Meeting, December 5-9 2011, San Francisco; Session SA07.

(4) **David Herne**, Mervyn Lynch, Anthea Coster, Charles Carrano, Keith Groves, John Kennewell, Jennifer Williams, Divya Oberoi (2011), **Characterisation of the ionosphere over the Murchison Radio**

**Astronomy Observatory**. Path to SKA-low Workshop - Perth, Western Australia, 6th-9th September 2011.

(5) Divya Oberoi, Lynn D. Matthews, Iver H. Cairns, David Emrich, Vasili Lobzin, Colin J. Lonsdale, Edward H. Morgan, T. Prabu, Harish Ved, Randall B. Wayth, Andrew Williams, Christopher Williams, Wayne Arcus, Leonid Benkevitch, Judd D. Bowman, Frank H. Briggs, John D. Bunton, Steve Burns, Roger C. Cappallo, Brian E. Corey, Ludi deSouza, Mark Derome, Avinash Deshpande, Sheperd S. Doeleman, Robert Goeke, M. R. Gopalakrishna, Lincoln J. Greenhill, **David Herne**, Jacqueline N. Hewitt, P. A. Kamini, Justin C. Kasper, Barton B. Kincaid, Jonathan Kocz, Errol Kowald, Eric Kratzenberg, Deepak Kumar, Mervyn J. Lynch, S. Madhavi, Michael Matejek, Daniel Mitchell. Miguel M. Morales, Steven Ord, Joseph Pathikulangara, Alan E.E. Rogers, Anish Roshi, Robert J. Sault, Joseph E. Salah, N. Udaya Shankar, K. S. Srivani, Jamie Stevens, Steven Tingay, Annino Vaccarella, Mark Waterson, Rachel L. Webster and Alan R. Whitney, (2011), **First Spectroscopic Imaging Observations of the Sun at Low Radio Frequencies with the Murchison Widefield Array Prototype**. ApJ Letters, Vol 728 , No 2, 7 pages, 20 Feb 2011, doi:10.1088/2041-8205/728/2/L27.

(6) M.J. Lynch, **David E. Herne**, (2010), **SKA Pathfinder Experiments at the Western Australia Radio Astronomy Park**. In preparation.

(7) **David E. Herne**, M.J. Lynch, (2010), **Remote sensing of the Ionosphere over the Murchison Radio Observatory, Murchison, Western Australia, Leading to an Understanding of Fine Scale Behaviour**. AGU Fall Meeting, December 13-17 2010, San Francisco; Session SA07. Poster session.

(8) Jennifer Williams, A Coster, **D Herne**, P Erickson, A Weatherwax, D Oberoi, K Groves, C Carrano, (2010), **GPS Receiver Bias Temper-**

**ature Dependence and its Implications for the Murchison Widefield Array (MWA)**. CEDAR, June 2010. Poster Session.

(9) S. M. Ord, D. A. Mitchell, R. B. Wayth, L. J. Greenhill, G. Bernardi, S. Gleadow, R. Edgar, M. A. Clark, G. Allen, W. Arcus, L. Benkevitch, J. D. Bowman, F. H. Briggs, J. D. Bunton, S. Burns, R. J. Cappallo, W. A. Coles, B. E. Corey, L. deSouza, S. S. Doeleman, M. Derome, A. Deshpande, R. Goeke, M. R. Gopalakrishna, D. Emrich, **D. Herne**, J. N. Hewitt, P. A. Kamini, D. L. Kaplan, J. C. Kasper, B. B. Kincaid, J. Kocz, E. Kowald, E. Kratzenberg, D. Kumar, C. J. Lonsdale, M. J. Lynch, S. R. McWhirter, S. Madhavi, M. Matejek, M. F. Morales, E. Morgan, D. Oberoi, J. Pathikulangara, T. Prabu, A. E. E. Rogers, A. Roshi, J. E. Salah, A. Schinkel, N. Udaya Shankar, K. S. Srivani, J. Stevens, S. J. Tingay, A. Vaccarella, M. Waterson, R. L. Webster, A. R. Whitney, A. Williams, C. Williams, (2010). **Interferometric imaging with the 32 element Murchison Wide-field Array**. In preparation.

(10) S. M. Ord[1], D. Mitchell[1], R. B. Wayth[1,9], L. Greenhill[1], G. Bernardi[1], R. Edgar[14], M. A. Clark[1,14], L. Benkevitch[2], J. D. Bowman[3], F. H. Briggs[4], J. D. Bunton[5], S. Burns[6], R. J. Cappallo[2], W. A. Coles[7] , B. E. Corey[2], L. deSouza[5], S. S. Doeleman[2], M. Derome[2], A. Deshpande[8], M. R. Gopalakrishna[8], D. Emrich[9], **D. E. Herne**[9], J. N. Hewitt[10], P. A. Kamini[8], J. C. Kasper[1], B. B. Kincaid[2], J. Kocz[4], E. Kowald[4], E. Kratzenberg[2], D. Kumar[8], C. J. Lonsdale[2], M. J. Lynch[9], S. Madhavi[8], M. Matejek[10], M. F. Morales[11], E. Morgan[10], D. Oberoi[2], J. Pathikulangara[5], T. Prabu[8], A. E. E. Rogers[2], A. Roshi[8], J. E. Salah[2], K. S. Srivani[8], J. Stevens[5], S. Tingay[9], S. N. Udaya[8], A. Vaccarella[4], M. Waterson[4], R. L. Webster[12], A. R. Whitney[2], A. Williams[13], C. Williams[10], (2010) **Wide-field interferometric imaging via the combination of warped snapshots**. In preparation.

(11) Daniel A. Mitchell, Lincoln J. Greenhill, Stephen M. Ord, Gianni Bernardi, Randall B. Wayth, Richard G. Edgar, Michael A. Clark, Kevin Dale, Hanspeter Pfister, Stewart J. Gleadow, W. Arcus, F.H.

Briggs, L. Benkevitch, J.D. Bowman, J.D. Bunton, S. Burns, R.J. Cappallo, B.E. Corey, A. de Oliviera Costa, L. Desouza, S.S. Doeleman, M. Derome, A. Deshpande, D. Emrich, M. Glossop, R. Goeke , M.R. Gopala, B. Hazelton, **D. E. Herne**, J.N. Hewitt, P.A. Kamini, D.L. Kaplan, J.C. Kasper, B.B. Kincaid, J. Kocz, E. Kowald, E. Kratzenberg, D. Kumar, C.J. Lonsdale, M.J. Lynch, S. Madhavi, M. Matejek, M.F. Morales, E. Morgan, D. Oberoi, J. Pathikulangara, T. Prabu, A. Rogers, A. Roshi, J.E. Salah, R.J. Sault, N.U. Shankar, K.S. Srivani, J. Stevens, S. Tingay, A. Vaccarella, M. Waterson, R.L. Webster, A.R. Whitney, A. Williams and C. Williams. **The Murchison Widefield Array**. RFI mitigation workshop 29-31 March 2010 Groningen, the Netherlands.

(12) **David E. Herne**, M.J. Lynch,(2009), **Characterisation of the Ionosphere over the Murchison Radio Observatory, Murchison, Western Australia**. AGU Fall Meeting, December 14-18 2009 San Francisco; Paper Number: SA23A-1460.

(13) Aaron R. Parsons[1,2], Donald C. Backer[1], Richard F. Bradley[3,4,5], James E. Aguirre[6], Erin E. Benoit[5], Chris L. Carilli[7], Griffin S. Foster[1], Nicole E. Gugliucci[3], **David E. Herne[8]**, Daniel C. Jacobs[6], Mervyn J. Lynch[8], Jason R. Manley[9,10], Chaitali R. Parashare[4], Daniel J. Werthimer[9,11], Melvyn C. H. Wright[1], (May 27, 2009) **The Precision Array for Probing the Epoch of Reionization.** arXiv.

(14) Colin J. Lonsdale, Roger J. Cappallo, Miguel F. Morales, Frank H. Briggs, Judd D. Bowman, John D. Bunton, Steven Burns, Brian E. Corey, Ludi deSouza, Sheperd S. Doeleman, Mark Derome, Avinash Deshpande, M. R. Gopalakrishna, Lincoln J. Greenhill, **David E. Herne**, Jacqueline N. Hewitt, P. A. Kamini, Justin C. Kasper, Barton B. Kincaid, Jonathan Kocz, Errol Kowald, Eric Kratzenberg, Deepak Kumar, Mervyn J. Lynch, S. Madhavi, Michael Matejek, Daniel Mitchell, Edward Morgan, Divya Oberoi, Steven Ord, Joseph Pathikulangara, T. Prabu, Alan E.E. Rogers, Anish Roshi, Joseph E.

Salah, Robert J. Sault, N. Udaya Shankar, K. S. Srivani, Jamie Stevens, Steven Tingay, Annino Vaccarella, Mark Waterson, Randall B. Wayth, Rachel L. Webster, Alan R. Whitney, Andrew Williams, Christopher Williams (August 2009) **The Murchison Widefield Array: Design Overview**. Proceedings IEEE, Volume 97, Issue 8.

(15) Anthony J. Smith, **David E. Herne**, Jeffrey V. Turner, (2009), **Wave Effects on Submarine Groundwater Seepage Measurement.** Elsevier Advances in Water Resources.

(16) Anthea Coster, Phil Erickson, **David Herne**, Divya Oberoi, Joseph Salah (August 2008) **The Murchison Widefield Array (MWA): A New Ionospheric Sensor**. URSI, Chicago.

(17) Judd D. Bowman, David G. Barnes, Frank H. Briggs, Brian E. Corey, Merv J. Lynch, N. D. Ramesh Bhat, Roger J. Cappallo, Sheperd S. Doeleman, Brian J. Fanous, **David Herne**, Jacqueline N. Hewitt, Chris Johnston, Justin C. Kasper, Jonathon Kocz, Eric Kratzenberg, Colin J. Lonsdale, Miguel F. Morales, Divya Oberoi, Joseph E. Salah, Bruce Stansby, Jamie Stevens, Glen Torr, Randall Wayth, Rachel L. Webster, J. Stuart B. Wyithe (2007) **Field Deployment Of Prototype Antenna Tiles for the Mileura Widefield Array—Low Frequency Demonstrator.** The Astronomical Journal.

(18) N. D. Ramesh Bhat, Randall B. Wayth, Haydon S. Knight, Judd D. Bowman, Divya Oberoi, David G. Barnes, Frank H. Briggs, Roger J. Cappallo, **David HERNE**, Colin J. Lonsdale, Mervyn J. Lynch, Bruce Stansby, Rachel L. Webster, and J. Stuart B. Wyithe (2006) **Detection of Crab Giant Pulses Using the Mileura Widefield Array Low Frequency Demonstrator Field Prototype System**. The Astrophysical Journal.

(19) Lynch, M. J., HERNE, D. E., Lyons, T, J. (2006). **Review and Implications of Lightning Statistics for the Square Kilometre Array, Australian Candidate Site**. In preparation.

(20) Beresford, R. **HERNE, D. E.** and Chippendale, A. (2006). **Radio Frequency Interference (RFI) Measurement Statistics for Mileura Station: the Australian SKA Candidate Site**. CSIRO ATNF report to the International Committee of the SKA consortium.

(21) Smith, A. J., **HERNE, D. E.,** Turner, J. V., (2006). **Wave Action and Implications for Direct Measurement of Submarine Groundwater Discharge**. Elsevier Science. In review.

# 9. Bibliography

Afraimovich, E. L., E. I. Astafyeva, I. V. Zhivetiev and I. K. Edemsky (2008). "Mapping technique for the USTEC-derived field of velocity of TEC redistribution." International Union of Radio Science: 437.

Alizadeh, M., D. Wijaya, T. Hobiger, R. Weber and H. Schuh (2013). Ionospheric Effects on Microwave Signals. Atmospheric Effects in Space Geodesy. J. Böhm and H. Schuh, Springer Berlin Heidelberg**:** 35-71.

Beardsley, A. P., B. J. Hazelton, M. F. Morales, W. Arcus, D. Barnes, G. Bernardi, J. D. Bowman, F. H. Briggs, J. D. Bunton, R. J. Cappallo, B. E. Corey, A. Deshpande, L. deSouza, D. Emrich, B. M. Gaensler, R. Goeke, L. J. Greenhill, D. Herne, J. N. Hewitt, M. Johnston-Hollitt, D. L. Kaplan, J. C. Kasper, B. B. Kincaid, R. Koenig, E. Kratzenberg, C. J. Lonsdale, M. J. Lynch, S. R. McWhirter, D. A. Mitchell, E. Morgan, D. Oberoi, S. M. Ord, J. Pathikulangara, T. Prabu, R. A. Remillard, A. E. E. Rogers, A. Roshi, J. E. Salah, R. J. Sault, N. Udaya Shankar, K. S. Srivani, J. Stevens, R. Subrahmanyan, S. J. Tingay, R. B. Wayth, M. Waterson, R. L. Webster, A. R. Whitney, A. Williams, C. L. Williams and J. S. B. Wyithe (2012) "The EoR Sensitivity of the 128 Antenna Murchison Widefield Array." ArXiv e-prints **1204**, 3111.

Beardsley, A. P., B. J. Hazelton, M. F. Morales, R. C. Cappallo, R. Goeke, D. Emrich, C. J. Lonsdale, W. Arcus, D. Barnes, G. Bernardi, J. D. Bowman, J. D. Bunton, B. E. Corey, A. Deshpande, L. deSouza, B. M. Gaensler, L. J. Greenhill, D. Herne, J. N. Hewitt, D. L. Kaplan, J. C. Kasper, B. B. Kincaid, R. Koeing, E. Kratzenberg, M. J. Lynch, S. R. McWhirter, D. A. Mitchell, E. Morgan, D. Oberoi, S. M. Ord, J. Pathikulangara, T. Prabu, R. A. Remillard, A. E. E. Rogers, A. Roshi, J. E. Salah, R. J. Sault, N. Uday Shankar, K. S. Srivani, J. Stevens, R.

Subrahmanyan, S. J. Tingay, R. B. Wayth, M. Waterson, R. L. Webster, A. R. Whitney, A. Williams, C. L. Williams and J. S. B. Wyithe (2012) "A new layout optimization technique for interferometric arrays, applied to the MWA." ArXiv e-prints **1203**, 1293.

Bell, M. E., T. Murphy, D. L. Kaplan, P. Hancock, B. M. Gaensler, J. Banyer, K. Bannister, C. Trott, N. Hurley-Walker, R. B. Wayth, J.-P. Macquart, W. Arcus, D. Barnes, G. Bernardi, J. D. Bowman, F. Briggs, J. D. Bunton, R. J. Cappallo, B. E. Corey, A. Deshpande, L. deSouza, D. Emrich, R. Goeke, L. J. Greenhill, B. J. Hazelton, D. Herne, J. N. Hewitt, M. Johnston-Hollitt, J. C. Kasper, B. B. Kincaid, R. Koenig, E. Kratzenberg, C. J. Lonsdale, M. J. Lynch, S. R. McWhirter, D. A. Mitchell, M. F. Morales, E. Morgan, D. Oberoi, S. M. Ord, J. Pathikulangara, T. Prabu, R. A. Remillard, A. E. E. Rogers, A. Roshi, J. E. Salah, R. J. Sault, N. Udaya Shankar, K. S. Srivani, J. Stevens, R. Subrahmanyan, S. J. Tingay, M. Waterson, R. L. Webster, A. R. Whitney, A. Williams, C. L. Williams and J. S. B. Wyithe (2014). "A survey for transients and variables with the Murchison Widefield Array 32-tile prototype at 154 MHz." Monthly Notices of the Royal Astronomical Society **438**: 352-367.

Bernardi, G., L. J. Greenhill, D. A. Mitchell, S. M. Ord, B. J. Hazelton, B. M. Gaensler, A. de Oliveira-Costa, M. F. Morales, N. Udaya Shankar, R. Subrahmanyan, R. B. Wayth, E. Lenc, C. L. Williams, W. Arcus, B. S. Arora, D. G. Barnes, J. D. Bowman, F. H. Briggs, J. D. Bunton, R. J. Cappallo, B. E. Corey, A. Deshpande, L. deSouza, D. Emrich, R. Goeke, D. Herne, J. N. Hewitt, M. Johnston-Hollitt, D. Kaplan, J. C. Kasper, B. B. Kincaid, R. Koenig, E. Kratzenberg, C. J. Lonsdale, M. J. Lynch, S. R. McWhirter, E. Morgan, D. Oberoi, J. Pathikulangara, T. Prabu, R. A. Remillard, A. E. E. Rogers, A. Roshi, J. E. Salah, R. J. Sault, K. S. Srivani, J. Stevens, S. J. Tingay, M. Waterson, R. L. Webster, A. R. Whitney, A. Williams and J. S. B. Wyithe (2013). "A 189 MHz, 2400

deg2 Polarization Survey with the Murchison Widefield Array 32-element Prototype." The Astrophysical Journal **771**: 105.

Bhat, N. D. R., R. B. Wayth, H. S. Knight, J. D. Bowman, D. Oberoi, D. G. Barnes, F. H. Briggs, R. J. Cappallo, D. Herne, J. Kocz, C. J. Lonsdale, M. J. Lynch, B. Stansby, J. Stevens, G. Torr, R. L. Webster and J. S. B. Wyithe (2007). "Detection of Crab Giant Pulses Using the Mileura Widefield Array Low Frequency Demonstrator Field Prototype System." The Astrophysical Journal **665**: 618-627.

Bhuyan, K. and P. K. Bhuyan (2007). "International Reference Ionosphere as a potential regularization profile for computerized ionospheric tomography." Advances in Space Research **39**(5): 851-858.

Bilitza, D., D. Altadill, Y. Zhang, C. Mertens, V. Truhlik, P. Richards, L.-A. McKinnell and B. Reinisch (2014). "The International Reference Ionosphere 2012 – a model of international collaboration☆." J. Space Weather Space Clim. **4**: A07.

Booker, H. G. (1979). "The role of acoustic gravity waves in the generation of spread-F and ionospheric scintillation." Journal of Atmospheric and Terrestrial Physics **41**(5): 501-515.

Borries, C., N. Jakowski and V. Wilken (2009). "Storm induced large scale TIDs observed in GPS derived TEC." Ann. Geophys. **27**(4): 1605-1612.

Bowman, G. G. (1981). "The nature of ionospheric spread-F irregularities in mid-latitude regions." Journal of Atmospheric and Terrestrial Physics **43**(1): 65-79.

Bowman, J. D., D. G. Barnes, F. H. Briggs, B. E. Corey, M. J. Lynch, N. D. R. Bhat, R. J. Cappallo, S. S. Doeleman, B. J. Fanous, D. Herne, J. N. Hewitt, C. Johnston, J. C. Kasper, J. Kocz, E. Kratzenberg, C. J. Lonsdale, M. F. Morales, D. Oberoi, J. E. Salah, B. Stansby, J. Stevens,

G. Torr, R. Wayth, R. L. Webster and J. S. B. Wyithe (2007). "Field Deployment of Prototype Antenna Tiles for the Mileura Widefield Array Low Frequency Demonstrator." The Astronomical Journal **133**: 1505-1518.

Bowman, J. D., I. Cairns, D. L. Kaplan, T. Murphy, D. Oberoi, L. Staveley-Smith, W. Arcus, D. G. Barnes, G. Bernardi, F. H. Briggs, S. Brown, J. D. Bunton, A. J. Burgasser, R. J. Cappallo, S. Chatterjee, B. E. Corey, A. Coster, A. Deshpande, L. deSouza, D. Emrich, P. Erickson, R. F. Goeke, B. M. Gaensler, L. J. Greenhill, L. Harvey-Smith, B. J. Hazelton, D. Herne, J. N. Hewitt, M. Johnston-Hollitt, J. C. Kasper, B. B. Kincaid, R. Koenig, E. Kratzenberg, C. J. Lonsdale, M. J. Lynch, L. D. Matthews, S. R. McWhirter, D. A. Mitchell, M. F. Morales, E. H. Morgan, S. M. Ord, J. Pathikulangara, T. Prabu, R. A. Remillard, T. Robishaw, A. E. E. Rogers, A. A. Roshi, J. E. Salah, R. J. Sault, N. U. Shankar, K. S. Srivani, J. B. Stevens, R. Subrahmanyan, S. J. Tingay, R. B. Wayth, M. Waterson, R. L. Webster, A. R. Whitney, A. J. Williams, C. L. Williams and J. S. B. Wyithe (2013). "Science with the Murchison Widefield Array." PASA - Publications of the Astronomical Society of Australia **30**.

Bowman, J. D. and A. E. E. Rogers (2010). "A lower limit of Delta z>0.06 for the duration of the reionization epoch." Nature **468**(7325): 796-798.

Budden, K. G. (1985). The Propagation of Radio Waves: The Theory of Radio Waves of Low Power in the Ionosphere and Magnetosphere. Cambridge, United Kingdom, Cambridge University Press.

Carrano, C. S., A. Anghel, R. A. Quinn and K. M. Groves (2009). "Kalman filter estimation of plasmaspheric total electron content using GPS." Radio Sci. **44**: RS0A10.

Cervera, M. A. and T. J. Harris (2014). "Modeling ionospheric disturbance features in quasi-vertically incident ionograms using 3-D magnetoionic

ray tracing and atmospheric gravity waves." Journal of Geophysical Research: Space Physics **119**(1): 431-440.

Chen, W.-S., C.-C. Lee, F.-D. Chu and S.-Y. Su (2011). "Spread F, GPS phase fluctuations, and medium-scale traveling ionospheric disturbances over Wuhan during solar maximum." Journal of Atmospheric and Solar-Terrestrial Physics **73**(4): 528-533.

Cornely, P.-R. (2013). Receiver Biases in Global Positioning Satellite Ranging.

Coster, A., D. Herne, P. Erickson and D. Oberoi (2012). "Using the Murchison Widefield Array to observe midlatitude space weather." Radio Science **47**(6): n/a-n/a.

Coster, A. J. (2007). Mitigation of Ionospheric Propagation Errors with GPS. Radar Conference, 2007 IEEE.

Croft, S., G. C. Bower, R. Ackermann, S. Atkinson, D. Backer, P. Backus, W. C. Barott, A. Bauermeister, L. Blitz, D. Bock, T. Bradford, C. Cheng, C. Cork, M. Davis, D. DeBoer, M. Dexter, J. Dreher, G. Engargiola, E. Fields, M. Fleming, J. R. Forster, C. Gutierrez-Kraybill, G. Harp, T. Helfer, C. Hull, J. Jordan, S. Jorgensen, G. Keating, T. Kilsdonk, C. Law, J. van Leeuwen, J. Lugten, D. MacMahon, P. McMahon, O. Milgrome, T. Pierson, K. Randall, J. Ross, S. Shostak, A. Siemion, K. Smolek, J. Tarter, D. Thornton, L. Urry, A. Vitouchkine, N. Wadefalk, J. Welch, D. Werthimer, D. Whysong, P. K. G. Williams and M. Wright (2010). "The Allen Telescope Array Twenty-centimeter Survey---A 690 deg2, 12 Epoch Radio Data Set. I. Catalog and Long-duration Transient Statistics." The Astrophysical Journal **719**: 45-58.

Daniell, R. E., C. S. Carrano, G. M. G. Fishman and N. A. Bonito (2007). A Computer Code for Calculating Tropospheric and Ionospheric Refraction Effects on Radar Systems. Radar Conference, 2007 IEEE.

Danilov, A. D. (2013). "Ionospheric F-region response to geomagnetic disturbances." Advances in Space Research **52**(3): 343-366.

Darrouzet, F. and J. De Keyser (2013). "The dynamics of the plasmasphere: Recent results." Journal of Atmospheric and Solar-Terrestrial Physics **99**(0): 53-60.

Davies, K. (1965). Ionospheric Radio Propagation. Washington D. C., United States Department of Commerce.

Davies, K. (1990). Ionospheric Radio Propagation. Washington D. C., United States Department of Commerce.

E. L. Afraimovich, S. V. Voyeikov, I. K. Edemskiy and Y. V. Yasyukevich (2009). Ionosphere Wave Packets Excited by the Solar Terminator: AGW or MHD Origin? Progress In Electromagnetics Research, Moscow, Russia, The Electromagnetics Academy.

Egeland, A. (1996). Ionosphere. Encyclopedia of Applied Physics. T. G. L., Wiley**:** 23.

Egeland, A. (1996). The Ionosphere. Encyclopedia of Applied Physics. T. G. L., Wiley**:** 23.

England, S. L., T. J. Immel, J. D. Huba, M. E. Hagan, A. Maute and R. DeMajistre (2010). "Modeling of multiple effects of atmospheric tides on the ionosphere: An examination of possible coupling mechanisms responsible for the longitudinal structure of the equatorial ionosphere." J. Geophys. Res. **115**(A5): A05308.

Feltens, J. (2001). CHAPMAN PROFILE APPROACH FOR

3-D GLOBAL TEC REPRESENTATION. E. I. D. GmbH. ESA, European Space Operations Centre,

Robert-Bosch-Str. 5, D-64293 Darmstadt, Germany, ESA.

Gaensler, B. M., T. L. Landecker, A. R. Taylor and P. Collaboration (2010). Survey Science with ASKAP: Polarization Sky Survey of the Universe's Magnetism (POSSUM). Bulletin of the American Astronomical Society. **215:** 515.

George, W. K. (2009). "Lectures in Turbulence for the 21st Century." Chalmers University of Technology.

Hajkowicz, L. A. (1994). "Types of ionospheric scintillations in southern mid-latitudes during the last sunspot maximum." Journal of Atmospheric and Terrestrial Physics **56**(3): 391-399.

Haldoupis, C., C. Meek, N. Christakis, D. Pancheva and A. Bourdillon (2006). "Ionogram height–time–intensity observations of descending sporadic E layers at mid-latitude." Journal of Atmospheric and Solar-Terrestrial Physics **68**(3–5): 539-557.

Harris, T. J., M. A. Cervera and D. H. Meehan (2012). "SpICE: A program to study small-scale disturbances in the ionosphere." Journal of Geophysical Research: Space Physics **117**(A6): A06321.

He, H., W. Li, X. Zhang, M. Xia and K. Yang (2012). "Light scattering by a spheroidal bubble with geometrical optics approximation." Journal of Quantitative Spectroscopy and Radiative Transfer **113**(12): 1467-1475.

He, H., M. Xia, W. Li, X. Zhang and K. Yang (2013). "Light scattering by a spheroid bubble with ray tracing method." Optik - International Journal for Light and Electron Optics **124**(10): 871-875.

Hedin, A. E. (1991). "Extension of the MSIS Thermosphere Model into the Middle and Lower Atmosphere." J. Geophys. Res. **96**(A2): 1159-1172.

Helmboldt, J. F., T. J. W. Lazio, H. T. Intema and K. F. Dymond (2012). "High-precision measurements of ionospheric TEC gradients with the Very Large Array VHF system." Radio Science **47**(6): RS0K02.

Herne, D., J. Kennewell, M. Lynch and C. Carrano (2013). Ionospheric Phenomena and Low-Frequency Radio Astronomy. 13th Australian Space Science Conference, Sydney, NSW, Australia, National Space Society of Australia Ltd.

Huang, X., U. o. M. L. Center for Atmospheric Research, MA, U.S.A., B. W. Reinisch, U. o. M. L. Center for Atmospheric Research, MA, U.S.A., D. Bilitza, G. Raytheon ITSS, Code 632, Greenbelt, MD, U.S.A., R. F. Benson and C. GSFC, Greenbelt, MD, U.S.A. (2002). "Electon density profiles of the topside ionosphere." Annals of Geophysics.

Hysell, D. L., E. Nossa, H. C. Aveiro, M. F. Larsen, J. Munro, M. P. Sulzer and S. A. González (2013). "Fine structure in midlatitude sporadic E layers." Journal of Atmospheric and Solar-Terrestrial Physics **103**(0): 16-23.

Jansky, K. G. (1933). "Electrical Disturbances Apparently Of Extraterrestrial Origin." Proceedings of the IEEE **86**(7): 1510-1515.

Johnston, S., R. Taylor, M. Bailes, N. Bartel, C. Baugh, M. Bietenholz, C. Blake, R. Braun, J. Brown, S. Chatterjee, J. Darling, A. Deller, R. Dodson, P. Edwards, R. Ekers, S. Ellingsen, I. Feain, B. Gaensler, M. Haverkorn, G. Hobbs, A. Hopkins, C. Jackson, C. James, G. Joncas, V. Kaspi, V. Kilborn, B. Koribalski, R. Kothes, T. Landecker, A. Lenc, J. Lovell, J.-P. Macquart, R. Manchester, D. Matthews, N. McClure-Griffiths, R. Norris, U.-L. Pen, C. Phillips, C. Power, R. Protheroe, E. Sadler, B. Schmidt, I. Stairs, L. Staveley-Smith, J. Stil, S. Tingay, A. Tzioumis, M. Walker, J. Wall and M. Wolleben (2008). "Science with ASKAP. The Australian square-kilometre-array pathfinder." Experimental Astronomy **22**: 151-273.

Kagan, L. M. (2002). "Effects of neutral gas motions on midlatitude E region irregular structure." Journal of Atmospheric and Solar-Terrestrial Physics **64**(12–14): 1479-1486.

Kaladze, T. D., G. D. Aburjania, O. A. Kharshiladze, W. Horton and Y. H. Kim (2004). "Theory of magnetized Rossby waves in the ionospheric E layer." J. Geophys. Res. **109**(A5): A05302.

Kennewell, J., J. Caruana, M. Terkildsen, J. Wu, P. Wilkinson and D. Cole (2005). "The Australian Ionosphere." 56.

Kennewell, J., J. Caruana, M. Terkildsen, J. Wu, P. Wilkinson and D. Cole (2005). The Australian Ionosphere - Report to CSIRO by IPS Radio and Space Services.

King, G. A. M. (1970). "Spread-F on ionograms." Journal of Atmospheric and Terrestrial Physics **32**(2): 209-221.

Komesaroff, M. (1960). "Ionospheric Refraction in Radio Astronomy. I. Theory." Australian Journal of Physics **13**(2): 153-167.

Kubyshkina, M., V. Sergeev, N. Tsyganenko, V. Angelopoulos, A. Runov, E. Donovan, H. Singer, U. Auster and W. Baumjohann (2011). "Time−dependent magnetospheric configuration and breakup mapping during a substorm." Journal of Geophysical Research: Space Physics (1978–2012) **116**(A5).

Kumar, S., S. Priyadarshi, S. Gopi Krishna and A. K. Singh (2012). "GPS-TEC variations during low solar activity period (2007–2009) at Indian low latitude stations." Astrophys Space Sci **339**.

Kung Chie, Y. and L. Chao-Han (1982). "Radio wave scintillations in the ionosphere." Proceedings of the IEEE **70**(4): 324-360.

Li, Z., M. Hudson, B. Kress and J. Paral (2015). "Three-dimensional test particle simulation of the 17–18 March 2013 CME shock-driven storm." Geophysical Research Letters **42**(14): 2015GL064627.

Liou, Y. A., A. G. Pavelyev, J. Wickert, S. F. Liu, A. A. Pavelyev, T. Schmidt and K. Igarashi (2006). "Application of GPS radio occultation method for observation of the internal waves in the atmosphere." Journal of Geophysical Research: Atmospheres **111**(D6): n/a-n/a.

Little, C. G., W. M. Rayton and R. B. Roof (1956). "Review of Ionospheric Effects at VHF and UHF." Proceedings of the IRE **44**(8): 992-1018.

Liu, Y., W. B. Manchester, IV, J. C. Kasper, J. D. Richardson and J. W. Belcher (2007). "Determining the Magnetic Field Orientation of Coronal Mass Ejections from Faraday Rotation." The Astrophysical Journal **665**: 1439-1447.

Lonsdale, C. J., R. J. Cappallo, M. F. Morales, F. H. Briggs, L. Benkevitch, J. D. Bowman, J. D. Bunton, S. Burns, B. E. Corey, L. deSouza, S. S. Doeleman, M. Derome, A. Deshpande, M. R. Gopala, L. J. Greenhill, D. E. Herne, J. N. Hewitt, P. A. Kamini, J. C. Kasper, B. B. Kincaid, J. Kocz, E. Kowald, E. Kratzenberg, D. Kumar, M. J. Lynch, S. Madhavi, M. Matejek, D. A. Mitchell, E. Morgan, D. Oberoi, S. Ord, J. Pathikulangara, T. Prabu, A. Rogers, A. Roshi, J. E. Salah, R. J. Sault, N. U. Shankar, K. S. Srivani, J. Stevens, S. Tingay, A. Vaccarella, M. Waterson, R. B. Wayth, R. L. Webster, A. R. Whitney, A. Williams and C. Williams (2009). "The Murchison Widefield Array: Design Overview." Proceedings of the IEEE **97**(8): 1497-1506.

Lonsdale, C. J., R. J. Cappallo, M. F. Morales, F. H. Briggs, L. Benkevitch, J. D. Bowman, J. D. Bunton, S. Burns, B. E. Corey, L. Desouza, S. S. Doeleman, M. Derome, A. Deshpande, M. R. Gopala, L. J. Greenhill, D. E. Herne, J. N. Hewitt, P. A. Kamini, J. C. Kasper, B. B. Kincaid, J.

Kocz, E. Kowald, E. Kratzenberg, D. Kumar, M. J. Lynch, S. Madhavi, M. Matejek, D. A. Mitchell, E. Morgan, D. Oberoi, S. Ord, J. Pathikulangara, T. Prabu, A. Rogers, A. Roshi, J. E. Salah, R. J. Sault, N. U. Shankar, K. S. Srivani, J. Stevens, S. Tingay, A. Vaccarella, M. Waterson, R. B. Wayth, R. L. Webster, A. R. Whitney, A. Williams and C. Williams (2009). "The Murchison Widefield Array: Design Overview." IEEE Proceedings **97**: 1497-1506.

Lutgens, F. K. (1995). The Atmosphere, Prentice Hall.

Lynn, K. J. W., R. Gardiner-Garden, M. Sjarifudin, M. Terkildsen, J. Shi and T. J. Harris (2008). "Large-scale travelling atmospheric disturbances in the night ionosphere during the solar–terrestrial event of 23 May 2002." Journal of Atmospheric and Solar-Terrestrial Physics **70**(17): 2184-2195.

Lyon, J. G. (2000). "The Solar Wind-Magnetosphere-Ionosphere System." Science **288**(5473): 1987-1991.

MacDougall, J., M. A. Abdu, I. Batista, P. R. Fagundes, Y. Sahai and P. T. Jayachandran (2009). "On the production of traveling ionospheric disturbances by atmospheric gravity waves." Journal of Atmospheric and Solar-Terrestrial Physics **71**(17–18): 2013-2016.

MacDougall, J. W. and P. T. Jayachandran (2011). "Solar terminator and auroral sources for traveling ionospheric disturbances in the midlatitude F region." Journal of Atmospheric and Solar-Terrestrial Physics **73**(17–18): 2437-2443.

Mannucci, A. J., B. T. Tsurutani, M. A. Abdu, W. D. Gonzalez, A. Komjathy, E. Echer, B. A. Iijima, G. Crowley and D. Anderson (2008). "Superposed epoch analysis of the dayside ionospheric response to four intense geomagnetic storms." Journal of Geophysical Research: Space Physics **113**(A3): n/a-n/a.

Mao, S. A., B. M. Gaensler, S. Stanimirovic, M. Haverkorn, N. M. McClure-Griffiths, L. Staveley-Smith and J. M. Dickey (2008). "A Radio and Optical Polarization Study of the Magnetic Field in the Small Magellanic Cloud." The Astrophysical Journal **688**: 1029-1049.

McFadden, R., R. Ekers and P. Roberts (2012). "A new method to calibrate ionospheric pulse dispersion for UHE cosmic ray and neutrino detection using the Lunar Cherenkov technique." Nuclear Instruments and Methods in Physics Research Section A: Accelerators, Spectrometers, Detectors and Associated Equipment **662, Supplement 1**(0): S234-S237.

Mitchell, D., L. J. Greenhill, M. Clark, F. Briggs, J. Bowman, R. Cappallo, D. L. Kaplan, J. Kasper, J. Kocz, C. J. Lonsdale, J. Stevens, S. Tingay and A. Whitney (2010). The Murchison Widefield Array. RFI Mitigation Workshop**:** 16.

Mitchell, D. A., L. J. Greenhill, R. B. Wayth, R. J. Sault, C. J. Lonsdale, R. J. Cappallo, M. F. Morales and S. M. Ord (2008). "Real-Time Calibration of the Murchison Widefield Array." Selected Topics in Signal Processing, IEEE Journal of **2**(5): 707-717.

Oberoi, D. and L. Benkevitch (2010). "Remote Sensing of the Heliosphere with the Murchison Widefield Array." Solar Physics **265**(1-2): 293-307.

Oberoi, D. and et al. (2011). "First Spectroscopic Imaging Observations of the Sun at Low Radio Frequencies with the Murchison Widefield Array Prototype." The Astrophysical Journal Letters **728**(2): L27.

Oberoi, D. and C. J. Lonsdale (2012). "Media responsible for Faraday rotation: A review." Radio Science **47**.

Oberoi, D., L. D. Matthews, I. H. Cairns, D. Emrich, V. Lobzin, C. J. Lonsdale, E. H. Morgan, T. Prabu, H. Vedantham, R. B. Wayth, A. Williams, C. Williams, S. M. White, G. Allen, W. Arcus, D. Barnes, L.

Benkevitch, G. Bernardi, J. D. Bowman, F. H. Briggs, J. D. Bunton, S. Burns, R. C. Cappallo, M. A. Clark, B. E. Corey, M. Dawson, D. DeBoer, A. De Gans, L. deSouza, M. Derome, R. G. Edgar, T. Elton, R. Goeke, M. R. Gopalakrishna, L. J. Greenhill, B. Hazelton, D. Herne, J. N. Hewitt, P. A. Kamini, D. L. Kaplan, J. C. Kasper, R. Kennedy, B. B. Kincaid, J. Kocz, R. Koeing, E. Kowald, M. J. Lynch, S. Madhavi, S. R. McWhirter, D. A. Mitchell, M. F. Morales, A. Ng, S. M. Ord, J. Pathikulangara, A. E. E. Rogers, A. Roshi, J. E. Salah, R. J. Sault, A. Schinckel, N. Udaya Shankar, K. S. Srivani, J. Stevens, R. Subrahmanyan, D. Thakkar, S. J. Tingay, J. Tuthill, A. Vaccarella, M. Waterson, R. L. Webster and A. R. Whitney (2011). "First Spectroscopic Imaging Observations of the Sun at Low Radio Frequencies with the Murchison Widefield Array Prototype." The Astrophysical Journal Letters **728**: L27.

Oberoi, D., R. Sharma, S. Bhatnagar, C. J. Lonsdale, L. D. Matthews, I. H. Cairns, S. J. Tingay, L. Benkevitch, A. Donea, S. M. White, G. Bernardi, J. D. Bowman, F. Briggs, R. J. Cappallo, B. E. Corey, A. Deshpande, D. Emrich, B. M. Gaensler, R. Goeke, L. J. Greenhill, B. J. Hazelton, M. Johnston-Hollitt, D. L. Kaplan, J. C. Kasper, E. Kratzenberg, M. J. Lynch, S. R. McWhirter, D. A. Mitchell, M. F. Morales, E. Morgan, A. R. Offringa, S. M. Ord, T. Prabu, A. E. E. Rogers, A. Roshi, J. E. Salah, N. Udaya Shankar, K. S. Srivani, R. Subrahmanyan, M. Waterson, R. B. Wayth, R. L. Webster, A. R. Whitney, A. William and C. L. Williams (2014) "Observing the Sun with the Murchison Widefield Array." ArXiv e-prints **1403**, 6250.

Opperman, B. D. L. (2007). "RECONSTRUCTING IONOSPHERIC TEC OVER SOUTH AFRICA USING SIGNALS FROM A REGIONAL GPS NETWORK (PhD Thesis)."

Ord, S. M., D. A. Mitchell, R. B. Wayth, L. J. Greenhill, G. Bernardi, S. Gleadow, R. G. Edgar, M. A. Clark, G. Allen, W. Arcus, L. Benkevitch, J. D. Bowman, F. H. Briggs, J. D. Bunton, S. Burns, R. J. Cappallo, W. A. Coles, B. E. Corey, L. Desouza, S. S. Doeleman, M. Derome, A. Deshpande, D. Emrich, R. Goeke, M. R. Gopalakrishna, D. Herne, J. N. Hewitt, P. A. Kamini, D. L. Kaplan, J. C. Kasper, B. B. Kincaid, J. Kocz, E. Kowald, E. Kratzenberg, D. Kumar, C. J. Lonsdale, M. J. Lynch, S. R. McWhirter, S. Madhavi, M. Matejek, M. F. Morales, E. Morgan, D. Oberoi, J. Pathikulangara, T. Prabu, A. E. E. Rogers, A. Roshi, J. E. Salah, A. Schinkel, N. Udaya Shankar, K. S. Srivani, J. Stevens, S. J. Tingay, A. Vaccarella, M. Waterson, R. L. Webster, A. R. Whitney, A. Williams and C. Williams (2010). "Interferometric Imaging with the 32 Element Murchison Wide-Field Array." Publications of the Astronomical Society of the Pacific **122**: 1353-1366.

Otsuka, Y., T. Tani, T. Tsugawa, T. Ogawa and A. Saito (2008). "Statistical study of relationship between medium-scale traveling ionospheric disturbance and sporadic E layer activities in summer night over Japan." Journal of Atmospheric and Solar-Terrestrial Physics **70**(17): 2196-2202.

Parkinson, M. L. and P. L. Dyson (1998). "Measurements of mid-latitude E-region, sporadic-E, and TID-related drifts using HF Doppler-sorted interferometry." Journal of Atmospheric and Solar-Terrestrial Physics **60**(5): 509-522.

Parsons, A. R., D. C. Backer, R. F. Bradley, J. E. Aguirre, E. E. Benoit, C. L. Carilli, G. S. Foster, N. E. Gugliucci, D. E. Herne and D. C. Jacobs (2009). "THE PRECISION ARRAY FOR PROBING THE EPOCH OF REIONIZATION: 8 STATION RESULTS."

Parsons, A. R., D. C. Backer, G. S. Foster, M. C. H. Wright, R. F. Bradley, N. E. Gugliucci, C. R. Parashare, E. E. Benoit, J. E. Aguirre, D. C. Jacobs, C. L. Carilli, D. Herne, M. J. Lynch, J. R. Manley and D. J.

Werthimer (2010). "The Precision Array for Probing the Epoch of Re-ionization: Eight Station Results." The Astronomical Journal **139**: 1468-1480.

Patra, A. K. and P. Pavan Chaitanya (2014). "Comparative anatomy of the day- and night-time radar echoes from the 130–170 km region of the low latitude ionosphere." Advances in Space Research **54**(3): 395-402.

Rasmussen, J. E., P. A. Kossey and E. A. Lewis (1980). "Evidence of an Ionospheric Reflecting Layer Below the Classical D Region." J. Geophys. Res. **85**(A6): 3037-3044.

Rawer, K. (1993). Wave Propagation in the Ionosphere. Dordrecht, Kluwer Academic Publishers.

Reber, G. (1942). "Cosmic Static." Proceedings of the IRE **30**(8): 367-378.

Roble, G. R. (1996). Atmospheric Structure. Encyclopedia of Applied Physics. T. G. L., Wiley**:** 24.

Roble, R. G. and E. C. Ridley (1994). "A thermosphere-ionosphere-mesosphere-electrodynamics general circulation model (time-GCM): Equinox solar cycle minimum simulations (30-500 km)." Geophys. Res. Lett. **21**(6): 417-420.

Rust, D. M., D. K. Haggerty, M. K. Georgoulis, N. R. Sheeley, Y.-M. Wang, M. L. DeRosa and C. J. Schrijver (2008). "On the Solar Origins of Open Magnetic Fields in the Heliosphere." The Astrophysical Journal **687**(1): 635.

Sabaka, T. J., N. Olsen and R. A. Langel (2002). "A comprehensive model of the quiet-time, near-Earth magnetic field: phase 3." Geophysical Journal International **151**(1): 32-68.

Shiokawa, K., M. Mori, Y. Otsuka, S. Oyama, S. Nozawa, S. Suzuki and M. Connors (2013). "Observation of nighttime medium-scale travelling ionospheric disturbances by two 630-nm airglow imagers near the auroral zone." Journal of Atmospheric and Solar-Terrestrial Physics **103**(0): 184-194.

Sieradzki, R., I. Cherniak and A. Krankowski (2013). "Near-real time monitoring of the TEC fluctuations over the northern hemisphere using GNSS permanent networks." Advances in Space Research **52**(3): 391-402.

Smith, F. G. (1959). "Radio studies of artificial satellites (Report on Progress of Astronomy)." Monthly Notices of the Royal Astronomical Society **119**: 433.

Sojka, J. J., D. Rice, J. V. Eccles, F. T. Berkey, P. Kintner and W. Denig (2004). "Understanding midlatitude space weather: Storm impacts observed at Bear Lake Observatory on 31 March 2001." Space Weather **2**(10): n/a-n/a.

Solomon, S. C., T. N. Woods, L. V. Didkovsky, J. T. Emmert and L. Qian (2010). "Anomalously low solar extreme-ultraviolet irradiance and thermospheric density during solar minimum." Geophys. Res. Lett. **37**(16): L16103.

Sotomayor-Beltran, C., C. Sobey, J. W. T. Hessels, G. de Bruyn, A. Noutsos, A. Alexov, J. Anderson, A. Asgekar, I. M. Avruch, R. Beck, M. E. Bell, M. R. Bell, M. J. Bentum, G. Bernardi, P. Best, L. Birzan, A. Bonafede, F. Breitling, J. Broderick, W. N. Brouw, M. Brüggen, B. Ciardi, F. de Gasperin, R.-J. Dettmar, A. van Duin, S. Duscha, J. Eislöffel, H. Falcke, R. A. Fallows, R. Fender, C. Ferrari, W. Frieswijk, M. A. Garrett, J. Grießmeier, T. Grit, A. W. Gunst, T. E. Hassall, G. Heald, M. Hoeft, A. Horneffer, M. Iacobelli, E. Juette, A. Karastergiou, E. Keane, J. Kohler,

M. Kramer, V. I. Kondratiev, L. V. E. Koopmans, M. Kuniyoshi, G. Kuper, J. van Leeuwen, P. Maat, G. Macario, S. Markoff, J. P. McKean, D. D. Mulcahy, H. Munk, E. Orru, H. Paas, M. Pandey-Pommier, M. Pilia, R. Pizzo, A. G. Polatidis, W. Reich, H. Röttgering, M. Serylak, J. Sluman, B. W. Stappers, M. Tagger, Y. Tang, C. Tasse, S. ter Veen, R. Vermeulen, R. J. van Weeren, R. A. M. J. Wijers, S. J. Wijnholds, M. W. Wise, O. Wucknitz, S. Yatawatta and P. Zarka (2013). "Calibrating high-precision Faraday rotation measurements for LOFAR and the next generation of low-frequency radio telescopes." Astronomy and Astrophysics **552**: 58.

Sotomayor-Beltran, C., C. Sobey, J. W. T. Hessels, G. de Bruyn, A. Noutsos, A. Alexov, J. Anderson, A. Asgekar, I. M. Avruch, R. Beck, M. E. Bell, M. R. Bell, M. J. Bentum, G. Bernardi, P. Best, L. Birzan, A. Bonafede, F. Breitling, J. Broderick, W. N. Brouw, M. Brüggen, B. Ciardi, F. de Gasperin, R.-J. Dettmar, A. van Duin, S. Duscha, J. Eislöffel, H. Falcke, R. A. Fallows, R. Fender, C. Ferrari, W. Frieswijk, M. A. Garrett, J. Grießmeier, T. Grit, A. W. Gunst, T. E. Hassall, G. Heald, M. Hoeft, A. Horneffer, M. Iacobelli, E. Juette, A. Karastergiou, E. Keane, J. Kohler, M. Kramer, V. I. Kondratiev, L. V. E. Koopmans, M. Kuniyoshi, G. Kuper, J. van Leeuwen, P. Maat, G. Macario, S. Markoff, J. P. McKean, D. D. Mulcahy, H. Munk, E. Orru, H. Paas, M. Pandey-Pommier, M. Pilia, R. Pizzo, A. G. Polatidis, W. Reich, H. Röttgering, M. Serylak, J. Sluman, B. W. Stappers, M. Tagger, Y. Tang, C. Tasse, S. ter Veen, R. Vermeulen, R. J. van Weeren, R. A. M. J. Wijers, S. J. Wijnholds, M. W. Wise, O. Wucknitz, S. Yatawatta and P. Zarka (2015). "Calibrating high-precision Faraday rotation measurements for LOFAR and the next generation of low-frequency radio telescopes (Corrigendum)." A&A **581**: C4.

Székely, G. J. and M. L. Rizzo (2012). "On the uniqueness of distance covariance." Statistics & Probability Letters **82**(12): 2278-2282.

Taylor, M. J., J. M. Jahn, S. Fukao and A. Saito (1998). "Possible evidence of gravity wave coupling into the mid-latitude F region ionosphere during the SEEK Campaign." Geophysical Research Letters **25**(11): 1801-1804.

Tingay, S. J., R. Goeke, J. D. Bowman, D. Emrich, S. M. Ord, D. A. Mitchell, M. F. Morales, T. Booler, B. Crosse, D. Pallot, A. Wicenec, W. Arcus, D. Barnes, G. Bernardi, F. Briggs, S. Burns, J. D. Bunton, R. J. Cappallo, T. Colegate, B. E. Corey, A. Deshpande, L. deSouza, B. M. Gaensler, L. J. Greenhill, J. Hall, B. J. Hazelton, D. Herne, J. N. Hewitt, M. Johnston-Hollitt, D. L. Kaplan, J. C. Kasper, B. B. Kincaid, R. Koenig, E. Kratzenberg, C. J. Lonsdale, M. J. Lynch, B. McKinley, S. R. McWhirter, E. Morgan, D. Oberoi, J. Pathikulangara, T. Prabu, R. A. Remillard, A. E. E. Rogers, A. Roshi, J. E. Salah, R. J. Sault, N. Udaya-Shankar, F. Schlagenhaufer, K. S. Srivani, J. Stevens, R. Subrahmanyan, S. Tremblay, R. B. Wayth, M. Waterson, R. L. Webster, A. R. Whitney, A. Williams, C. L. Williams and J. S. B. Wyithe (2012) "The Murchison Widefield Array: the Square Kilometre Array Precursor at low radio frequencies." ArXiv e-prints **1206**, 6945.

Tingay, S. J., D. L. Kaplan, B. McKinley, F. Briggs, R. B. Wayth, N. Hurley-Walker, J. Kennewell, C. Smith, K. Zhang, W. Arcus, N. D. R. Bhat, D. Emrich, D. Herne, N. Kudryavtseva, M. Lynch, S. M. Ord, M. Waterson, D. G. Barnes, M. Bell, B. M. Gaensler, E. Lenc, G. Bernardi, L. J. Greenhill, J. C. Kasper, J. D. Bowman, D. Jacobs, J. D. Bunton, L. deSouza, R. Koenig, J. Pathikulangara, J. Stevens, R. J. Cappallo, B. E. Corey, B. B. Kincaid, E. Kratzenberg, C. J. Lonsdale, S. R. McWhirter, A. E. E. Rogers, J. E. Salah, A. R. Whitney, A. Deshpande, T. Prabu, N. U. Shankar, K. S. Srivani, R. Subrahmanyan, A. Ewall-Wice, L. Feng, R. Goeke, E. Morgan, R. A. Remillard, C. L. Williams, B. J. Hazelton, M. F. Morales, M. Johnston-Hollitt, D. A. Mitchell, P. Procopio, J. Riding, R. L. Webster, J. S. B. Wyithe, D. Oberoi, A. Roshi, R. J. Sault and A.

Williams (2013). "On the Detection and Tracking of Space Debris Using the Murchison Widefield Array. I. Simulations and Test Observations Demonstrate Feasibility." The Astronomical Journal **146**(4): 103.

Titheridge (1986). "Starting models for the real height analysis of ionograms." Journal of Atmospheric and Terrestrial Physics **48**(5): 435-446.

Uma, G., P. S. Brahmanandam, Y. Kakinami, A. Dmitriev, N. S. M. P. Latha Devi, K. Uday Kiran, D. S. V. V. D. Prasad, P. V. S. Rama Rao, K. Niranjan, C. Seshu Babu and Y. H. Chu (2012). "Ionospheric responses to two large geomagnetic storms over Japanese and Indian longitude sectors." Journal of Atmospheric and Solar-Terrestrial Physics **74**(0): 94-110.

Vadas, S. L., H. L. Liu and R. S. Lieberman (2014). "Numerical modeling of the global changes to the thermosphere and ionosphere from the dissipation of gravity waves from deep convection." Journal of Geophysical Research: Space Physics **119**(9): 7762-7793.

van Haarlem, M. P., M. W. Wise, A. W. Gunst, G. Heald, J. P. McKean, J. W. T. Hessels, A. G. de Bruyn, R. Nijboer, J. Swinbank, R. Fallows, M. Brentjens, A. Nelles, R. Beck, H. Falcke, R. Fender, J. Hörandel, L. V. E. K. G. Mann, G. Miley, H. Röttgering, B. W. Stappers, R. A. M. J. Wijers, S. Zaroubi, M. van den Akker, A. Alexov, J. Anderson, K. Anderson, A. van Ardenne, M. Arts, A. Asgekar, I. M. Avruch, F. Batejat, L. Bähren, M. E. Bell, M. R. Bell, I. van Bemmel, P. Bennema, M. J. Bentum, G. Bernardi, P. Best, L. Bîrzan, A. Bonafede, A.-J. Boonstra, R. Braun, J. Bregman, F. Breitling, R. H. van de Brink, J. Broderick, P. C. Broekema, W. N. Brouw, M. Brüggen, H. R. Butcher, W. van Cappellen, B. Ciardi, T. Coenen, J. Conway, A. Coolen, A. Corstanje, S. Damstra, O. Davies, A. T. Deller, R.-J. Dettmar, G. van Diepen, K. Dijkstra, P. Donker, A. Doorduin, J. Dromer, M. Drost, A. van Duin, J. Eislöffel, J. van Enst, C.

Ferrari, W. Frieswijk, H. Gankema, M. A. Garrett, F. de Gasparin, M. Gerbers, E. de Geus, J.-M. Grießmeier, T. Grit, P. Gruppen, J. P. Hamaker, T. Hassall, M. Hoeft, H. Holties, A. Horneffer, A. van der Horst, A. van Houwelingen, A. Huijgen, M. Iacobelli, H. Intema, N. Jackson, V. Jelic, A. de Jong, D. Kant, A. Karastergiou, A. Koers, H. Kollen, V. I. Kondratiev, E. Kooistra, Y. Koopman, A. Koster, M. Kuniyoshi, M. Kramer, G. Kuper, P. Lambropoulos, C. Law, J. van Leeuwen, J. Lemaitre, M. Loose, P. Maat, G. Macario, S. Markoff, J. Masters, D. McKay-Bukowski, H. Meijering, H. Meulman, M. Mevius, R. Millenaar, J. C. A. Miller-Jones, R. N. Mohan, J. D. Mol, J. Morawietz, R. Morganti, D. D. Mulcahy, E. Mulder, H. Munk, L. Nieuwenhuis, R. van Nieuwpoort, J. E. Noordam, M. Norden, A. Noutsos, A. R. Offringa, H. Olofsson, A. Omar, E. Orrú, R. Overeem, H. Paas, M. Pandey-Pommier, V. N. Pandey, R. Pizzo, A. Polatidis, D. Rafferty, S. Rawlings, W. Reich, J.-P. de Reijer, J. Reitsma, A. Renting, P. Riemers, E. Rol, J. W. Romein, J. Roosjen, M. Ruiter, A. Scaife, K. van der Schaaf, B. Scheers, P. Schellart, A. Schoenmakers, G. Schoonderbeek, M. Serylak, A. Shulevski, J. Sluman, O. Smirnov, C. Sobey, H. Spreeuw, M. Steinmetz, C. G. M. Sterks, H.-J. Stiepel, K. Stuurwold, M. Tagger, Y. Tang, C. Tasse, I. Thomas, S. Thoudam, M. C. Toribio, B. van der Tol, O. Usov, M. van Veelen, A.-J. van der Veen, S. ter Veen, J. P. W. Verbiest, R. Vermeulen, N. Vermaas, C. Vocks, C. Vogt, M. de Vos, E. van der Wal, R. van Weeren, H. Weggemans, P. Weltevrede, S. White, S. J. Wijnholds, T. Wilhelmsson, O. Wucknitz, S. Yatawatta, P. Zarka, A. Zensus and J. van Zwieten (2013) "LOFAR: The LOw-Frequency ARray." ArXiv e-prints **1305**, 3550.

Van Velthoven, P. F. J., C. Mercier and H. Kelder (1990). "Simultaneous observations of travelling ionospheric disturbances by two-dimensional radio interferometry and the differential Doppler technique applied to satellite signals." Journal of Atmospheric and Terrestrial Physics **52**(4): 305-312.

van Velthoven, P. F. J. and T. A. T. Spoelstra (1992). "Climatology of medium scale travelling ionospheric disturbances from radio interferometric observations." Advances in Space Research **12**(6): 211-214.

Wakai, N., H. Ohyama and T. Koizumi (1987). "Manual of Ionogram Scaling - Third Version." Radio Research Laboratory.

Waldock, J. A. and T. B. Jones (1984). "The effects of neutral winds on the propagation of medium-scale atmospheric gravity waves at mid-latitudes." Journal of Atmospheric and Terrestrial Physics **46**(3): 217-231.

Waldock, J. A. and T. B. Jones (1987). "Source regions of medium scale travelling ionospheric disturbances observed at mid-latitudes." Journal of Atmospheric and Terrestrial Physics **49**(2): 105-114.

Williams, C. L., J. N. Hewitt, A. M. Levine, A. de Oliveira-Costa, J. D. Bowman, F. H. Briggs, B. M. Gaensler, L. L. Hernquist, D. A. Mitchell, M. F. Morales, S. K. Sethi, R. Subrahmanyan, E. M. Sadler, W. Arcus, D. G. Barnes, G. Bernardi, J. D. Bunton, R. C. Cappallo, B. W. Crosse, B. E. Corey, A. Deshpande, L. deSouza, D. Emrich, R. F. Goeke, L. J. Greenhill, B. J. Hazelton, D. Herne, D. L. Kaplan, J. C. Kasper, B. B. Kincaid, R. Koenig, E. Kratzenberg, C. J. Lonsdale, M. J. Lynch, S. R. McWhirter, D. A. Mitchell, M. F. Morales, E. H. Morgan, D. Oberoi, S. M. Ord, J. Pathikulangara, T. Prabu, R. A. Remillard, A. E. E. Rogers, A. A. Roshi, J. E. Salah, R. J. Sault, N. Udaya Shankar, K. S. Srivani, J. B. Stevens, S. J. Tingay, R. B. Wayth, M. Waterson, R. L. Webster, A. R. Whitney, A. J. Williams and J. S. B. Wyithe (2012) "Low Frequency Imaging of Fields at High Galactic Latitude with the Murchison Widefield Array 32-Element Prototype." ArXiv e-prints **1203**, 5790.

Xiao, F., C. Yang, Z. He, Z. Su, Q. Zhou, Y. He, C. A. Kletzing, W. S. Kurth, G. B. Hospodarsky, H. E. Spence, G. D. Reeves, H. O. Funsten, J. B. Blake, D. N. Baker and J. R. Wygant (2014). "Chorus acceleration of radiation belt relativistic electrons during March 2013 geomagnetic storm." Journal of Geophysical Research: Space Physics **119**(5): 3325-3332.

Yokoyama, T. "Hemisphere-coupled modeling of nighttime medium-scale traveling ionospheric disturbances." Advances in Space Research(0).

Zhang, M.-L., B. W. Reinisch, J.-K. Shi, S.-Z. Wu and X. Wang (2006). "Diurnal and seasonal variation of the ionogram-derived scale height at the F2 peak." Advances in Space Research **37**(5): 967-971.